eXPRESS Polymer Letters Vol.10, No.8 (2016) 627
Available online at www.expresspolymlett.com
DOI: 10.3144/expresspolymlett.2016.57

Editorial corner – a personal view

'Waking sleeping beauty': Regeneration of vulcanized rubber by triggering dynamicity of the inherent sulfur network

*M. Q. Zhang**

Materials Science Institute, Sun Yat-sen (Zhongshan) University, 510275 Guangzhou, P. R. China

Vulcanized rubber has been widely applied in modern society, which causes severe impact on environment in the meantime. This is because there are no proper disposals of the scraps, which are full of infusible and insoluble crosslinked networks. So far, methods have been developed to convert waste rubbers into small molecular weight fragments with commercial value, or granules as fillers of thermoplastics and asphalt. In some cases, the used rubber products are simply burned and buried. The bad resource management leads to significant pollution accordingly (DOI: 10.3144/expresspolymlett.2016.17).

When reviewing vulcanized rubber, we can find that the key technique of fabrication, i.e. vulcanization, remains nearly unchanged since the invention of Goodyear about two hundred years ago. The crosslinked networks contain tremendous disulfide and polysulfide bonds. Recent investigation indicates that metathesis of disulfide enables self-healing of polymers. In this context, so long as disulfide metathesis among different disulfide and polysulfide bonds can be triggered in sulfur crosslinked networks, the vulcanized rubber would acquire self-healability and recyclability.

In a patented invention, tiny amount of catalysts ($CuCl_2$ and copper(II) methacrylate) are incorporated into polybutadiene and chloroprene rubber, which are then compounded with the usual fillers and curatives following industrial formulation. The preliminary results (DOI: 10.1039/c5gc00754b and DOI: 10.1021/acssuschemeng.6b00224) show that the catalysts can effectively initiate metathesis of disulfide bonds, so that the inherent sulfur crosslinks of the vulcanized rubbers are allowed to be dynamically rearranged and reshuffled at 110~120 °C. It means that the sulfur crosslinks are as stable as the version excluding the catalysts under conventional circumstances without fear of loosing stability during service at lower temperature (typically below 110 °C). More importantly, by taking advantage of the activated crosslinked networks, the vulcanized rubbers can be repeatedly self-healed, reshaped, and recycled in solid phase at 110~120 °C without environmentally unfriendly de-crosslinking. Additionally, mechanical properties of the healed and recycled materials approach to those of the original version. The catalysts do not react with the other additives in the matrix and do not accelerate aging of the rubbers.

The availability of self-healing, reshaping and reprocessing of vulcanized rubber offers new possibilities of cyclic utilization. Different circulation loops can be selected by various combinations of the smart functionalities according to actual demand. Life cycle of rubbers would thus be extended, while waste of resources is reduced.

There maybe other 'sleeping beauties' like the above in everyday life, which are waiting for being waked.

Prof. Dr. Ming Qiu Zhang
Member of International Advisory Board

*Corresponding author, e-mail: ceszmq@mail.sysu.edu.cn

eXPRESS Polymer Letters Vol.10, No.8 (2016) 628–646
Available online at www.expresspolymlett.com
DOI: 10.3144/expresspolymlett.2016.58

Semiconducting, biodegradable and bioactive fibers for drug delivery

M. M. Pérez-Madrigal[1,2], E. Llorens[1,2], L. J. del Valle[1,2], J. Puiggalí[1,2], E. Armelin[1,2], C. Alemán[1,2]*

[1]Departament d'Enginyeria Química, Universitat Politècnica de Catalunya, Av. Diagonal 647, E-08028 Barcelona, Spain
[2]Center for Research in Nano-Engineering, Universitat Politècnica de Catalunya, Campus Sud, Edifici C', C/Pasqual i Vila s/n, E-08028 Barcelona, Spain

Received 4 December 2015; accepted in revised form 25 February 2016

Abstract. In this work we present the drug release properties and morphological studies of fibers formed by mixing different ratios of poly(lactic acid) (PLA) and poly(3-thiophene methyl acetate) (P3TMA) loaded with four drugs (ciprofloxacin, chlorhexidine dihydrochloride, triclosan and ibuprofen sodium salt). Thus, the main aim of this study is to prove that the excellent cellular response of PLA-P3TMA biocompatible scaffolds can be successfully combined with essential applications as drug carrier and delivery systems. Atomic force microscopic (AFM) and scanning electron microscopic (SEM) micrographs of PLA-P3TMA fibers indicate that the presence of the conducting polymer inside the PLA matrix affects the surface morphology, resulting in a significant increment of the bulk conductivity with respect to PLA fibers. Electrospun hybrid fibers of PLA and P3TMA successfully load both hydrophilic and hydrophobic drugs, the release profiles depending on the release environment (*i.e.* the release rate increases with the hydrophobicity of the medium). Finally, our results prove that the antibacterial activity of the drugs is not affected by their interactions with the PLA-P3TMA matrix.

Keywords: *biopolymers, biocomposites, conducting polymers, nanotechnology, atomic force microscopy (AFM), drug delivery systems*

1. Introduction

Research based on the use of bioplastics and biosolvents for the development of advanced materials has increased considerably in the last decade. Poly(lactic acid) (PLA), a 100% biodegradable biopolymer, has been extensively investigated and used in different commercial and industrial applications, such as automotive parts, clothing and carpet fibers, food packaging, among others. PLA can be synthesized by polycondensation from lactic acid, which is a renewable resource derived from the starch of either corn of sugar beets that is fermented to form glucose and, consequently, converted to lactic acid. Accordingly, PLA can be considered as active player in green chemistry as it reduces significantly the carbon footprint when compared to other oil based traditional plastics. Furthermore, due to its good mechanical integrity, biodegradability and biocompatibility, PLA and its copolymers are widely used in biomedical fields. Thus, these materials have been employed for the fabrication of drug loading and release devices, surgical sutures, and scaffolds for tissue and nerve regeneration [1–7].

On the other hand, electroactive conducting polymers (CPs) represent another important family of organic materials with proved biocompatibility [5, 8–14]. More specifically, CPs have attracted the attention of biomedical engineers because cells respond to external electrical and/or electrochemical stimuli *in vitro* and *in vivo* when in contact with CPs [12–14]. Thus, application of external potentials has been found to promote cellular adhesion, proliferation,

*Corresponding author, e-mail: elaine.armelin@upc.edu

growth and differentiation. For example, Schmidt and co-workers proved that neurite length of PC-12 cells cultured on polypyrrole (PPy) films increase upon the application of electrical stimuli [15]. These observations suggested that rationally designed conducting and electroactive nanoconstructs (*e.g.* nanomembranes and nanofibers) could act simultaneously as scaffolds for tissue engineering [14, 15] and efficient systems for drug targeting and delivery [16–18]. Indeed, CPs are attractive for a number of biomedical applications as was reviewed by Schmidt and co-workers [19].

One of the major drawbacks in the use of CPs for biomedical applications is the lack of mechanical integrity and restricted processability of many of these materials, combined with their non-degradability [5]. Limitations of CPs are frequently overcome by blending these materials with biodegradable polymers [5–20]. Albertsson and co-workers have vastly studied the combination of biodegradable polymers with CPs for bioengineering applications [20]. For example, such group studied the degradability and cytotoxicity of blends made of caprolactone and hyperbranched degradable CPs as good candidates for neural tissue engineering application [21]. More recently, free-standing nanomembranes for tissue regeneration were prepared by spin-coating mixtures of polyester [22, 23] or thermoplastic polyurethane [24] with a soluble polythiophene derivative, poly(3-thiophene methyl acetate) (P3TMA). The same approach has also been used to fabricate electroactive biodegradable 3D scaffolds. For example, regular microfibers were recently obtained by electrospinning a mixture of P3TMA and biodegradable poly(ester urea) [25]. Overall the results obtained in this field proved the synergy associated with the combination of biodegradable polymers and CPs, their mixtures showing biodegradability and both electrochemical and electrical activities.

In the last years some studies based on nanofibers made of PLA–CP blends have been reported. However, the preparation of such nanoconstructs has been essentially restricted to the combination of biodegradable polymer with small electroactive oligomers (*e.g.* oligothiophenes [26] and oligoanilines [27, 28], polyaniline (PAni) or PPy derivatives [20, 29–31]. On the other hand, antecedents on drug delivery systems fabricated with nanofibers based on biodegradable polymers–CP blends are very scarce. Martin and co-workers developed electrospun poly (lactide-*co*-glycolide)–poly(3,4-ethylenedioxythiophene) conductive core-sheath nanofibers (PLGA–PEDOT) able to modulate the release of dexamethasone, an anti-inflammatory drug for the central nervous system [32]. More recently, we designed and synthesized series of linear micro/nanofibers for tissue engineering applications using PLA–P3TMA blends with different compositions [33]. Scaffolds containing P3TMA exhibited enhanced cellular proliferation and adhesion in comparison to those made of pristine PLA. Such improvement was attributed to the electrochemical properties (*i.e.* ability to exchange ions) and wettability properties provided by the CP.

The objective of the present work is to show the multifunctionality of scaffolds made of PLA–P3TMA fibers, which is based on the combination of the already known cellular response [33] with their high activity as drug carrier and delivery systems. In order to prove this duality, the encapsulation and delivery of different drugs in PLA–P3TMA systems have been investigated by controlling both the fiber morphology and the composition of the blend. Four drugs have been considered for this purpose: ciprofloxacin (CIP), chlorhexidine dihydrochloride (CHX), triclosan (TCS), and ibuprofen sodium salt (IBU). The selection of these compounds was based on the fact they are typically considered as model antibiotics (CIP), biocides (CHX and TCS) and anti-inflammatories (IBU).

2. Experimental section

2.1. Materials

3-Thiophene acetic acid (3TAA) (98.0%) was purchased from Fluka (Sigma-Aldrich). Iron chloride anhydrous (97.0%), dry methanol (99.5%) and chloroform (99.9%) were purchased from Panreac Quimica S.A.U. (Spain) and used as received without further purification. PLA, a product of Natureworks (polymer 2002D), was kindly supplied by Nupik International (Polinyà, Spain). According to the manufacturer, this PLA has a D-lactide content of 4.25%, a residual monomer content of 0.3%, a density of 1.24 g/cc, a glass transition temperature (T_g) of 58 °C, a melting point of 153 °C and molecular weights of M_n = 59 300 g·mol^{-1} and M_w = 117 500 g·mol^{-1}. CIP (≥98% HPLC), CHX (≥98%), TCS (irgasan, ≥97% HPLC), and IBU (≥98% GC) were purchased from Sigma-Aldrich. *Escherichia coli* CECT 101 and *Staphylococcus epidermidis* CECT 231 bacterial strains

were obtained from the Spanish Collection of Type Culture (Valencia, Spain), and culture media were purchased from Difco (Detroit, MI, USA).

2.2. Synthesis of poly(3-thiophene methyl acetate)

P3TMA was synthesized by chemical oxidative coupling polymerization in dry chloroform following the procedure described by Kim *et al.* [34], which was successfully used in previous works [22–25]. Anhydrous ferric chloride ($FeCl_3$) was used as both oxidant and dopant. The monomer 3-thiophene methyl acetate (3TMA) was obtained with a 74% yield by refluxing 3TAA in dry methanol for 24 hours at a temperature of 90 °C. P3TMA was subsequently prepared by a chemical oxidative coupling polymerization in dry chloroform and using anhydrous ferric chloride ($FeCl_3$) as oxidant and dopant. The polymerization yield was *ca*. 61% after removing the residual oxidant oligomers. Molecular weights were estimated by size exclusion chromatography (SEC) using 1,1,1,3,3,3-hexafluoroisopropanol as eluent. The number and weight average molecular weights found were M_n = 10 700 g·mol^{-1} and M_w = 22 500 g·mol^{-1} for P3TMA. ^{1}H-NMR (400 MHz, $CDCl_3$) δ = 7.28–7.07 (m, 1H, Ar-H), 3.68(s, 2H, –CH_2–), 3.63 (s, 3H, O–CH_3); ^{13}C-NMR (100 MHz, $CDCl_3$) δ = 170.8 (C=O), 136–124 (Ar–C), 52.1 (O–CH_3), 34.3 (CH_2); FTIR-ATR (cm^{-1}): 3095-–3010 (=C–H β, thiophene ring), 2998 (C–H aliphatic), 1735 (C=O, ester), 1436 (–CH_2–), 1375 (–O–CH_3, ester), 1255–1160 (C–O–CH_3, ester), 840 (C–H β, thiophene ring).

2.3. Preparation of PLA–P3TMA fibers

For the nanofiber preparation, mixtures of PLA and P3TMA were electrospun from chloroform/acetone (2:1 v/v) at polymer concentrations of 5 w/v% and 0–5 w/v% for PLA and P3TMA, respectively. Samples will be identified indicating the PLA and P3TMA ratio. According to our previous optimization of the processing conditions [33], PLA electrospun fibers were collected on a target with a deposition distance of 12 cm, applying a voltage of 20 kV with a portable High Voltage Source (model ES30-5W, Gamma High Voltage Research, Ormond Beach (FL), USA) and a flow rate of 4 mL·h^{-1}. The voltage and flow-rate used to prepare PLA–P3TMA fibers was 25 kV and 4 mL·h^{-1}, respectively. Polymer solutions were delivered via a KDS100 infusion syringe pump (code KDS100, KD Scientific Inc., Holliston (MA), USA) to control the mass-flow rate, and the tip used had an inside diameter of 0.84 mm (syringe needle 18G). All electrospinning experiments were carried out at room temperature. The diameter of the fibers prepared under such conditions ranged from 600 to 800 nm.

2.4. PLA–P3TMA (2:1 ratio) fibers drug-loading

PLA (0.5 g) was dissolved in 5 mL of chloroform-acetone mixture (2:1 v/v) and P3TMA (0.25 g) in 4 mL of the same solvent mixture. Then, 1 mL of dimethylsulfoxide (DMSO) containing the drug (0.1 g) was added, and the mixture was homogenized by vortexing to obtain an electrospinnable solution of 5 w/v% PLA, 2.5 w/v% P3TMA and 1 w/v% drug. The electrospinning process was conducted at room temperature, fibers being collected at a distance of 12 cm from the needle (18G, inside diameter of 0.84 mm). The applied voltage and the flow rate was of 25 kV and 4 mL·h^{-1}, respectively.

2.5. Characterization

^{1}H-NMR and ^{13}C-NMR spectra were acquired with a Bruker AMX-300 spectrometer (Bruker Corporation, Billerica (MA), USA) operating at 300.1 MHz. Chemical shifts were calibrated using tetramethylsilane as an internal standard. Deuterated chloroform was used as the solvent.

Infrared absorption spectra were recorded with a Fourier Transform FTIR 4100 Jasco spectrometer (Jasco Analytical Instruments, Easton, (MD), USA) in the 4000–600 cm^{-1} range. An attenuated total reflection (ATR) system with a heated Diamond ATR Top-Plate (model MKII Golden Gate™, Specac Ltd., Orpington (Kent), UK) was used.

Atomic force microscopy (AFM) images were obtained for all the samples in tapping mode with an AFM Dimension 3100 microscope and a NanoScope® V controller (Veeco Instruments Inc., Plainview (NY), USA) at ambient conditions. A silicon probe (model Tap150-G, Budget Sensors®, Innovative Solutions Bulgaria Ltd., Sofia, Bulgaria) with a resonant frequency and spring constant of 150 kHz and 5 N·m^{-1}, respectively, was used. The row scanning frequency was set at 0.8 Hz and the scan window size varied from 1×1 μm^2 to 20×20 μm^2. Data were acquired using the Reasearch NanoScope software (v. 7.30) and, afterwards, they were analyzed using the NanoScope Analysis analysis software (v. 1.20).

The Root Mean Square (RMS) roughness, which is the average height deviation taken from the mean data plane, was determined using the statistical application of the NanoScope Analysis software (1.20, Veeco).

A Confocal Raman-AFM microscope (model a300R+, WITec – Wissenschaftliche Instrumente und Technologie GmbH-, Ulm, Germany) was used to collect Raman spectra from the homopolymers, PLA–P3TMA blends and drug loaded samples. For excitation, a laser with wavelength of 785 nm was used. The integration time was between 0.3 and 2.1 seconds depending on the scan, and high resolution Raman images were obtained by collecting complete Raman spectra at less than 3 cm^{-1} per pixel. Fibers were analyzed as obtained after the electrospining process, without any additional preparation, at room temperature and after the exposure time necessary to decay the fluorescence.

The number-average molecular weight (M_n) and weight-average molecular weight (M_w) were measured by gel permeation chromatography (GPC) at 25 °C using a chromatograph (model 1525 – Binary HPLC Pump) equipped with a refractive index detector (model 2414) from Waters Cromatografía, S.A., (Cerdanyola del Vallès, Spain). GPC measurements were carried out using tetrahydrofuran (THF) as eluent with a flow rate of 1.0 $mL \cdot min^{-1}$, respectively. Polystyrene standards were used for calibration.

Optical morphologic observations were performed using Zeiss Axioskop 40 microscope (Carl Zeiss Microscopy, LLC, USA). Micrographs were taken with Zeiss AxiosCam MRC5 digital camera (Carl Zeiss Microscopy, LLC, USA). Morphological characterization of the electrospun samples was conducted by scanning electron microscopy (SEM) using a Focus Ion Beam Zeiss Neon 40 instrument (Carl Zeiss, Germany). Prior sample observation, carbon coating was accomplished by using a Sputter Coater (model Mitec K950, Quorum Technologies Ltd., Ashford (Kent), UK) fitted with a film thickness monitor *k*150×. Samples were visualized at an accelerating voltage of 5 kV. Diameter of electrospun fibers was measured with the SmartTiff software from Carl Zeiss SMT Ltd (Jena, Germany).

Contact angle (CA) measurements were performed using an OCA 15EC (DataPhysics Instruments GmbH, Filderstadt, Germany) equipment and using the sessile droplet method at room temperature. Three different polar solvents were tested: ultrapure water, formamide and ethylene glycol. For the static contact angle (sCA) measurements, 0.5 μL droplets of liquid were dispensed on the respective surfaces. Images were recorded after drop stabilization (30 s) using the SCA 20 software. CA values were obtained as the average of fourteen independent measures for each sample. The surface energy (SE) of PLA–P3TMA samples was calculated based on the sCA data by applying several mathematical approaches: Equation-of-State (EoS), Fowkes, Owens-Wendt-Rabel-Kaelble (OWRK) and Wu models. Finally, the work of adhesion (W_A) was determined to quantify the wettability of a liquid droplet on the sample.

2.6. Electrochemical impedance spectroscopy (EIS)

EIS measurements were performed using a potentiostat/galvanostat (model AUTOLAB PGSTAT302N, Metrohm AG, Herisau, Switzerland) in the 100 kHz to the 10 mHz frequency range and the amplitude of the sinusoidal voltage was 10 mV. All experiments were carried at room temperature. The fiber mats were cut in a disc format (1.766 cm^2) and were sandwiched between two stainless steel electrodes assembled into an isolating resin holder [35]. The cell was tightened with screws to ensure constant pressure fastening. The thickness of the films, which was determined by a micrometer, varied between 18.9 and 26.0 μm. Prior to cell closing, samples were immersed in phosphate buffer saline (PBS, pH 7.4) at room temperature for 24 h and the water excess wiped out with a tissue. After data collection, EIS results were then processed and fitted to an electrical equivalent circuit (EEC).

2.7. Drug-release experiments

Drug-loaded mats were cut into small square pieces (20×20×0.1 mm^3) which were weighed and placed into polypropylene tubes. PBS and PBS supplemented with 70 v/v% of ethanol (PBS-EtOH) were considered as release media. The addition of ethanol to hydrophilic PBS increases the hydrophobicity of the medium and provokes some swelling effect, both favoring the release of hydrophobic drugs as TCS [36]. The release of TCS from PLA fibers in PBS containing 10 and 70 v/v% of ethanol was found to be 40 and 98% after 48 h, respectively, indicating that the composition of PBS-EtOH is adequate to alter the equilibrium defined by the affinity of PLA towards

hydrophobic drugs [36]. Drug-release assays were carried out by immersing sample mats in 50 mL of the release medium at 25 °C for 1 week. Aliquots (1 mL) were drawn from the release medium at predetermined intervals, and an equal volume of fresh medium was added to the release vessel. The drug concentration in the release medium was evaluated by UV-vis spectroscopy (UV-VIS-NIR Spectrophotometer model UV-3600 Plus from Shimadzu Corporation, Kyoto, Japan). Calibration curves were obtained by plotting the absorbance measured at the corresponding wavelengths (*i.e.* 322, 254, 281, and 260 nm for CIP, CHX, TCS and IBU, respectively) against drug concentration. Finally, the mats were dissolved in chloroform and the residual drug was extracted in ethanol for quantification. All tests were performed in triplicate to control the homogeneity of the release, and the results were averaged.

2.8. Agar diffusion test

Escherichia coli and *Staphylococcus epidermidis* were cultured aerobically overnight in 15 mL of brain–heart infusion (BHI) broth at 37 °C. The bacterial suspension was spread on Plate Count Agar (PCA) (Difco™ MI Agar, from Becton, Dickinson and Company, Franklin Lakes (NJ), USA) using a nylon swab. Uniform disks of 1 mm thick and 5 mm in diameter were prepared by perforating the drug-loaded PLA–P3TMA electrospun mats. Then, samples were placed on the surface of the agar plates and incubated at 37 °C. After 24 h, the inhibition zone around each specimen was observed to determine the activity of the drug.

3. Results and discussion

3.1. Topography and RAMAN analyses of PLA–P3TMA fibers

The electrospinning conditions and morphology of PLA–P3TMA fiber mats were examined in our previous study [33]. Scanning electron microscopy (SEM) micrographs evidenced that the incorporation of P3TMA in the electrospinning solution induced some structural changes in the PLA fiber: (1) the fiber diameter decreased slightly; (2) the fiber surface became smoother; and (3) heterogeneous clusters made of P3TMA aggregates appeared inside the fibers. Furthermore, both the electrochemical activity and the bioactivity of the fibers increased with the content of P3TMA.

AFM analyses (Figure 1) provided more precise information about the roughness of electrospun PLA and of PLA–P3TMA fibers. PLA fibers exhibit remarkable irregularities on their surface, their average RMS roughness ±2 times the corresponding standard deviation (calculated using five different samples) being 41.4±3.8 nm. The average RMS roughness determined for 5:1, 2:1 and 1:1 PLA–P3TMA compositions (Figures 1b–d) is 34.8±2.5, 39.9±3.0 and 35.6±4.5 nm, respectively. AFM phase images allow us to distinguish a phase contrast for PLA–P3TMA samples that is not observed for the PLA fibers. This supports that the two polymers mixed in the chloroform solution successfully incorporate into the electrospun fibers, even though it is not possible to associate each region (*i.e.* dark or bright areas) to a specific polymer-rich phase.

Further studies were carried out to understand P3TMA compositional distribution on PLA-P3TMA fibers by means of Raman spectroscopy. Figure 2a shows optical images taken with the Raman confocal microscope of PLA fibers, the Raman spectrum being displayed in Figure 2b. As it can be seen, the PLA spectrum presents identifiable peaks at well-known positions [37]. The most intense band, which corresponds to the *ν*C–COO stretching is located at *ca*. 874 cm^{-1} (Figure 2b).

Optical images of PLA–P3TMA fibers are displayed in Figures 2c and 2e. P3TMA powder was analyzed by Raman spectroscopy and the resulting spectrum is depicted in Figure 2d). As the fluorescence induced by the laser at 532 nm used for PLA fibers is very high for P3TMA, CP-containing samples were analyzed using the laser at 785 nm. This leaded to less fluorescence overlapping but also to a lower peak resolution. The most intense line for the P3TMA spectra is identified at *ca*. 1480 cm^{-1}, which corresponds to the totally symmetric in–phase vibration of the thiophene rings spread over the polymer chains [38]. Raman spectra were recorded from three different spots of the PLA–P3TMA fibers (Figures 2c and 2d) as well as from P3TMA particles, which are clearly visible as dark spots inside the fibers (Figures 2c and 2e). These results corroborate the homogenous distribution of P3TMA among the PLA fibers, even though some CP agglomerates are also detected. Moreover, 2:1 PLA–P3TMA fibers loaded with drugs were also evaluated by Raman spectroscopy (discussed below).

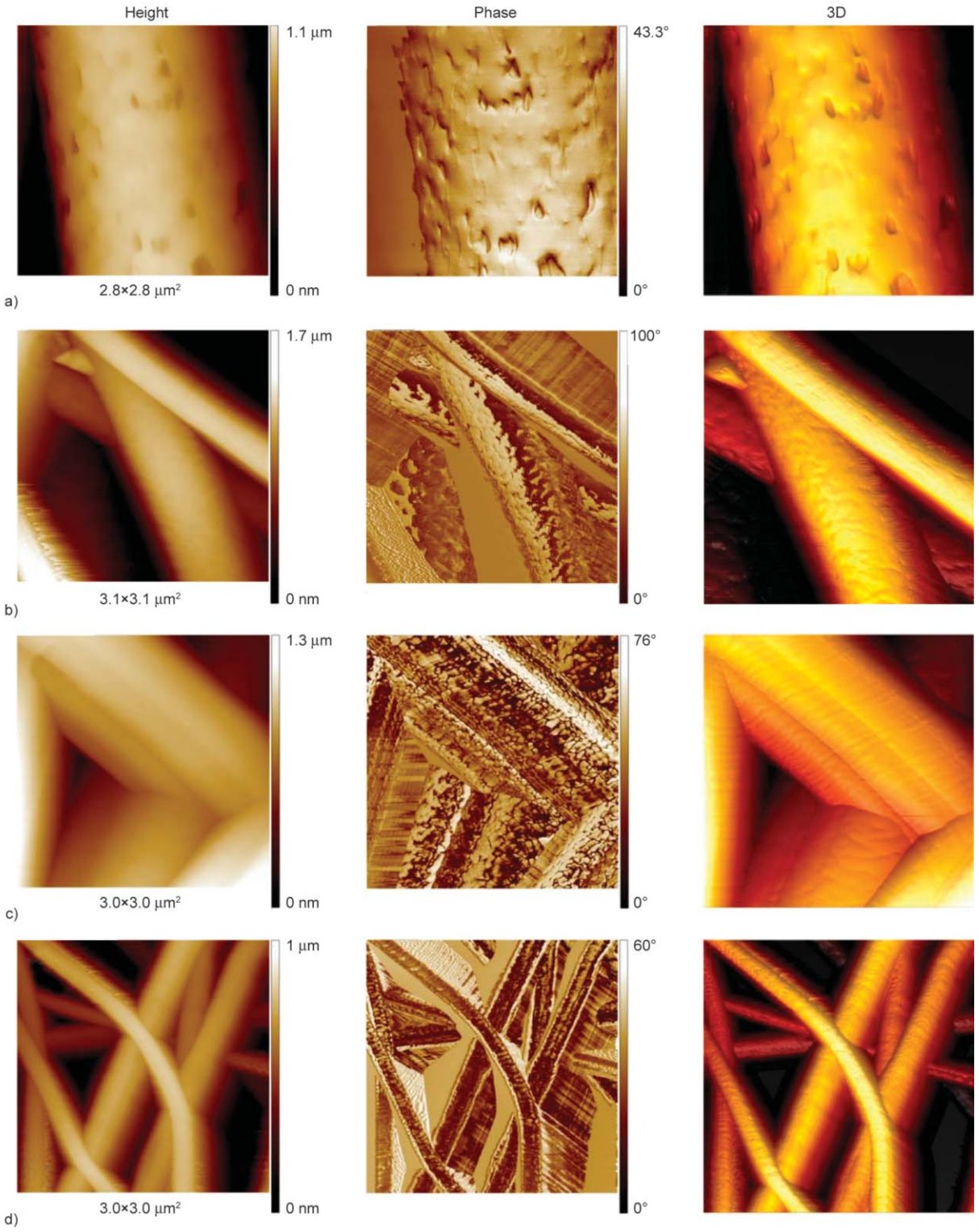

Figure 1. AFM micrographs from PLA and PLA–P3TMA fibers scaffolds prepared by electrospinning: (a) PLA, (b) 5:1 PLA–P3TMA, (c) 2:1 PLA–P3TMA and (d) 1:1 PLA–P3TMA

3.2. Wettability and surface energy determination

Understanding of the wetting properties of PLA–P3TMA fibers is crucial for their use as drug carrier and delivery systems. Two wetting states have been defined for hydrophobic surfaces [39]. In the Wenzel state, which corresponds to a homogeneous wetting regime, the liquid completely penetrates into the grooves defined by the surface roughness, while air bubbles are inside the grooves underneath the liquid in the heterogeneous wetting regime associated with the Cassie-Baxter state. Air entrapped into 3D fi-

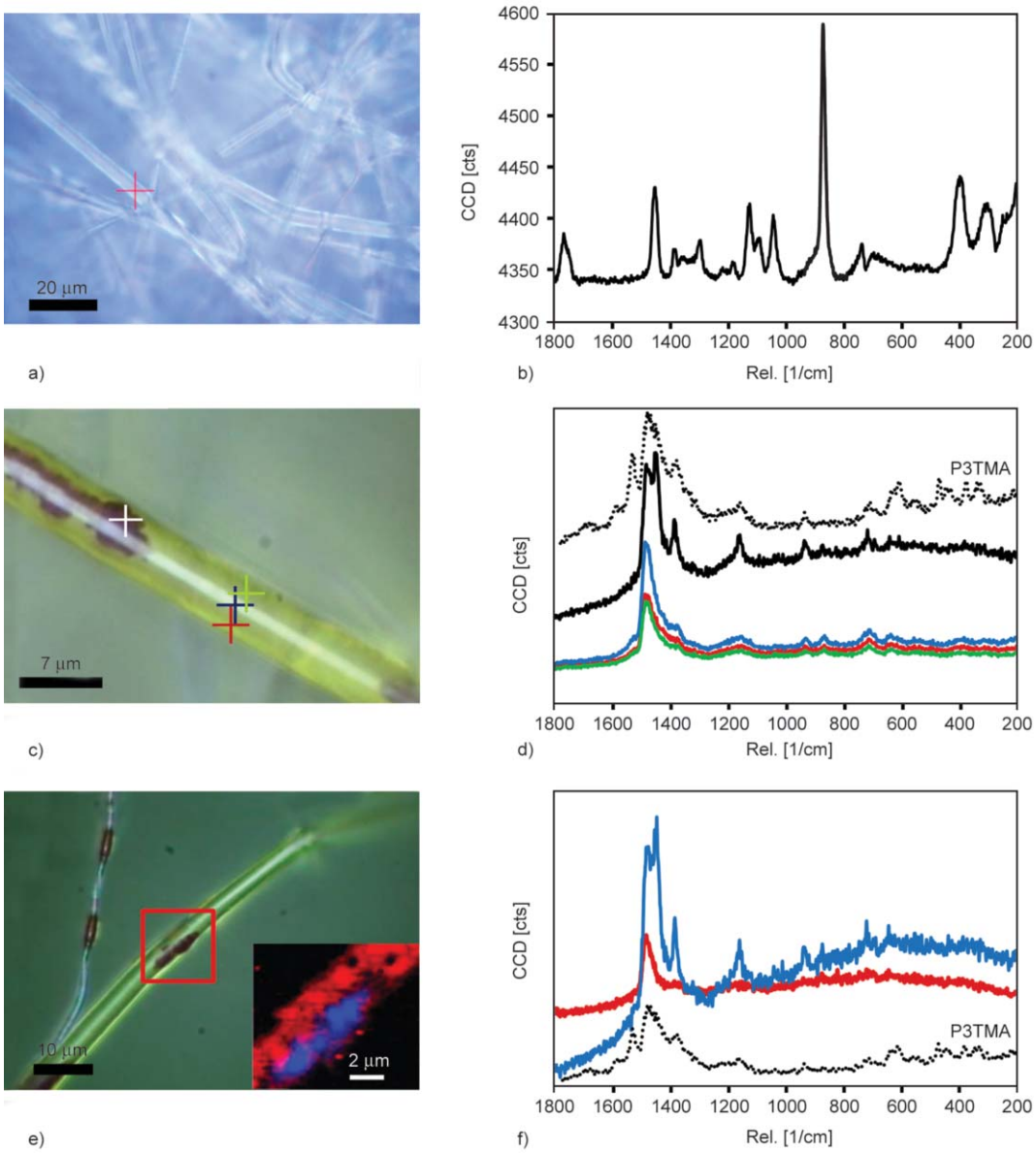

Figure 2. (a) PLA fiber optical image, (b) PLA Raman spectra at the cross point from (a). (c) PLA–P3TMA (2:1) fiber optical image. (d) Raman spectra at the cross points from (b). The solid black line corresponds to the white cross in (c) and the discontinued line to powder P3TMA. (e) PLA–P3TMA (2:1) fiber optical image. Inset: scanned area (red box). (f) Raman spectra associated with the inset in (e).

brous scaffolds may act as a barrier precluding water penetration and, therefore, affecting the drug-delivery. However, a transition from the Cassie-Baxter state to the Wenzel state may occur whenever air regions are no longer thermodynamically stable and liquid infiltrates the surface. Thus, the drug-delivery rate can be tuned by controlling the wettability of drug-loaded systems [40].

Table 1 gives the static contact angles (sCA) values of deionized water, formamide and ethylene glycol solvents determined for PLA and PLA–P3TMA scaffolds. Results are compared with those obtained for films prepared by solvent-casting a chloroform solution of the corresponding blend. As it can be seen, the wetting behavior depends on the organization. For each solvent, the sCA of scaffolds made of fiber diameters varying from 600 to 800 nm is higher than that of films prepared by solvent evaporation for PLA and all blend compositions. Hence, the fiber matrix is able to block the liquid phase resulting in a less wettable surface (Figure 3), which has been attributed to both the fiber roughness and the air entrapped at the surface. In spite of this, the exact final frontier of the three-phase contact line (TPCL) is unclear since the liquid may penetrate the porous matrix through the space left among adjacent fibers. Therefore, it is not possible to ascertain which state (*i.e.* Wenzel, Cassie-Baxter or the transition between them) is the

Table 1. Static contact angle values (in degrees) for PLA and PLA–P3TMA scaffolds prepared by electrospinning and for films obtained by solvent casting, respectively

Composition	Water[a]		Formamide		Ethylene glycol	
	Scaffolds	Solvent casting[b]	Scaffolds	Solvent casting[b]	Scaffolds	Solvent casting[b]
PLA	132.0±2.2	76.1±3.1	121.8±5.4	55.3±2.2	110.5±2.7	50.0±2.4
PLA–P3TMA 5:1	130.5±2.1	90.5±3.4	118.7±3.2	56.0±2.3	123.8±3.8	55.8±2.1
PLA–P3TMA 2:1	135.3±1.5	86.9±5.2	121.6±4.7	55.4±3.2	130.1±2.0	55.0±3.4
PLA–P3TMA 1:1	134.6±2.4	87.7±3.8	127.4±2.4	68.6±5.6	126.7±2.0	54.9±1.6

[a]Taken from reference 33. [b]PLA and PLA–P3TMA films were solvent casted from a solution of 16 mg·mL^{-1} of polymer in $CHCl_3$ solvent. Mean values correspond to the average of at least 14 droplets of water, formamide and ethylene glycol.

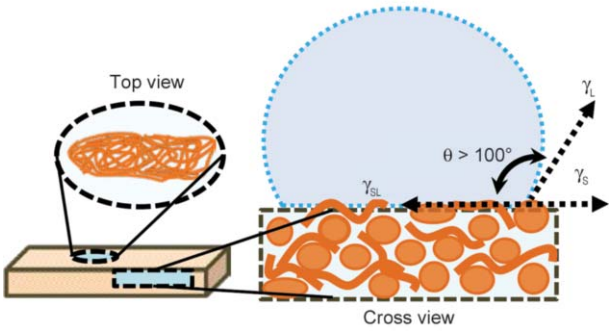

Figure 3. Expected wetting behavior of PLA-P3TMA scaffold samples where air pockets avoid the liquid infiltration

most appropriated to adjust the wetting behavior of PLA and PLA–P3TMA fibrous scaffolds.

Also, sCA values of water and formamide indicate that the incorporation of P3TMA into PLA fibers does not provoke significant changes in the wettability of the polyester (Table 1), independently of the blend composition. For ethylene glycol, PLA–P3TMA fibers exhibit lower wettability than PLA, the sCA of the polyester increasing 13–20° upon the addition of the CP. This is a very attractive result for drug-release applications since the low wettability of PLA–P3TMA scaffolds in such solvents is expected to be accompanied by a slow release.

Surface phenomena, like wetting, adsorption and adhesion, are controlled by the surface energy (SE) of the materials used for deposition. The sCA values displayed in Table 1 have been used to estimate the SE using the Equation-of-State (EoS) [41], Fowkes [42], and Owens-Wendt-Rabel-Kaelble (OWRK) [43, 44] theoretical models. As each model considers different physical assumptions and interactions for the calculation of the SE components, comparison among such approaches is not an easy task. Results derived from the different models, which are displayed in Table 2, reveal a general tendency. The SE of the solid-gas interface (γ_S) and its dispersion and polar components (γ_s^d and γ_s^p, respectively) decrease with increasing P3TMA content. Samples with high SE, like PLA fibers, interact more readily with liquids because of their bonding potential. Results allow us to conclude that a small percentage of P3TMA adequately dispersed in the electrospinning process is able to reduce the γ_S components, precluding rapid drug release.

The influence of the fibrous morphology in the SE of PLA and PLA–P3TMA was examined by comparing results displayed in Table 2 with those obtained for films prepared by solvent casting using chloroform solutions (Table 3). As it can be seen, the γ_S was one order of magnitude higher for films than for fibers. For PLA films, the γ_S values displayed in Table 3 are in good agreement with those reported in the literature, which range from 35.1 to 50 mJ·m^{-2} (up to 50 mJ·m^{-2}), with γ_s^d *ca.* 26.9–29.7, and γ_s^p *ca.* 8.2–10.5 mJ·m^{-2} [45]. Similarly, the SE values of PLA–P3TMA interfaces and, therefore, their wetting response, are influenced by their morphology.

The highest work of adhesion (W_A), calculated using the results derived from the OWRK model, was obtained for PLA scaffolds, which was attributed to the fact that PLA exhibits the highest γ_S (Table 2). Accordingly, this surface is less repellent to liquid than

Table 2. Surface energy parameters and W_A values [mJ·m^{-2}] for PLA–P3TMA scaffold samples

	EoS	Fowkes	OWRK			Work of adhesion[a] (W_A)		
	γ_S	γ_s^d	γ_s^d	γ_s^p	γ_S	Water	Formamide	Ethylene glycol
PLA	7.07±0.26	7.09±0.23	10.99±0.00	0.62±0.00	11.61±0.00	49.08	49.02	44.72
PLA–P3TMA 5:1	6.53±0.36	5.05±0.21	3.95±0.00	0.11±0.00	4.06±0.00	34.68	33.18	30.23
PLA–P3TMA 2:1	5.02±0.38	3.51±0.28	3.61±0.00	0.00±0.00	3.62±0.00	33.72	33.13	29.26
PLA–P3TMA 1:1	4.43±0.18	3.61±0.14	2.52±0.00	0.13±0.00	2.65±0.00	30.37	28.45	25.91

[a]W_A values for PLA–P3TMA scaffolds based on data derived from the OWRK model.

Table 3. Surface energy parameters of PLA and PLA-P3TMA samples prepared by solvent casting

	EoS	Fowkes	OWRK		
PLA–P3TMA	γ_S	γ_s^d	γ_s^d	γ_s^p	γ_S
1:0	37.65±0.24	35.99±0.02	33.99±0.03	4.42±0.01	38.41±0.03
5:1	33.79±0.77	53.67±0.10	73.08±0.00	2.31±0.01	75.39±0.00
2:1	34.75±0.69	54.60±0.10	58.20±0.02	0.10±0.00	58.31±0.02
1:1	32.04±0.38	47.93±0.10	37.66±0.02	0.95±0.00	39.62±0.02

systems with CP. In conclusion, the SE and W_A of PLA–P3TMA fibrous scaffolds prepared by electrospinning are substantially lower than those obtained for film. Thus, the surface of the fibers is more repellent to polar liquids than that of films.

3.3. Electrochemical impedance spectroscopy

The presence of the CP in the PLA fiber mat serves to meet two purposes. First, as it was discussed in the previous section, a small amount of adequately dispersed P3TMA is able to reduce the SE parameters, thus decreasing the wetting behavior and slowing down the rapid drug release in polar solvents. Second, it is expected that cells will respond to an external electrical or electrochemical stimuli when in contact with the CP. Therefore, before drug-loading, the bulk conductivity of PLA–P3TMA fiber mats was evaluated by EIS. Samples were prepared by electrospinning and cut in disc-shaped formats for adaptation to the capacitor cell [35]. As it is illustrated in Figure 4, scaffolds become darker with increasing content of CP.

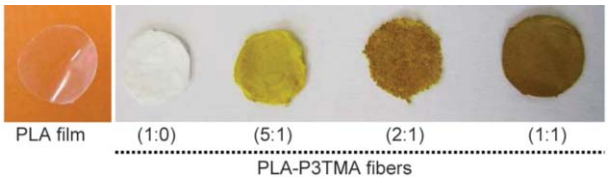

Figure 4. Photographs of PLA–P3TMA and PLA electrospun fibers and PLA saolvent casted films prepared for EIS analyses using a capacitor cell

The Nyquist and Bode plots provide information about the distribution of the CP in the biopolymer matrix. Figure 5a indicates that PLA and 5:1 PLA–P3TMA scaffolds exhibit similar resistance and capacitance, indicating that the incorporation of a low concentration of CP does not alter the electrochemical properties of PLA fibers. Results for the three replicated samples of each system were alike and, therefore, only one curve was represented. Spectra show a very compressed and very small beginning of a semicircle in the high frequency range, and an inclined straight line in the low frequency range. It is well known that the high frequency semicircle is associated with the bulk relaxation of the film and its irregular thickness and morphology, while the straight line refers to the migration of ions and the surface inhomogeneity of the electrodes [46].

On the other hand, spectra for the 1:1 PLA–P3TMA scaffolds, which contain the highest P3TMA concentration, show a slightly different behavior as it is observed in the corresponding Bode plot (Figure 5b). The phase angle for samples with such composition is very low in the high frequency region, which only can be explained by the presence of defects caused

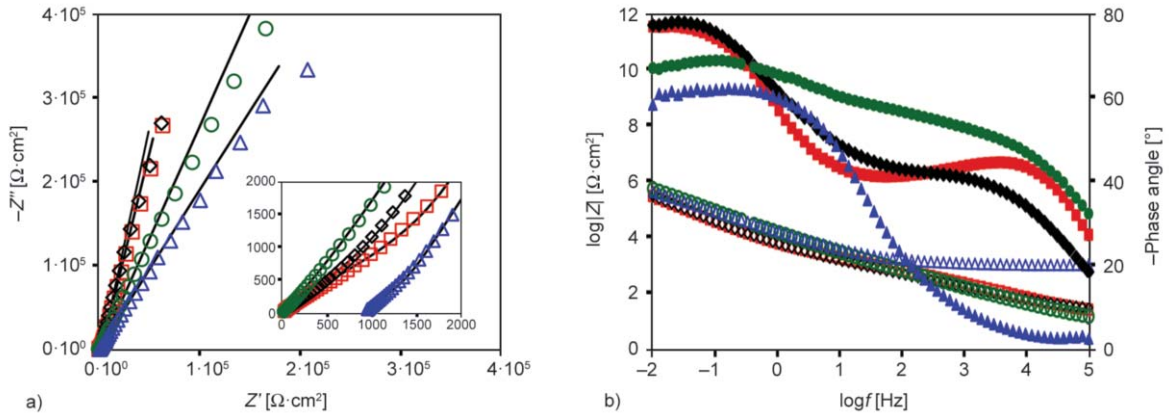

Figure 5. (a) Nyquist plots of PLA (square) and 5:1, 2:1 and 1:1 PLA–P3TMA (diamond, round and triangle, respectively) fiber matrices obtained using a capacitor cell. The inset in the diagram shows the impedance plot with magnified scale axes. Continuous lines correspond to the fitting of results obtained using the EEC to the experimental data. (b) Bode diagram from Nyquist plot. Filled figures refer to the angle phase axis, while empty figures refer to the log|*Z*| axis.

by an irregular distribution of P3TMA aggregates inside the fibers. Such distribution favors the rapid penetration and conduction of the electrolyte across the scaffold. In contrast, P3TMA seems to be homogeneously distributed in 2:1 PLA–P3TMA fibers showing a Nyquist plot with the lowest resistance and capacitance values (Figure 5a), whereas the Bode plot (Figure 5b) presents the highest phase angle (32.1°) and the lowest log|*Z*| (1.15) at the high frequencies zone (10^5 Hz). Quantitative analyses of these results required fitting with an adequate electrical equivalent circuit (EEC) for each system (Figure 6).

In our experiments, a PLA–P3TMA film was placed between two stainless steel (SS) electrodes forming through-plane cell geometry for bulk resistance and capacitance measurements across the film, *i.e.* forming a capacitor cell [35]. This means that, under polarization, an electrical double layer will be formed at the electrodes interface. This charged ion monolayer includes the electrolyte ions arranged in a monolayer at the electrode surface since they cannot trespass the electrode and the layer of opposite ionic charge at the electrode surface [46]. As it was carefully explained by Soboleva *et al*. [47], the idealized circuit for such a system has several elements and can be represented by the EEC displayed in Figure 6a. Briefly, each film/blocking electrode interface is represented by the parallel combination of a capacitance, which models the capacitance of the double layer (C_1 and C_2), and the resistance of the blocking electrode (R_1 and R_2). Besides, the bulk properties of the polymer film are represented by means of a bulk membrane capacitance (C_b) and a bulk resistance (R_b). However, the above circuit can be simplified into the one shown in Figure 6b by taking into account the following considerations: (*i*) the electrode/electrolyte interface is merely capacitive, therefore resistances R_1 and R_2 can be omitted; and (*ii*) the dominant process at the proton conducting electrode can be considered as a double layer capacitance. The elements of this equivalent electric circuit are the C_{dl}, which models the interfacial capacitance that arises from the double layer capacitance at the film/electrode interface, and R_b and C_b, associated in parallel, which represent the bulk resistance and the geometrical capacitance of the film/electrode interface, respectively.

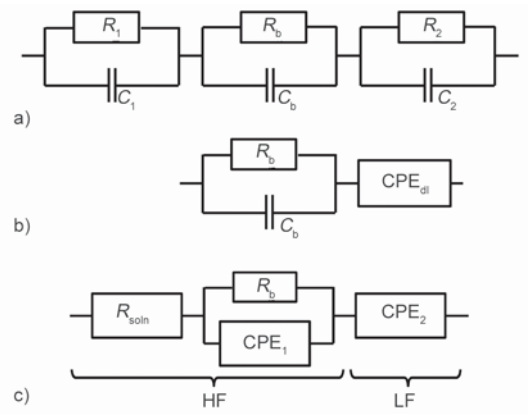

Figure 6. Equivalent electrical circuit for the scaffold films between two blocking electrodes: (a) idealized circuit, (b) simplified circuit and (c) electrical equivalent circuit of PLA–P3TMA system. HF stands for High Frequency range and LF for Low Frequency range.

As the real system is much more complicated and the capacitance at solid electrodes does not behave ideally, two constant phase elements substitute the capacitors C_{dl} and C_b considering the inhomogeneity of the system and the roughness and irregularities of the electrode surface [48, 49]. After fitting the experimental data to an equivalent electrical circuit it was found that PLA and PLA–P3TMA blends of wt% ratio 5:1 and 2:1 adjust to the circuit depicted in Figure 6c, while the fitting of a circuit to the 1:1 blend was much more difficult to achieve. This has been attributed to the fact that the high concentration of CP in the 1:1 film provokes the formation of P3TMA agglomerates inside the polymer matrix, resulting in a complex interface distribution. Thus, only the experimental data of one tested sample was properly fitted with the previous circuit. Therefore, in terms of the equivalent circuit elements analysis, the values displayed in Table 4 for the 1:1 blend are not averages. The electrical equivalent circuit used for the fitting of PLA and PLA–P3TMA EIS data was: $R_{soln}(R_bCPE_1)CPE_2$. It only differs from the general circuit described above (Figure 6b) in the presence of R_{soln}, which models the PBS electrolyte resistance. The parallel combination of R_b and CPE_1 re-

Table 4. Thickness and bulk conductivity values for the PLA–P3TMA fiber scaffolds obtained by EIS measurements

#	Thickness [μm]	$\sigma \cdot 10^{-7}$ [S·cm^{-1}]
PLA	18.9±4.2	4.33±0.91[a]
PLA–P3TMA 5:1	26.0±5.9	5.39±0.72[a]
PLA–P3TMA 2:1	25.2±10.6	8.26±0.59[a]
PLA–P3TMA 1:1	24.8±5.8	8.16[b]

[a]Average of three independent samples fitted to the proposed electrical equivalent circuit (EEC).

[b]Only one sample fitted properly to the proposed EEC.

sults in the high frequency semicircle while the CPE_2 represents de double layer capacitance. The mean of the simulated values for the EIS data are summarized in Table 4. The CPE impedance can be expressed as is indicated in Equations (1) and (2):

$$Z_{CPE} = B(j\omega)^{-n} \quad (1)$$

$$\alpha = (1-n)\frac{\pi}{2} \quad (2)$$

where $B = C_d^{-1}$ only when $n = 1$, and n is related to α which is the deviation from the vertical of the line in the Nyquist plot. Thus, $n = 1$ equals an ideal capacitance, and lower n values reflect the roughness of the electrode employed [46].

The EIS results showed that the density of the charge carriers and their mobility increase with the P3TMA content in the scaffold, improving the bulk conductivity. More specifically, the bulk conductivity of the fiber matrix films can be calculated by applying the Equation (3):

$$\delta = \frac{1}{R_b} \cdot \frac{d}{A} \quad (3)$$

where δ is the bulk conductivity, d is the thickness of the fiber film, A is the area of the polymer discs and R_b is the bulk resistance.

The good dispersion of P3TMA particles in the polymer matrix, under electrospinning conditions, is critical to obtain good electrical properties in the isolating fiber blends. Table 5 lists the bulk conductivity for all examined system. Comparison of the results obtained for 2:1 PLA-P3TMA and PLA indicates that the incorporation of 33 wt% of P3TMA into the fibers composition increases the bulk conductivity by 91%. According to these results, 2:1 PLA–P3TMA fiber mats were chosen for drug-loading and release assays since they accomplish the two-fold characteristic described before: good wettability and the highest bulk conductivity ($8.26 \cdot 10^{-7}$ S·cm^{-1}).

Bulk conductivities were recently reported for other biodegradable polymer–CP blended systems. For example, the electrical conductivity of electrospun fibers made of PLA blended with undoped polyaniline (PLA–PAni) and with polyaniline doped with camphorsulfonic acid (PLA–PAni·CSA) was reported to be $1.5 \cdot 10^{-5}$ and $8.4 \cdot 10^{-2}$ S·cm^{-1}, respectively [50]. Also, McKeon *et al*. [51] electrospun several polyaniline and poly(D,L-lactide) (PANi/PDLA) mixtures using different weight percent values. The electrical conductivity of the 75/25 electrospun scaffold, which was the only able to conduct a current of 5 mA, was $4.37 \cdot 10^{-2}$ S·cm^{-1}. In another work, PAni·CSA was blended with poly(L-lactide-*co*-ε-caprolactone) (PLCL) to obtain uniform nanofibers with good electrical properties [52]. Recently, incorporation of PAni into polycaprolactone (PCL) fibers significantly increased the electrical conductivity from a non-detectable level for the PCL fibers to $63.6 \cdot 10^{-3} \pm 6.6 \cdot 10^{-3}$ S·cm^{-1} for the fibers containing 3 wt% PANi [53]. Forciniti *et al*. [54] suggested that blends of poly(lactic-*co*-glycolic acid) and chloride-doped PPy exhibit the same electrical properties that the individual CP. Conductive PPy coating polyamide 6 (PA6) nanofibers were prepared by polymerizing pyrrole monomers directly onto the fiber [55].

3.4. PLA-P3TMA fibers loaded with drugs

Once the PLA–P3TMA-drug (2:1:0.4 w/w) samples were prepared considering CIP (antibiotic), CHX and TCS (biocides), and IBU (anti-inflammatory), SEM micrographs were taken to identify the possible morphological changes induced by the loading process. The surface of the loaded fibers was found to be less smooth and homogeneous than those of unloaded fiber samples. The lack of uniformity is reflected in Figures 7a and 7b for IBU and CIP drug loaded fibers, respectively, exhibiting enhanced flexibility and non-homogeneous diameters (*i.e*. varying from 1.58 to 5.09 μm) with respect to unloaded PLA–P3TMA. Besides, fibers tend to agglomerate without directional preference forming disorganized branches with diameters between 11 and 40 μm. Furthermore, the porosity of IBU loaded fibers is very high

Table 5. Data of EIS results obtained from the electrical equivalent circuit showed in Figure 6 for all polymeric blends

PLA-P3TMA	R_{sol} [Ω]	CPE_1 [$F \cdot s^{n-1}$]	n_1	R_b [kΩ]	CPE_2 [$F \cdot s^{n-1}$]	n_2
1:0	8.24±3.34	$5.00 \cdot 10^{-5} \pm 1.71 \cdot 10^{-5}$	0.50±0.08	2.47±0.09	$2.27 \cdot 10^{-5} \pm 1.82 \cdot 10^{-5}$	0.73±0.13
5:1	11.73±3.91	$1.55 \cdot 10^{-4} \pm 3.02 \cdot 10^{-5}$	0.51±0.02	2.74±0.54	$4.21 \cdot 10^{-5} \pm 1.90 \cdot 10^{-6}$	0.87±0.03
2:1	11.62±5.58	$1.47 \cdot 10^{-4} \pm 5.76 \cdot 10^{-5}$	0.50±0.03	1.75±0.82	$1.51 \cdot 10^{-5} \pm 8.83 \cdot 10^{-6}$	0.73±0.05
1:1[a]	939	$1.32 \cdot 10^{-5}$	0.66	1.456	$4.88 \cdot 10^{-6}$	0.80

[a]Only one sample properly fitted to the equivalent circuit proposed.

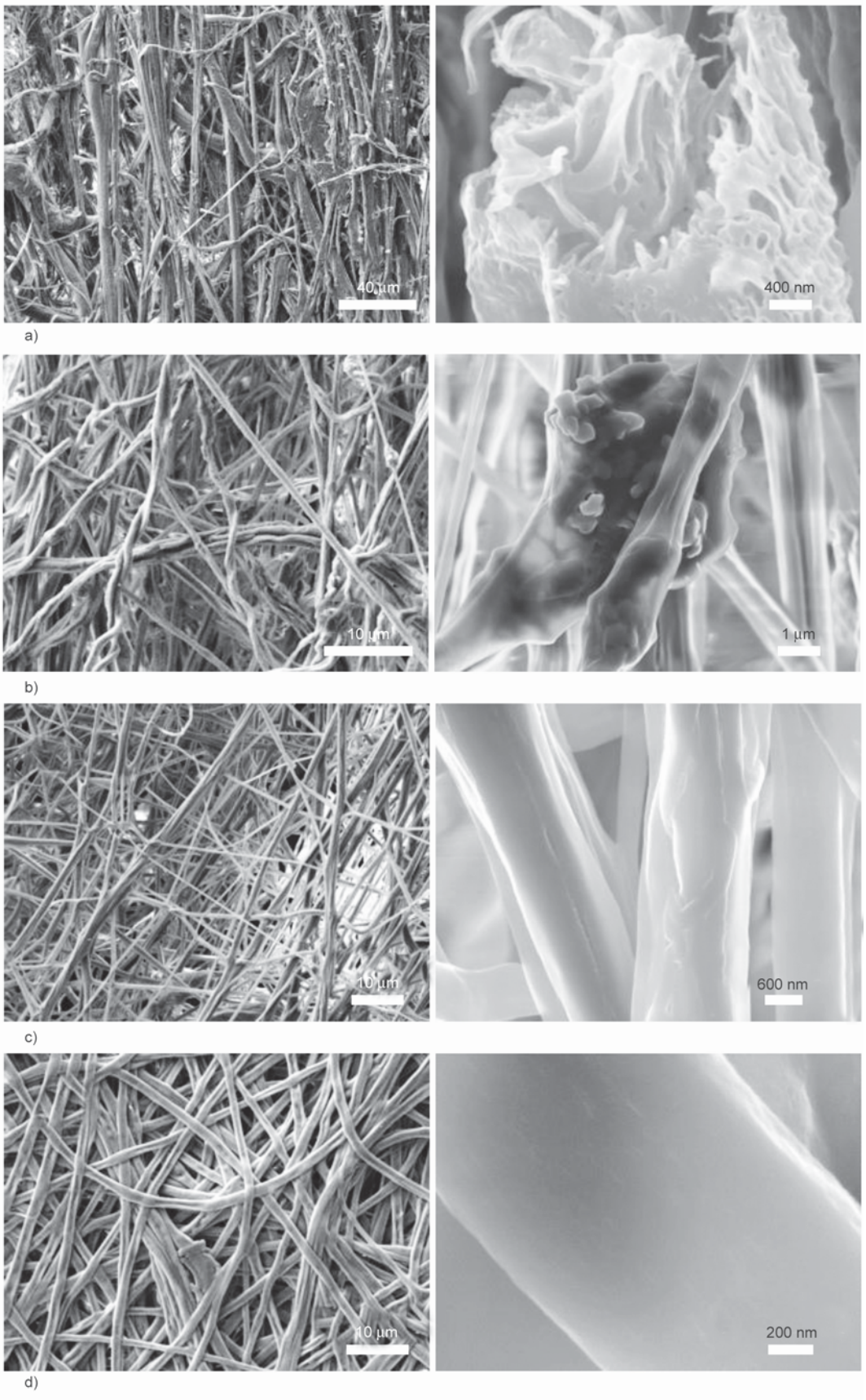

Figure 7. SEM images of 2:1 PLA–P3TMA fibers loaded with: (a) IBU, (b) CIP, (c) CHX and (d) TCS. Left and right images correspond to small and high magnifications.

in both outside and inside, as is reflected in the micrographs of the interior of broken morphologies (Figure 7a, right). Figure 7b (right), which displays a PLA–P3TMA-CIP fiber, allows us to distinguish embedded drug particles.

Morphological changes are less severe for CHX loaded samples than for IBU- and CIP-containing ones. Thus, well-formed and homogeneous scaffolds made of fibers with morphology, diameter and surface roughness similar to the unloaded ones are obtained (Figure 7c). Finally, TCS-containing samples provide the most homogenous fibers, exhibiting a highly smooth surface that largely resembles the texture of unloaded 2:1 PLA–P3TMA fibers (Figure 7d). In spite of this, AFM images displayed in Figure 8 evidence that TCS provokes a drastic change in the shape of the fibers. Thus, compact and regular PLA–P3TMA–TCS fibers present a ribbon-like shape rather than a tubular shape like that observed for 2:1 PLA–P3TMA fibers (Figure 1c). Variations in the fiber texture with respect to PLA–P3TMA are reflected in the AFM images of PLA–P3TMA–CHX, PLA–P3TMA–CIP and PLA–P3TMA–IBU, which are displayed in Figure 9. The different effects of loaded drugs into fiber dimensions have been attributed to the changes induced by drug···drug, drug···PLA and drug···P3TMA interactions, which alter the polymer···polymer interactions established in unloaded fibers. Thus, attractive and repulsive interactions may provoke the collapse and expansion of the polymeric matrix, respectively. Similarly, the balance between the different interactions is expected to affect the texture and roughness of the fibers.

On the other hand, considering the homogeneity of the electrospinning media, which were obtained by adding the drug dissolved in DMSO to a chloroform-acetone mixture containing the two polymers, and the fact SEM and AFM micrographs indicate that the drugs were not located outside the fibers, the drug loading efficiency is considered to be very high in all cases.

Confocal Raman spectroscopy was also used to examine the drug-loading into the PLA–P3TMA samples. Figure 10, which shows the spectrum for the PLA–P3TMA–CIP samples, reflects the presence of several peaks (brown-shadowed) coming from the drug and the main absorption band from P3TMA at about 1480 cm^{-1}. The corresponding optical image

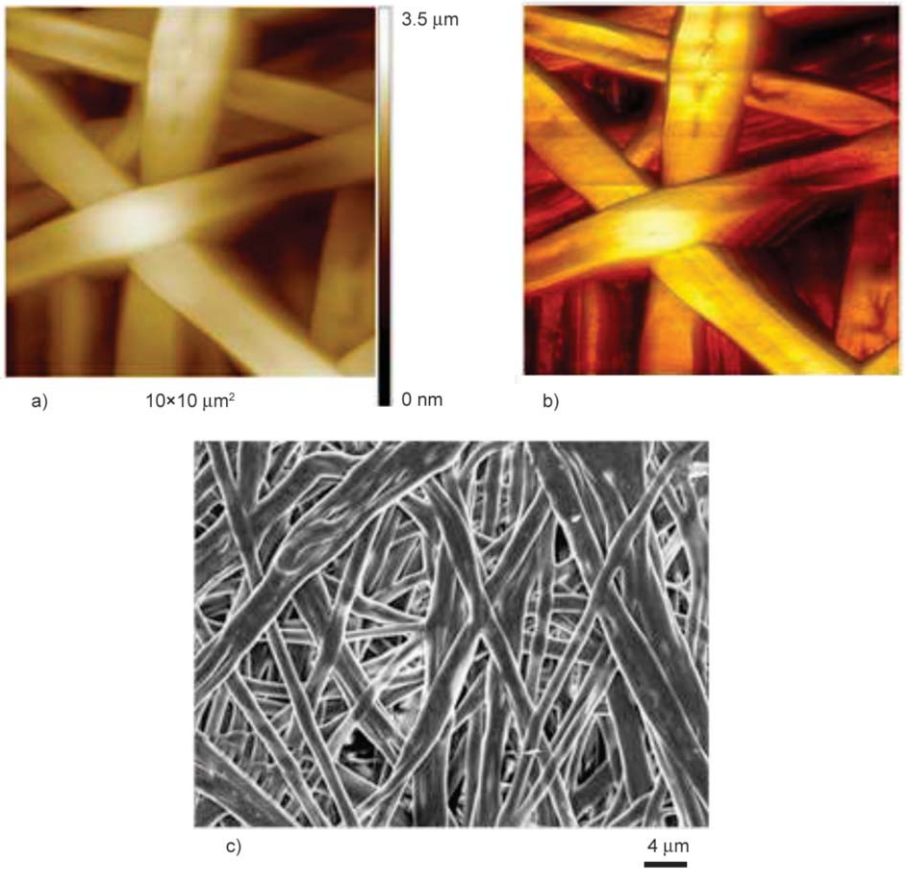

Figure 8. AFM micrographs from PLA–P3TMA–TCS fibers: (a) 2D height image, (b) 3D image (10×10 μm^2) and (c) SEM micrograph (scale bar: 4 µm)

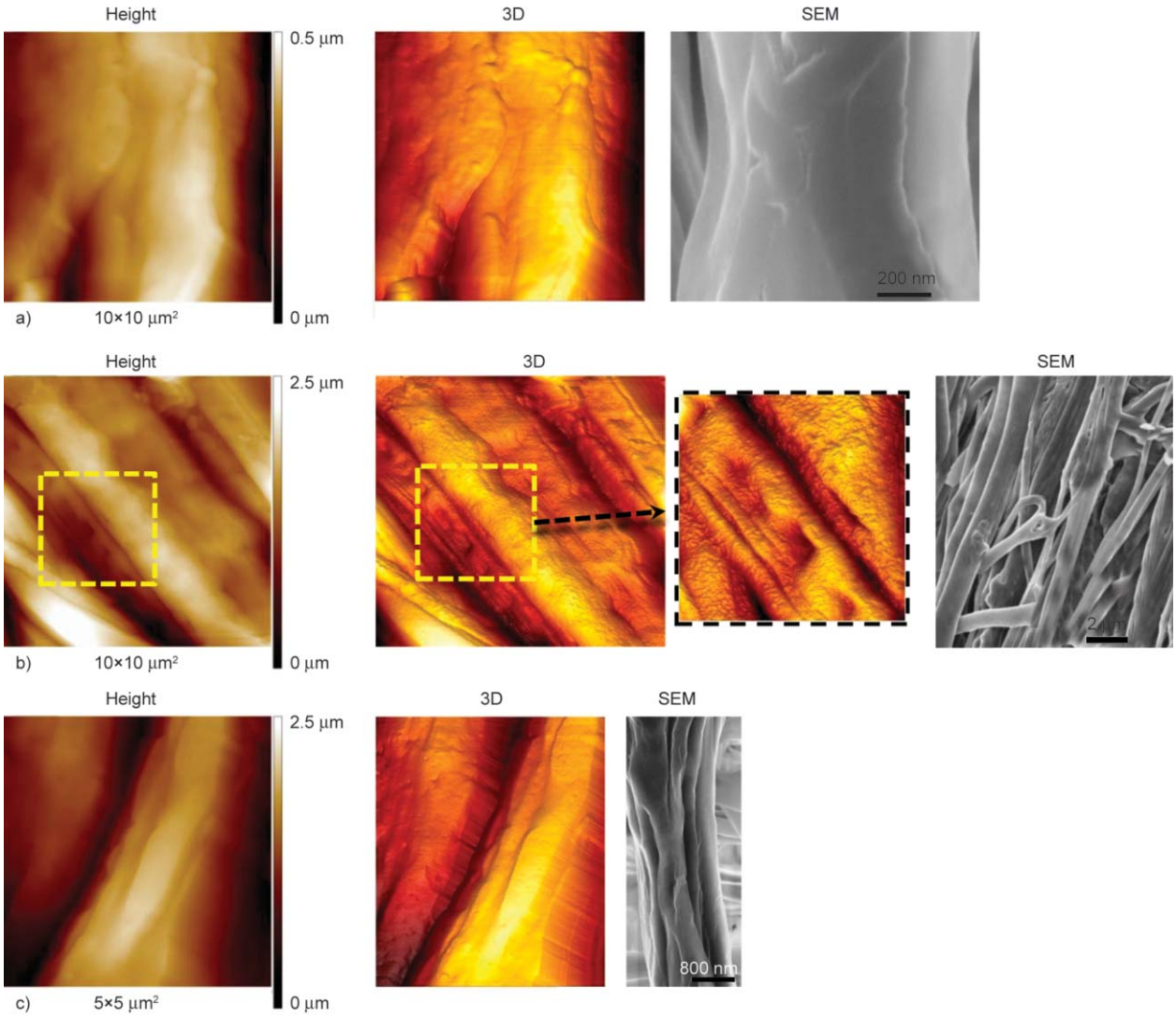

Figure 9. AFM micrographs from PLA:P3TMA 2:1 loaded with CHX (a), IBU (b) and CIP (c): 2D height image, 3D images and SEM micrograph

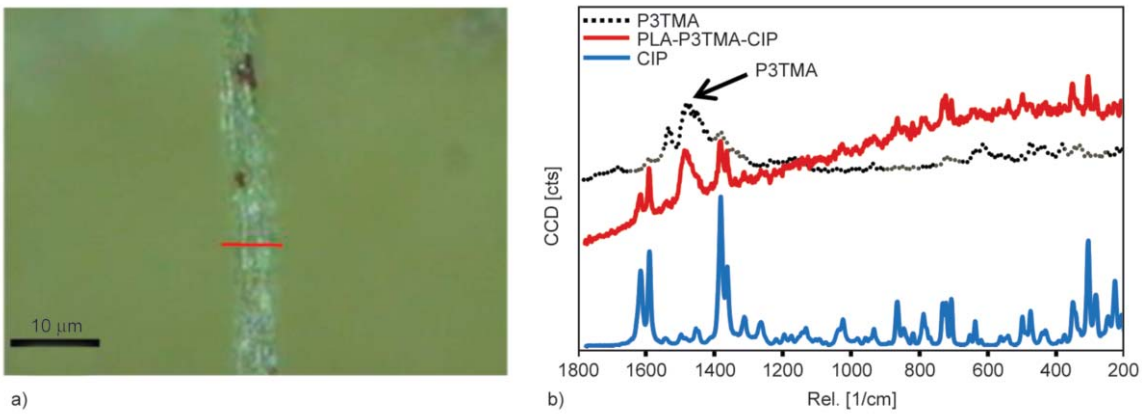

Figure 10. (a) Optical image of PLA–P3TMA–CIP fibers. The red line shows the spot in which the Raman spectrum was taken. (b) Raman spectra: the dotted line corresponds to P3TMA powder, the blue line to CIP powder and the red line to the PLA–P3TMA–CIP sample.

displays a white shine along the fiber that has been attributed to the drug. Unfortunately, identification of the loaded drug was less clear for the other three cases (not shown; available upon request to the authors), which has been attributed to its small concentration (12 wt%).

3.5. Drug release study

Drug release from electrospun fibers in a given medium usually relates to: (*i*) the morphology and crystallinity of such fibers; and (*ii*) the intermolecular interactions established between the drugs and the polymeric matrix. Within this context, it should be noted that the crystallinity and thermal behavior of PLA–P3TMA fibers was previously examined [33]. Quantitative release studies were performed considering PLA–P3TMA matrices loaded with CIP, CHX, TCS and IBU. Both PBS and PBS-EtOH were used as release media. According to previous studies [36], the ethanol supplement facilitates the delivery of highly hydrophobic molecules, such as TCS and IBU, precluding the establishment of early equilibrium conditions that limit their release in PBS. Figure 11a shows the release profiles in PBS for all four drugs loaded in PLA–P3TMA. The lower values were obtained for TCS (30%) and IBU (25%), suggesting that the retention into the polymer crystalline domains was higher for these drugs than for CIP and CHX. However, the release of TCS and IBU increases to 90 and 80%, respectively, when the delivery was performed using the more hydrophobic PBS-EtOH environment (Figure 11b).

On the other hand, release percentages in PBS of CIP and CHX from loaded PLA–P3TMA (*i.e.* ~90 and ~70%, respectively) are higher than those obtained for TCS and IBU. Furthermore, the release of CHX in PBS-EtOH was also very fast, reaching a value of ~70% after only seven hours of exposure (Figure 11b). Previous studies [56–58] indicated that the release kinetics of these drugs can be explained by the Higuchi and first-order models, which are usually combined to describe the first (from the beginning to 60%) and second (40–100%) stages of the release [59], respectively. In both cases, the delivery process is explained by the diffusion of the drug through the polymer matrix, which is facilitated by the ethanol-induced swelling of PLA [36].

Accordingly, the release profiles of CIP, CHX, TCS and IBU drugs loaded in the PLA–P3TMA scaffolds allowed us to reach some important conclusions: a) the electrospun hybrid fibers of PLA and P3TMA can be successfully used to load either hydrophilic and hydrophobic drugs; and b) the behavior of loaded 2:1 PLA–P3TMA fibers depends on the release environment, drug release being faster in a more hydrophobic medium.

3.6. Evaluation of bactericide activity of 2:1 PLA–P3TMA–drug scaffolds

Agar diffusion tests were conducted to demonstrate qualitatively the biological activity of the antimicrobial drugs (CIP, CHX, and TCS) loaded into 2:1 PLA–P3TMA electrospun fibers (Figure 12). *E. coli* and *S. epidermidis* bacteria were chosen as representative Gram negative and Gram positive bacteria groups, respectively. There was no inhibition halo in the growth plate of *E. coli* and *S. epidermidis* (Figures 12a and 12b, respectively) around the unloaded and IBU-loaded PLA–P3TMA samples. This expected result is consistent with the lack of bactericidal activity of PLA, P3TMA and IBU.

In contrast, halos of inhibition were observed for PLA–P3TMA electrospun fibers loaded with TCS, CHX and CIP, evidencing the antimicrobial activity of these drugs [36, 56, 57, 60]. The formation of such

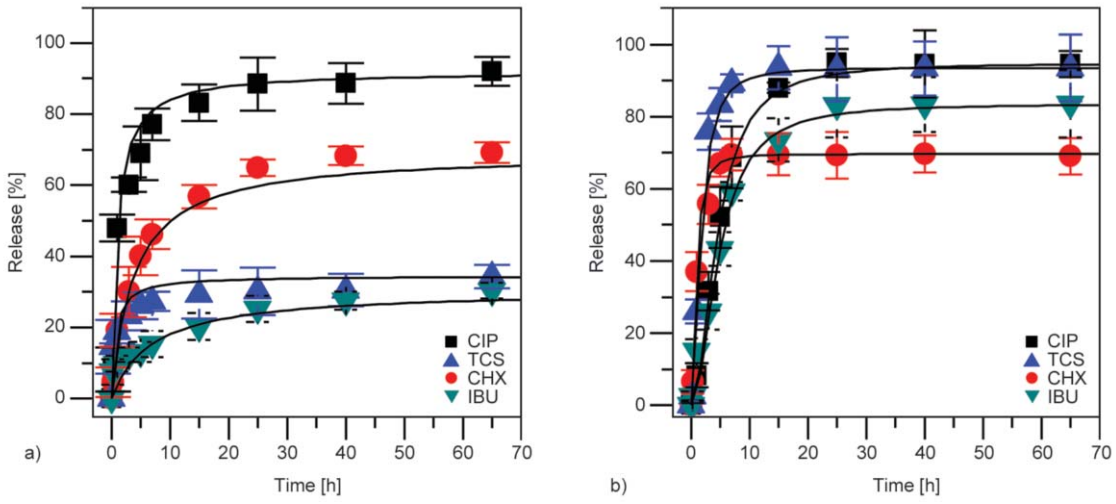

Figure 11. Drug release profile from 2:1 PLA–P3TMA scaffolds in (a) PBS and (b) PBS-EtOH

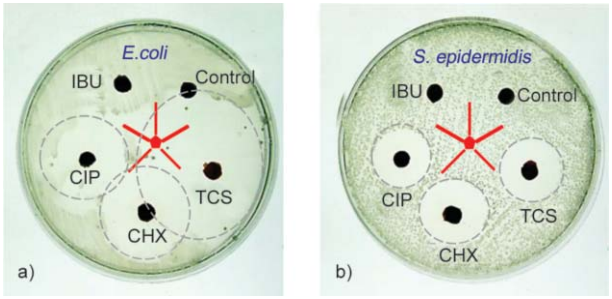

Figure 12. Inhibition of bacteria growth for (a) *Escherichia coli* and (b) *Staphylococcus epidermidis*. Unloaded 2:1 PLA–P3TMA scaffold was used as control disk. TCS, CHX, CIP and IBU disks refer to 2:1 PLA–P3TMA fibers loaded with the corresponding drug. Red lines indicate the areas of the plates occupied by each samples. The inhibition zones are highlighted with dotted lines.

halos corresponds to the drug released from the scaffold and, subsequently, diffused through the agar. The diameters of the three halos displayed in Figure 12b are similar, suggesting that the susceptibility of *S. epidermidis* towards TCS, CHX and CIP is similar. However, the response of *E. coli* towards such drugs is completely different, as it is reflected by the different sizes of the halos in Figure 12a. Although the agar diffusion test can also be used as a quantitative method, the diameter of the halos is only indicative of bacterial susceptibility towards the drug. In summary, these results clearly prove that the biological activity of the drugs is not affected by the electrospinning process or by the formation of interactions between the drugs and the PLA–P3TMA matrix.

4. Conclusions

Fibers made of PLA and P3TMA, a biopolymer and a CP, respectively, have been prepared by electrospinning and, subsequently, characterized. The first step consisted in the optimization of the electrospinning parameters, surface and conducting properties of fibers prepared using 5:1, 2:1 and 1:1 PLA–P3TMA compositions being examined. After this, fibers were loaded with different drugs and both their release and activity were studied.

Our results demonstrate that the incorporation of P3TMA into PLA scaffolds provokes changes in the surface morphology and decreases the bulk resistance. Fibers prepared using 2:1 PLA–P3TMA exhibited an increment in the bulk conductivity of ~90% in comparison to PLA. The observed semiconducting behavior suggests that scaffolds prepared using such composition would be appropriate for the development of electrically stimulated drug-delivery systems. Furthermore, wettability measurements prove that P3TMA reduces the surface energy parameters of PLA. This has been shown to improve the applicability of the prepared fibers as drug delivery systems.

Drug release experiments in PBS and PBS-EtOH with 2:1 PLA–P3TMA–drug scaffolds proved that the release kinetics depends on the hydrophilicity of solution medium, being faster for the least hydrophilic medium. Moreover, CHX showed a stable release behavior either in PBS or in PBS-EtOH solutions (65–70%), combined with a good fiber formation by electrospinning. As it was expected, unloaded fibers (blank samples) do not show antibacterial activity against *E. coli* and *S. epidermidis* bacteria. However, PLA–P3TMA electrospun matrices loaded with TCS, CHX and CIP drugs showed normal activity against such two bacteria, proving that the bioactivity of these drugs was not altered by the electrospinning process. Overall, these results demonstrate that the drugs are well mixed in the PLA–P3TMA scaffold matrices. Future work is oriented towards the release of drugs loaded on PLA–CP fibers by electro stimulation.

Acknowledgements

Authors are indebted to supports from MICINN and FEDER (MAT2012-34498 and MAT2012-36205). M.M.P.-M. thanks financial support through a FPI-UPC grant. Support for the research of C.A. was received through the prize 'ICREA Academia' for excellence in research funded by the Generalitat de Catalunya.

References

[1] Okada H., Toguchi H.: Biodegradable microspheres in drug delivery. Critical Reviews in Therapeutic Drug Carrier Systems, **12**, 1–99 (1995).
DOI: 10.1615/CritRevTherDrugCarrierSyst.v12.i1.10

[2] Kitchell J., Wise D.: Poly(lactic/glycolic acid) biodegradable drug–polymer matrix systems. Methods in Enzymology, **112**, 436–448 (1985).
DOI: 10.1016/S0076-6879(85)12034-3

[3] Kane J. M., Eerdekens M., Lindenmayer J-P., Keith S. J., Lesem M., Karcher K.: Long-acting injectable risperidone: Efficacy and safety of the first long-acting atypical antipsychotic. The American Journal of Psychiatry, **160**, 1125–1132 (2003).
DOI: 10.1176/appi.ajp.160.6.1125

[4] Hans M., Shimoni K., Danino D., Siegel S. J., Lowman A.: Synthesis and characterization of mPEG–PLA prodrug micelles. Biomacromolecules, **6**, 2708–2717 (2005). DOI: 10.1021/bm050188k

[5] Pérez-Madrigal M. M., Armelin E., Puiggalí J., Alemán C.: Insulating and semiconducting polymeric free-standing nanomembranes with biomedical applications. Journal of Materials Chemistry B, **3**, 5904–5932 (2015). DOI: 10.1039/c5tb00624d

[6] Widmer M. S., Gupta P. K., Lu L., Meszlenyi R. K., Evans G. R. D., Brandt K., Savel T., Gukrlek A., Patrick C. W., Mikos A. G.: Manufacture of porous biodegradable polymer conduits by an extrusion process for guided tissue regeneration. Biomaterials, **19**, 1945–1955 (1998). DOI: 10.1016/S0142-9612(98)00099-4

[7] Rangappa N., Romero A., Nelson K. D., Eberhart R. C., Smith G. M.: Laminin-coated poly(L-lactide) filaments induce robust neurite growth while providing directional orientation. Journal of Biomedical Materials Research, **51**, 625–634 (2000). DOI: 10.1002/1097-4636(20000915)51:4<625::AID-JBM10>3.0.CO;2-U

[8] Wei Y., Lelkes P. I., MacDiarmid A. G., Guterman E., Cheng S., Palouian K.: Electroactive polymers and nanostructured materials for neural tissue engineering. in 'Contemporary topics in advanced polymer science and technology' (eds.: Zhou Q. F., Cheng S. Z. D.) Peking University Press, Beijing, 430–436 (2004).

[9] Bidez P., Li S., MacDiarmid A. G., Venancio E. C., Wei Y., Lelkes P. I.: Polyaniline, an electroactive polymer, supports adhesion and proliferation of cardiac myoblasts. Journal of Biomaterials Science, Polymer Edition, **17**, 199–212 (2006). DOI: 10.1163/156856206774879180

[10] Kotwal A., Schmidt C. E.: Electrical stimulation alters protein adsorption and nerve cell interactions with electrically conducting biomaterials. Biomaterials, **22**, 1055–1064 (2001). DOI: 10.1016/S0142-9612(00)00344-6

[11] Valentini R. F.: Nerve guidance channels. in 'The biomedical engineering handbook' (ed.: Bronzino J. D.) CRC Press, Boca Raton, Section XIII, Chapter 135, p.13 (2000).

[12] Lee J. Y., Bashur C. A., Milroy C. A., Forciniti L., Goldstein A. S., Schmidt C. E.: Nerve growth factor-immobilized electrically conducting fibrous scaffolds for potential use in neural engineering applications. IEEE Transactions on NanoBioscience, **11**, 15–21 (2012). DOI: 10.1109/TNB.2011.2159621

[13] Gizdavic-Nikolaidis M., Ray S., Bennett J. R., Easteal A. J., Cooney R. P.: Electrospun functionalized polyaniline copolymer-based nanofibers with potential application in tissue engineering. Macromolecular Bioscience, **10**, 1424–1431 (2010). DOI: 10.1002/mabi.201000237

[14] del Valle L. J., Estrany F., Armelin E., Oliver R., Alemán C.: Cellular adhesion, proliferation and viability on conducting polymer substrates. Macromolecular Bioscience, **8**, 1144–1151 (2008). DOI: 10.1002/mabi.200800101

[15] Schmidt C. E., Shastri V. R., Vacanti J. P., Langer R.: Stimulation of neurite outgrowth using an electrically conducting polymer. Proceedings of the National Academy of Sciences of the United States of America, **94**, 8948–8953 (1997). DOI: 10.1073/pnas.94.17.8948

[16] Svirskis D., Travas-Sejdic J., Rodgers A., Garg S.: Electrochemically controlled drug delivery based on intrinsically conducting polymers. Journal of Controlled Release, **146**, 6–15 (2010). DOI: 10.1016/j.jconrel.2010.03.023

[17] Bidan G., Lopez C., Mendes-Viegas F., Vieil E.: Incorporation of sulphonated cyclodextrins into polypyrrole: An approach for the electro-controlled delivering of neutral drugs. Biosensors and Bioelectronics, **10**, 219–229 (1994). DOI: 10.1016/0956-5663(95)96808-C

[18] Richardson R. T., Wise A. K., Thompson B. C., Flynn B. O., Atkinson P. J., Fretwell N. J., Fallon J. B., Wallace G. G., Shepherd R. K., Clark G. M., O'leary S. J.: Polypyrrole-coated electrodes for the delivery of charge and neurotrophins to cochlear neurons. Biomaterials, **30**, 2614–2624 (2009). DOI: 10.1016/j.biomaterials.2009.01.015

[19] Guimard N. K., Gomez N., Schmidt C. E.: Conducting polymers in biomedical engineering. Progress in Polymer Science, **32**, 876–921 (2007). DOI: 10.1016/j.progpolymsci.2007.05.012

[20] Guo B., Glavas L., Albertsson A-C.: Biodegradable and electrically conducting polymers for biomedical applications. Progress in Polymer Science, **38**, 1263–1286 (2013). DOI: 10.1016/j.progpolymsci.2013.06.003

[21] Guo B., Sun Y., Finne-Wistrand A., Mustafa K., Albertsson A-C.: Electroactive porous tubular scaffolds with degradability and non-cytotoxicity for neural tissue regeneration. Acta Biomaterialia, **8**, 144–153 (2012). DOI: 10.1016/j.actbio.2011.09.027

[22] Armelin E., Gomes A. L., Pérez-Madrigal M. M., Puiggalí J., Franco L., del Valle L. J., Rodríguez-Galán A., Campos J. S. C., Ferrer-Anglada N., Alemán C.: Biodegradable free-standing nanomembranes of conducting polymer: Polyester blends as bioactive platforms for tissue engineering. Journal of Materials Chemistry, **22**, 585–594 (2012). DOI: 10.1039/C1JM14168F

[23] Pérez-Madrigal M. M., Armelin E., del Valle L. J., Estrany F., Alemán C.: Bioactive and electroactive response of flexible polythiophene: Polyester nanomembranes for tissue engineering. Polymer Chemistry, **3**, 979–991 (2012). DOI: 10.1039/c2py00584k

[24] Pérez-Madrigal M. M., Giannotti M. I., del Valle L. J., Franco L., Armelin E., Puiggalí, J., Sanz F., Alemán C.: Thermoplastic polyurethane: Polythiophene nanomembranes for biomedical and biotechnological applications. ACS Applied and Material Interfaces, **6**, 9719–9732 (2014).
DOI: 10.1021/am502150q

[25] Planellas M., Pérez-Madrigal M. M., del Valle L. J., Kobauri S., Katsarava R., Alemán C., Puiggalí J.: Microfibres of conducting polythiophene and biodegradable poly(ester urea) for scaffolds. Polymer Chemistry, **6**, 925–937 (2015).
DOI: 10.1039/C4PY01243G

[26] Guimard N. K. E., Sessler J. L., Schmidt C. E.: Toward a biocompatible and biodegradable copolymer incorporating electroactive oligothiophene units. Macromolecules, **42**, 502–511 (2009).
DOI: 10.1021/ma8019859

[27] Zhao W., Glavas L., Odelius K., Edlund U., Albertsson A-C.: Facile and green approach towards electrically conductive hemicellulose hydrogels with tunable conductivity and swelling behavior. Chemistry of Materials, **26**, 4265–4273 (2014).
DOI: 10.1021/cm501852w

[28] Glavas L., Odelius K., Albertsson A-C.: Induced redox responsiveness and electroactivity for altering the properties of micelles without external stimuli. Soft Matter, **10**, 4028–4036 (2014).
DOI: 10.1039/C4SM00258J

[29] Shi G., Rouabhia M., Wang Z., Dao L., Zhang Z.: A novel electrically conductive and biodegradable composite made of polypyrrole nanoparticles and polylactide. Biomaterials, **25**, 2477–2488 (2004).
DOI: 10.1016/j.biomaterials.2003.09.032

[30] Xu H., Holzwarth J. M., Yan Y., Xu P., Zheng H., Yin Y., Li S., Ma P. X.: Conductive PPY/PDLLA conduit for peripheral nerve regeneration. Biomaterials, **35**, 225–235 (2014).
DOI: 10.1016/j.biomaterials.2013.10.002

[31] Jeong S. I., Jun I. D., Choi M. J., Nho Y. C., Lee Y. M., Shin H.: Development of electroactive and elastic nanofibers that contain polyaniline and poly(L-lactide-*co*-ε-caprolactone) for the control of cell adhesion. Macromolecular Bioscience, **8**, 627–637 (2008).
DOI: 10.1002/mabi.200800005

[32] Abidian M. R., Kim D-H., Martin D. C.: Conducting-polymer nanotubes for controlled drug release. Advanced Materials, **18**, 405–409 (2006).
DOI: 10.1002/adma.200501726

[33] Llorens E., Pérez-Madrigal M. M., Armelin E., del Valle L. J., Puiggalí J., Alemán C.: Hybrid nanofibers from biodegradable polylactide and polythiophene for scaffolds. RSC Advances, **4**, 15245–15255 (2014).
DOI: 10.1039/C3RA42829J

[34] Kim B., Chen L., Gong J., Osada Y.: Titration behavior and spectral transitions of water-soluble polythiophene carboxylic acids. Macromolecules, **32**, 3964–3969 (1999).
DOI: 10.1021/ma981848z

[35] Müller F., Ferreira C. A., Azambuja D. S., Alemán C., Armelin E.: Measuring the proton conductivity of ion-exchange membranes using electrochemical impedance spectroscopy and through-plane cell. Journal of Physical Chemistry B, **118**, 1102–1112 (2014).
DOI: 10.1021/jp409675z

[36] del Valle L. J., Camps R., Díaz A., Franco L., Rodríguez-Galán A., Puiggalí J.: Electrospinning of polylactide and polycaprolactone mixtures for preparation of materials with tunable drug release properties. Journal of Polymer Research, **18**, 1903–1917 (2001).
DOI: 10.1007/s10965-011-9597-3

[37] Kister G., Cassanas G., Vert M.: Effects of morphology, conformation and configuration on the IR and Raman spectra of various poly(lactic acid)s. Polymer, **39**, 267–273 (1998).
DOI: 10.1016/S0032-3861(97)00229-2

[38] Shi G., Xu J., Fu M.: Raman spectroscopic and electrochemical studies on the doping level changes of polythiophene films during their electrochemical growth processes. Journal of Physical Chemistry B, **106**, 288–292 (2002).
DOI: 10.1021/jp013023o

[39] Marmur A.: Wetting on hydrophobic rough surfaces: To be heterogeneous or not to be? Langmuir, **19**, 8343–8348 (2003).
DOI: 10.1021/la0344682

[40] Kaplan J. A., Lei H., Liu R., Padera R., Colson Y. L., Grinstaff M. W.: Imparting superhydrophobicity to biodegradable poly(lactide-*co*-glycolide) electrospun meshes. Biomacromolecules, **15**, 2548–2554 (2014).
DOI: 10.1021/bm500410h

[41] Neumann A. W., Good R. J., Hope C. J., Sejpal M.: An equation-of-state approach to determine surface tensions of low-energy solids from contact angles. Journal of Colloid and Interface Science, **49**, 291–304 (1974).
DOI: 10.1016/0021-9797(74)90365-8

[42] Fowkes F. M.: Additivity of intermolecular forces at interfaces. I. Determination of the contribution to surface and interfacial tensions of dispersion forces in various liquids. Journal of Physical Chemistry, **67**, 2538–2541 (1963).
DOI: 10.1021/j100806a008

[43] Owens D. K., Wendt R. C.: Estimation of the surface free energy of polymers. Journal of Applied Polymer Science, **13**, 1741–1747 (1969).
DOI: 10.1002/app.1969.070130815

[44] Kaelble D. H.: Dispersion-polar surface tension properties of organic solids. The Journal of Adhesion, **2**, 66–81 (1970).
DOI: 10.1080/0021846708544582

[45] Singh A., Naskar A. K., Haynes D., Drews M. J., Smith Jr. D. W.: Synthesis, characterization and surface properties of poly(lactic acid)–perfluoropolyether block copolymers. Polymer International, **60**, 507–516 (2010). DOI: 10.1002/pi.2982

[46] Quian X., Gu N., Cheng Z., Yang X., Wang E., Dong S.: Impedance study of $(PEO)_{10}LiClO_4$–Al_2O_3 composite polymer electrolyte with blocking electrodes. Electrochimica Acta, **46**, 1829–1836 (2001). DOI: 10.1016/S0013-4686(00)00723-4

[47] Soboleva T., Xie Z., Shi Z., Tsang E., Navessin T., Holdcroft S.: Investigation of the through-plane impedance technique for evaluation of anisotropy of proton conducting polymer membranes. Journal of Electroanalytical Chemistry, **622**, 145–152 (2008). DOI: 10.1016/j.jelechem.2008.05.017

[48] Rodrigues I. R., de Camargo Forte M. M., Azambuja D. S., Castagno K. R. L.: Synthesis and characterization of hybrid polymeric networks (HPN) based on polyvinyl alcohol/chitosan. Reactive and Functional Polymers, **67**, 708–715 (2007). DOI: 10.1016/j.reactfunctpolym.2007.05.010

[49] Douglass Jr. E. F., Driscoll P. F., Liu D., Burnham N. A., Lambert C. R., McGimpsey W. G.: Effect of electrode roughness on the capacitive behavior of self-assembled monolayers. Analytical Chemistry, **80**, 7670–7677 (2008). DOI: 10.1021/ac800521z

[50] Peng S., Zhu P., Wu Y., Mhaisalkar S. G., Ramakrishna S.: Electrospun conductive polyaniline–polylactic acid composite nanofibers as counter electrodes for rigid and flexible dye-sensitized solar cells. RSC Advances, **2**, 652–657 (20012). DOI: 10.1039/C1RA00618E

[51] McKeon K. D., Lewis A., Freeman J. W.: Electrospun poly(D,L-lactide) and polyaniline scaffold characterization. Journal of Applied Polymer Science, **115**, 1566–1572 (2010). DOI: 10.1002/app.31296

[52] Jeong S. I., Jun I. D., Choi M. J., Nho Y. C., Lee Y. M., Shin H.: Development of electroactive and elastic nanofibers that contain polyaniline and poly(L-lactide-*co*-ε-caprolactone) for the control of cell adhesion. Macromolecular Bioscience, **8**, 627–637 (2008). DOI: 10.1002/mabi.200800005

[53] Chen M-C., Sun Y-C., Chen Y-H.: Electrically conductive nanofibers with highly oriented structures and their potential application in skeletal muscle tissue engineering. Acta Biomaterialia, **9**, 5562–5572 (2013). DOI: 10.1016/j.actbio.2012.10.024

[54] Forciniti L., Guimard N. K., Lee S., Schmidt C. E.: Unique electrochemically synthesized polypyrrole: Poly (lactic-*co*-glycolic acid) blends for biomedical applications. Journal of Materials Chemistry, **20**, 8865–8874 (2010). DOI: 10.1039/C0JM01015D

[55] Granato F., Bianco A., Bertarelli C., Zerbi G.: Composite polyamide 6/polypyrrole conductive nanofibers. Macromolecular Rapid Communications, **30**, 453–458 (2009). DOI: 10.1002/marc.200800623

[56] Zurita R., Puiggalí J., Rodríguez-Galán A.: Triclosan release from coated polyglycolide threads. Macromolecular Bioscience, **6**, 58–69 (2006). DOI: 10.1002/mabi.200500147

[57] del Valle L. J., Roa M., Díaz A., Casas M. T., Puiggalí J., Rodríguez-Galán A.: Electrospun nanofibers of a degradable poly(ester amide). Scaffolds loaded with antimicrobial agents. Journal of Polymer Research, **19**, 9792–9805 (2012). DOI: 10.1007/s10965-011-9792-2

[58] del Valle L. J., Roca D., Franco L., Puiggalí J., Rodríguez-Galán A.: Preparation and release study of ibuprofen-loaded porous matrices of a biodegradable poly(ester amide) derived from L-alanine units. Journal of Applied Polymer Science, **122**, 1953–1967 (2012). DOI: 10.1002/app.34017

[59] Baker R.: Controlled release of biologically active agents. Wiley, New York (1987).

[60] Bottino M. C., Kamocki K., Yassen G. H., Platt J. A., Vail M. M., Ehrlich Y., Spolnik K. J., Gregory R. L.: Bioactive nanofibrous scaffolds for regenerative endodontics. Journal of Dental Research, **92**, 963–969 (2013). DOI: 10.1177/0022034513505770

eXPRESS Polymer Letters Vol.10, No.8 (2016) 647–663
Available online at www.expresspolymlett.com
DOI: 10.3144/expresspolymlett.2016.59

Influence of reprocessing on fibre length distribution, tensile strength and impact strength of injection moulded cellulose fibre-reinforced polylactide (PLA) composites

N. Graupner[1*], *K. Albrecht*[1], *G. Ziegmann*[2], *H. Enzler*[2], *J. Müssig*[1]

[1]HSB - City University of Applied Sciences, Dept. Biomimetics, The Biological Materials Group, Neustadtswall 30, D-28199 Bremen, Germany
[2]Institute for Polymer Materials and Plastics Processing, Clausthal University of Technology, Agricolastr. 6, D-38678 Clausthal-Zellerfeld, Germany

Received 5 December 2015; accepted in revised form 29 February 2016

Abstract. The present study focuses on the reprocessing behaviour of recycled injection moulded polylactide (PLA) composites. The composites are reinforced with regenerated cellulose fibres (lyocell) of variable fineness and a fibre mass content of 30%. They were reprocessed up to three times. The influence of reprocessing on the fibre length distribution and the resulting composite mechanical properties (tensile and impact strength) was analysed. While the first reprocessing cycle does not affect the mechanical characteristics of the neat PLA matrix, the strength of the composites decreases significantly due to a decreasing fibre aspect ratio. It was shown that fibres having a larger cross-sectional area display a lower aspect ratio than finer fibres, after reprocessing. This phenomenon leads to a larger decrease in tensile strength of composites reinforced with coarser fibres when compared to composites reinforced with finer fibres. A comparison of virgin composites and threefold reprocessed composites with a similar fibre length distribution resulted in a significantly higher tensile strength compared to the virgin sample. This result leads to the conclusion that not only the fibre length is drastically reduced by reprocessing but also that the fibres and the matrix were damaged.

Keywords: *polymer composites, recycling, biocomposites, mechanical properties, processing technologies*

1. Introduction

Due to increasing environmental awareness, the demand for recycled and reprocessed composites is growing, especially for man-made fibre-reinforced petrochemical-based plastics. Oliveux *et al.* [1] give an overview of the characteristics of recycled glass, carbon and aramid fibre-reinforced plastics and summarise the influences of different recycling techniques on the composite mechanical properties.

Many studies deal with the reprocessing of glass fibre-reinforced composites. For the greater part virgin composites are reprocessed mechanically via shredding and injection moulding. While the Young's modulus is usually little affected, the tensile strength of reprocessed composites typically decreases with an increasing number of reprocessing steps due to fibre shortening. These effects were observed by Bourmaud and Baley [2, 3] as well as by Dickson *et al.* [4] for glass fibre-reinforced polypropylene (PP) or by Bernasconi *et al.* [5] for glass fibre-reinforced polyamide (PA) 6.6 among others.

Recycling is becoming even more important for natural fibre-reinforced composites. 30 000 tonnes of natural fibres were used 2012 in the European automotive industry, an increase from around 19 000 tonnes of natural fibres towards 2005 [6]. Since 2015, the

*Corresponding author, e-mail: nina.graupner@hs-bremen.de

European automotive industry must recycle 95 mass% of an automobile [7]. Only 5% of the materials may be discarded. 10% may be incinerated and 85% must be recycled. Since the mass of natural fibre-reinforced composites in automotive applications has significantly increased in recent years, recycling is becoming increasingly important for this class of materials. Most natural fibre-reinforced composites are produced with thermoplastic polymers as a matrix. Some approaches exist for the mechanical reprocessing of composites and the further processing by injection moulding, e.g. for flax fibre-reinforced PP [4, 8], flax fibre-reinforced polylactide (PLA) [9], hemp fibre-reinforced PP [2, 3], sisal fibre-reinforced PP [2, 3], wood fibre-reinforced PP [4, 10], wood fibre-reinforced high density polyethylene (HD-PE) [11] or alfa fibre-reinforced polyvinylchloride (PVC) [12]. A decrease in fibre length during reprocessing was found for all cited studies. An opposite trend was observed for the void fraction, which was observed to decrease during reprocessing, leading to a more homogeneous composite structure and a better wetting of the fibres within the matrix [12, 13].

The main problem which appears during reprocessing is the shortening of fibres, leading to a lower aspect ratio when single man-made fibres are considered. Since the most plant fibres are arranged in fibre bundles, it is possible that these fibre bundles are split into smaller fibre bundles or single fibres. It should be noted that different natural fibre bundles show different breakage during processing. Depending on their chemical composition, elementary fibre cells and mechanical strength, natural fibres present more or less extensive breaking and disaggregation during processing. Beaugrand and Berzin have shown that the aspect ratio of hemp fibres in a polycaprolactone (PCL) matrix increases when plasticised in water [14]. Le Moigne *et al.* [15] investigated the length and aspect ratio of flax, sisal and wheat straw extracted from their PP based composites after injection moulding. Flax was mainly broken into elementary fibres whereas sisal still showed fibre bundles and single fibres. In contrast to this, wheat straw showed bundles and particles of low aspect ratios. In the case where fibre bundles are opened to smaller bundles or single fibres the aspect ratio may increase during reprocessing, in contrast to single glass fibres which have a decreasing aspect ratio. The lower decreasing aspect ratio of flax fibres leads to a lower decrease of the composites' tensile strength after reprocessing when compared to glass fibre-reinforced composites [9]. Moreover the interface quality influences the fibre breakage. As shown for lyocell fibre-reinforced composites, the length of fibres extracted from injection moulded PP composites with a weaker fibre/matrix adhesion was higher when compared to fibres extracted from an injection moulded PLA composite [16]. Generally, the tensile strength decreases when the fibre length of short fibres is reduced. This is especially the case for changes in length of fibres with values around the critical fibre length, e.g. by (re)processing, as it has a large effect on the composites' tensile strength. A work by Fu and Lauke [17] has shown that an increase of the fibre length around and even above the critical fibre length, up to a value where the maximum tensile strength of a composite is achieved, has a significant influence on the composites' tensile strength. In particular, an increasing number of fibres with length values below the critical fibre length leads to a decrease of composite tensile strength values [18]. Hence, an investigation of processing and reprocessing of composites as a function of the fibre length is very important. No recent studies were found which address the reprocessing behaviour of composites reinforced with regenerated cellulose fibres. This study is an attempt to identify the influences on the composite mechanical properties as a function of the fibre fineness and the number of reprocessing cycles of lyocell fibre-reinforced PLA.

2. Materials and methods

2.1. Fibres and matrix

Composites were produced from lyocell staple fibres (type Tencel®, Lenzing AG, Lenzing, AT) with a length >38 mm and a fineness of 1.3, 6.7 and 15.0 dtex (equivalent diameter: 10.5, 24.7 and 35.7 μm). The polylactide (PLA) matrix was supplied in the form of staple fibres (type Ingeo SLN 2660 D; Eastern Textile Ltd., Taipei, TW) with a fineness of 6.7 dtex and a length of 64 mm. Fibres were produced from NatureWorks™ 6202 D PLA with a density of 1.24 g/cm^3, a melting temperature of 160–170 °C and a glass transition temperature of 60–65 °C.

2.2. Composite processing

2.2.1. Composite production

Multilayer webs were manufactured with a laboratory carding machine with a working width of 200 mm (Shirley Developments Limited SDL, Stockport, UK, serial number 02895) as semi-finished products. Lyocell fibres and PLA fibres were mixed during the carding process at environmental conditions (approx. 25 °C, 45% relative humidity). The initial mass of lyocell and PLA fibres was calculated on the basis of the dry mass for a lyocell fibre mass content of 30%. As reference samples multilayer webs were produced from 100% PLA fibres. The multilayer webs were then dried for 2 h at 105 °C in a forced air oven (Thermicon®, Heraeus GmbH, Hanau, DE). Following this, composite boards were produced with a compression moulding technique between two Teflon sheets. Hot compression moulding was carried out at 180 °C for 3 min (press type HP-S10, Joos, Pfalzengrafenweiler, DE). Afterwards, the boards were compression moulded in a cold press (type HP-S60, Joos, Pfalzengrafenweiler, DE) at 25 °C for 3 min. The pressure was set to 5 MPa for the PLA reference sample and to 12 MPa for the composites. Composite boards were shredded to granules (shredder type EBA 2326C, Krug & Priester GmbH & Co. KG, Balingen, DE) and were dried in a forced air oven for 2 h at 105 °C (type 2111520000200, Windaus-Labortechnik GmbH & Co. KG, Tullingen, DE). Injection moulding was carried out with an Arburg 320C Allrounder 600–250 machine (Arburg GmbH + Co KG, Loßburg, DE; Screw: ø30 mm, circumferential speed 20 m/min; nozzle diameter: 5 mm) at a temperature profile of 170–172–175–177–180 °C. The injection moulding machine nozzle was heated to 180 °C and the injection mould was cooled to 25 °C. The injection pressure, the backpressure and the hold pressure were set to 600, 10 and 480 bar, respectively. The cooling time was 30 s in a standard test specimen tool (type 1 A according to DIN EN ISO 527-2 [19]).

2.2.2. Reprocessing

Injection moulded composites were shredded into granules (G) with a cutting mill type S15/20L (No. K10300; H. Dreher GmbH & Co. KG, DE) equipped with a sieve of rectangular holes (8 × 8 mm^2). Granules were pre-dried for 2 h at 105 °C and then injection moulded in the same manner as described above. Composites reinforced with lyocell 1.3, 6.7 and 15.0 dtex were reprocessed once (R1). As an example lyocell/PLA composites reinforced with medium fine lyocell 6.7 dtex fibres were additionally reprocessed two (R2) and three times (R3).

2.3. Composite testing

Prior to mechanical composite characterisation, test specimens were conditioned according to DIN EN ISO 291 [20] at 23 °C and 50% relative humidity.

2.3.1. Tensile strength

At least 5 test specimens (type 1A, DIN EN ISO 527-2 [19]) were tested with a universal testing machine type Zwick Z 020 (Zwick/Roell, Ulm, DE) working with a load cell of 20 kN and a Zwick/Roell pneumatic clamping system (clamping pressure: 1–2 bar). The gauge length was fixed to 100 mm. A preload of 50 N was used and the test was performed with a speed of 2 mm/min.

2.3.2. Impact strength

The unnotched Charpy impact strength was determined with a pendulum impact testing machine (type 5101, Zwick, Ulm, DE) operating with a pendulum hammer of 2 J according to DIN EN ISO 179 [21]. In deviation from the standard, 5 test specimens instead of the usual 10 with the dimensions of 80 × 10 × 4 mm^3 were investigated. The bearing distance was set to 40 mm. The sample was hit on the flatwise impact direction.

2.3.3. Differential scanning calorimetry (DSC)

DSC of PLA composites was carried out with a DSC device type Q2000 V24.11 Build 124 (TA instruments, New Castle, USA) in a temperature range between 0 and 200 °C (ramp 10 °C/min) under a nitrogen flow of 50 mL/min. The first and second heating cycles were analysed.

2.4. Fibre extraction

For the determination of the fibre length distribution and the actual fibre mass content, fibres were extracted from granules and composites. For this purpose the composites were conditioned according to DIN EN ISO 139 [22]. Ca. 1 g of a composite from the parallel section of a tensile test specimen was weighed

exactly in a Duran® filter crucible with a porosity of 3 and a volume of 30 mL (Carl Roth GmbH & Co. KG, Karlsruhe, DE) with a scale (type Kern ABT 120-5 DM, d = 0.00001 g; Kern und Sohn GmbH, Balingen, DE). The crucibles were then boiled for 15 min in xylene (97%, Carl Roth GmbH & Co. KG, Karlsruhe, DE) and filtered with suction using a vacuum pump and a filter flask. The procedure was repeated up to five times until no precipitated polymer appears. Then the crucibles were dried for 0.5 h at 105 °C, conditioned and weighed a second time according to DIN EN ISO 139 [22]. The fibre mass content was calculated from the initial mass and the fibre mass after extraction. The extracted fibres were used for the measurement of the fibre length.

2.5. Fibre testing

Prior to the investigations, fibres were conditioned according to DIN EN ISO 139 [22] at 20 °C and 65% relative humidity.

2.5.1. Tensile test

Tensile characteristics of raw lyocell fibres were determined with a Fafegraph M testing machine (Textechno, Mönchengladbach, DE) working with a pneumatic clamping system (PVC/PMMA clamps). More than 70 fibres were investigated with a load cell of 100 cN at a gauge length of 3.2 mm and a testing speed of 2 mm/min.

2.5.2. Fibre length

The measurement of the fibre length distribution was performed for more than 500 fibres in each sample with the image analysis software Fibreshape 5.1.1 (IST AG, Vilters, CH). Fibres were prepared on a slide frame (40 × 40 mm^2, glass thickness 2 mm, company Gepe, Zug, CH) and scanned (4000 dpi resolution for lyocell 1.3, 2400 dpi resolution for lyocell 6.7 dtex and 2000 dpi resolution for lyocell 15.0 dtex). Intersecting fibres were not considered for the evaluation. An image used for the measurement of the fibre length is shown as an example in Figure 1. Red ellipses indicate intersecting fibres. A high number of intersecting fibres may lead to a reduction of the length value, since the probability for fibre intersections increase with increasing fibre length. Therefore, care should be taken during fibre preparation to reduce the number of fibre intersections.

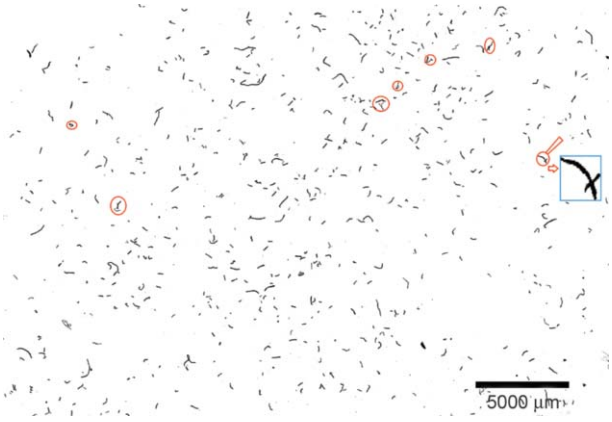

Figure 1. Scan of extracted fibres from a PLA composite reinforced with lyocell 15.0 dtex (R1). Red ellipses show intersecting fibres.

A comparison of the measured fibre length L with the critical fibre length L_c (fibre length which is necessary to reach a reinforcing effect in a matrix) is of particular importance. When the interfacial shear strength τ between fibre and matrix is known, L_c can be calculated according to Equation (1) with the tensile strength σ_f of the fibre and the equivalent fibre diameter d_f. L_c was determined for lyocell in PLA with a pull-out test in a previous study [23]:

$$L_c = \frac{\sigma_f \cdot d_f}{2 \cdot \tau} \quad (1)$$

2.5.3. Scanning electron microscopy (SEM)

Fibre surfaces and fracture surfaces of composites were investigated with a SEM type JSM 6510 (Jeol, Eching, DE) operating with emission electrons at a current of 10 kV. Prior to SEM investigation the samples were sputtered with gold for 90 s under a current of 56 mA with a Bal-Tec sputter coater type SCD 005 (Bal-Tec, Liechtenstein).

2.6. Statistics

The statistical evaluation of the results was carried out with the open source R software (http://www.r-project.org/) with a Shapiro-Wilk test [24] regarding a normal distribution of $n < 5000$. To discover if there were significant differences between the data of variable samples, for normally distributed data with homogenous variances the Tukey-test [25] was used and for data which were not distributed normally the Wilcoxon test [26] was chosen. All tests were performed with a level of significance a = 0.05. Results are shown as Box-Whisker plots or histograms

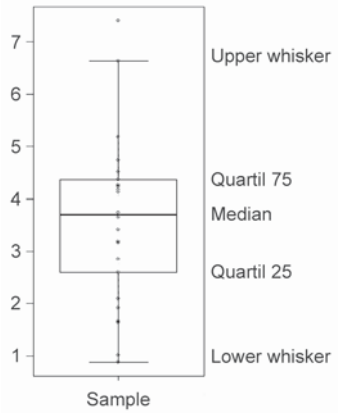

Figure 2. Box-Whisker plot with median value and the second and third quartile

[27, 28]. A typical Box-Whisker plot, showing the median, the 2nd (Quartil 25) and 3rd quartile (Quartil 75) and 1.5 times the interquartile length (Whiskers) is shown in Figure 2. Since many results are not distributed normally, values reported in the text are given as median value ± mean arithmetic deviation. Significant differences within one series of experiments are marked with different letters above the plots and an asterisk shows results which are not distributed normally.

3. Results and discussion

3.1. Fibre mass content

In order to compare the properties of the composites with each other, the fibre mass fraction of the composites should not deviate significantly from each other. Table 1 shows the fibre mass content of virgin composites, reprocessed granules (G) and reprocessed composites (R1, R2, R3) resulting from the fibre extraction. Reprocessed granules were produced from tensile test specimens via shredding and were then used for the production of reprocessed composites via injection moulding. The results show that the maximum deviation of the fibre mass content compared to the nominal fibre mass content (30%) is 3% for lyocell 1.3 dtex/PLA, R1. The maximum deviation of composites within one series of experiments is 2%. The extraction method itself provides an accuracy of ± 1%. Therefore, the measured deviations are negligible and the results of the composites are comparable.

Table 1. Fibre mass content of virgin composites as well as reprocessed granules and composites determined by fibre extraction (G: granules, R1: first reprocessing step, R2: second reprocessing step, R3: third reprocessing step)

Composite	Fibre mass content [%]	
	Actual value	Nominal value
30% lyocell 1.3 dtex/PLA	28	30
30% lyocell 1.3 dtex/PLA, R1	27	30
30% lyocell 6.7 dtex/PLA	28	30
30% lyocell 6.7 dtex/PLA, G, R1	29	30
30% lyocell 6.7 dtex/PLA, R1	29	30
30% lyocell 6.7 dtex/PLA, G, R2	29	30
30% lyocell 6.7 dtex/PLA, R2	29	30
30% lyocell 6.7 dtex/PLA, G, R3	29	30
30% lyocell 6.7 dtex/PLA, R3	30	30
30% lyocell 15.0 dtex/PLA	28	30
30% lyocell 15.0 dtex/PLA, R1	28	30

3.2. Fibre tensile strength

As shown in Figure 3, the results of the tensile strength values of virgin lyocell fibres are not distributed normally and decrease significantly with increasing fibre cross-section. The median fibre strength decreases from 511 (±71) MPa for lyocell 1.3 dtex to 448 (±52) MPa for lyocell 6.7 dtex and 348 (±64) MPa for lyocell 15.0 dtex, respectively. This behaviour could be explained by a higher probability for defects in the cross-sectional area due to the higher fibre volume. This trend was confirmed by Moon *et al.* [29] and Wilson [30] for glass and ceramic fibres as well. The lower fibre strength and specific fibre surface of coarser fibres compared to fine fibres should be considered in the evaluation of the composite mechanical characteristics.

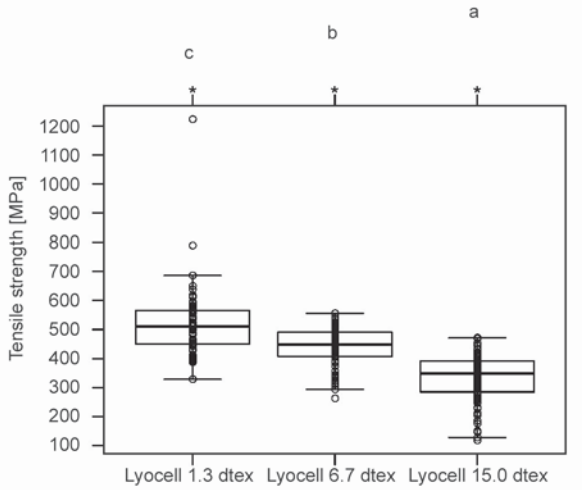

Figure 3. Tensile strength of lyocell fibres of variable fineness shown as Box-Whisker plots (significant differences are marked with different letters; an asterisk shows results which are not distributed normally)

3.3. Influence of fibre fineness and reprocessing on the composite mechanical properties

3.3.1. Tensile and impact strength of composites

The tensile strength was investigated for composites reinforced with lyocell of variable fineness as well as for the neat PLA reference sample. PLA matrix and composites were reprocessed once. The tensile strength results are shown in Figure 4. It is shown that the tensile strength of neat PLA was reduced only slightly from 60 (±0.1) to 58 (±0.2) MPa due to reprocessing. Courgneau *et al.* [31] reported that the molecular weight of neat PLA decreases due to compounding which has a strong impact on the degradation. It was shown that the combination of water granulation after compounding and a following drying leads to a clear reduction of the molecular mass of PLA. Since our granules were prepared via compression moulding and shredding this aspect can be negated. Moreover Courgneau *et al.* [31] stated that injection moulding itself does not have a significant impact on the degradation of neat PLA. Lekube [32] confirmed the low degradation of neat PLA due to injection moulding and showed only a slightly lower tensile strength of neat PLA reprocessed in five cycles compared to virgin PLA.

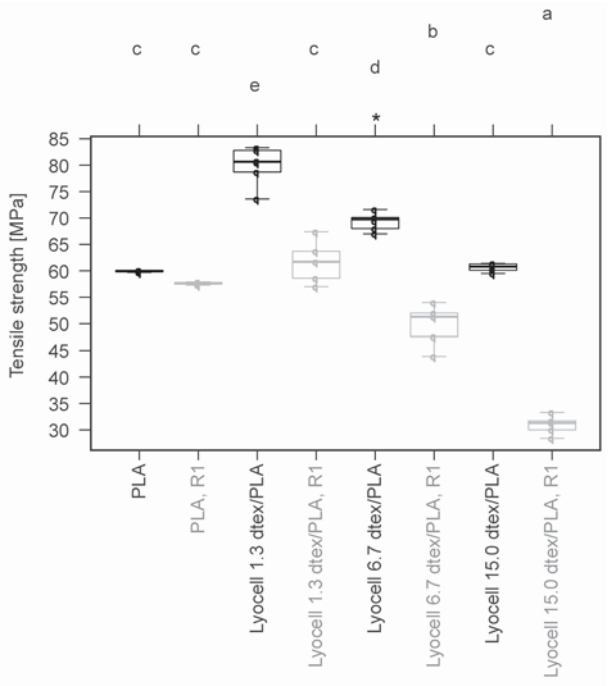

Figure 4. Tensile strength of PLA matrix and lyocell/PLA composites in virgin state and reprocessed (R1) shown as Box-Whisker plots (significant differences are marked with different letters; an asterisk shows results which are not distributed normally)

When considering the virgin composites, a significant decrease of tensile strength with increasing fibre cross-section can be seen. This effect is caused by the decreasing tensile strength of fibres with an increasing cross-sectional area as well as a decreasing specific fibre surface for fibre/matrix interaction as described by Moon *et al.* [29] for glass fibres embedded in epoxy and HDPE. Significantly the highest reinforcing effect was determined for composites reinforced with the finest fibre (1.3 dtex) resulting in a tensile strength of 81 (±2.5) MPa. Compared to the neat matrix this is an increase by factor 1.34. Moreover, a significant enhancement effect was measured for lyocell 6.7 dtex/PLA with a value of 70 (±1.2) MPa which is an improvement by a factor of 1.16. For the composite reinforced with the coarse lyocell 15.0 dtex fibres with a tensile strength of 61 (±0.7) MPa no reinforcement effect was detected (factor 1.01).

Reprocessed composites show significantly lower values when compared to virgin samples. As presented in Figure 4, the tensile strength of virgin composites decreases drastically with an increasing fibre cross-section. Compared to virgin composites no significant reinforcement effect was achieved for lyocell 1.3 dtex/PLA with a tensile strength of 62 (±3.1) MPa (factor of 1.07). For lyocell 6.7 dtex/PLA and lyocell 15.0 dtex/PLA decreases by factors of 0.89 and 0.54 with tensile strength values of 51 (±3.2) and 31 (±1.4) MPa were measured, respectively.

As reported by Courgneau *et al.* [31] an additional aspect besides process induced fibre shortening, resulting in reduced tensile strength data of composites could be the degradation of the PLA matrix due to the higher moisture content of cellulose fibres compared to PLA. Moisture leads to a reduction of the molecular weight of PLA due to hydrolysis and a decrease in length of the polymer chains. This effect might be increased by reprocessing, since the granules in the intermediate processing step can absorb moisture, which may result in further hydrolysis of the polymer chains of the PLA matrix during the following injection moulding step.

The crack initiation measured with the unnotched Charpy impact test (Figure 5) shows similar trends as described for the tensile strength. The impact strength of virgin neat PLA decreases only slightly from 11 (±1.5) to 10 (±1.0) kJ/m^2 for the reprocessed

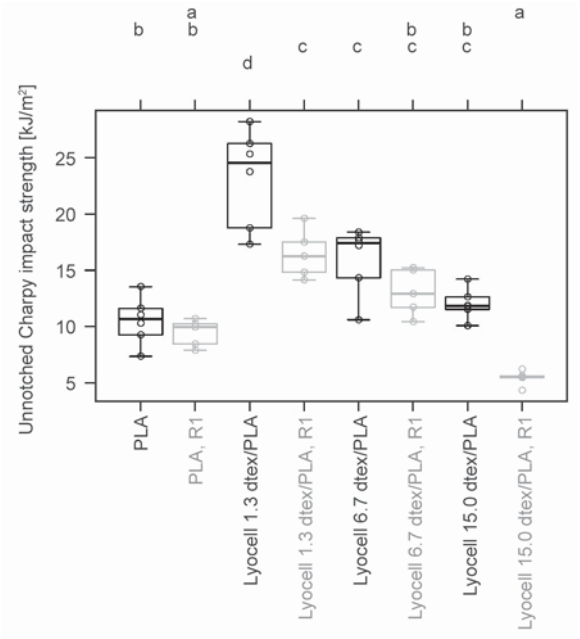

Figure 5. Unnotched Charpy impact strength of PLA and lyocell/PLA composites in virgin state and reprocessed (R1) shown as Box-Whisker plots (significant differences are marked with different letters; all results are distributed normally)

PLA. For both virgin and reprocessed composites, a clear influence by fibre fineness was detected with decreasing impact strength values for composites reinforced with coarser fibres. But in comparison to the tensile strength, the reinforcing effect of the fibres is higher. For virgin lyocell 1.3 dtex/PLA the impact strength increased up to a value of 25 (±3.5) kJ/m^2 which is an improvement by a factor of 2.30. For lyocell 6.7 and 15.0 dtex values of 17 (±2.4) and 12 (±0.9) kJ/m^2 were achieved (improvement factors of 1.63 and 1.11, respectively). In contrast to the tensile strength data, reprocessed composites reinforced with lyocell 1.3 dtex and lyocell 6.7 dtex display significantly higher impact values compared to the neat matrix. Values of 16 (±1.7) and 13 (±1.6) kJ/m^2 were achieved corresponding to improvement factors of 1.63 and 1.30. A decrease of impact strength by a factor of 0.55 was determined for lyocell 15.0 dtex/PLA (6 (±0.4) kJ/m^2). The reasons for the lower values of reprocessed composites compared to virgin samples are the same as those described for the tensile strength.

Despite a multiple higher tensile strength of the fibres compared to the PLA matrix a reinforcement effect was not achieved for the tensile strength of lyocell 15.0 dtex/PLA. A previous study has shown a 1.5 times higher tensile strength with a value of 76 MPa for lyocell 15.0 dtex/PLA when compared to pure PLA [33]. In contrast to the present study, the composites were processed with much longer fibres (fibre length 60 mm) via compression moulding leading to a higher reinforcing effect. Therefore, it is important to evaluate the fibre length distribution and the influence of the fibre length on the mechanical composite properties.

3.3.2. Fibre length distribution

The first reprocessing step (R1) has shown to significantly influence the mechanical characteristics of the composites. From this standpoint, the hypothesis, that fibres are strongly damaged due to the recycling process is verified. It is known that processing via extrusion and injection moulding leads to a clear fibre shortening as shown by Joffre *et al.* [13] for wood/PLA composites or Erdmann and Ganster [34] for Cordenka fibre-reinforced PLA composites. Hence, any further reprocessing can lead to additional fibre shortening.

In this study, the fibre length distribution was investigated for fibres which were extracted from virgin and reprocessed composites. Figure 6 shows the percentages of fibre length distributions as histograms. A higher frequency of longer fibres was observed for both, virgin and reprocessed composites, with increasing fibre cross-section. As a result, 67% of lyocell 1.3 dtex fibres, extracted from virgin composites, have a fibre length of >300 µm while lyocell 6.7 dtex and lyocell 15.0 dtex show values of 76 and 73%, respectively. However, reprocessed composites contain fibres of a length >300 µm only to 36, 48 and 62% of lyocell 1.3 dtex, lyocell 6.7 dtex and lyocell 15.0 dtex respectively.

The critical fibre length of lyocell fibres of variable fineness was determined and calculated in previous studies [33, 35] and is presented as rhombuses in Figure 7a. Since the results of the fibre length measurements are not distributed normally, the median values are utilised. As reported by Le Moigne *et al.* [15] fibre length can be strongly influenced and biased by extreme values. It is obvious that the median fibre length of virgin lyocell 1.3 dtex/PLA with a value of 467 µm is clearly higher than the critical fibre length L_c (220 µm [35]), while the fibre length of the reprocessed composite is on the level with the L_c

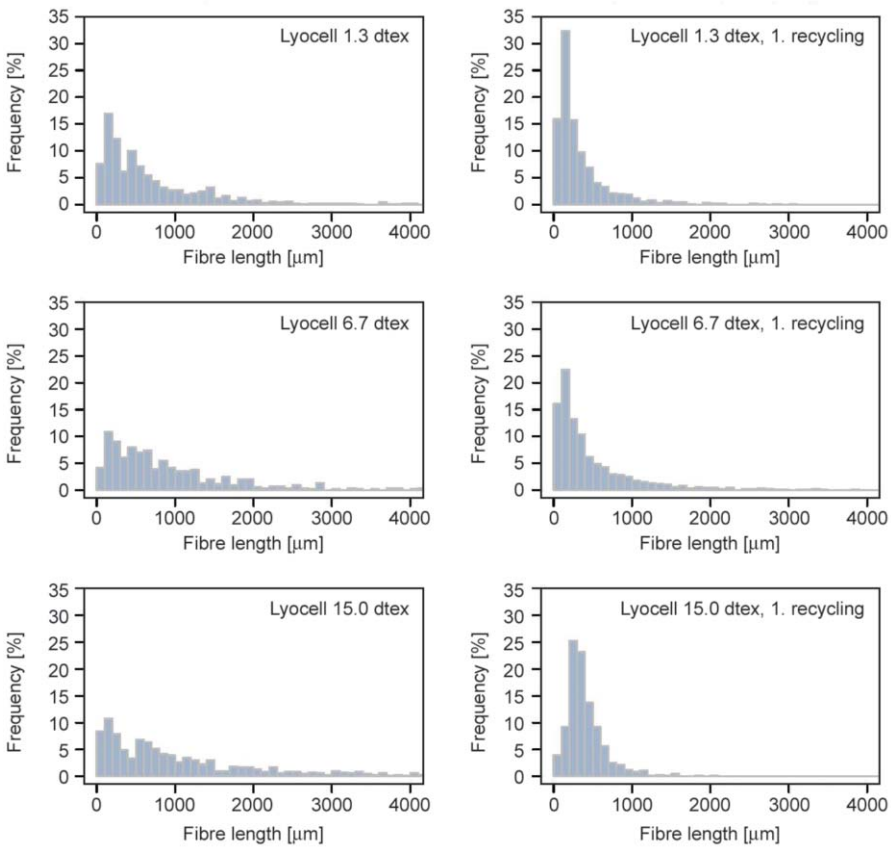

Figure 6. Histograms of fibre length distribution of fibres extracted from virgin and reprocessed (R1) PLA composites reinforced with lyocell fibres of various fibre fineness. Results are pooled in 200 µm steps.

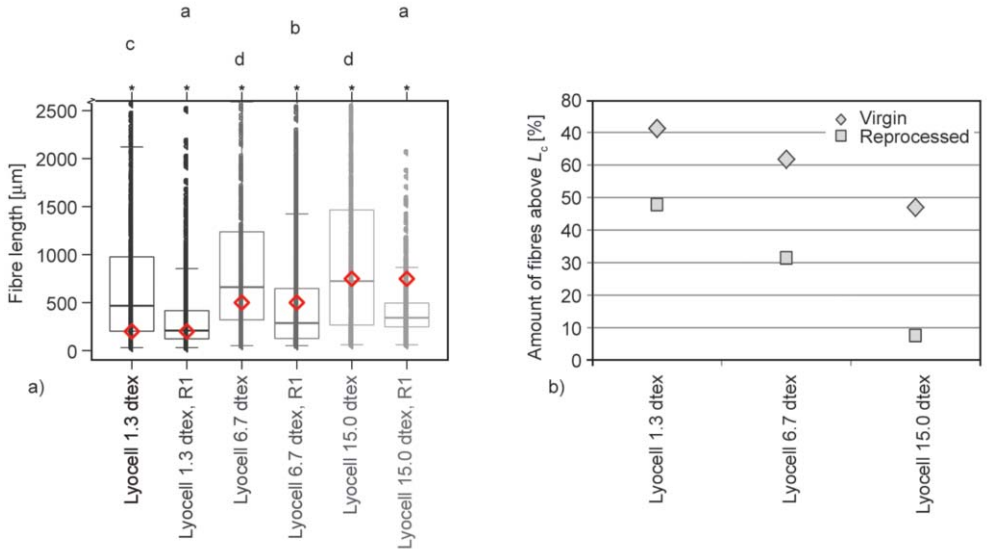

Figure 7. a) Fibre length of fibres with different fineness, extracted from virgin and reprocessed (R1) lyocell/PLA composites. Rhombuses show the critical fibre length of the different fine fibres (significant differences are marked with different letters; an asterisk shows results which are not distributed normally). b) Percental amount of fibres extracted from virgin and reprocessed composites above the critical fibre length L_c.

value of 209 µm. 71% of the fibres used in the virgin lyocell 1.3 dtex/PLA composite display length values above L_c (view Figure 7b); the reprocessed composite contains 48% fibres longer than L_c. For virgin lyocell 6.7 dtex/PLA the median fibre length of 661 µm is slightly higher than L_c (500 µm [35]) and represents 62% of fibres having length values higher than L_c. The median fibre length of the reprocessed com-

posite is with 287 µm below L_c; in which only 31% of the fibres display a fibre length above L_c. The virgin lyocell 15.0 dtex/PLA composite displays fibres with a median fibre length of 724 µm which are on the level with the L_c (748 µm [35]) and a total amount of 47% of fibres being longer than L_c. The corresponding reprocessed composite shows the highest deviation between the median fibre length of 342 µm and L_c, with only 8% of fibres longer than L_c.

These findings are in close alignment with the tensile strength results of the composites (compare Figure 4) and show tensile strength as a function of fibre length. The higher the fibre length compared to L_c, the higher the tensile strength of the composite. Composites with a median fibre length close to the critical fibre length do not display a reinforcement effect and composites with a fibre length below the critical fibre length resulted in lower tensile strength values compared to the PLA matrix. It is known that even a slight increase in fibre length when around L_c, leads to a considerably higher reinforcing effect as shown for the lyocell 6.7 dtex/PLA composite. This trend is confirmed by the work of Fu and Lauke [17] who reported considerable impacts by small changes of the fibre length made around L_c on the tensile strength of glass fibre-reinforced plastics.

The lower tensile strength of composites reinforced with coarser fibres is therefore based on one hand on lower fibre strength and on the other hand on the fibre length, especially the lower aspect ratio. As already discussed the coarse fibre breakages are lower during injection moulding and reprocessing compared to finer fibres (Figure 7). However, finer fibres display a lower equivalent diameter resulting in a higher aspect ratio despite the lower median fibre length (view Figure 8).

The critical aspect ratio which is necessary for a reinforcement effect was determined to be 21 in a previous study for lyocell [33, 35]. The critical aspect ratio is calculated from the critical fibre length of lyocell divided by the fibre diameter. In the case of lyocell 15.0 dtex the critical fibre length of 748 µm is divided by the equivalent diameter of 35.7 µm [33, 35].

Despite of the higher fibre length of the coarser fibres Figure 8a shows a decrease in the fibre aspect ratio with an increasing fibre cross-section. This effect is based on the higher equivalent fibre diameter of coarser fibres when compared to finer fibres

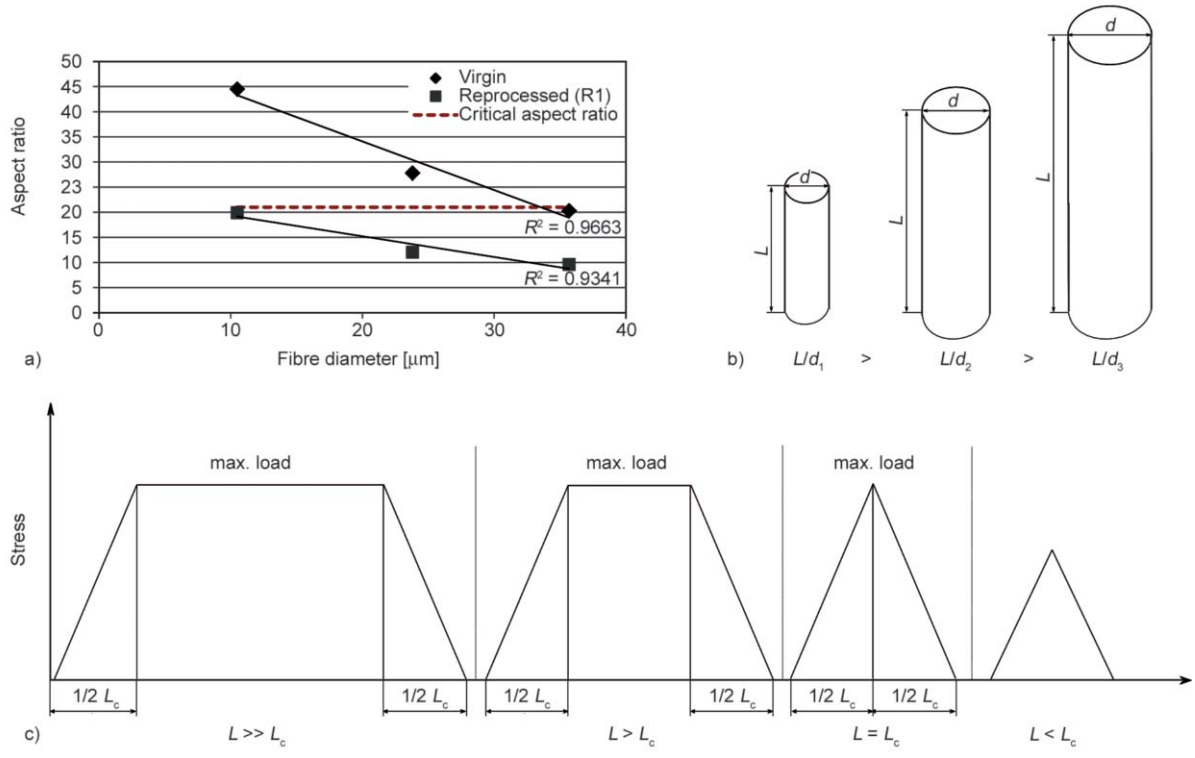

Figure 8. Aspect ratio of fibres extracted from virgin and reprocessed composites as a function of the equivalent fibre diameter (a); influence of fibre diameter on the aspect ratio (b) and maximum loaded fibre surface area (cylindrical fibre surface) as a function of the fibre length (c).

(compare Figure 8b). E.g., the coarser the fibre the higher L_c. Moreover, it is known that the debonding between a fibre and a matrix under mechanical loading usually starts at the fibre end [36, 37]. In composites with the same fibre mass shorter fibres mean a higher number of fibre ends where debonding can start. Fibres with a length equivalent to L_c may lead to a reinforcing effect, however, they cannot provide their full reinforcing potential. The fibres can be fully loaded, but only in a small area in the center (Figure 8c). Fibres with a length > L_c have a significantly higher surface area in which the fibre can be fully loaded, resulting in a higher tensile strength of the composite. The shorter the fibre, the easier it is to pull out from the matrix.

The median aspect ratio of fibres in virgin composites decreased from 45 for lyocell 1.3 dtex/PLA, to 28 for lyocell 6.7 dtex/PLA and 20 for lyocell 15.0 dtex. Fine (1.3 dtex) and medium fine (6.7 dtex) fibres used in virgin composites display a clearly higher aspect ratio when compared to the critical aspect ratio. The aspect ratio of the coarsest fibre is equal to the critical aspect ratio.

Reprocessed fibres show an aspect ratio comparable to the critical aspect ratio in the case of the finest fibres with a value of 20, while the medium fine and the coarse fibres display an aspect ratio below the critical aspect ratio with values of 12 and 10, respectively. It can be concluded that the fibre length, and especially the aspect ratio, have a significant impact on the decreasing tensile strength after reprocessing since the mechanical characteristics of PLA were only slightly reduced after one reprocessing step (view Figure 4). As already discussed the tensile strength of neat PLA is only slightly affected by reprocessing. Besides the decreasing fibre length and possible fibre damage due to reprocessing the residual moisture content may affect the molecular weight of PLA and the mechanical characteristics of the whole composite structure. As shown by Courgneau *et al.* [31] the residual moisture content of PLA composites reinforced with 10 mass% 'highly pure' cellulose fibres is nearly three times higher (640 ppm) than that of neat PLA (260 ppm). This effect leads to a reduction of the molecular weight and a shortening of the polymer chains of the PLA matrix which is highly sensitive towards moisture. NatureWorks™ recommends keeping the moisture content of 6202 D PLA matrix lower than 50 ppm to prevent viscosity degradation and potential loss of properties of the PLA. Reinforcement with cellulose fibres leads to a higher degradation of the PLA matrix. It is assumed that a higher fibre mass fraction of 30% results in a higher moisture content. Moreover the increasing viscosity of the polymer melt due to an increasing cellulose fibre mass fraction may lead to a higher degradation of polymer chains due to higher thermal degradation. Hence, the degradation after one recycling step seems to be mainly influenced by fibre shortening while fibre damage, moisture resulting in a reduction of the length of the polymer chains, and thermal degradation additional affect the degradation of the composite.

3.4. Influence of reprocessing cyles (R1, R2 and R3) on the mechanical composite characteristics

3.4.1. Fibre length

To investigate the influence of the reprocessing cycle, three reprocessing steps were carried out exemplary for composites reinforced with the medium fine fibre (lyocell 6.7 dtex). Virgin composites, reprocessed granules and reprocessed composites were investigated for their fibre length distribution.

Figure 9 shows that there is a trend of an increasing number of shorter fibres as the number of reprocessing cycles increases. Due to the shredding process of the virgin lyocell 6.7 dtex/PLA composites, the fibre length was shortened during reprocessing in the granules (G, R1). While the virgin composite contains 62% fibres > L_c, the reprocessed granules only contain 40% fibres > L_c (L_c = 500 μm). The following injection moulding process (R1) leads to a further fibre shortening and to only 31% of fibres with a length above L_c. As it appears on the graph (Figure 9), shredding of reprocessed lyocell 6.7 dtex/PLA (R1) into granules (G, R2) resulted in a higher number of fibres with a length longer than L_c (37%). It is assumed that very short fibres were lost during sample preparation for fibre length measurements. Otherwise, the short fibre fraction would not be represented after the following reprocessing step (R2). The second reprocessing (R2) led to a lower amount of fibres > L_c (25%) in lyocell 6.7 dtex/PLA (R2) as well as in lyocell 6.7 dtex/PLA granules (G, R3) with 24% of fibres > L_c. Finally, after the third reprocessing step (R3) only 22% of fibres have a length > L_c.

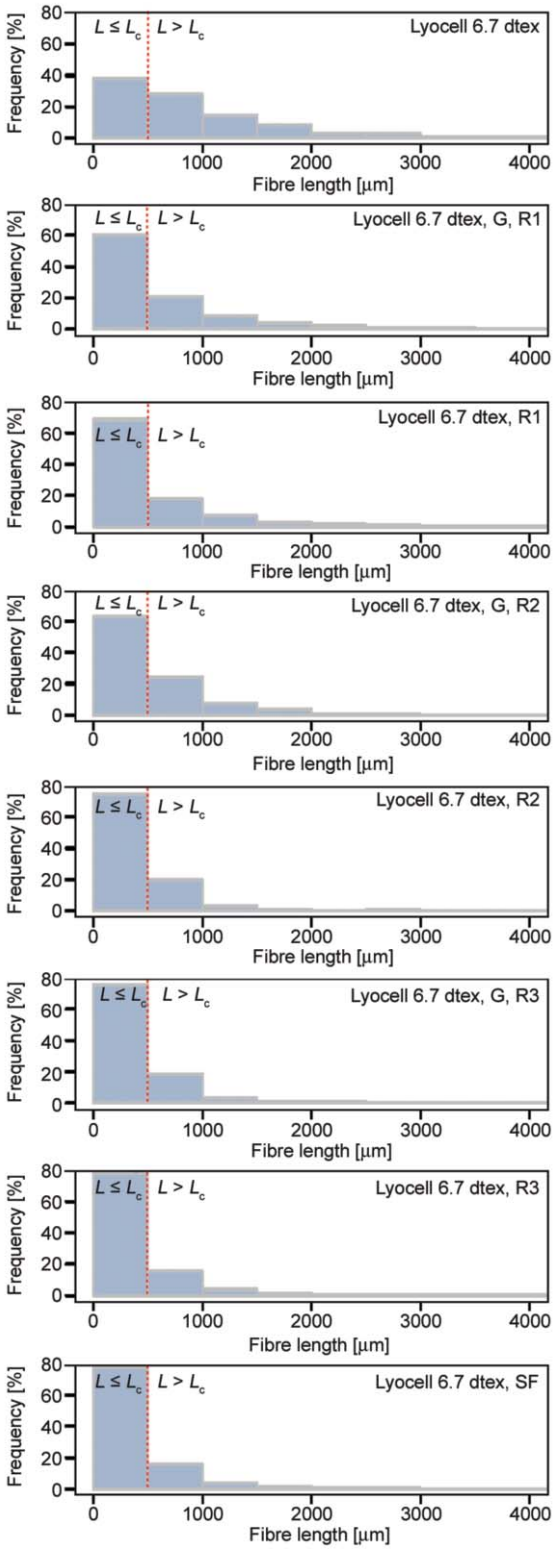

Figure 9. Histograms of the fibre length distribution of lyocell fibres with a fineness of 6.7 dtex extracted from PLA composites in virgin state, from reprocessed granules (G) and composites reprocessed in one (R1), two (R2) and three (R3) cycles, compared to short fibres (SF) extracted from virgin SF-reinforced composites. Results are pooled in 500 µm steps. Bars below 500 µm indicate fibres with a fibre length below the critical fibre length L_c.

To evaluate whether the fibre length distribution has an influence on the composites and/or the fibre strength is affected by the reprocessing, additional experiments with virgin composites reinforced with short fibres (SF) were carried out (SF were produced from lyocell 6.7 dtex staple fibres with a cutting mill type SM100 (Retsch, Haan, DE) with a sieve size of 6 mm).

The fibre length distribution of SF-reinforced composites as well as the median fibre length of 275 µm is comparable to that of R3 reprocessed composites with a fibre length of 265 µm (view Figure 9). Both composites contain 22% fibres of a length above L_c (500 µm).

In Figure 10 the value of L_c of lyocell 6.7 dtex (500 µm) is added as rhombuses to the Box-Whisker plots of the fibre length distribution. It can be seen that the median fibre length in virgin lyocell 6.7 dtex/PLA (661 µm) is higher than L_c, while reprocessing leads to lower values. The third reprocessing step resulted in a decrease in the median fibre length to a value of 265 µm. The results are summarised in Table 2. Additionally the weighted mean value and the polydispersity of the fibre length distributions were evaluated according to ISO 22315 [38]. The mean values, as well as the weighted mean values are

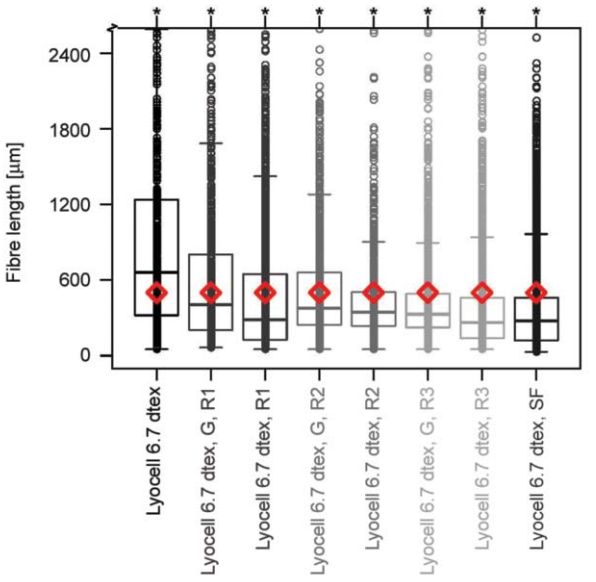

Figure 10. Fibre length of lyocell fibres with a fineness of 6.7 dtex extracted from PLA composites in virgin state, reprocessed granules (G) and composites reprocessed one (R1), two (R2) and three times (R3) compared to short fibres (SF) extracted from virgin (SF)-reinforced composites. The critical fibre length of lyocell 6.7 dtex (500 µm) is shown as rhombuses

Table 2. Median fibre length, median aspect ratio and mean fibre length as well as weighted mean fibre length and polydispersity determined according to ISO 22314 [38] of lyocell 6.7 dtex fibres extracted from virgin and reprocessed composites

Sample	Median [µm]	Median aspect ratio	Mean [µm]	Weighted mean [µm]	Polydispersity	N
30% lyocell 6.7 dtex, virgin	661	27.8	983	2051	1.9	526
30% lyocell 6.7 dtex, R1	287	12.1	519	1337	2.3	2009
30% lyocell 6.7 dtex, R2	347	14.6	456	915	1.5	981
30% lyocell 6.7 dtex, R3	265	11.1	392	873	1.7	2689
30% lyocell 6.7 dtex, SF	275	11.6	345	623	1.7	7295

shown to decrease with an increasing number of reprocessing cycles (Table 2). Compared to the median value, the weigthed mean of virgin SF-reinforced composites is clearly lower compared to the three-time reprocessed composite (R3). The polydispersity, which is a measure of the heterogeneity of sizes of fibre lengths within the distribution, shows the same value of 1.7.

3.4.2. Tensile strength

As described for composites reinforced with fibres of variable fineness, the tensile strength of one, two and three-times reprocessed lyocell 6.7 dtex/PLA composites is in alignment with the findings of the fibre length distribution. The influence of reprocessing on the composites' tensile strength is shown in Figure 11 for virgin and reprocessed composites. Additionally, the tensile strength of SF-reinforced composites is presented. A drastic decrease in tensile strength by a factor of 0.72 when compared to the virgin composite with a value of 70 (±1.2) MPa is visible for the once recycled (R1) composite (51 (±3.2) MPa). The second reprocessing step leads to a further decrease in tensile strength to a value of 40 (±1.3) MPa, compared to the first reprocessing step this is a factor of 0.78. The third step only results in a slight decrease by a factor of 0.95 (38 (±1.6) MPa) compared to the second reprocessing cycle.

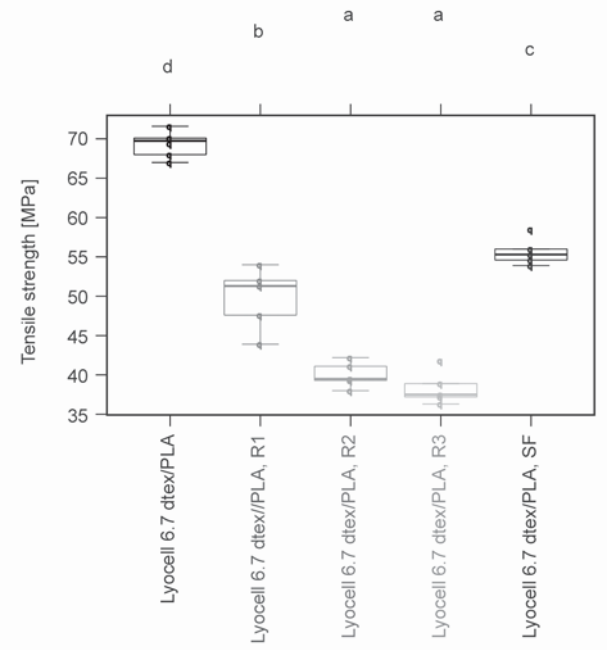

Figure 11. Tensile strength of lyocell 6.7 dtex/PLA in virgin state, reprocessed and reinforced with short fibres (SF) shown as Box-Whisker plots (significant differences are marked with different letters; all results are distributed normally)

As presented in Figure 9 and 10, the fibre lengths show a similar distribution for R3 composites and virgin SF composites. Despite a slightly lower fibre length of SF composites compared to R1 composites a significantly higher reinforcement effect was determined resulting in a tensile strength of 55 (±1.3) MPa. From these findings we conclude that the strength of reprocessed composites is not only reduced by fibre shortening but may also be a result of fibre damage and a possible degradation of the PLA matrix due to residual moisture. Residual moisture is higher in cellulose fibre-reinforced composites compared to the neat matrix leading to a decreasing molecular weight and lower strength of PLA. Multiple drying steps and reprocessing may lead to further hydrolysis of polymer chains [31], and thus a lower strength compared to the SF-reinforced composite.

3.4.3. Thermal behaviour

The DSC scan in Figure 12 shows the heat flow as a function of temperature for the first and second heating cycle of a virgin lyocell SF-reinforced 6.7 dtex/PLA and a threefold (R3) recycled lyocell 6.7 dtex/PLA composite with a similar fibre length distribution. The curve progression is comparable to neat PLA [39, 40]. Not any significant differences were found between the virgin and the recycled composites. The first heating shows a clear glass transition

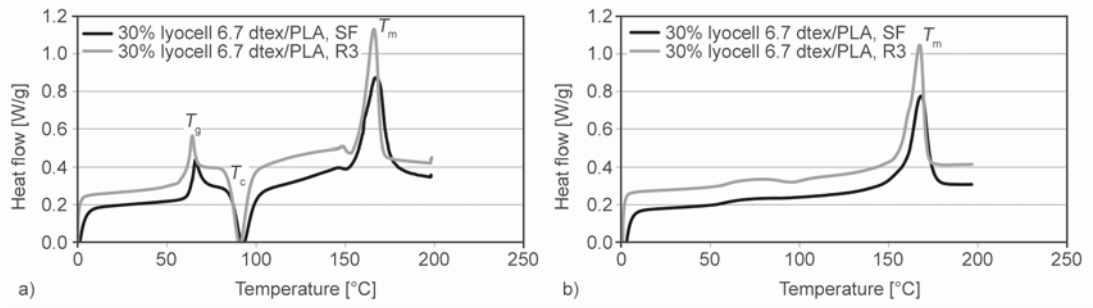

Figure 12. DSC scan of the first heating cycle (a) (first peak: glass transition temperature T_g, second peak: cold crystallisation temperature T_c, third peak: melting temperature T_m) and the second heating cycle (b) of virgin SF lyocell 6.7 dtex/PLA composites and threefold recycled lyocell 6.7 dtex/PLA

and crystallisation temperature peak while this information is lost after the second heating due to crystallisation of the PLA matrix. The glass transition temperature T_g of the first heating, was determined to be at 60.3 °C for both samples. The cold crystallisation temperature T_c was only slightly lower for the recycled composite with 90.5 °C compared to the virgin composites with 91.6 °C. Moreover, the melting temperature T_m was determined to be 167 °C for the virgin sample which shifted slightly to 166 °C for the recycled composite. The second heating resulted in a similar melting temperature which was determined to be 168 °C for the virgin sample and 167 °C for the reprocessed sample. Thus it can be concluded that the thermal behaviour of cellulose fibre-reinforced PLA does not significantly change due to reprocessing.

3.4.4. Fracture behaviour and fibre damage

SEM micrographs of fracture surfaces of virgin lyocell 6.7 dtex/PLA, lyocell 6.7 dtex SF/PLA and reprocessed (R1, R2 and R3) lyocell 6.7 dtex/PLA indicate a trend of higher fibre pull-out with an increasing number of reprocessing cycles (compare Figure 13). When comparing virgin composites with virgin SF-reinforced composites, one can see that fibres of the virgin composites show a higher pull-out length. This phenomenon occurs due to the longer fibres since the production procedures were exactly the same. Usually fibre debonding starts at the fibre ends and the shorter the fibre, the easier the fibre is pulled out of the matrix [35]. The gaps between fibre and matrix however appear to be in a similar range which indicates a similar fibre/matrix adhesion. Gaps or voids respectively, would lead to a clear decrease of the fibre/matrix adhesion.

Aside from fibre shortening, the fibres are clearly damaged as a result of reprocessing. SEM investigations of at least 50 reprocessed fibres were carried out. For example the appearance of SF fibres extracted from a virgin composite and fibres from a reprocessed composite (R3) are shown in Figure 14. Figure 14a and 14b indicate a smooth surface and display the low damage to SF. Threefold reprocessed fibres show the beginning of fibre fibrillation (Figure 14c) and strong fibre damage (Figure 14d) which may result in reduced fibre tensile strength.

3.5. Recycling behaviour of man-made cellulose fibre-reinforced PLA compared to other composites

It is well known that the mechanical performance of fibre-reinforced plastics depends on the nature and intrinsic properties of the polymer matrix, surface characteristics, strength, shape and orientation of fibres, the interfacial quality between fibre and matrix as well as the processing stages and applied parameters, etc.. Clearly the fibre length may be affected by the production process. Usually the reprocessing or recycling of fibre-reinforced plastics leads to a clear reduction in the fibre length. However, the aspect ratio is not necessarily reduced. Unlike regenerated or man-made fibres, natural fibres can exist as individual fibres or fibre bundles. An advantage of natural fibre bundles is that they may be split into smaller fibre bundles or single fibres, reducing the global cross-section leading to a higher aspect ratio despite length reduction [9]. Therefore, a recycling of composites reinforced with natural fibre bundles often only has a negative influence on the composite strength after several recycling steps. This phenomenon was observed by different authors for different natural fibre bundles in variable matrices, eg. for flax/PLA [9], flax/PP [4, 8], hemp/PP [2, 3], sisal/PP [2, 3], wood fibre/PP [4] or alfa fibre/PVC [12]. Nevertheless, the

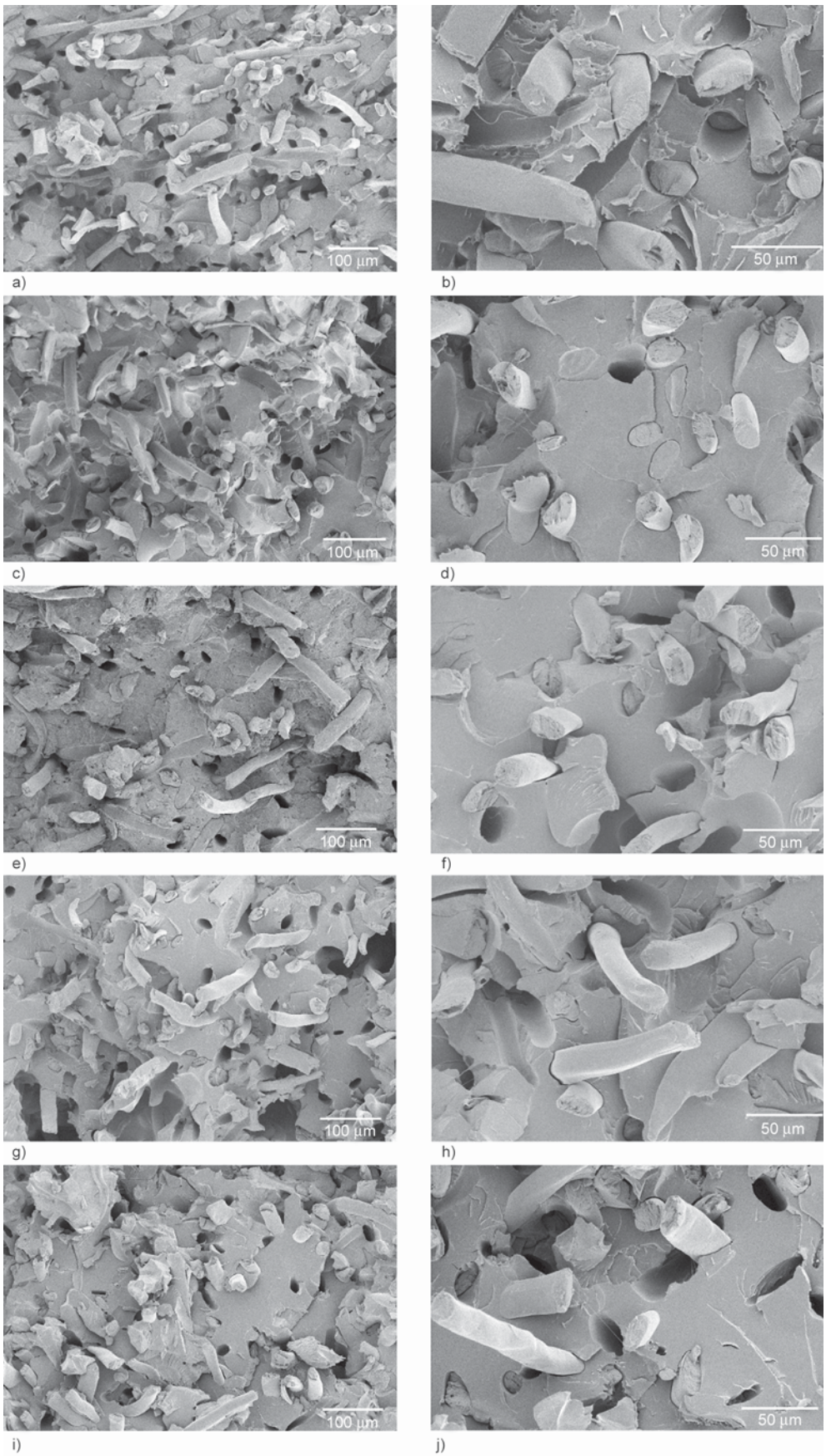

Figure 13. SEM micrographs of virgin lyocell/PLA (a and b), virgin lyocell SF/PLA (c and d), reprocessed R1 (e and f), reprocessed R2 (g and h) and reprocessed R3 lyocell/PLA (i and j).

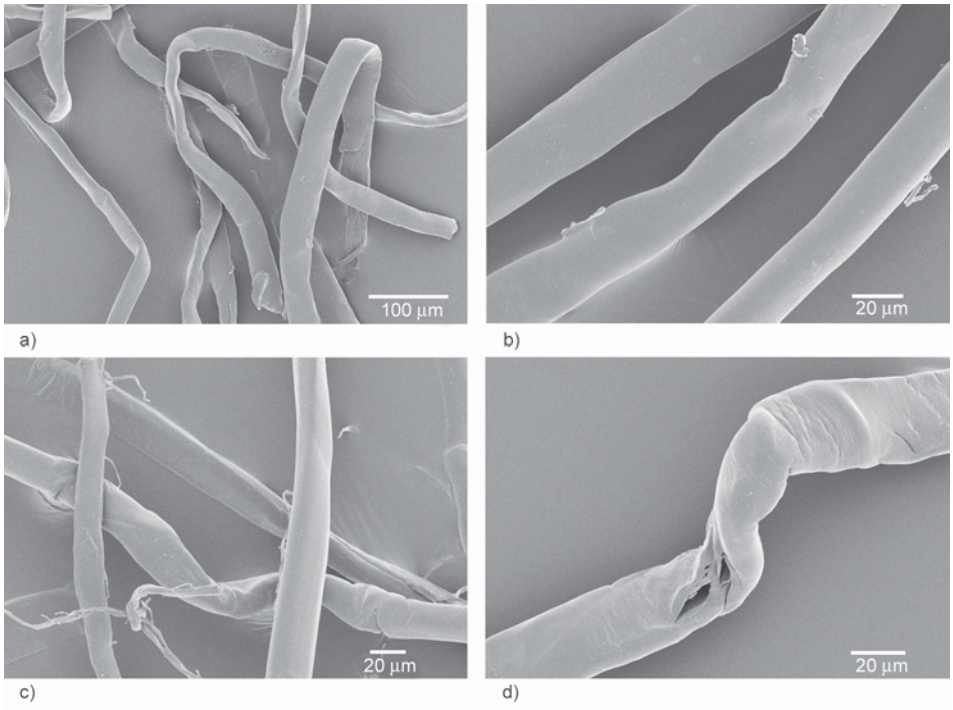

Figure 14. SEM micrographs of fibres extracted from virgin SF lyocell/PLA composites (a and b) and reprocessed (R3) lyocell/PLA composites (c and d)

fibre bundle may be damaged with an increasing number of recycling steps, especially if the fibre bundles are already split into single fibres, leading to lower mechanical composite characteristics as a consequence of reprocessing [2, 3].

In contrast to this man-made single fibres, such as glass fibres, break if a critical stress is reached. This breakage reduces the fibre length which leads to a reduced aspect ratio and a reduction in tensile strength of the composites [4]. During the recycling of lyocell, fibre breakage also leads to a decreased aspect ratio and thus, among other aspects such as degradation of matrix and fibre damage, to a significant reduction of the composite strength. Regarding the recycling behaviour, natural fibre bundles therefore display the greater potential compared to regenerated cellulose fibres.

4. Conclusions

Similarly to other single fibres, the aspect ratio of lyocell fibres decreases clearly as a result of reprocessing. A DSC analysis of virgin composites and three times reprocessed composites with a similar fibre length distribution resulted in similar thermal behaviour regarding glass transition, crystallisation and melting temperature.

The tensile and impact strength of pure PLA was only slightly affected by reprocessing. It is concluded that pure PLA was not significantly damaged due to reprocessing, however the mechanical characteristics of the composites are significantly reduced by the first reprocessing step. It can be shown that the decrease in fibre length was higher for finer fibres when compared to coarser fibres. Finer fibres however display a higher aspect ratio leading to a higher reinforcing potential. All results of tensile strength fit well with the determined fibre length and aspect ratio values. While fibres with a median fibre length higher than the critical fibre length lead to a reinforcing effect in the composite, a fibre length at the level of the critical fibre length leads to tensile strength values with the level of a pure matrix. A fibre length smaller than the critical fibre length resulted in a lower tensile strength when compared to neat PLA. Besides fibre shortening, the degradation and damage of the fibres and the matrix as a result of hydrolysis due to the higher moisture level of cellulose fibres during reprocessing has a negative impact on the tensile strength of the composites. This aspect should be addressed in further research activities. Regarding the recycling potential, natural fibre bundles should be prefererred to single cellulose fibres due to the advantage of being able

to split them into finer bundles or single fibres leading to a lower decrease of the composite strength.

Acknowledgements

The authors acknowledge Petra Droettbroom (Institute for polymer materials and plastics processing, TU Clausthal, Germany) for DSC analyses and Birgit Uhrlaub (The Biological Materials Group, HSB – Hochschule Bremen, City University of Applied Sciences, Germany) for SEM investigations. The authors would also like to acknowledge the reviewers who helped to improve this manuscript and Peter Weir for proof reading.

References

[1] Oliveux G., Dandy L. O., Leeke G. A.: Current status of recycling of fibre reinforced polymers: Review of technologies, reuse and resulting properties. Progress in Materials Science, **72**, 61–99 (2015).
DOI: 10.1016/j.pmatsci.2015.01.004

[2] Bourmaud A., Baley C.: Investigations on the recycling of hemp and sisal fibre reinforced polypropylene composites. Polymer Degradation and Stability, **92**, 1034–1045 (2007).
DOI: 10.1016/j.polymdegradstab.2007.02.018

[3] Bourmaud A., Baley C.: Rigidity analysis of polypropylene/vegetal fibre composites after recycling. Polymer Degradation and Stability, **94**, 297–305 (2009).
DOI: 10.1016/j.polymdegradstab.2008.12.010

[4] Dickson A. R., Even D., Warnes J. M., Fernyhough A.: The effect of reprocessing on the mechanical properties of polypropylene reinforced with wood pulp, flax or glass fibre. Composites Part A: Applied Science and Manufacturing, **61**, 258–267 (2014).
DOI: 10.1016/j.compositesa.2014.03.010

[5] Bernasconi A., Rossin D., Armanni C.: Analysis of the effect of mechanical recycling upon tensile strength of a short glass fibre reinforced polyamide 6,6. Engineering Fracture Mechanics, **74**, 627–641 (2007).
DOI: 10.1016/j.engfracmech.2006.10.002

[6] Barth M., Carus M.: Carbon footprint and sustainability of different natural fibre for biocomposites and insulation material. Study providing data for the automotive and insulation industry. Nova Institute, Hürth, Germany (2015).

[7] Directive 2000/53/ec of the European parliament and of the council of 18 September 2000 – on end-of life vehicles. Official Journal of the European Communities, p.15 (2000).

[8] Arbelaiz A., Fernández B., Ramos J., Retegi A., Llano-Ponte R., Mondragon I.: Mechanical properties of short flax fibre bundle/polypropylene composites: Influence of matrix/fibre modification, fibre content, water uptake and recycling. Composites Science and Technology, **65**, 1582–1592 (2005).
DOI: 10.1016/j.compscitech.2005.01.008

[9] Le Duigou A., Pillin I., Bourmaud A., Davies P., Baley C.: Effect of recycling on mechanical behaviour of biocompostable flax/poly(L-lactide) composites. Composites Part A: Applied Science and Manufacturing, **39**, 1471–1478 (2008).
DOI: 10.1016/j.compositesa.2008.05.008

[10] Beg M., Pickering K.: Reprocessing of wood fibre reinforced polypropylene composites. Part I: Effects on physical and mechanical properties. Composites Part A: Applied Science and Manufacturing, **39**, 1091–1100 (2008).
DOI: 10.1016/j.compositesa.2008.04.013

[11] Fonseca-Valero C., Ochoa-Mendoza A., Arranz-Andrés J., González-Sánchez C.: Mechanical recycling and composition effects on the properties and structure of hardwood cellulose-reinforced high density polyethylene eco-composites. Composites Part A: Applied Science and Manufacturing, **69**, 94–104 (2015).
DOI: 10.1016/j.compositesa.2014.11.009

[12] Hammiche D., Bourmaud A., Boukerrou A., Djidjelli H., Grohens Y.: Number of processing cycle effect on the properties of the composites based on alfa fiber. Journal of Thermoplastic Composite Materials, in press, (2016).
DOI: 10.1177/0892705714563116

[13] Joffre T., Miettinen A., Wernersson E. L., Isaksson P., Gamstedt E. K.: Effects of defects on the tensile strength of short-fibre composite materials. Mechanics of Materials, **75**, 125–134 (2014).
DOI: 10.1016/j.mechmat.2014.04.003

[14] Beaugrand J., Berzin F.: Lignocellulosic fiber reinforced composites: Influence of compounding conditions on defibrization and mechanical properties. Journal of Applied Polymer Science, **128**, 1227–1238 (2013).
DOI: 10.1002/app.38468

[15] Le Moigne N., van den Oever M., Budtova T.: A statistical analysis of fibre size and shape distribution after compounding in composites reinforced by natural fibres. Composites Part A: Applied Science and Manufacturing, **42**, 1542–1550 (2011).
DOI: 10.1016/j.compositesa.2011.07.012

[16] Graupner N., Müssig J.: A comparative study on cellulose fibre-reinforced PLA and PP composites: Compression moulding vs. injection moulding. in 'ICNF 2015 – From Nature to Market: 2nd International Conference on Natural Fibres. Ponta Delgada, Portugal (2015).

[17] Fu S-Y., Lauke B.: Effects of fiber length and fiber orientation distributions on the tensile strength of short-fiber-reinforced polymers. Composites Science and Technology, **56**, 1179–1190 (1996).
DOI: 10.1016/S0266-3538(96)00072-3

[18] Thomson C., Lowe R., Ragauskas A.: Imaging cellulose fibre interfaces with fluorescence microscopy and resonance energy transfer. Carbohydrate Polymers, **69**, 799–804 (2007).
DOI: 10.1016/j.carbpol.2007.01.023

[19] DIN EN ISO 527-2: Plastics - Determination of tensile properties – Part 2: Test conditions for moulding and extrusion plastics (1996).
[20] DIN EN ISO 291: Plastics – Standard atmospheres for conditioning and testing (2006).
[21] DIN EN ISO 179: Plastics - Determination of Charpy impact properties – Part 1: Non-instrumented impact test (1997).
[22] DIN EN ISO 139: Textiles – Standard atmospheres for conditioning and testing (2005).
[23] Graupner N., Rößler J., Ziegmann G., Müssig J.: Fibre/matrix adhesion of cellulose fibres in PLA, PP and MAPP: A critical review of pull-out test, microbond test and single fibre fragmentation test results. Composites Part A: Applied Science and Manufacturing, **63**, 133–148 (2014).
DOI: 10.1016/j.compositesa.2014.04.011
[24] Shapiro S. S., Wilk M. B.: An analysis of variance test for normality (complete samples). Biometrika, **52**, 591–611 (1965).
DOI: 10.1093/biomet/52.3-4.591
[25] Tukey J. W.: Comparing individual means in the analysis of variance. Biometrics, **5**, 99–114 (1949).
[26] Wilcoxon F.: Individual comparisons by ranking methods. Biometrics Bulletin, **1**, 80–83 (1945).
[27] Sachs L.: Angewandte Statistik Anwendung statistischer Methoden (in German). Springer, Berlin (1984).
[28] Frigge M., Hoaglin D. C., Iglewicz B.: Some implementations of the boxplot. The American Statistician, **43**, 50–54 (1989).
[29] Moon C. K., Lee J-O., Cho H. H., Kim K. S.: Effect of diameter and surface treatment of fiber on interfacial shear strength in glass fiber/epoxy and HDPE. Journal of Applied Polymer Science, **45**, 443–450 (1992).
DOI: 10.1002/app.1992.070450309
[30] Wilson D. M.: Statistical tensile strength of Nextel™ 610 and Nextel™ 720 fibres. Journal of Materials Science, **32**, 2535–2542 (1997).
DOI: 10.1023/A:1018538030985
[31] Courgneau C., Rusu D., Henneuse C., Ducruet V., Lacrampe M-F., Krawczak P.: Characterisation of low-odour emissive polylactide/cellulose fibre biocomposites for car interior. Express Polymer Letters, **7**, 787–804 (2013).
DOI: 10.3144/expresspolymlett.2013.76
[32] Lekube B.: The influence of bioplastics on the recycling of conventional plastics. in '23rd annual meeting of the Bio-Environmental Polymer Society (BEPS), Karlsruhe, Germany' (2015).
[33] Graupner N.: Analyse und Optimierung der Struktur- und Eigenschaftsbeziehungen von cellulosefaserverstärkten Polylactid-Verbundwerkstoffen (in German). Papierflieger Verlag, Clausthal-Zellerfeld (2014).
[34] Erdmann J., Ganster J.: Einfluss des Faserdurchmessers auf die Struktur und Mechanik Cellulosefaser-verstärkter PLA-Komposite (in German). Lenzinger Berichte, **89**, 91–102 (2011).
[35] Graupner N., Ziegmann G., Wilde F., Beckmann F., Müssig J.: Procedural influences on compression and injection moulded cellulose fibre-reinforced polylactide (PLA) composites: Influence of fibre loading, fibre length, fibre orientation and voids. Composites Part A: Applied Science and Manufacturing, **81**, 158–171 (2016).
DOI: 10.1016/j.compositesa.2015.10.040
[36] Piggott M. R.: Why interface testing by single-fibre methods can be misleading. Composites Science and Technology, **57**, 965–974 (1997).
DOI: 10.1016/S0266-3538(97)00036-5
[37] Zhang H., Ericson M. L., Varna J., Berglund L. A.: Transverse single-fibre test for interfacial debonding in composites: 1. Experimental observations. Composites Part A: Applied Science and Manufacturing, **28**, 309–315 (1997).
DOI: 10.1016/S1359-835X(96)00123-6
[38] ISO 22314: Plastics. Glass-fibre-reinforced products. Determination of fibre length (2006).
[39] Gregorova A.: Application of differential scanning calorimetry to the characterization of biopolymers. in 'Applications of calorimetry in a wide context – Differential scanning calorimetry, isothermal titration calorimetry and microcalorimetry' (eds.: Elkordy A. A.) InTech, Rijeka, p.18 (2013).
DOI: 10.5772/53822
[40] Chun K. S., Husseinsyah S.: Polylactic acid/corn cob eco-composites. Effect of new organic coupling agent. Journal of Thermoplastic Composite Materials, **27**, 1667–1678 (2014).
DOI: 10.1177/0892705712475008

eXPRESS Polymer Letters Vol.10, No.8 (2016) 664–678
Available online at www.expresspolymlett.com
DOI: 10.3144/expresspolymlett.2016.60

Evaluating a simple blending approach to prepare magnetic and stimuli-responsive composite hydrogel particles for application in biomedical field

H. Ahmad[1], M. S. Sultana[1], M. A. Alam[1], M. M. Rahman[1], K. Tauer[2], M. A. Gafur[3], M. K. Sharafat[1]*

[1]Department of Chemistry, Rajshahi University, 6205 Rajshahi, Bangladesh
[2]Max Planck Institute of Colloid and Interfaces, Am Mühlenberg, 14476 Golm, Germany
[3]Pilot Plant and Process Development Centre, BCSIR, 1205 Dhaka, Bangladesh

Received 30 January 2016; accepted in revised form 1 March 2016

Abstract. The inclusion of super paramagnetic iron oxide (Fe_3O_4) nanoparticles in stimuli-responsive hydrogel is expected to enhance the application potential for cellular therapy in cell labeling, separation and purification, protein immobilization, contrasting enhancement in magnetic resonance imaging (MRI), localized therapeutic hyperthermia, biosensors etc. in biomedical field. In this investigation two different magnetic and stimuli-responsive composite hydrogel particles with variable surface property were prepared by simply blending Fe_3O_4/SiO_2 nanocomposite particles with stimuli-responsive hydrogel particles. Of the hydrogel particles prepared by free-radical precipitation polymerization poly(styrene-N-isopropylacrylamide-methyl methacrylate-polyethylene glycol methacrylate) or P(S-NIPAM-MMA-PEGMA) was temperature-sensitive and poly(S-NIPAM-methacrylic acid-PEGMA) or P(S-NIPAM-MAA-PEGMA) was both temperature- and pH-responsive. The morphological structure, size distributions and volume phase transitions of magnetic and stimuli-responsive composite hydrogel particles were analyzed. Temperature-responsive absorptions of biomolecules were observed on both magnetic and stimuli-responsive Fe_3O_4/SiO_2/P(S-NIPAM-MMA-PEGMA) and Fe_3O_4/SiO_2/P(S-NIPAM-MAA-PEGMA) composite hydrogel particles and separation of particles from the dispersion media could be achieved by applying magnetic field without time consuming centrifugation or decantation method.

Keywords: *smart polymers, stimuli-responsive hydrogel, magnetic nanocomposite, blending, magnetic composite hydrogel*

1. Introduction

Stimuli-responsive hydrogels known as smart materials are macromolecules that undergo reversible volume phase transition in response to a small change of external stimuli such as temperature [1–9], pH [9–13], light [14–16], electric current [17–19], ionic strength [20–22] or chemical species [23]. Researchers are showing much attention in these materials for their wide range of biomedical and pharmaceutical applications [24–29]. However, temperature-sensitive hydrogels are the most studied class of stimuli-responsive polymers as they have strong application potential in pharmaceutical formulation. Poly(N-isopropylacrylamide) (PNIPAM) based temperature-responsive hydrogels have been extensively studied because their physicochemical properties can easily be tailored by insertion of other comonomers into the polymer chain, they exhibit low cytotoxicity and can be drained out from the organism [30, 31]. With the increase in temperature PNIPAM chains soluble in aqueous medium dehydrate at the temperature above the lower critical solution temperature (LCST) of ~32 °C as attractive segmental interactions among the hydrophobic isopropyl groups dominate. This in-

*Corresponding author, e-mail: hahmad@ru.ac.bd

duces a conformation change from a coil to globular state and turns the transparent PNIPAM solution into turbid emulsion.

The design of magnetic and stimuli-responsive composite hydrogel particles would be interesting because of wide application probability in magnetic bioseparation, drug delivery, magnetic resonance imaging contrast enhancement [32–39]. In magnetic and stimuli-responsive composite hydrogel particles, the first allows a suitable and energy efficient separation capability of biomolecule/drug loaded composite particles from the complex culture medium and the latter allows easy uptake and elution of absorbed biomolecule/drug. It is also plausible to assume that poor mechanical strength and flame-retardant property of hydrogel particles will be improved due to the inclusion of an inorganic component. These improved properties may offer additional advantage in industrial applications as well as in catalysis. In the literature several approaches are available for the preparation of magnetic composite polymer microspheres. Some works are available on the synthesis of magnetic hybrid composite particles based on the precipitation of magnetic (Fe_3O_4) nanoparticles in bulk solution where polymer particles have been previously dispersed [7, 37, 40]. However for temperature-sensitive hydrogels, this process may affect the thermal response because high specific surface area of nanoparticles would favor interaction between nanoparticles and hydrogel matrix. Some authors cover the surface of the magnetic nanoparticles with SiO_2 prior to the polymerization because surface of Fe_3O_4 nanoparticles inhibit polymerization [35, 41, 42]. Despite of this limitation, reports are available on direct precipitation polymerization of NIPAM and monomers in aqueous media using anionic initiator in the presence of stabilized iron oxide nanoparticles [43, 44]. Rahman and Elaissari [45] reported the preparation of divinylbenzene (DVB) cross-linked magnetic seed particles by emulsion polymerization of DVB while using potassium persulfate as initiator in the presence of native Fe_3O_4 emulsion followed by precipitation polymerization of NIPAM to induce temperature sensitive PNIPAM shell. Few are also available on the direct dispersion polymerization in ethanol/water media [46, 47]. In these methods the size of obtained microspheres often showed broad distribution. Other authors functionalized the surface of Fe_3O_4 or Fe_3O_4/SiO_2 nanoparticles with reactive vinyl group using silane coupling agent prior to the precipitation polymerization with NIPAM and/comonomers [35, 48–51]. Additionally grafting-to [52–54] and grafting-from [38, 54–56] approaches for the preparation of metal/metal oxide-polymer core-shell nanoparticles on iron oxide core, different polymerization methods such as atom transfer radical polymerization (ATRP) [54, 56, 57], nitroxide mediated polymerization (NMP) [56] and reversible addition-fragmentation transfer radical polymerization (RAFT) [53, 58] have been reported. All these processes require a tedious time consuming multistep procedure which often limit their applications. In a recently published article Illés *et al*. [59] discussed the preparation biocompatible carboxyl functional magnetic fluids consisting of core–shell PEG-acrylate-acrylic acid (PEGA-AA) comb-like copolymer by simple adsorption technique. Prior to this (PEGA-AA) was synthesized by quasiliving ATRP using a complex of Cu(I)-chloride and hexamethyl-triethylene-tetramine as catalyst.

In the present research a simple economically feasible route is evaluated to prepare two different magnetic and stimuli-responsive nanocomposite hydrogel particles. In one series temperature-sensitive poly (styrene-NIPAM-methyl methacrylate-polyethylene glycol methacrylate) or P(S-NIPAM-MMA-PEGMA) hydrogel particles and in another series temperature- and pH-responsive poly(S-NIPAM-methacrylic acid-PEGMA) or P(S-NIPAM-MAA-PEGMA) hydrogel particles were prepared by free-radical precipitation copolymerization using cationic 2,2′-azobis(2-amidinopropane)dihydrochloride (V-50) initiator. The weight ratio of styrene/MMA/PEGMA and styrene/MAA/PEGMA in the recipe was optimized in order to produce stable emulsion and could not be maintained at the same ratio. Styrene was used as a hydrophobic comonomer avoiding the use of crosslinker. MMA/MAA was added to improve the solubility of styrene in the aqueous dispersion media for facilitating smooth copolymerization with NIPAM as the latter in absence of MMA/MAA may produce larger proportion of water soluble homopolymer due to its comparatively high reaction rate. The hydrophobic-hydrophobic interactions among hydrophobic PS-PMMA or PS segments in the prepared conetworks are expected to form microgels in water, a phenom-

enon generally observed for amphiphilic copolymer networks consisting of hydrophilic and hydrophobic polymer segments [60–64]. Then in one pot synthesis Fe_3O_4 nanoparticles were encapsulated with SiO_2 to obtain Fe_3O_4/SiO_2 nanocomposite particles and subsequently blended with hydrogel particles to obtain Fe_3O_4/SiO_2/P(S-NIPAM-MMA-PEGMA) and Fe_3O_4/SiO_2/P(S-NIPAM-MAA-PEGMA) composite hydrogel particles. The preparation scheme of these magnetic and stimuli-responsive composite hydrogel particles is shown in Figure 1. Under the preparation conditions Fe_3O_4/SiO_2 nanocomposite particles are negatively charged due to the presence of silanol groups. Since the blending was carried out in presence of NH_4OH solution with pH >10, the P(S-NIPAM-MAA-PEGMA) hydrogel particles carried both positive and negative charges derived from initiator fragments and deprotonated carboxyl groups respectively. So the electrostatic attraction among Fe_3O_4/SiO_2 nanocomposite particles and P(S-NIPAM-MAA-PEGMA) hydrogel particles may be not that good for successful blending. Compared to this in the preparation of Fe_3O_4/SiO_2/P(S-NIPAM-MMA-PEGMA) composite hydrogel particles electrostatic attraction is expected to dominate among negatively charged Fe_3O_4/SiO_2 nanocomposite particles and positively charged P(S-NIPAM-MMA-PEGMA) hydrogel particles. The morphology, size and size distribution, surface structure, swelling phenomena of two different composite hydrogel particles were characterized. The absorption behavior of biomolecules were also studied and compared.

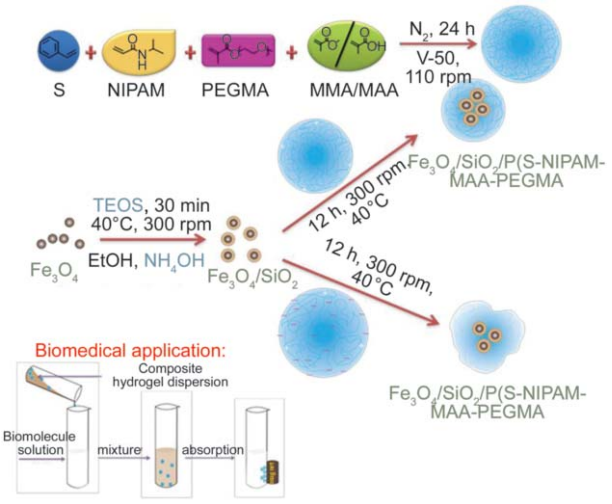

Figure 1. Preparation scheme of magnetic and stimuli-responsive composite hydrogel particles by blending

2. Experimental section

2.1. Materials and instruments

NIPAM of monomer grade obtained from Across Organics, USA, was recrystallized from a mixture of 90% hexane and 10% acetone, dried under vacuum at a low temperature before preserving in the refrigerator. Styrene, MMA and MAA of monomer grade obtained from Fluka Chemica, Switzerland, were purified by passing through activated basic alumina. PEGMA (molecular weight 500 $g \cdot mol^{-1}$ for PEG) was obtained from Sigma Aldrich, USA. V-50 from LOBA Chem. India, was recrystallized from distilled water and ethanol. The biomolecules, trypsin (TR) from E. Merck, Darmstadt, Germany, and albumin (AL) from Fluka Chemika, Switzerland, were used without any purification. Ferrous sulphate heptahydrate ($FeSO_4 \cdot 7H_2O$), ferric chloride ($FeCl_3$), citric acid, NH_4OH and other chemicals were of analytical grade. Ethanol and deionized water was distilled using a glass (Pyrex) distillation apparatus.

Transmission electron microscope (TEM) (Zeiss EM-912, Omega), Fourier Transform Infrared (FTIR) spectrophotometer (Perkin Elmer, FTIR-100, USA), Centrifuge machine (TG16-WS) from Kokuson Corporation, Tokyo, Japan, NICOMP 380 particle sizer (USA), X-ray photoelectron spectroscopy (XPS) (PHI X-tool, ULVAC-PHI, Japan) and X-ray diffractometer (XRD) (Bruker D8 Advance, Germany) were used for characterization of prepared particles. Microprocessor pH meter from HANNA instruments and Sherwood Scientific Magnetic Susceptibility Balance were also used.

2.2. Preparation of hydrogel particles

Temperature- and pH-responsive P(S-NIPAM-MAA-PEGMA) hydrogel particles were prepared by free-radical precipitation copolymerization from 0.6 g styrene, 1.95 g NIPAM, 0.3 g MAA and 0.15 g PEGMA. The copolymerization reaction was carried out in a three necked round bottomed flask dipped in thermostat water bath maintained at 75 °C using cationic V-50 (0.045 g) initiator. Distilled water (200 g) was used as the dispersion medium. Polymerization was carried out under a nitrogen atmosphere and the reaction mixture was mechanically stirred at 110 rpm for 24 h.

Compared to this a slightly different recipe was used to prepare stable emulsion of temperature-responsive

P(S-NIPAM-MMA-PEGMA) hydrogel. This was prepared by free-radical precipitation copolymerization of styrene (0.75 g), NIPAM (2.04 g), MMA (0.15 g) and PEGMA (0.06 g) in a three necked round flask dipped in thermostat water bath at 70 °C. The copolymerization reaction was started using cationic V-50 (0.06 g) initiator in 100 g distilled water as the dispersion medium. The reaction mixture was mechanically stirred at 110 rpm for 24 h under a nitrogen atmosphere.

In both cases the conversion was nearly 100% measured gravimetrically. The hydrogel emulsion was repeatedly washed with distilled water by centrifugation prior to the characterization.

2.3. Preparation of Fe_3O_4 nanoparticles

Nano-sized Fe_3O_4 particles were prepared by co-precipitation of Fe^{2+} (2.855 g) and Fe^{3+} (3.127 g) from their aqueous solutions (molar ratio 1:2) containing 25% 54.05 g NH_4OH. The reaction was carried out in a three necked round flask under a nitrogen atmosphere for 2 h. The prepared Fe_3O_4 emulsion was treated with 10 g HNO_3 (2M) for 15 min. and washed with water until the solution was neutral. Citric acid (40 g) was added slowly and stirred overnight to stabilize the Fe_3O_4 dispersion. The produced Fe_3O_4 particles were repeatedly washed by magnetic separation and subsequent redispersion in deionized distilled water to remove salt and excess stabilizer.

2.4. Preparation of reference Fe_3O_4/SiO_2 nanocomposite particles

At first 50 g ethanol, 1.0 g deionized water and 2.38 g NH_4OH were taken in a three necked flask under vigorous stirring, then 1.56 g TEOS was charged into the above mixture and the flask was heated to 40 °C gradually in a hot water bath with constant stirring at 300 rpm. 20 min later water-based 0.44 g magnetic (Fe_3O_4) fluid containing 0.025 g solid was added into the above mixture and the process was continued for 30 min. Fe_3O_4 nanoparticles were encapsulated within the SiO_2 layer, forming Fe_3O_4/SiO_2 nanocomposite particles. The produced particles were washed repeatedly through magnetic separation and redispersion in fresh distilled water before characterization.

2.5. Preparation of composite hydrogel particles

Fe_3O_4/SiO_2 nanocomposite emulsion was prepared as discussed in the previous section. Calculated amount of hydrogel emulsion (nanocomposite/hydrogel: 1/10 w/w) was added and the mixture was stirred continuously at 40 °C for 12 h. The composite hydrogel particles were washed repeatedly by distilled water employing centrifugation followed by magnetic separation to remove any nonmagnetic hydrogel particles.

2.6. Characterization

The sample for TEM was prepared by diluting the respective emulsion down to about 0.01% solid by distilled water and a drop was placed on a carbon-coated copper grid. The sample was dried at ambient temperature before observation by an electron microscope at an accelerating voltage of 100 kV.

FTIR analysis of the powder samples was performed in KBr pellets and scanned over the range 4000–400 cm^{-1} in the deflection mode. Prior to the analysis the washed emulsion was dried under vacuum at low temperature.

The surface composition after modification was evaluated by an XPS equipped with a monochromatic Al Kα radiation (1486.6 eV) at 104 W and 20 kV and an X-ray current of 20 μA. The pressure in the measurement chamber was ca. $8.0 \cdot 10^{-7}$ Pa. The step size was 0.25 eV for the both survey and high resolution spectra (pass energy 280 eV). The washed dispersion was dried onto carbon tape prior to the analyses.

The XRD patterns of the powder samples were taken with a scanning XRD using Cu Kα radiation ($\lambda \approx$ 1.5406 Å), a tube voltage of 33 kV and a tube current of 45 mA. The intensities were measured at 2θ values from 2 to 90° at a continuous scan rate of $10° \cdot min^{-1}$ with a position-sensitive detector aperture at 3° (equivalent to $0.5° \cdot min^{-1}$ with a scintillation counter).

Thermogravimetric properties (TGA) of the dry powdered samples were measured by heating samples under flowing nitrogen atmosphere from 30 to 600 °C at a heating rate of 30 °C/min and the mass loss was recorded. The initial mass of each sample was around 20 mg.

For the measurement of average hydrodynamic diameters the washed composite/hydrogel dispersion was diluted down to around 0.01% solid content using water. The pH value of the diluted emulsion was adjusted whenever necessary. At each temperature the intensity weighted average hydrodynamic diameter of the particles was recorded. Each measurement was carried out in twice and the average value is reported. The reproducibility of the size measurement was within ±5%.

Sherwood Magnetic Susceptibility Balance was used for susceptibility measurement of Fe_3O_4, Fe_3O_4/SiO_2 nanocomposite, Fe_3O_4/SiO_2/P(S-NIPAM-MAA-PEGMA) and Fe_3O_4/SiO_2/P(S-NIPAM-MMA-PEGMA) composite hydrogel particles. The particles were separated from their respective dispersion by using a magnet and dried in oven at 70 °C for several hours. The dried powders were placed in a preweighed sample tube and measured the magnetic susceptibility (χ_g) using Equation (1):

$$\chi_g = \frac{C \cdot L \cdot (R - R_0)}{m \cdot 10^9} \quad (1)$$

where C, is calibration constant of balance, L is length of the sample in [cm], R_0 and R are the readings of the empty and sample tubes and m is the weight of sample in [g].

2.7. Absorption of biomolecules

A mixture of 20 mL was prepared from each purified emulsion containing 0.1 g solid and biomolecule (200 mg/g) aqueous solution. The pH value of the emulsion-biomolecule mixture was adjusted at the respective isoelectric point (TR, pH 10.0; AL, pH 6.0) using buffer solution and the mixture was allowed to stand for 45 min. Then the particles were separated magnetically and finally by centrifugation to remove any wafting particles. This same procedure was carried out at two different temperatures of 20 and 40 °C. The concentration of the biomolecule in the supernatant was measured by a UV-visible spectrophotometer at the wave length of 280 nm. The amount of biomolecule absorbed was calculated by subtracting the concentration of free biomolecule from initial concentration. A calibration curve was used for this purpose.

3. Results and discussion

Figure 2 represents the TEM images of Fe_3O_4, Fe_3O_4/SiO_2 nanocomposite, P(S-NIPAM-MAA-PEGMA) hydrogel and Fe_3O_4/SiO_2/P(S-NIPAM-MAA-PEGMA) composite hydrogel particles. The average diameters and coefficients of variation (CV) calculated from TEM images are 8.8 nm and 14.48% for Fe_3O_4 nanoparticles, 28.9 nm and 10.19% for Fe_3O_4/SiO_2 nanocomposite particles, 590.8 nm and 36% for P(S-NIPAM-MAA-PEGMA) hydrogel particles and 49.44 nm and 12.99% for Fe_3O_4/SiO_2/P(S-NIPAM-MAA-PEGMA) composite hydrogel particles. The average size of the Fe_3O_4/SiO_2 nanocomposite particles increases after encapsulation with SiO_2 layer. It is worth to mention that Fe_3O_4/SiO_2 nanocomposite particles undergo drying mediated self assembly into linear chain structure rarely observed in case of magnetic nanoparticles as shown in inset image [65]. P(S-NIPAM-MAA-PEGMA) hydrogel particles exhibit different morphology with central darker parts possibly represents the hydrophobic PS rich segment. The hydrophobic-hydrophobic interactions among PS segments in amphiphilic P(S-NIPAM-MAA-PEGMA) conetwork led to the reorientation of polymer chains forming core-shell type microgels in water [60–64]. Compared to P(S-NIPAM-MAA-PEGMA) hydrogel particles the size of Fe_3O_4/SiO_2/P(S-NIPAM-MAA-PEGMA) composite hydrogel particles decreases after blending with Fe_3O_4/SiO_2 nanocomposite particles. The blending was carried out under highly alkaline condition (~pH >10). Okubo and coworkers [66, 67] proposed the formation mechanism of microparticles from P(S-MAA) copolymer particles dispersed in alkaline solution by simple dissolution method. In case of P(S-NIPAM-MAA-PEGMA) hydrogel particles the ionization of carboxyl groups of PMAA under alkaline condition and subsequent swelling and dissolution of copolymer chains from polymer hydrogel particle may take place. It is also possible that hydrophilic soft P(S-NIPAM-MAA-PEGMA) hydrogel particles collapsed while the sample was dried during sample preparation for TEM and might not represent the true size of the hydrogel particles as shown in Figure 2c. The presence of negative charges on both Fe_3O_4/SiO_2 nanocomposite and P(S-NIPAM-MAA-PEGMA) hydrogel

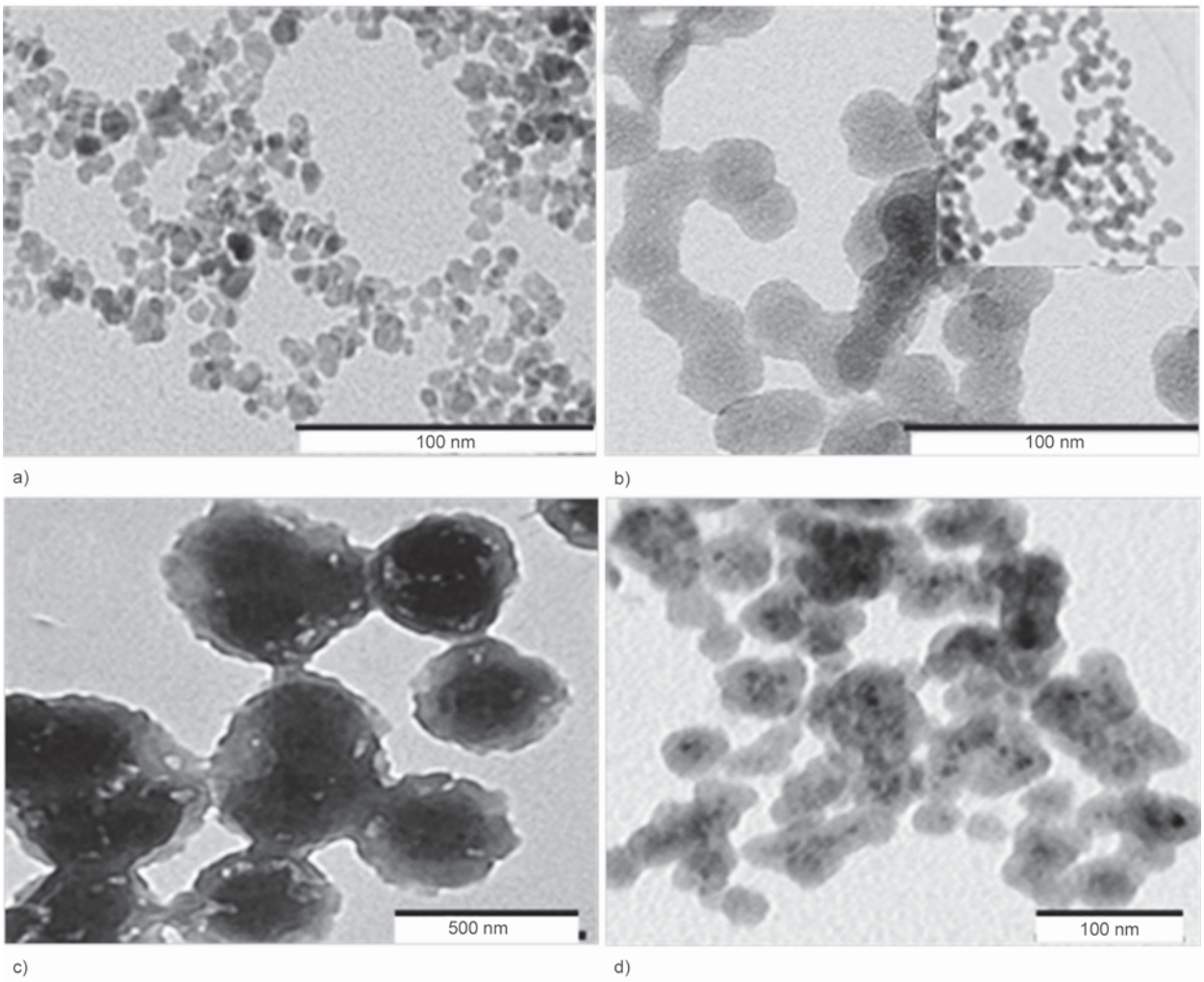

Figure 2. TEM images of a) Fe_3O_4, b) Fe_3O_4/SiO_2 nanocomposite, c) P(S-NIPAM-MAA-PEGMA) hydrogel and d) Fe_3O_4/SiO_2/P(S-NIPAM-MAA-PEGMA) composite hydrogel particles

particles is also expected to reduce the degree of agglomeration though the later also contain additional positive charges from initiator fragments. These above factors may contribute to the reduction in composite particle size. It is apparent that the morphology of Fe_3O_4/SiO_2/P(S-NIPAM-MAA-PEGMA) composite hydrogel particles is different from both P(S-NIPAM-MAA-PEGMA) hydrogel particles and Fe_3O_4/SiO_2 nanocomposite particles and the average size is larger than those of Fe_3O_4/SiO_2 nanocomposite. The tiny nanoparticles inside Fe_3O_4/SiO_2/P(S-NIPAM-MAA-PEGMA) composite hydrogel particles may correspond to Fe_3O_4. TEM image of P(S-NIPAM-MMA-PEGMA) hydrogel particles shown in Figure 3 suggest that hydrogel particles deformed and possibly collapsed as PMMA is weak to electron beam [68, 69]. Compared to these P(S-NIPAM-MMA-PEGMA) hydrogel particles, Fe_3O_4/SiO_2/P(S-NIPAM-MMA-PEGMA) composite hydrogel particles are rather spherical. The average diameter and coefficient of variation of Fe_3O_4/SiO_2/P(S-NIPAM-MMA-PEGMA) composite hydrogel particles are 43.43 nm and 10.19% and the average size is greater than that of Fe_3O_4/SiO_2 nanocomposite particles. The darker central spot may correspond to Fe_3O_4/SiO_2 nanocomposite particles as shown in the magnified particle image. These above results suggest that during blending the electrostatic interaction among nanosized Fe_3O_4/SiO_2 particles and comparatively softer and larger hydrogel particles initiated the formation of magnetic composite hydrogel particles. The size distribution, nature of charge and charge distribution, particle rigidity, degree of swelling and difference in hydrophilicity all played a role in the formation of nearly core-shell morphology with Fe_3O_4/ SiO_2 core.

FTIR spectral analysis is one way to detect surface structural composition of inorganic and/polymer colloidal particles (Figure 4). In the spectrum of Fe_3O_4

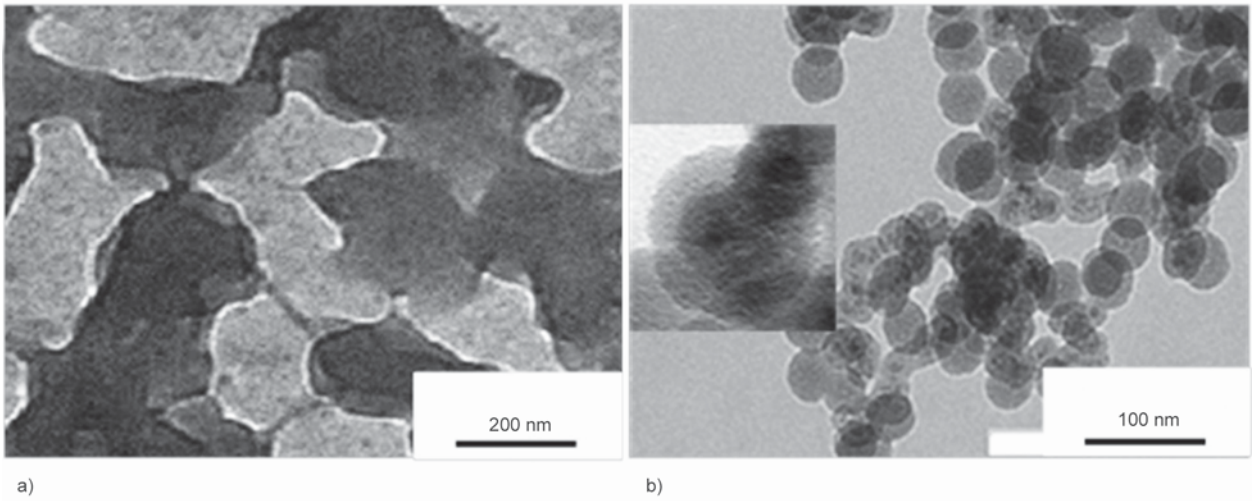

Figure 3. TEM photographs of a) P(S-NIPAM-MMA-PEGMA) hydrogel and b) Fe_3O_4/SiO_2/P(S- NIPAM-MMA-PEGMA) composite hydrogel particles

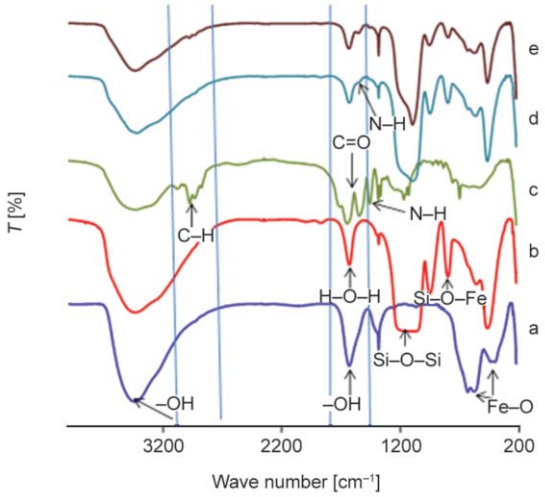

Figure 4. FTIR spectra of a) Fe_3O_4, b) Fe_3O_4/SiO_2 nanocomposite, c) P(S-NIPAM-MAA-PEGMA) hydrogel, d) Fe_3O_4/ SiO_2/P(S-NIPAM-MAA-PEGMA) and e) Fe_3O_4/SiO_2/P(S-NIPAM-MMA-PEGMA) composite hydrogel particles recorded in KBr pellets

nanoparticles (Figure 4 curve a) the intense broad band at 3435.93 cm^{-1} represents the presence of water traces and non-dissociated –OH groups of citric acid. At 1630.95 cm^{-1}, an intense band is visible which corresponds to the symmetric stretching of –OH from –COOH group, revealing the binding of a citric acid radical to the magnetic surface. Also the neighbor band at 1385 cm^{-1} can be assigned to the asymmetric stretching of CO from –COOH group. The characteristic stretching vibrations due to Fe–O bonds appear at 406 and 583 cm^{-1} weakened in Fe_3O_4/ SiO_2 nanocomposite particles. The weak absorption signal at 800 cm^{-1} and intense band at 1105 cm^{-1} in the spectrum of Fe_3O_4/SiO_2 nanocomposite particles corresponding to Si–O–Fe and Si–O-Si bonds suggest the bonding of SiO_2 to Fe_3O_4. In P(S-NIPAM-MAA-PEGMA) hydrogel particles the characteristic signals due to stretching vibrations of carboxyl and amide C=O groups and amide N–H bending appear at 1738, 1670 and 1566 cm^{-1} respectively. Compared to P(S-NIPAM-MAA-PEGMA) hydrogel particles a small but distinct N–H bending signal of amide group appears in Fe_3O_4/SiO_2/P(S-NIPAM-MAA-PEGMA) composite hydrogel particles. The broad absorption signal at 1671–1528 cm^{-1} due to H–O–H bending in Fe_3O_4/SiO_2 nanocomposite particles deviates to 1703–1490 cm^{-1} in Fe_3O_4/SiO_2/P(S-NIPAM-MAA-PEGMA) composite hydrogel particles. This deviation suggests the inclusion of stretching vibrations of carboxyl and amide C=O groups and amide N–H bending from copolymer network with the H–O–H bending from Fe_3O_4/SiO_2 nanocomposite particles. In other word we can say that bands corresponding to carboxyl and amide C=O groups are overlapped with the H–O–H band. Weak C–H stretching vibrations of the aliphatic and aromatic ring appear in the region 3085–2798 cm^{-1}. The almost same explanation is also valid for Fe_3O_4/SiO_2/P(S-NIPAM-MMA-PEGMA) composite hydrogel particles.

The XPS C1s, N1s and Fe2p core-line spectra of Fe_3O_4, Fe_3O_4/SiO_2 nanocomposite, Fe_3O_4/SiO_2/P(S-NIPAM-MAA-PEGMA) and Fe_3O_4/SiO_2/P(S-NIPAM-MMA-PEGMA) composite hydrogel particles are shown in Figure 5. The C1s signal intensity in Fe_3O_4/SiO_2 nanocomposite particles is 5.4 atom%

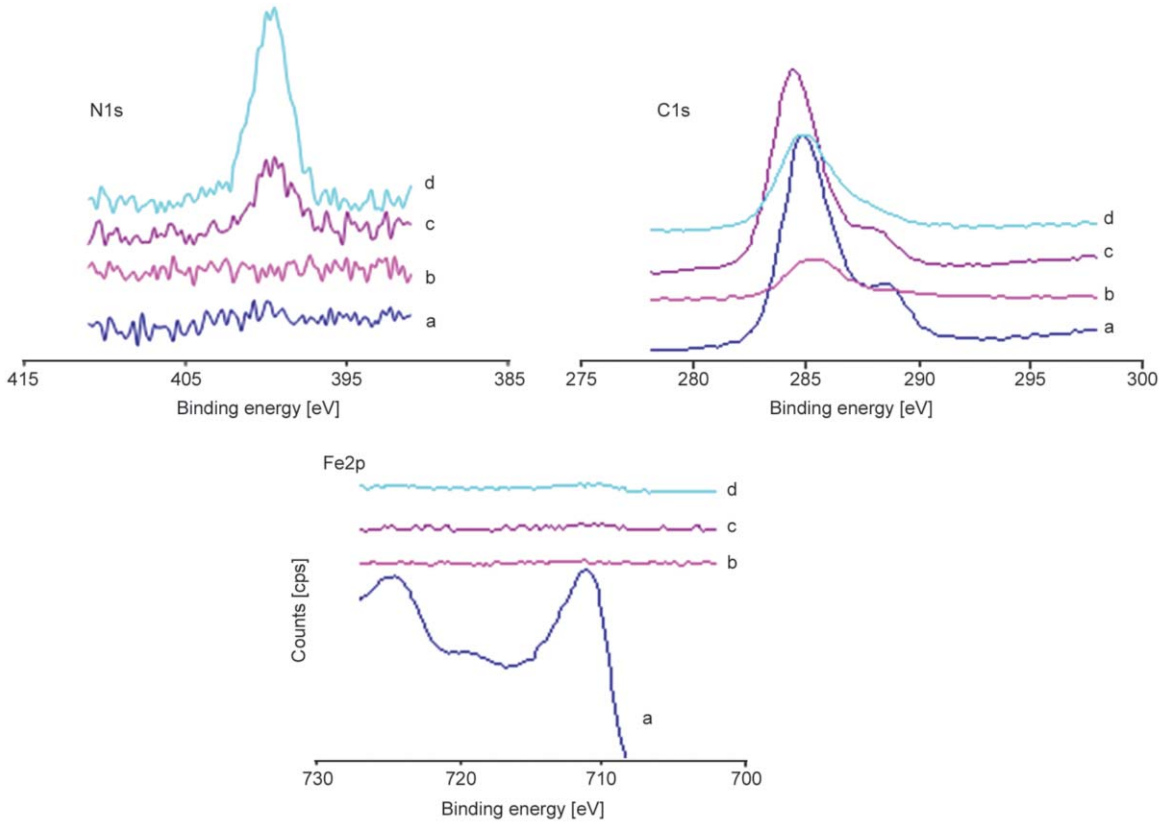

Figure 5. XPS C1s, N1s and Fe2p core-line spectra of curves a) Fe_3O_4, b) Fe_3O_4/SiO_2 nanocomposite, c) Fe_3O_4/SiO_2/P(S-NIPAM-MAA-PEGMA) and d) Fe_3O_4/SiO_2/P(S-NIPAM-MMA-PEGMA) composite hydrogel particles

which increases to 29.7 and 14.8 atom% in Fe_3O_4/SiO_2/P(S-NIPAM-MAA-PEGMA) and Fe_3O_4/SiO_2/P(S-NIPAM-MMA-PEGMA) composite hydrogel particles. The signal appearance also widened in composite hydrogel particles. The difference in C1s signal intensity between Fe_3O_4/SiO_2/P(S-NIPAM-MAA-PEGMA) and Fe_3O_4/SiO_2/P(S-NIPAM-MMA-PEGMA) composite hydrogel particles is attributed to the difference in styrene, MMA and PEGMA contents in the recipe. As expected N1s signal is not visible in Fe_3O_4/SiO_2 nanocomposite particles whereas in Fe_3O_4/SiO_2/P(S-NIPAM-MAA-PEGMA) and Fe_3O_4/SiO_2/P(S-NIPAM-MMA-PEGMA) composite hydrogel particles such signal intensity approaches 0.8 and 2.2 atom%. The Fe2p core-line spectrum shown in Figure 5 for Fe_3O_4 nanoparticles exhibits two signals at 711.5 and 725.4 eV, the characteristic doublets of $Fe2p_{3/2}$ and $2p_{1/2}$ core-level spectra of magnetite [70]. The encapsulation by SiO_2 followed by polymer layers eliminates the Fe2p signal. The almost three fold increase in N1s signal intensity derived from PNIPAM segment suggest that specifically the blending of Fe_3O_4/SiO_2 nanocomposite and P(S-NIPAM-MMA-PEGMA) hydrogel particles produces better agglomeration leading to Fe_3O_4/SiO_2/P(S-NIPAM-MMA-PEGMA) composite hydrogel particles. The ionization of carboxyl group in P(S-NIPAM-MAA-PEGMA) hydrogel particles and negative surface charge on Fe_3O_4/SiO_2 nanocomposite particles may inhibit the process of agglomeration necessary for composite formation.

The two theta sharp peaks appear at 30.08, 35.45, 43.5, 53.54, 57.11 and 62.78 in the XRD spectrum of Fe_3O_4 nanoparticles confirm the crystalline cubic spinal structure of Fe_3O_4 nanoparticles as shown in Figure 6. These diffraction peaks are in good agreement with those XRD patterns of Fe_3O_4 nanoparticles reported in the JCPDS-International Center (JCPDS file No. 19-0629) [71, 72]. The broad reflection centers at ~20° appear in Fe_3O_4/SiO_2 nanocomposite particles, Fe_3O_4/SiO_2/P(S-NIPAM-MAA-PEGMA) and Fe_3O_4/SiO_2/P(S-NIPAM-MMA-PEGMA) composite hydrogel particles. These broad signals are attributed to the transition of crystalline Fe_3O_4 structure into amorphous character following encapsulation by amorphous SiO_2 and then polymer layers. The presence of weak characteristic signals of Fe_3O_4 in nanocomposite and composite hydrogel particles also con-

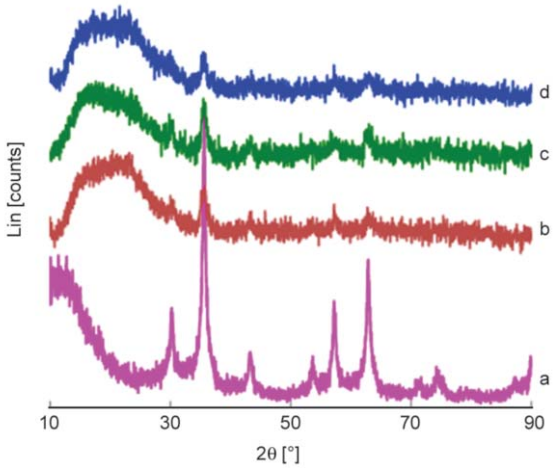

Figure 6. XRD spectra of a) Fe_3O_4, b) Fe_3O_4/SiO_2 nanocomposite, c) Fe_3O_4/SiO_2/P(S-NIPAM-MAA-PEGMA) and d) Fe_3O_4/SiO_2/P(S-NIPAM-MMA-PEGMA) composite hydrogel particles

firms that the crystalline structure of Fe_3O_4 is retained during different steps of modification.

The surface modification of Fe_3O_4 as well as the presence of inorganic (Fe_3O_4/SiO_2) part in thermo-responsive composite hydrogel particles can quantified from the percentage of weight loss using TGA curves. It is evident from Figure 7 that both hydrogel particles loss ~98% of their initial weight. The onset decomposition temperature of P(S-NIPAM-MMA-PEGMA) hydrogel particles is slightly high (~329 °C) compared to P(S-NIPAM-MAA-PEGMA) hydrogel particles (~281 °C). Relatively high hydrophobicity and particle rigidity possibly contributed to this higher

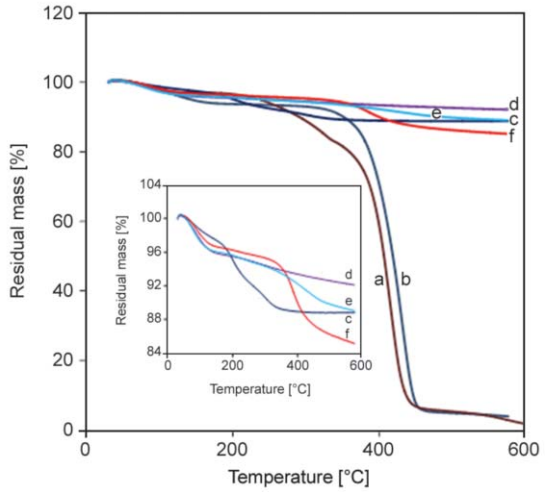

Figure 7. TGA thermograms of a) P(S-NIPAM-MAA-PEGMA) hydrogel, b) P(S-NIPAM-MMA-PEGMA) hydrogel, c) Fe_3O_4, d) Fe_3O_4/SiO_2 nanocomposite, e) Fe_3O_4/SiO_2/P(S-NIPAM-MAA-PEGMA) and f) Fe_3O_4/SiO_2/P(S-NIPAM-MMA-PEGMA) composite hydrogel particles

onset decomposition temperature for P(S-NIPAM-MMA-PEGMA) hydrogel particles. The incorporation of SiO_2 layer in Fe_3O_4 reduces the weight loss by 3.5% indicating the increase in inorganic content. In Fe_3O_4/SiO_2/P(S-NIPAM-MAA-PEGMA) composite hydrogel particles the weight loss increases by 3.1% relative to Fe_3O_4/SiO_2 nanocomposite particles. Whereas in Fe_3O_4/SiO_2/P(S-NIPAM-MMA-PEGMA) composite hydrogel particles the weight loss increases by 6.7% compared to reference Fe_3O_4/SiO_2 nanocomposite particles. Overall these results suggest that magnetic composite hydrogel particles are formed in both cases and the use of MMA instead of MAA as a comonomer increases the incorporation of organic polymer. As predicted the ionization of carboxyl group in PMAA under the preparation conditions reduces the extent of agglomeration. The electrostatic repulsion among negatively charged hydrogel particles and negatively charged Fe_3O_4/SiO_2 nanocomposite particles may have occurred during blending. It has earlier been mentioned that the negative surface charge on Fe_3O_4/SiO_2 nanocomposite particles is derived from the presence of silanol groups. However, based on the recipe the amount of organic part in Fe_3O_4/SiO_2/P(S-NIPAM-MMA-PEGMA) composite hydrogel particles is still low. Under the preparation condition it is reasonable to assume that some hydrogel particles remained free as also observed during washing by magnetic decantation method.

The temperature dependent average hydrodynamic diameters of P(S-NIPAM-MAA-PEGMA) and P(S-NIPAM-MMA-PEGMA) hydrogel particles illustrated in Figure 8 show that both hydrogel particles are hydrophilic and swell with water at temperature below the LCST. As the temperature increases the hydrogel particles shrink and deswell at temperature above the LCST. It is apparent that LCST is dependent on the hydrogel composition. The incorporation of hydrophilic PMAA shifts the LCST to relatively higher temperature (37 °C) in P(S-NIPAM-MAA-PEGMA) hydrogel particles and the same behavior is also reported elsewhere [73]. The P(S-NIPAM-MAA-PEGMA) hydrogel particles also show volume phase transition with respect to variation in pH value. At higher pH value the increase in hydrodynamic diameter results from the deprotonation of carboxyl group and hence the coulombic repulsion among polymer chains [74].

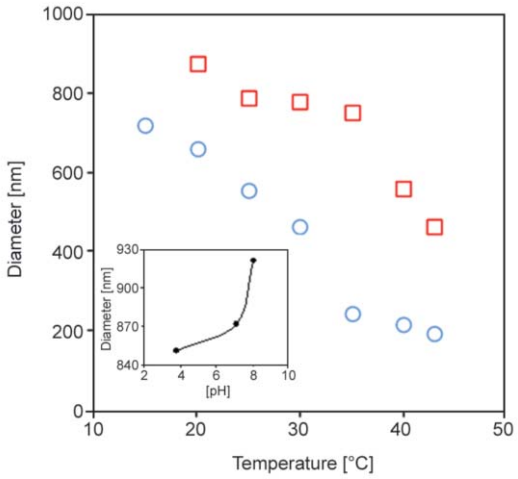

Figure 8. Temperature dependent variations of average hydrodynamic diameters of P(S-NIPAM-MAA-PEGMA) (square) and P(S-NIPAM-MMA-PEGMA) (circle) hydrogel particles at pH 7. pH-dependent variation of average hydrodynamic diameters of P(S-NIPAM-MAA-PEGMA) hydrogel particles at 20 °C is shown in the inset

The average hydrodynamic diameters of both composite hydrogel particles shown in Figure 9 also decrease with increasing temperature showing LCST behavior. The LCST of Fe_3O_4/SiO_2/P(S-NIPAM-MAA-PEGMA) composite hydrogel particles is relatively high compared to Fe_3O_4/SiO_2/P(S-NIPAM-MMA-PEGMA) composite hydrogel particles. Comparatively low hydrodynamic diameter of Fe_3O_4/SiO_2/P(S-NIPAM-MAA-PEGMA) composite hydrogel microspheres indicate the poor incorporation of polymer hydrogel as predicted in XPS and TGA analyses.

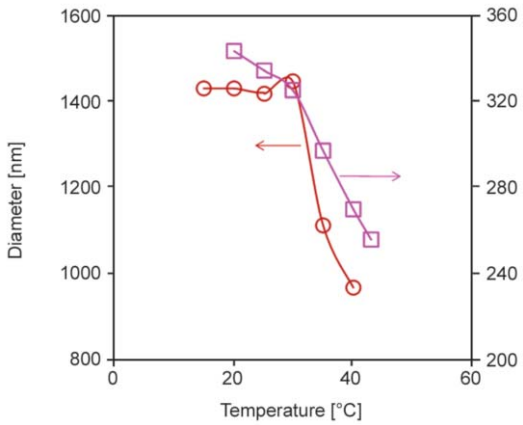

Figure 9. Temperature dependent variations of average hydrodynamic diameters of Fe_3O_4/SiO_2/P(S-NIPAM-MAA-PEGMA) (square) and Fe_3O_4/SiO_2/P(S-NIPAM-MMA-PEGMA) (circle) composite hydrogel particles measured at pH 7

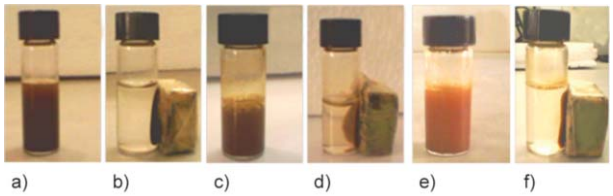

Figure 10. Digital photographic images of colloidal dispersions of a, b) Fe_3O_4 nanoparticles, c, d) Fe_3O_4/SiO_2/P(S-NIPAM-MAA-PEGMA) and e, f) Fe_3O_4/SiO_2/P(S-NIPAM-MMA-PEGMA) composite hydrogel particles in absence (a, c, e) and presence (b, d, f) of external magnetic field

The magnetic susceptibilities of Fe_3O_4/SiO_2/P(S-NIPAM-MAA-PEGMA) and Fe_3O_4/SiO_2/P(S-NIPAM-MMA-PEGMA) composite hydrogel particles remain high and positive ($2.90 \cdot 10^{-3}$ and $1.03 \cdot 10^{-3}$) indicating strong paramagnetic character. The magnetic property is a vital property in separation as well as in targeted drug delivery system because one can drive magnetic particles by applying external magnetic field. Magnetic particles need to be accumulated in presence of magnet and should be well dispersed once the magnet is removed. Figure 10 shows the images of magnetic separation of different magnetic particles. It is observed that the magnetic composite hydrogel particles are well dispersed in absence of magnetic field and accumulated towards the magnet leaving behind almost clear supernatant.

Figures 11 and 12 show the absorption behavior of TR and AL on reference Fe_3O_4/SiO_2 nanocomposite and Fe_3O_4/SiO_2/P(S-NIPAM-MAA-PEGMA) and Fe_3O_4/SiO_2/P(S-NIPAM-MMA-PEGMA) composite hydrogel particles at temperature above and below the LCST. The absorption behavior of biomolecule is a rather complex phenomena depending on the environment as well as nature of sorbent and biomolecules in terms of flexibility, molecular size, hydrophobicity etc. However, irrespective of nature of biomolecules it is evident that magnitude of absorption on composite polymer particles at temperature above the LCST (40 °C) is higher than that at below the LCST (20 °C). Relative to this on Fe_3O_4/SiO_2 nanocomposite particles the magnitude of absorption is pretty low. This higher absorption capacity on magnetic and temperature-responsive composite hydrogel particles correspond to comparatively high hydrophobic character. The slight difference in magnitude of absorption between 20 and 40 °C on Fe_3O_4/SiO_2 nanocomposite particles is possibly due to the tem-

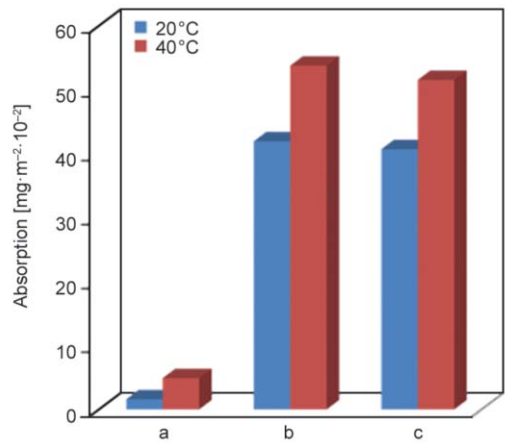

Figure 11. Bar diagram represents the amount of absorptions of trypsin (TR) on a) Fe_3O_4/SiO_2 nanocomposite, b) Fe_3O_4/SiO_2/P(S-NIPAM-MAA-PEGMA) and c) Fe_3O_4/SiO_2/P(S-NIPAM-MMA-PEGMA) composite hydrogel particles at temperature above (40 °C) and below (20 °C) the LCST. Absorption: immobilization 200 mg/g of particles, pH 10.0, immobilization time 45 min

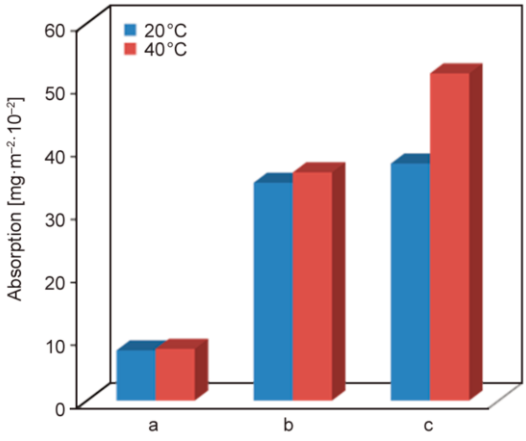

Figure 12. Bar diagram represents the amount of absorptions of albumin (AL) on a) Fe_3O_4/SiO_2 nanocomposite, b) Fe_3O_4/SiO_2/P(S-NIPAM-MAA-PEGMA) and c) Fe_3O_4/SiO_2/P(S-NIPAM-MMA-PEGMA) composite hydrogel particles at temperature above (40 °C) and below (20 °C) the LCST. Absorption: immobilization 200 mg/g of particles, pH 6.0, immobilization time 45 min.

perature effect rather than the surface property of the reference particles.

4. Conclusions

Attempt was made to prepare dual temperature- and pH-responsive Fe_3O_4/SiO_2/P(S-NIPAM-MAA-PEGMA) and temperature-responsive Fe_3O_4/SiO_2/P(S-NIPAM-MMA-PEGMA) composite hydrogel particles by blending Fe_3O_4/SiO_2 nanocomposite particles with respective hydrogel particles. It was evident that electrostatic attraction among negatively charged Fe_3O_4/SiO_2 nanocomposite particles and positively charged P(S-NIPAM-MMA-PEGMA) hydrogel particles favors the formation of magnetic composite hydrogel particles. Compared to this electrostatic repulsion was dominant when P(S-NIPAM-MAA-PEGMA) hydrogel particles were used and produces limited agglomeration. The morphological and chemical structures of magnetic composite particles were evaluated and showed that Fe_3O_4/SiO_2 nanocomposite particles are mostly localized at the centre of composite particles with thin copolymer shell layer. The magnetic composite particles exhibited temperature-responsive absorption behavior of biomolecules and can be accumulated towards the external magnetic field.

Acknowledgements

The author (HA) gratefully acknowledges the partial financial support from the Faculty of Science, Rajshahi University, Bangladesh. The author is also grateful to the Central Science Laboratory, Rajshahi University, for necessary instrument support.

References

[1] Ha W., Yu J., Song X-Y., Chen J., Shi Y-P.: Tunable temperature-responsive supramolecular hydrogels formed by prodrugs as a codelivery system. ACS Applied Material and Interfaces, **6**, 10623–10630 (2014). DOI: 10.1021/am5022864

[2] Zhang J., Peppas N. A.: Synthesis and characterization of pH- and temperature-sensitive poly(methacrylic acid)/poly(*N*-isopropylacrylamide) interpenetrating polymeric networks. Macromolecules, **33**, 102–107 (2000). DOI: 10.1021/ma991398q

[3] Kosik K., Wilk E., Geissler E., László K.: Influence of a crown ether comonomer on the temperature-induced phase transition of poly(*N*-isopropylacrylamide) hydrogels. The Journal of Physical Chemistry B, **112**, 1065–1070 (2008). DOI: 10.1021/jp075227w

[4] Gupta M. K., Martin J. R., Werfel T. A., Shen T., Page J. M., Duvall C. L.: Cell protective, ABC triblock polymer-based thermoresponsive hydrogels with ROS-triggered degradation and drug release. Journal of the American Chemical Society, **136**, 14896–14902 (2014). DOI: 10.1021/ja507626y

[5] Mu J., Zheng S.: Poly(*N*-isopropylacrylamide) nanocrosslinked by polyhedral oligomeric silsesquioxane: Temperature-responsive behavior of hydrogels. Journal of Colloid and Interface Science, **307**, 377–385 (2007). DOI: 10.1016/j.jcis.2006.12.014

[6] Burek M., Czuba Z. P., Waskiewicz S.: Novel acid-degradable and thermo-sensitive poly(*N*-isopropylacrylamide) hydrogels cross-linked by α,α-trehalose diacetals. Polymer, **55**, 6460–6470 (2014). DOI: 10.1016/j.polymer.2014.10.032

[7] Ahmad H., Nurunnabi M., Rahman M. M., Kumar K., Tauer K., Minami H., Gafur M. A.: Magnetically doped multi stimuli-responsive hydrogel microspheres with IPN structure and application in dye removal. Colloids and Surfaces A: Physicochemical and Engineering Aspects, **459**, 39–47 (2014). DOI: 10.1016/j.colsurfa.2014.06.038

[8] Zhang J-T., Jandt K. D.: A novel approach to prepare porous poly(*N*-isopropylacrylamide) hydrogel with superfast shrinking kinetics. Macromolecular Rapid Communications, **29**, 593–597 (2008). DOI: 10.1002/marc.200700778

[9] Varaprasad K., Ravindra S., Reddy N., Vimala K., Raju K. M.: Design and development of temperature sensitive porous poly(NIPAAm-AMPS) hydrogels for drug release of doxorubicin-A cancer chemotherapy drug. Journal of Applied Polymer Science, **116**, 3593–3602 (2010). DOI: 10.1002/app.31917

[10] Mishra R. K., Ramasamy K., Majee A. B. A.: pH-responsive poly(DMAPMA-*co*-HEMA)-based hydrogels for prolonged release of 5-fluorouracil. Journal of Applied Polymer Science, **126**, E98–E107 (2012). DOI: 10.1002/app.36714

[11] Cheng R., Liu J., Xie P., Wu Y., Deng J.: Chiral, pH-sensitive polyacrylamide hydrogels: Preparation and enantio-differentiating release ability. Polymer, **68**, 246–252 (2015). DOI: 10.1016/j.polymer.2015.05.034

[12] Longo G. S., de la Cruz M. O., Szleifer I.: Equilibrium adsorption of hexahistidine on pH-responsive hydrogel nanofilms. Langmuir, **30**, 15335–15344 (2014). DOI: 10.1021/la5040382

[13] Shi L., Khondee S., Linz T. H., Berkland C.: Poly(*N*-vinylformamide) nanogels capable of pH-sensitive protein release. Macromolecules, **41**, 6546–6554 (2008). DOI: 10.1021/ma800812z

[14] Suzuki A., Tanaka T.: Phase transition in polymer gels induced by visible light. Nature, **346**, 345–347 (1990). DOI: 10.1038/346345a0

[15] Lee M. S., Kim J-C.: Photodependent release from poly(vinyl alcohol)/epoxypropoxy coumarin hydrogels. Journal of Applied Polymer Science, **124**, 4339–4345 (2012). DOI: 10.1002/app.35411

[16] Liu D., Bastiaansen C. W. M., den Toonder J. M. J., Broer D. J.: (Photo-)thermally induced formation of dynamic surface topographies in polymer hydrogel networks. Langmuir, **29**, 5622–5629 (2013). DOI: 10.1021/la4005906

[17] Yang S., Liu G., Wang X., Song J.: Electroresponsive behavior of a sulfonated poly(vinyl alcohol) hydrogel and its application to electrodriven artificial fish. Journal of Applied Polymer Science, **117**, 2346–2353 (2010). DOI: 10.1002/app.32069

[18] Jin S., Kang H., Huang Y., Liu H., Hu Y.: Synthesis and properties of electrically-sensitive poly(acrylic acid-*co*-acetoacetoxy ethyl methacrylate) gels. Journal of Applied Polymer Science, **110**, 3690–3696 (2008). DOI: 10.1002/app.28982

[19] Luo R., Li H., Birgersson E., Lam K. Y.: Modeling of electric-stimulus-responsive hydrogels immersed in different bathing solutions. Journal of Biomedical Materials Research Part A, **85**, 248–257 (2008). DOI: 10.1002/jbm.a.31586

[20] Li H., Lai F., Luo R.: Analysis of responsive characteristics of ionic-strength-sensitive hydrogel with consideration of effect of equilibrium constant by a chemo-electro-mechanical model. Langmuir, **25**, 13142–13150 (2009). DOI: 10.1021/la901833m

[21] Zhao B., Moore J. S.: Fast pH- and ionic strength-responsive hydrogels in microchannels. Langmuir, **17**, 4758–4763 (2001). DOI: 10.1021/la001709m

[22] Rasool N., Yasin T., Heng J. Y. Y., Akhter Z.: Synthesis and characterization of novel pH-, ionic strength and temperature- sensitive hydrogel for insulin delivery. Polymer, **51**, 1687–1693 (2010). DOI: 10.1016/j.polymer.2010.02.013

[23] Hokray F., Basser P. J., Hecht A-M., Geissler E.: Calcium-induced volume transition in polyacrylate hydrogels swollen in physiological salt solutions. Macromolecular Bioscience, **2**, 207–213 (2002). DOI: 10.1002/1616-5195(200206)2:5<207::AID-MABI207>3.0.CO;2-5

[24] Bucatariu S., Fundueanu G., Prisacaru I., Balan M., Stoica I., Harabagiu V., Constantin M.: Synthesis and characterization of thermosensitive poly(*N*-isopropylacrylamide-*co*-hydroxyethylacrylamide) microgels as potential carriers for drug delivery. Journal of Polymer Research, **21**, 580/1–580/12 (2014). DOI: 10.1007/s10965-014-0580-7

[25] Gan T., Guan Y., Zhang Y.: Thermogelable PNIPAM microgel dispersion as 3D cell scaffold: Effect of syneresis. Journal of Materials Chemistry, **20**, 5937–5944 (2010). DOI: 10.1039/c0jm00338g

[26] Belger C., Weis J. G., Egap E., Swager T. M.: Colorimetric stimuli-responsive hydrogel polymers for the detection of nerve agent surrogates. Macromolecules, **48**, 7990–7994 (2015). DOI: 10.1021/acs.macromol.5b01406

[27] Li L., Gu J., Zhang J., Xie Z., Lu Y., Shen L., Dong Q., Wang Y.: Injectable and biodegradable pH-responsive hydrogels for localized and sustained treatment of human fibrosarcoma. ACS Applied Material and Interfaces, **7**, 8033–8040 (2015).
DOI: 10.1021/acsami.5b00389

[28] Popescu M-T., Mourtas S., Pampalakis G., Antimisiaris S. G., Tsitsilianis C.: pH-responsive hydrogel/liposome soft nanocomposites for tuning drug release. Biomacromolecules, **12**, 3023–3030 (2011).
DOI: 10.1021/bm2006483

[29] Deng K., Dong L., Li Q., Gou Y., Zhang P., Ren X., Zhong H.: Drug release behaviors of a novel pH/temperature-responsive chitosan-poly(*N*-acryloylglycinate) hydrogel. Journal of Applied Polymer Science, **120**, 3297–3303 (2011).
DOI: 10.1002/app.33522

[30] Wang X., Qiu X., Wu C.: Comparison of the coil-to-globule and the globule-to-coil transitions of a single poly(*N*-isopropylacrylamide) homopolymer chain in water. Macromolecules, **31**, 2972–2976 (1998).
DOI: 10.1021/ma971873p

[31] Li Y., Guo H., Gan J., Zheng J., Zhang Y., Wu K., Lu M.: Novel fast thermal-responsive poly(*N*-isopropylacrylamide) hydrogels with functional cyclodextrin interpenetrating polymer networks for controlled drug release. Journal of Polymer Research, **22**, 91/1–91/14 (2015).
DOI: 10.1007/s10965-015-0720-8

[32] Alam M. A., Sultana T., Rahman M. A., Nuri M. A., Miah M. A. J., Ahmad H.: Preparation of carboxylated temperature-responsive magnetic nano composite polymer particles. Macromolecules: An Indian Journal, **9**, 85–90 (2013).

[33] Brazel C. S.: Magnetothermally-responsive nanomaterials: Combining magnetic nanostructures and thermally-sensitive polymers for triggered drug release. Pharmaceutical Research, **26**, 644–656 (2008).
DOI: 10.1007/s11095-008-9773-2

[34] Zhang J. L., Srivastava R. S., Misra R. D. K.: Core–shell magnetite nanoparticles surface encapsulated with smart stimuli-responsive polymer: Synthesis, characterization, and LCST of viable drug-targeting delivery system. Langmuir, **23**, 6342–6351 (2007).
DOI: 10.1021/la0636199

[35] Luo B., Song X-J., Zhang F., Xia A., Yang W-L., Hu J-H., Wang C-C.: Multi-functional thermosensitive composite microspheres with high magnetic susceptibility based on magnetite colloidal nanoparticle clusters. Langmuir, **26**, 1674–1679 (2010).
DOI: 10.1021/la902635k

[36] Zhang B., Zhang H., Fan X., Li X., Yin D., Zhang Q.: Preparation of thermoresponsive Fe_3O_4/P(acrylic acid–methyl methacrylate–*N*-isopropylacrylamide) magnetic composite microspheres with controlled shell thickness and its releasing property for phenolphthalein. Journal of Colloid and Interface Science, **398**, 51–58 (2013).
DOI: 10.1016/j.jcis.2013.01.042

[37] Reddy N. N., Ravindra S., Reddy N. M., Rajinikanth V., Raju K. M., Vallabhapurapu V. S.: Temperature responsive hydrogel magnetic nanocomposites for hyperthermia and metal extraction applications. Journal of Magnetism and Magnetic Materials, **394**, 237–244 (2015).
DOI: 10.1016/j.jmmm.2015.06.065

[38] Majewski A. P., Schallon A., Jérôme V., Freitag V. R., Müller A. H. E., Schmalz H.: Dual-responsive magnetic core–shell nanoparticles for nonviral gene delivery and cell separation. Biomacromolecules, **13**, 857–866 (2012).
DOI: 10.1021/bm2017756

[39] Rahman M. M., Chehimi M. M., Fessi H., Elaissari A.: Highly temperature responsive core–shell magnetic particles: Synthesis, characterization and colloidal properties. Journal of Colloid and Interface Science, **360**, 556–564 (2011).
DOI: 10.1016/j.jcis.2011.04.078

[40] Pich A., Bhattacharya S., Lu Y., Boyko V., Adler H-J. P.: Temperature-sensitive hybrid microgels with magnetic properties. Langmuir, **20**, 10706–10711 (2004).
DOI: 10.1021/la040084f

[41] Dagallier C., Dietsch H., Schurtenberger P., Scheffold F.: Thermoresponsive hybrid microgel particles with intrinsic optical and magnetic anisotropy. Soft Matter, **6**, 2174–2177 (2010).
DOI: 10.1039/c000305k

[42] Karg M., Pastoriza-Santos I., Liz-Marzán L. M., Hellweg T.: A versatile approach for the preparation of thermosensitive PNIPAM core–shell microgels with nanoparticle cores. ChemPhysChem, **7**, 2298–2301 (2006).
DOI: 10.1002/cphc.200600483

[43] Shamim N., Hong L., Hidajat K., Uddin M. S.: Thermosensitive-polymer-coated magnetic nanoparticles: Adsorption and desorption of bovine serum albumin. Journal of Colloid and Interface Science, **304**, 1–8 (2006).
DOI: 10.1016/j.jcis.2006.08.047

[44] Purushotham S., Ramanujan R. V.: Thermoresponsive magnetic composite nanomaterials for multimodal cancer therapy. Acta Biomaterialia, **6**, 502–510 (2010).
DOI: 10.1016/j.actbio.2009.07.004

[45] Rahman M. M., Elaissari A.: Multi-stimuli responsive magnetic core–shell particles: Synthesis, characterization and specific RNA recognition. Journal of Colloid Science and Biotechnology, **1**, 3–15 (2012).
DOI: 10.1166/jcsb.2012.1006

[46] Ding X. B., Sun Z. H., Wan G. X., Jiang Y. Y.: Preparation of thermosensitive magnetic particles by dispersion polymerization. Reactive and Functional Polymers, **38**, 11–15 (1998).
DOI: 10.1016/S1381-5148(97)00154-5

[47] Ahmad H., Rahman M. A., Miah M. A. J., Tauer K.: Magnetic and temperature-sensitive composite polymer particles and adsorption behavior of emulsifiers and trypsin. Macromolecular Research, **16**, 637–643 (2008).
DOI: 10.1007/BF03218573

[48] Liu C., Guo J., Yang W., Hu J., Wang C., Fu S.: Magnetic mesoporous silica microspheres with thermo-sensitive polymer shell for controlled drug release. Journal of Materials Chemistry, **19**, 4764–4770 (2009). DOI: 10.1039/b902985k

[49] Baharvand H.: A new method for preparation of magnetic polymer particles. Colloid and Polymer Science, **292**, 3311–3318 (2014). DOI: 10.1007/s00396-014-3386-6

[50] Cai J., Guo J., Ji M., Yang W., Wang C., Shoukuan F.: Preparation and characterization of multiresponsive polymer composite microspheres with core–shell structure. Colloid and Polymer Science, **285**, 1607–1615 (2007). DOI: 10.1007/s00396-007-1735-4

[51] Guo J., Yang W., Deng Y., Wang C., Fu S.: Organic-dye-coupled magnetic nanoparticles encaged inside thermoresponsive PNIPAM microcapsules. Small, **1**, 737–743 (2005). DOI: 10.1002/smll.200400145

[52] Narain R., Gonzales M., Hoffman A. S., Stayton P. S., Krishnan K. M.: Synthesis of monodisperse biotinylated p(NIPAAm)-coated iron oxide magnetic nanoparticles and their bioconjugation to streptavidin. Langmuir, **23**, 6299–6304 (2007). DOI: 10.1021/la700268g

[53] Kakwere H., Leal M. P., Materia M. E., Curcio A., Guardia P., Niculaes D., Marotta R., Falqui A., Pellegrino T.: Functionalization of strongly interacting magnetic nanocubes with (thermo)responsive coating and their application in hyperthermia and heat-triggered drug delivery. ACS Applied Material and Interfaces, **7**, 10132–10145 (2015). DOI: 10.1021/am5088117

[54] Kurzhals S., Zirbs R., Reimhult E.: Synthesis and magneto-thermal actuation of iron oxide core–PNIPAM shell nanoparticles. ACS Applied Materials and Interfaces, **7**, 19342–19352 (2015). DOI: 10.1021/acsami.5b05459

[55] Frimpong R. A., Hilt J. Z.: Poly(*N*-isopropylacrylamide)-based hydrogel coatings on magnetite nanoparticles via atom transfer radical polymerization. Nanotechnology, **19**, 175101/1–175101/8 (2008). DOI: 10.1088/0957-4484/19/17/175101

[56] Binder W. H., Gloger D., Weinstabl H., Allmaier G., Pittenauer E.: Telechelic poly(*N*-isopropylacrylamides) via nitroxide-mediated controlled polymerization and '*click*' chemistry: Livingness and '*grafting-from*' methodology. Macromolecules, **40**, 3097–3107 (2007). DOI: 10.1021/ma0628376

[57] Prai-in Y., Tankanya K., Rutnakornpituk B., Wichai U., Montembault V., Pascual S., Fontaine L., Rutnakornpituk M.: Azlactone functionalization of magnetic nanoparticles using ATRP and their bioconjugation. Polymer, **53**, 113–120 (2012). DOI: 10.1016/j.polymer.2011.11.021

[58] Ohno K., Ma Y., Huang Y., Mori C., Yahata Y., Tsujii Y., Maschmeyer T., Moraes J., Perrier S.: Surface-initiated reversible addition–fragmentation chain transfer (RAFT) polymerization from fine particles functionalized with trithiocarbonates. Macromolecules, **44**, 8944–8953 (2011). DOI: 10.1021/ma202105y

[59] Illés E., Tombácz E., Szekeres M., Tóth I. Y., Szabó Á., Iván B.: Novel carboxylated PEG-coating on magnetite nanoparticles designed for biomedical applications. Journal of Magnetism and Magnetic Materials, **380**, 132–139 (2015). DOI: 10.1016/j.jmmm.2014.10.146

[60] Szabó Á., Wacha A., Thomann R., Szarka G., Bóta A., Iván B.: Synthesis of poly(methyl methacrylate)-poly (poly(ethylene glycol) methacrylate)-polyisobutylene abcba pentablock copolymers by combining quasiliving carbocationic and atom transfer radical polymerizations and characterization thereof. Journal of Macromolecular Science Part A: Pure and Applied Chemistry, **52**, 252–259 (2015). DOI: 10.1080/10601325.2015.1007268

[61] Kali G., Vavra S., László K., Iván B.: Thermally responsive amphiphilic conetworks and gels based on poly(*N*-isopropylacrylamide) and polyisobutylene. Macromolecules, **46**, 5337–5344 (2013). DOI: 10.1021/ma400535r

[62] Kali G., Iván B.: Poly(methacrylic acid)-*l*-polyisobutylene amphiphilic conetworks by using an ethoxyethyl-protected comonomer: Synthesis, protecting group removal in the cross-linked state, and characterization. Macromolecular Chemistry and Physics, **216**, 605–613 (2015). DOI: 10.1002/macp.201400478

[63] Haraszti M., Tóth E., Iván B.: Poly(methacrylic acid)-*l*-polyisobutylene: A novel polyelectrolyte amphiphilic conetwork. Chemistry of Materials, **18**, 4952–4958 (2006). DOI: 10.1021/cm061119v

[64] Iván B., Haraszti M., Erdődi G., Scherble J., Thomann R., Mülhaupt R.: New nanophase separated intelligent amphiphilic conetworks and gels. Macromolecular Symposia, **227**, 265–274 (2005). DOI: 10.1002/masy.200550926

[65] Poddar P., Telem-Shafir T., Fried T., Markovich G.: Dipolar interactions in two- and three-dimensional magnetic nanoparticle arrays. Physical Review B, **66**, 060403/1–060403/4 (2002). DOI: 10.1103/PhysRevB.66.060403

[66] Okubo M., Fukami N., Shinohara R.: Behavior of nonionic emulsifier molecules on the preparation of nanoparticles from submicron-sized ionized styrene–methacrylic acid copolymer particles by the particle dissolution method. Colloid and Polymer Science, **277**, 900–904 (1999). DOI: 10.1007/s003960050469

[67] Okubo M., Ichikawa K.: Production of multihollow polymer particles by the stepwise alkali/acid method IV. Acid treatment process. Colloid and Polymer Science, **272**, 933–937 (1994).
DOI: 10.1007/BF00658890

[68] Sawyer L. C., Grubb D. T.: Polymer microscopy. Chapman and Hall, New York (1994).

[69] Ahmad H., Miah M. A. J., Pervin M. S., Rahman M. M.: Composite polymer particles prepared with different amounts of acrylic acid and their usefulness as carriers for biomolecules. Colloid and Polymer Science, **281**, 897–901 (2003).
DOI: 10.1007/s00396-002-0856-z

[70] Márquez F., Campo T., Cotto M., Polanco R., Roque R., Fierro P., Sanz J. M., Elizalde E., Morant C.: Synthesis and characterization of monodisperse magnetite hollow microspheres. Soft Nanoscience Letters, **1**, 25–32 (2011).
DOI: 10.4236/snl.2011.12005

[71] Hui C., Shen C., Yang T., Bao L., Tian J., Ding H., Li C., Gao H-J.: Large-scale Fe_3O_4 nanoparticles soluble in water synthesized by a facile method. The Journal of Physical Chemistry C, **112**, 11336–11339 (2008).
DOI: 10.1021/jp801632p

[72] Salem N. M., Ahmad A. L., Awwad A. M.: New route for synthesis magnetic nanoparticles from ferrous ions and pistachio leaf extract. Nanoscience and Nanotechnology, **3**, 48–51 (2013).
DOI: 10.5923/j.nn.20130303.03

[73] Okubo M., Ahmad H., Komura M.: Preparation of temperature-sensitive polymer particles having different lower critical solution temperatures. Colloid and Polymer Science, **274**, 1188–1191 (1996).
DOI: 10.1007/BF00655691

[74] Alam M. A., Miah M. A. J., Ahmad H.: Synthesis and characterization of dual-responsive micrometer-sized core-shell composite polymer particles. Polymers for Advanced Technologies, **19**, 181–185 (2008).
DOI: 10.1002/pat.993

eXPRESS Polymer Letters Vol.10, No.8 (2016) 679–692
Available online at www.expresspolymlett.com
DOI: 10.3144/expresspolymlett.2016.61

Synergistically improved thermal conductivity of polyamide-6 with low melting temperature metal and graphite

Y. C. Jia, H. He, P. Yu, J. Chen, X. L. Lai*

School of Materials Science and Engineering, South China University of Technology, Wushan Road, Tianhe District, 510640 Guangzhou City, Guangdong Province, China

Received 30 December 2015; accepted in revised form 6 March 2016

Abstract. Low melting temperature metal (LMTM)-tin (Sn) was introduced into polyamide-6 (PA6) and PA6/graphite composites respectively to improve the thermal conductivity of PA6 by melt processing (extruding and injection molding). After introducing Sn, the thermal conductivity of PA6/Sn was nearly constant because of the serious agglomeration of Sn. However, when 20 wt% (5.4 vol%) of Sn was added into PA6 containing 50 wt% (33.3 vol%) of graphite, the thermal conductivity of the composite was dramatically increased to 5.364 versus 1.852 $W\cdot(m\cdot K)^{-1}$ for the PA6/graphite composite, which suggests that the incorporation of graphite and Sn have a significant synergistic effect on the thermal conductivity improvement of PA6. What is more, the electrical conductivity of the composite increased nearly 8 orders of magnitudes after introducing both graphite and Sn. Characterization of microstructure and energy dispersive spectrum analysis (EDS) indicates that the dispersion of Sn in PA6/graphite/Sn was much more uniform than that of PA6/Sn composite. According to Differential Scanning Calorimetry measurement and EDS, the uniform dispersion of Sn in PA6/graphite/Sn and the high thermal conductivity of PA6/graphite/Sn are speculated to be related with the electron transfer between graphite and Sn, which makes Sn distribute evenly around the graphite layers.

Keywords: *polymer composites, low melting temperature metal, tin, graphite, thermal conductivity*

1. Introduction

Low melting temperature metal (LMTM), which have melting temperatures less than 231.9 °C , are frequently used to prepare electrically conducive polymer composites since their high conductivity, liquid state and low viscosity during processing [1–6]. Simultaneously, polymeric materials have attracted increasing interests in the field of thermally conductive materials for the excellent processability, low density and low cost [7]. However, most polymeric materials are thermally insulating and have low thermal conductivities between 0.1–0.5 $W\cdot(m\cdot K)^{-1}$ [8]. Traditional thermally conductive materials metal crystals for instance, have a large number of free electrons outside the nuclei which arrange neatly as shown in Figure 1a. At the heat flow direction, free electrons equipped with thermal energy could move towards low temperature region directly. Most metals have high thermal conductivities for the efficient manner of thermal conduction. Nonmetal crystals arrange neatly as shown in Figure 1b and thus the collision of vibrating crystals becomes a major form of thermal conduction. Because of the long-range order of nonmetal crystals, the thermal conductivities of nonmetal crystals are relatively high compared with polymeric materials which have neither free electrons nor perfect arrangement of crystals [9]. Introducing high thermally conductive fillers into polymer matrix is

*Corresponding author, e-mail: pshuihe@scut.edu.cn

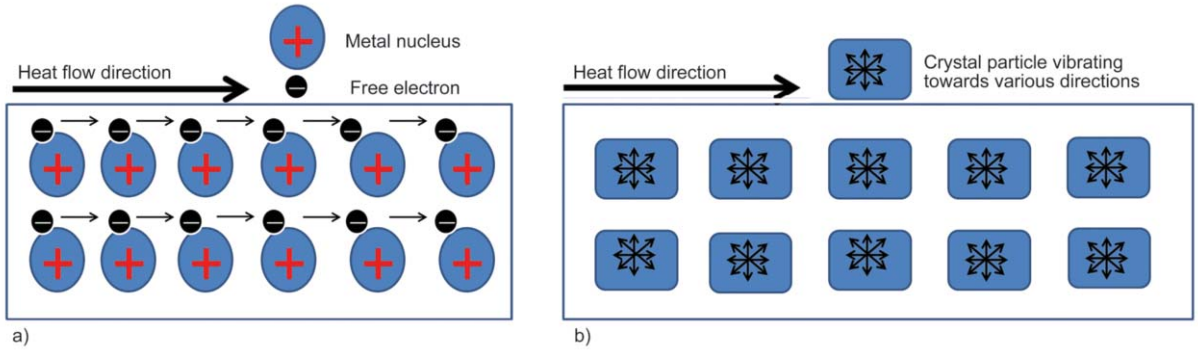

Figure 1. Sketch maps of the structures of (a) metal crystals, and (b) nonmetal crystals

a facile way to increase the thermal conductivities of polymeric materials [10].

There are two critical factors contributing to the thermal conductivities of polymeric materials. One is the formation of heat conduction paths, another is the stacking density of the thermally conductive fillers in the composites [11]. Studies on filling thermally conductive fillers into polymer resin have been frequently reported so far. Ishida and Rimdusit [10] prepared polybenzoxazine filled with BN and achieved a thermal conductivity of 32.5 $W\cdot(m\cdot K)^{-1}$ when the filler loading was 88 wt%. Kozako *et al*. [12] filled Al_2O_3 with a particle size of 10 μm into epoxy resin and the thermal conductivity reached 4.3 $W\cdot(m\cdot K)^{-1}$ when the Al_2O_3 content was 60 vol%. Shengtai Zhou [13] investigated the PA6/PC immiscible blends with a mass proportion of 7/3 filled with graphite and got a thermal conductivity of 4.75 $W\cdot(m\cdot K)^{-1}$ at the graphite loading of 50 wt%.

Graphene and carbon nanotubes have attracted much interests for the ultrahigh thermal conductivity of about 5000 and 3000 $W\cdot(m\cdot K)^{-1}$ respectively [14, 15]. Graphene or carbon nanotubes filled polymers are considered to be very promising candidates for thermally conductive materials and expected to promote thermal conductivity at lower filler loading [16–18]. Zhang *et al.* [19] prepared PVDF filled with 10 wt% of carbon nanotubes and 1 wt% of oxidized graphene. The thermal conductivity of the composite reached 0.95 $W\cdot(m\cdot K)^{-1}$. Graphene and carbon nanotubes could enhance the thermal conductivity of polymer to some extent at lower filler content but far from meeting requirements. What is more, the high cost of graphene or carbon nanotubes arisen from the complicated preparation process [20] would severely restrict their application in industrial manufacture.

As we discussed, the filler content would still be an important factor to thermal conductivities of polymer materials in mass production. Although relatively high thermal conductivity was achieved at high filler loading, the processing of polymer would be difficult because of the high melt viscosity for large number of solid particles existing in the polymer melt, and the device abrasion would be unavoidable. As mentioned above, LMTM have low melting point and low viscosity under melting state. Compared with solid particles, LMTM fillers would be more beneficial to the processing of polymer composites. Zhang *et al*. [21] investigated the rheological properties of polymer/LMTM and found that the LMTM filler decreases the melt viscosity at temperatures above the melting point. Until now, most of the studies on Polymer/LMTM composites concentrated on enhancing the electrically conductive property [1–5]. For instance, Michaeli and Pfefferkorn [1] prepared electrically conductive PA6 with copper fibers and Sn-Zn alloy which was molten during processing. So far, studies on the thermal conductivities of polymer/LMTM composites have been rarely reported [22, 23]. Suplicz and Kovács [22] developed thermally conductive polymer/LMTM composites which can be processed easily with injection molding.

However, the extremely low viscosity and ultrahigh surface tension of liquid metal compared with polymer melt [6, 24–26] would lead to serious agglomeration of LMTM. Thus the content and the dispersion of LMTM in polymer matrix would be severely restricted [27]. Mrozek *et al*. [5] studied on electrically conductive polymer composites based on nickel and low melting eutectic metal. They concluded that the addition of the nickel particulate is critical for maintaining eutectic dispersion. In this work,

LMTM-Sn which has a thermal conductivity of 61.7 $W\cdot(m\cdot K)^{-1}$ [28] was introduced into PA6 to investigate the distribution of Sn and the thermal conductivity of PA6. Then, in dealing with the agglomeration of Sn, graphite was introduced into PA6/Sn composite to enhance the filler distribution and the thermal conductivity of the composite. Besides, the PA6/graphite composites were also prepared as control. The goal of this work is to develop a novel PA6 based material, which has a good thermal conduction.

2. Experimental

2.1. Materials

PA6 (UBE Nylon 1013b) with a density of 1.14 g/cm^3 was obtained from UBE Engineering Plastics, S.A. (Japan). Flake graphite (F-2, Hexagonal structure, Standard No: Q/GHYP1-2012) with an average size of 15 μm and carbon content of 99% was purchased from Shanghai Yifan graphite co., LTD (China). The Sn powder (300 mesh) with a melting point of 231.9 °C and prepared by electrolysis was purchased from Zhengzhou Hengchang metal materials co., LTD. (China). The component of Sn powder is listed in Table 1. All of the properties data were provided by the manufactures.

Table 1. Component of Sn powder

Sn content [≥%]	Impurity content [≤%]						
	Fe	Pb	Cu	S	Bi	As	Sb
99.50	0.04	0.10	0.02	0.001	0.03	0.01	0.04

Table 2. Materials designation and detailed formulations

Component	Designation	PA6 [wt%]	Graphite [wt%]	Sn [wt%]
PA6/graphite	G10	90	10	0
	G20	80	20	0
	G30	70	30	0
	G40	60	40	0
	G50	50	50	0
PA6/Sn	S04	96	0	4
	S08	92	0	8
	S12	88	0	12
	S16	84	0	16
	S20	80	0	20
PA6/graphite/Sn	GS04	46	50	4
	GS08	42	50	8
	GS12	38	50	12
	GS16	34	50	16
	GS20	30	50	20

2.2. Preparation of PA6/Sn, PA6/graphite and PA6/graphite/Sn composites

Prior to blending, the PA6 pellets and graphite were dried at 80 °C for 10 h, while Sn powder was dried under vacuum at 80 °C for 5 h. The raw materials and fillers without any modification were premixed in plastic bags by drastically shaking manually. The materials designation and the detailed formulations of PA6/graphite, PA6/Sn and PA6/graphite/Sn composites are shown in Table 2. The composites systems were fabricated using a Haake twin-screw extruder (polylab OS 16/40, Germany). The extruding temperatures were set as 220, 250, 250, 270, 270, 270, 270, 270, 250, 230 °C (from feeding section (T_1) to extruding die (T_{10})). The screw speed was set as 60 r/min. Then the extrudates were pelletized and dried under vacuum for 10 h at 80 °C. Then the pellets were molded into circular plate samples with a diameter of 12.7 mm (and a thickness of 2 mm) and rectangular samples with a dimension of 80×10×4 mm via an ONLY injection molding machine (P Series 50 e, China). The injection temperatures were set as 220, 270, 270, 270 °C (from feeding zone to nozzle). The injection pressure, injection rate, holding pressure, backpressure, mold temperature and cooling time were set as 30 MPa, 40 mm/s, 20 MPa, 3 MPa, 28 °C and 20 s respectively.

2.3. Characterization

2.3.1. Morphology and element distribution

The circular plate samples were cryogenically fractured in liquid nitrogen along the red arrow as shown in Figure 2a to observe the filler distribution. Then the fractured surfaces were coated with a gold layer before the observation. The fractured surface morphology of the composites was observed via an en-

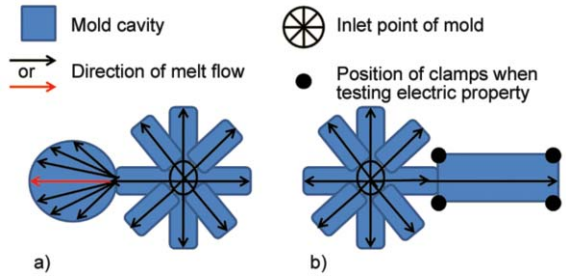

Figure 2. Sketch maps of melt flow in the mold ((a) for circular samples and (b) for rectangular samples)

vironmental scanning electron microscope (ESEM, Quanta 200, FEI, Holland) with an acceleration voltage of 10 kV in high vacuum mode. The element distribution images of Sn were obtained via Energy Disperse Spectroscopy (EDS) which was an accessory of the ESEM.

2.3.2. Thermal conductivity measurement

The circular plate samples with a diameter of 12.7 mm and a thickness of 2 mm were used for the test of thermal diffusivity (through-plane) by Netzsch (Germany) laser flash thermal diffusivity apparatus (LFA 447 NanoFlash) at 30 °C . The apparatus fires a laser pulse on the bottom surface of the sample, then the temperature variation of the top surface is detected and the thermal diffusivity is calculated according to the temperature variation. The test mode and calculation model were set as single layer and Cowan+pulse respectively. Calculation range was 10 times of half-heating up time. The specific heat capacity of the sample at 30 °C were determined via Netzsch (Germany) differential scanning calorimeter (DSC-200 F3). The density was measured by water displacement method and the value was taken from the average of three samples. Then, the thermal conductivity κ [W·(m·K)$^{-1}$] was calculated using Equation (1) [29]:

$$\kappa = \rho \cdot \alpha \cdot C_p \tag{1}$$

where ρ is the density [g/cm^3], C_p is the specific heat capacity [J·(g·K)$^{-1}$], and α is the thermal diffusivity [mm^2/s].

2.3.3. Electrical conductivity measurement

Rectangular samples (80×10×4 mm) were used for resistivity measurement. The electrical resistance R [Ω] was determined by an electrometer (Keithley (USA) 2611B SYSTEM SourceMeter®), which measures the electrical resistance according to the voltage applied on the sample and electric current flow through it. The four clamps of the electrometer were fixed on the four corners of the rectangle sample as shown in Figure 2b. The sweep voltage was set from 20 to 50 V and sweep type was set as linear. The R value was the average taken from 5 specimens. Then the electrical resistance R was converted into volume conductance σ [S/m] with Equation (2):

$$\sigma = \frac{1}{\rho} = \frac{L}{RS} \tag{2}$$

where L [m] is the distance (along the length direction of the sample) between clamps, ρ [Ω·m] is the volume resistivity, and S [m^2] is the cross-sectional area of the sample.

2.3.4. Differential scanning calorimetry (DSC)

The crystallization and melting behavior of the composites were measured using a Netzsch (Germany) differential scanning calorimeter (DSC-200 F3). Experiments were performed with about 15 mg samples under nitrogen atmosphere. The samples were firstly heated to 270 °C at a rate of 20 °C/min to eliminate thermal history and then held at 270 °C for 2 min. Subsequently, the samples were cooled at a rate of 10 °C /min to 20 °C and held at 20 °C for 2 min, then scanned from 20 to 270 °C at a rate of 10 °C/min. The crystallization and melting temperatures were obtained from the cooling and re-heating curves respectively. The crystallinity (χ_c) [%] of the composites was calculated with Equation (3):

$$\chi_c = \frac{\Delta H_m}{(1-\omega)\Delta H_m'} \tag{3}$$

where ΔH_m [J/g] is the melting enthalpy of the composite and ω [wt%] is the weight fraction of fillers. Besides, $\Delta H_m'$ [J/g] is the melting enthalpy of 100% crystalline PA6 and we adopted 230 J/g [30].

2.3.5. Thermal stability of the composites

The thermal stability of the composites was characterized by a thermogravimetric analyzer (TGA Q5000, TA Instrument, U.S.A.). All measurements were performed under nitrogen gas condition with a flow rate of 25 mL/min from 30 to 700 °C at a heating rate of 10 °C/min.

3. Results and discussion

3.1. Morphology and element distribution

The fractured surface morphology of the composites filled with graphite as single filler are shown in Figure 3. The pictures demonstrate an incremental mass ratio of graphite in the matrix from 30 wt% (17.6 vol%) to 50 wt% (33.3 vol%). Graphite particles were oriented along the processing flow direction (Figure 3), consistent with Amesöder *et al.*'s [31] results. It is ascribed to the processing method-injection molding. The graphite flakes would parallel to the direction of melt flow (as shown in Figure 2)

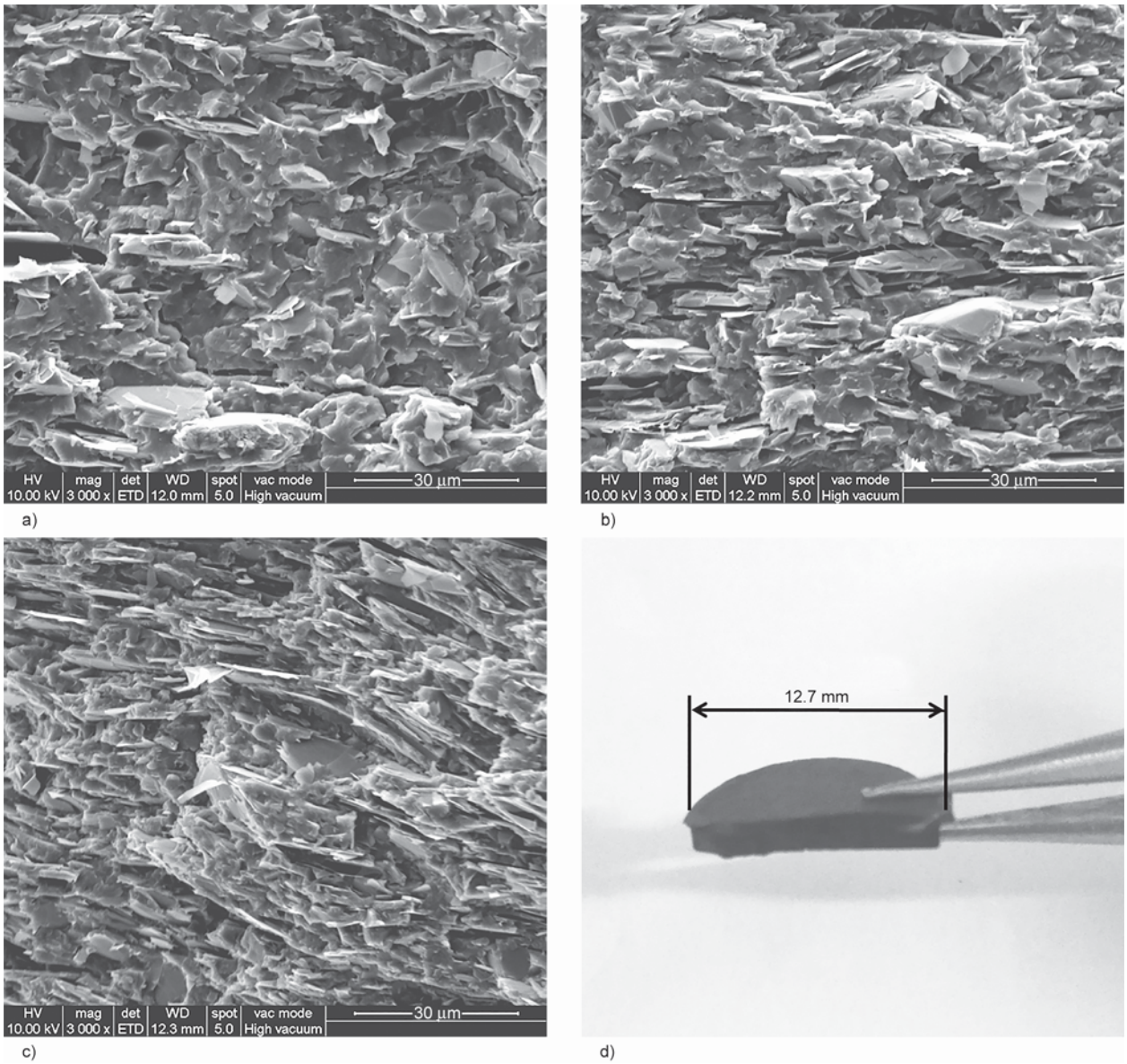

Figure 3. SEM images of the surfaces of the cryogenically fractured composites ((a) for G30, (b) for G40 and (c) for G50). (All the micrograph were obtained from the fractured surfaces of the samples as shown in (d)).

to make the least flow resistance. It is obvious that graphite particles disperse discretely in the matrix and the space between graphite particles is relatively larger when the graphite content is 30 wt% (17.6 vol%). With the increase of graphite content, the space between graphite particles reduces. When the graphite content reaches 50 wt% (33.3 vol%), the graphite particles have already interconnected together and a network structure consisted of flake graphite particles has already been formed.

However, when adding Sn as single filler into PA6 matrix, the agglomeration of Sn could be easily observed with naked eyes in Figure 4a, b and c. The agglomeration of Sn could be clearly observed from SEM images as shown in the red frames in Figure 4d, e and f. With the increase of the Sn content, the agglomerate size increases gradually. When the Sn content is 20 wt% (3.79 vol%) the agglomerate size reaches about 70 µm. This is mainly ascribed to the extremely low viscosity (1.4–1.8 mPa·s during 500–600 K) [6] and ultrahigh surface tension (400–620 mN/m during 400–1600 K) [22] for liquid metal versus the high viscosity (about 100 Pa·s during shear rate of 100–1000/s) [24] and low surface tension (lower than 40 mN/m at 230 °C) [23] for polymer melt, which leads to poor compatibility between PA6 and Sn. The fact that Sn has good flowability and a strong trend of shrinking superficial area in the state of liquid leads to serious agglomeration in the PA6 matrix. Another reason for the agglomeration is that

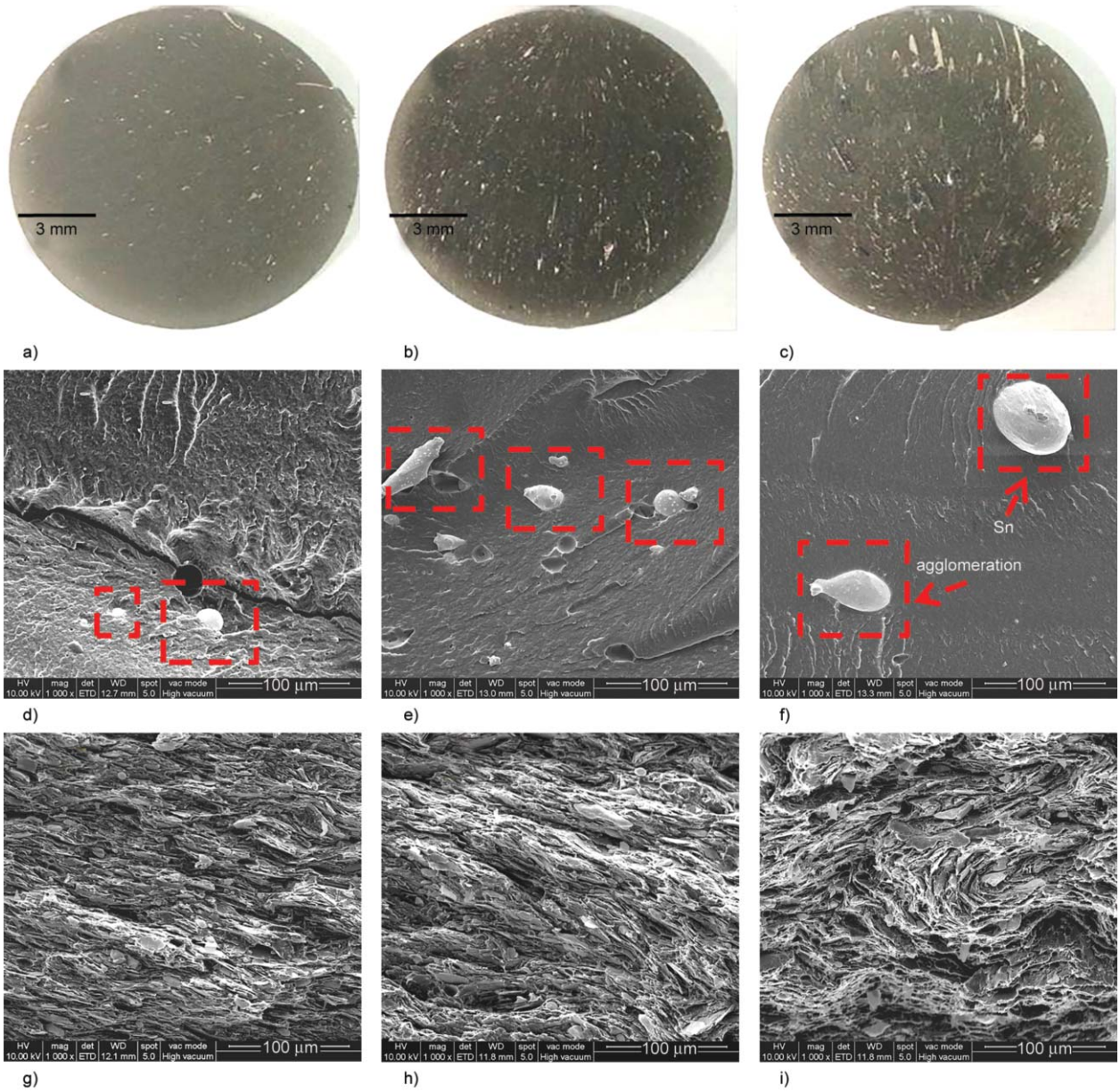

Figure 4. Digital photos of the composites ((a) for S12, (b) for S16 and (c) for S20) and SEM images of the surfaces of cryogenically fractured composites ((d) for S12, (e) for S16, (f) for S20, (g) for GS12, (h) for GS16 and (i) or GS20)

metal and organic polymer have different chemical and physical properties, thus they have poor compatibility.

The SEM images of the composites filled with 50 wt% of graphite and Sn content various from 12 wt% (2.91 vol%) to 20 wt% (5.42 vol%) as hybrid fillers are shown in Figure 4g, h and i. It could be observed that there is no agglomerate even the Sn content reaches 20 wt% (5.42 vol%). And most of the flake graphite particles in GS12 and GS16 are oriented along the direction of the melt flow as well. Interestingly, the distribution form of flake graphite in GS20 is circinate. This is due to the existence of friction between graphite particles. With the increase of weight fraction of Sn, the volume fraction of graphite particles (50 wt%) increases because the density of Sn is much higher than that of graphite. The increase of the volume fraction of graphite particles leads to the increase of the friction between graphite particles and the poor flowability of the polymer melt, which leads to decrease of orientation degree of flake graphite particles in GS20.

Figure 5 shows the EDS images of Sn in S20 and GS20. The Sn in S20 concentrates together and forms spherical-like agglomerate (Figure 5a), while the distribution of Sn in GS20 is much more uniform as

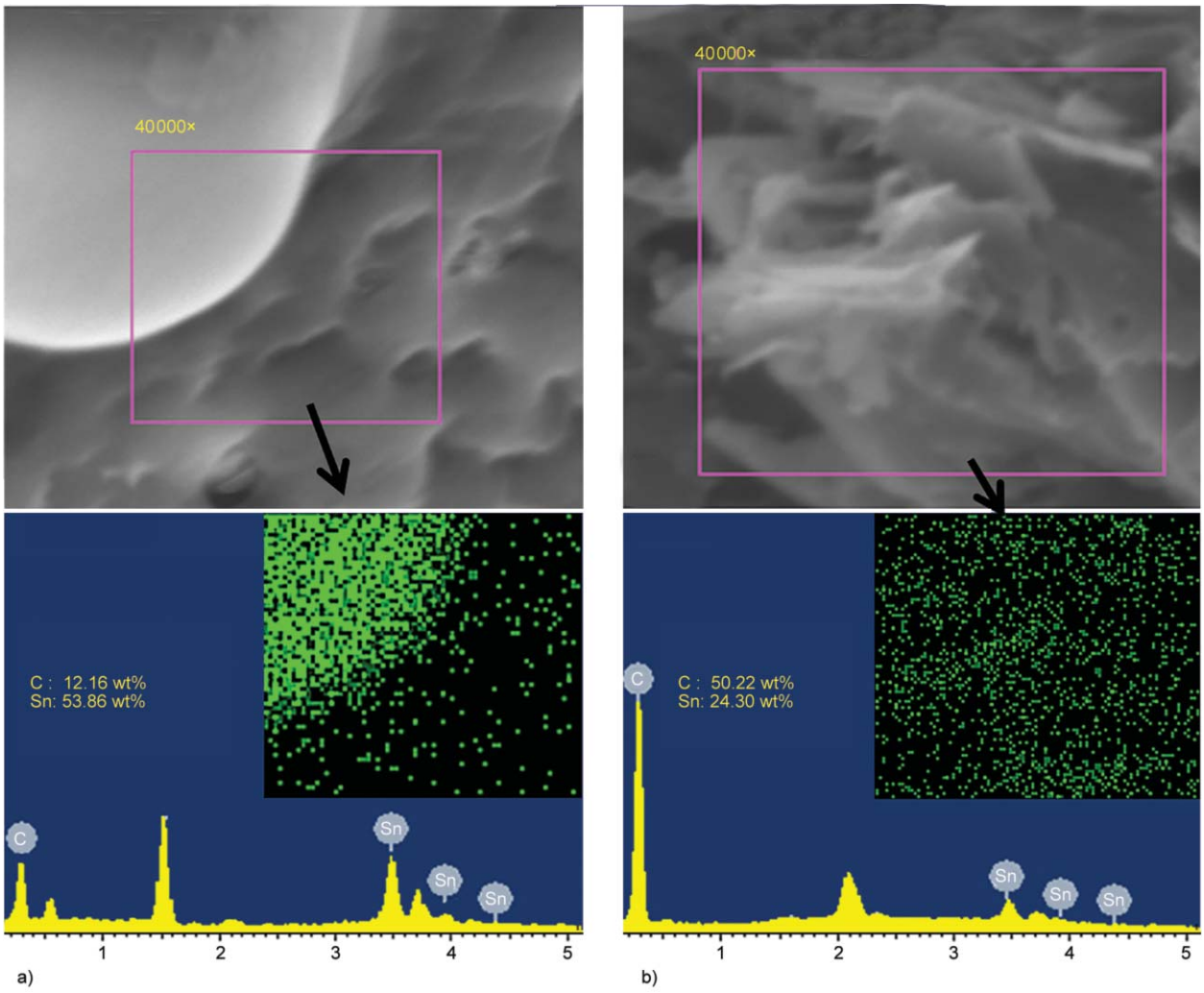

Figure 5. EDS images of Sn in (a) S20 and (b) GS20

shown in Figure 5b. The reason why Sn could disperse well in GS20 may be the fact that the flowability of liquid Sn is hindered by the solid graphite particles. Thus the encounter chance of Sn fluid decreases for the decline of liquidity, which leads to the decrease of agglomeration. Besides, the even dispersion of Sn is speculated to be related to the interaction between Sn and graphite, which will be discussed in the part of DSC measurements.

3.2. Thermal conductivities of the composites

The thermal conductivities of PA6/graphite composites are shown in Figure 6a. The thermal conductivity increases slowly as a function of graphite content below 25.0 vol% (40 wt%). And a sharp increase appears when the graphite content exceeds 25.0 vol% (40 wt%). The flake graphite particles could occupy enough volume in the PA6 matrix to contact each other and form the thermally conductive networks (Figure 3) when the graphite content exceeds 25.0 vol% (40 wt%), and the thermal energy could pass through quickly along the thermally conductive networks. The thermal conductivity of PA6/graphite (33.3 vol%) composite reaches 1.852 $W\cdot(m\cdot K)^{-1}$, agreeing with Amesöder *et al.* [31]. However, there is almost no increase in the thermal conductivities of the PA6/Sn composites as shown in Figure 6b. There are two main reasons for this phenomenon, one is that the Sn content is not enough to form conductive networks. Another is that the distribution of Sn is extremely non-uniform in the matrix (Figure 4a–f and Figure 5a), which would give rise to high thermal resistance at the interface between filler and polymer matrix [32, 33].

When adding Sn into PA6/graphite composite, the thermal conductivities increase obviously as shown in Figure 6b. The thermal conductivity reaches 3.879 $W\cdot(m\cdot K)^{-1}$ when the Sn content is 4.10 vol% (16 wt%) versus 1.852W $W\cdot(m\cdot K)^{-1}$ for G50 and 0.297 $W\cdot(m\cdot K)^{-1}$ for the virgin PA6. This is ascribed

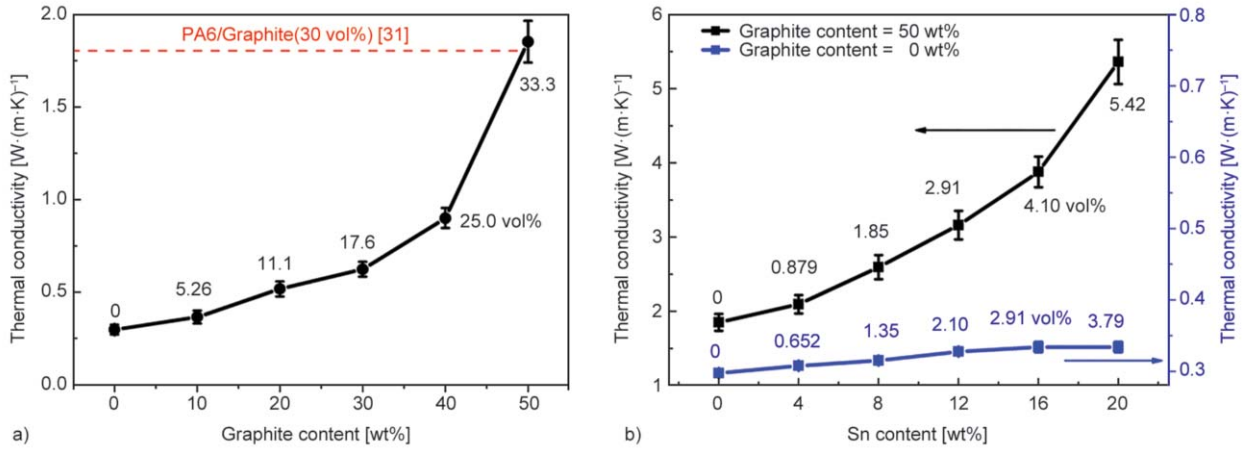

Figure 6. Thermal conductivities of (a) PA6/graphite composites, (b) PA6/Sn and PA6/graphite(50 wt%)/Sn composites as a function of filler content. (The values beside every data point refer to the volume fraction [vol%] of graphite (a) and Sn (b)in the corresponding composites).

to four reasons, one is that Sn is high conductive filler with a thermal conductivity of 61.7 W·(m·K)$^{-1}$ [28] and the distribution of Sn is uniform in the composites under the effect of graphite particles. The second is that the increase of the volume fraction of graphite is accompanied by the addition of Sn, while the weight fraction of graphite remains 50 wt% as discussed in the part of 3.1 (Morphology and element distribution). The thermally conductive networks become strong because the volume occupied by graphite is increased. The third, graphite particles could be more uniform dispersed in matrix for the Sn, which is in a state of low viscosity liquid [6] when processed under high temperature. The fourth, the interaction between Sn and graphite is speculated to be related to the high thermal conductivity (discussed in the part of DSC measurements). The thermal conductivity of the composite sharply increases to 5.364 W·(m·K)$^{-1}$ when the Sn content reaches 5.42 vol% (20 wt%). This is associated with the microstructure of the composite and the test method we adopted. The through plane thermal conductivities were tested in this study, and Figure 4i shows that the distribution form of flake graphite in GS20 is circinate. Indicating that the number of graphite flakes along the perpendicular direction of the plate samples increases. It has been reported that the thermal conductivity along the graphite layers is much larger than that of cross layers [34, 35]. We could conclude that the Sn has a synergistic effect with graphite on the improvement of the thermal conductivity of PA6.

3.3. Electrical conductivities of PA6/graphite and PA6/graphite/Sn composites

The log electrical conductivities (σ) values are plotted as a function of filler content in Figure 7. It is easy

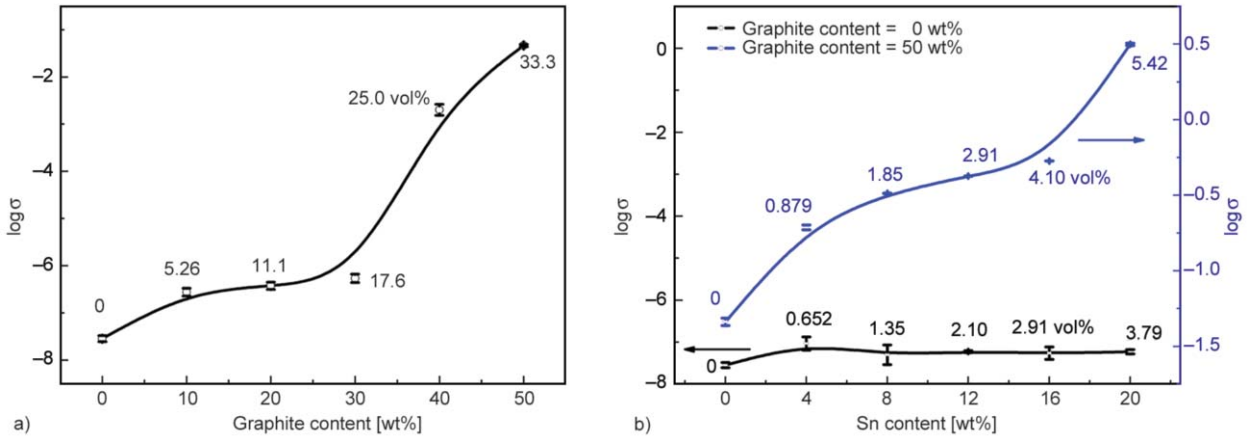

Figure 7. Electrical conductivities (σ) of (a) PA6/graphite composites and (b) PA6/graphite(50 wt%)/Sn composites and PA6/Sn composites as a function of filler content. (The values beside every data point refer to the volume fraction [vol%] of graphite (a) and Sn (b) in the corresponding composites).

to understand that the σ increase as a function of filler content, except that the logσ of PA6/Sn remain almost constant because of the poor distribution of Sn (Figure 7b). Notably, the sharp increase of σ of PA6/graphite composites occurs during the graphite content between 17.6 vol% (30 wt%) and 25.0 vol% (40 wt%), while the thermal conductivity increases sharply between 25.0 vol% (40 wt%) and 33.3 vol% (50 wt%). It is probably ascribed to that the conductive networks are easy to form along the direction of melt flow (Figure 2b) because of the orientation of graphite flakes (Figure 3). And the test method we adopted just detected the σ in the direction of melt flow as described before. Moreover, field emission theory [36] believes that the huge electric field existing between conductive particles would induce the occurrence of field emission when the conductive particles close to 10 nm or more closer, even though there is insulation layer between the conductive particles. Thus the electricity could happen without the contact of graphite particles. The electrical conductivity of PA6 increased nearly 8 orders of magnitude at the maximum filler content.

3.4. DSC measurements

The DSC curves of the composites are shown in Figure 8. For clarity, the vertical distance of the curves is enlarged. And Table 3 shows related DSC data of the PA6/graphite composites. Figure 8a shows that

Table 3. DSC data for the cooling procedure and the re-heating procedure

Samples	T_c [°C]	T_m [°C]	ΔH_m [–J/g]	χ_c [%]
PA6	188.3	223.5	47.72	20.8
G10	193.3	222.1	45.31	21.9
G20	194.9	222.2	41.25	22.4
G30	195.4	221.4	42.14	26.2
G40	195.5	222.6	36.30	26.3
G50	195.1	222.4	32.20	28.0

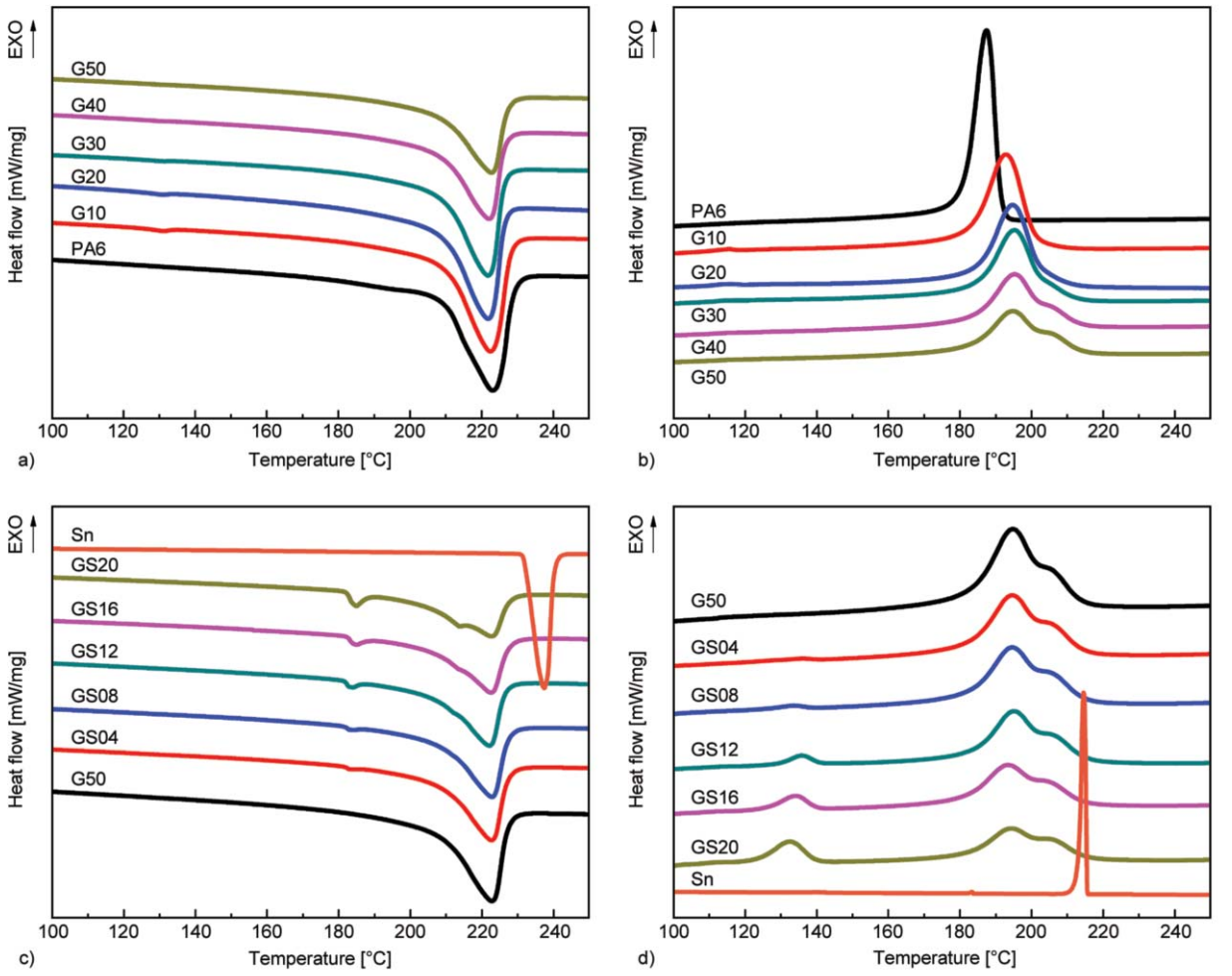

Figure 8. (a) Second-heating curves obtained from PA6/graphite composites, (b) cooling curves obtained from PA6/graphite composites, (c) second-heating curves obtained from Sn and PA6/graphite(50 wt%)/Sn composites, (d) cooling curves obtained from Sn and PA6/graphite(50 wt%)/Sn composites

all the samples exhibit strong melting peaks at about 220 °C, corresponding to the melting event of α-form crystals of PA6 [37, 38]. It is evident that the incorporation of graphite has little effect on the melting behavior of the composites except the decrease of ΔH_m. Unlike the melting behavior of the composites, the crystallization process is greatly affected by the introduction of graphite. It could be observed from Figure 8b and Table 3 that the crystallization temperature and crystallinity of the composites increase with the addition of graphite. This could be ascribed to the facilitating effect of graphite particles which act as nucleating agent on the crystallization of PA6 [39–41]. It is interesting to observe that the new peaks on the exotherms of PA6/graphite composites appear at higher temperature with the increasing amount of graphite content. Similar appearance of exotherms with double peaks in PA6/MWNTs composites was reported before [42–44]. The appearance of higher crystallization temperature is related to the increase of graphite content. More heterogeneous nucleation sites are available with the increasing amount of graphite particles. Therefore, the crystallization of polymer chains could occur at higher temperature and different morphology of crystals might be induced by the large number of graphite particles [42, 43].

As to the thermal behavior of PA6/graphite/Sn composites, it is interesting to observe from Figure 8c that two small endothermic peaks gradually expand with the increase of Sn content at about 180 and 210 °C respectively. It is also found from Figure 8d that a range of peaks on the exotherms of PA6/graphite/Sn composites at about 135 °C become stronger with the increase of Sn content. However, the melting peak and exotherm of pure Sn is not observed from DSC curves of PA6/graphite/Sn composites (Figure 8c and d). It is obvious that the unusual fact is relative to the special heat effect of Sn under the existence of graphite. As is well known, Sn melt consists of Sn ions and free electrons (e_f). Large number of Sn ions arrange neatly and form the close packing when crystallizing alone, while free electrons distribute around nucleus, shared by large number of Sn ions [45, 46]. However, there are abundant π electrons (e_π) arising from π-bonds of carbon atoms moving along the graphite layers. The e_π could move freely along the corresponding carbon atomic layers, which resembles to e_f. Thus we suppose that the crystallization of Sn would be affected by e_π under the existence of graphite particles. As shown in Figure 9, the Sn ions may be strongly attracted by numerous e_π and distribute evenly around graphite layers when Sn melt flows through graphite layers. The free electrons participate in the conjugated system of graphite layers to keep electric neutrality. Unlike crystallization of pure Sn, the Sn ions loosely arrange when crystallizing since there is not enough Sn ions around a certain site because of the strong attraction of e_π. Thus the electron transfer between graphite and Sn occurs. Lots of reports about electron transfer between metal and carbon materials were reported before [47–50]. The endothermic peaks (Figure 8c) at about 180 and 210 °C are supposed to be related to the melting of the loose crystal of Sn. And the peaks on the exotherms (Figure 8d) at about 135 °C correspond to the crystallization of Sn under the effect of e_π. Besides, the uniform dispersion of Sn in the matrix is speculated to be related to the interaction between graphite and Sn. As Figure 9 shown, the e_f originally belongs to Sn participate in the graphite system along with e_π, which make the density of free electrons in the composites increases. Similar to the thermally conductive mech-

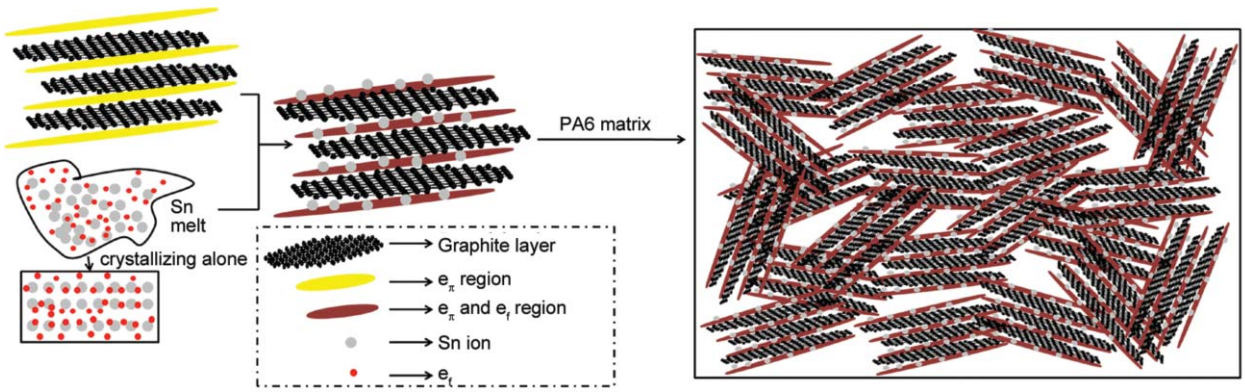

Figure 9. Sketch maps of interaction between Sn melt and graphite and filler distribution in the matrix

anism of metal, the carrier quantity of thermal energy increases, which leads to the increase of thermal conductivity.

3.5. Thermal degradation behavior of the composites

The TGA curves and data of the composites are shown in Figure 10 and Table 4 respectively. For PA6/graphite composites (Figure 10a), there is only one decomposition stage in the heating process and the temperatures of weight loss at 5% ($T_{5\%}$) and 10% ($T_{10\%}$) increase as a function of graphite content. The maximum weight loss rate (R_{max}) decreases with the increase of graphite content (Table 4). This indicates that the thermostability of the composites is enhanced, which is consistent with Kim and Jeong [51] and Zhao *et al*. [52]. It is believed that the graphite particles serve as the mass transfer barriers against the volatile pyrolized products in the PA6 matrix, eventually retarding thermal degradation of the composites [51, 52].

Interestingly, it could be found from Figure 10b and Table 4 that with the increasing loading of Sn, both $T_{5\%}$ and $T_{10\%}$ of the composites initially decrease, and when the Sn content is higher than 4 wt%, $T_{5\%}$ and $T_{10\%}$ start to rise. Compared with G50, there is an obvious decrease of the $T_{5\%}$ and $T_{10\%}$ when Sn is introduced. However, the $T_{5\%}$ and $T_{10\%}$ of PA6/graphite/Sn composites are all higher than that of virgin PA6. The R_{max} of PA6/graphite/Sn composites decreases with the addition of Sn. As noted before, graphite particles serve as the mass transfer barriers against the volatile pyrolized products in the PA6 matrix [51, 52]. When adding slight Sn, the volatile pyrolized products would permeate the barriers of graphite easier because the low viscosity liquid metal decreases the viscosity of the system, which accounts for the initial decrease of $T_{5\%}$ and $T_{10\%}$. However, with the increase of Sn content, the quantity of graphite particles in the unit volume increases as discussed in the part of 3.1 (Morphology and element distribution) and the graphite's hindering effect towards the volatile increases, which explains the following increase of $T_{5\%}$ and $T_{10\%}$. The decrease of R_{max} of the composites is relative to the decrease of weight fraction of PA6 matrix which accounts for the major part of weight loss. In conclusion, the thermostability of the composites meliorated compared with virgin PA6.

Table 4. Thermal degradation data of the composites

Samples	$T_{5\%}$ [°C]	$T_{10\%}$ [°C]	R_{max} [%/°C]
PA6	376.0	404.3	2.03
G10	380.2	405.5	1.94
G20	387.4	408.3	1.70
G30	390.2	410.6	1.59
G40	391.9	412.8	1.40
G50	398.3	417.5	1.18
GS04	379.9	407.2	1.00
GS08	379.9	407.1	0.87
GS12	382.1	407.9	0.86
GS16	388.0	411.2	0.77
GS20	390.2	414.1	0.64

4. Conclusions

A novel PA6 based material, which has a good thermal conduction was prepared by extruding and injection molding. According to this research, the distribution of single filler-Sn in PA6/Sn composites was seriously non-uniform while it had great uniformity

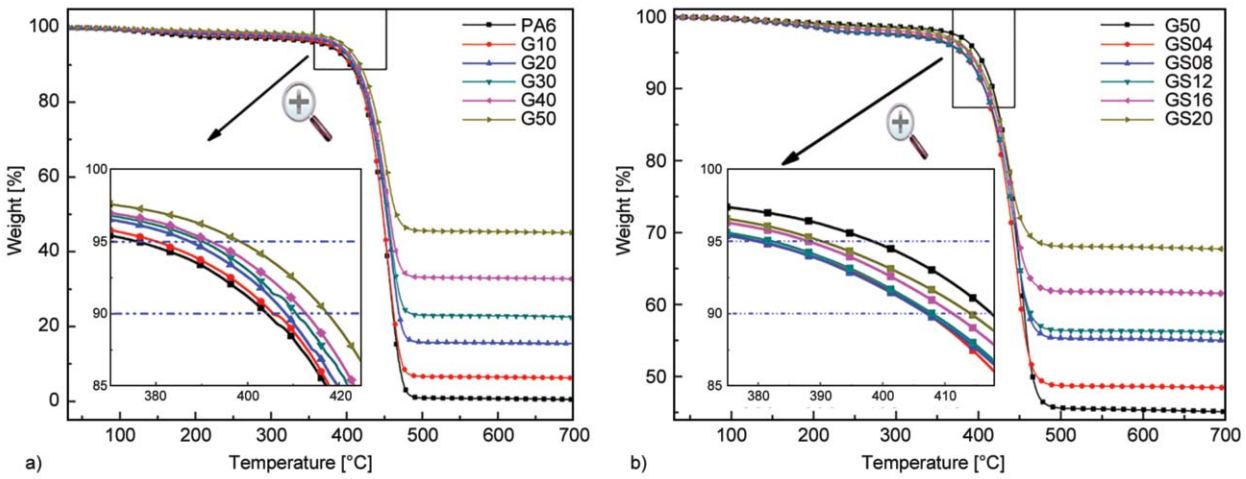

Figure 10. TGA thermograms of (a) PA6/graphite composites, and (b) PA6/graphite(50 wt%)/Sn composites

in PA6/graphite/Sn composites. The thermal conductivity is nearly constant when introducing Sn alone into PA6 matrix, while the addition of Sn could strongly boost the thermal conductivity of the PA6/graphite composites, suggesting that the introduction of graphite and further introduction of Sn have significant synergistic effect on the thermal conductivity improvement of PA6. The reason is speculated to be chemical and/or physical reaction between graphite and Sn, which would be further studied systematically in the near future. Besides, the electrical conductivity and the thermostability were also improved. The value of this work lies in the fact that apparent thermally conductive property improvement of PA6/graphite/Sn composites has been achieved by simple and practical extruding and injection molding, which may be fruitful for the industrial-scale production of thermally conductive polymer composites.

Acknowledgements

All the authors are grateful to the Science and Technology Project of Guangdong Province 2015B010122002 for financial supports.

References

[1] Michaeli W., Pfefferkorn T. G.: Electrically conductive thermoplastic/metal hybrid materials for direct manufacturing of electronic components. Polymer Engineering and Science, **49**, 1511–1524 (2009). DOI: 10.1002/pen.21374

[2] Bormashenko E., Sutovski S., Pogreb R., Sheshnev A., Bormashenko Y., Levin M., Westfrid A.: Development of novel binary and ternary conductive composites based on polyethylene, low-melting-point metal alloy and carbon black. Journal of Thermoplastic Composite Materials, **17**, 245–257 (2004). DOI: 10.1177/0892705704041160

[3] Lu D., Wong C.: Isotropic conductive adhesives filled with low-melting-point alloy fillers. IEEE Transactions on Electronics Packaging Manufacturing, **23**, 185–190 (2000). DOI: 10.1109/6104.873246

[4] Kim J-M., Yasuda K., Rito M., Fujimoto K.: New electrically conductive adhesives filled with low-melting-point alloy fillers. Materials Transactions, **45**, 157–160 (2004).

[5] Mrozek R. A., Cole P. J., Mondy L. A., Rao R. R., Bieg L. F., Lenhart J. L.: Highly conductive, melt processable polymer composites based on nickel and low melting eutectic metal. Polymer, **51**, 2954–2958 (2010). DOI: 10.1016/j.polymer.2010.04.067

[6] Gancarz T., Moser Z., Gąsior W., Pstruś J., Henein H.: A comparison of surface tension, viscosity, and density of Sn and Sn–Ag alloys using different measurement techniques. International Journal of Thermophysics, **32**, 1210–1233 (2011). DOI: 10.1007/s10765-011-1011-1

[7] Hu M., Feng J., Ng K. M.: Thermally conductive PP/AlN composites with a 3-D segregated structure. Composites Science and Technology, **110**, 26–34 (2015). DOI: 10.1016/j.compscitech.2015.01.019

[8] He M., Qiu F., Lin Z.: Towards high-performance polymer-based thermoelectric materials. Energy and Environmental Science, **6**, 1352–1361 (2013). DOI: 10.1039/c3ee24193a

[9] Chu J. R., Zhang X. H., Xu C. X.: Research and applications of thermal conducting polymer. Polymer Materials Science and Engineering, **16**, 17–21 (2000).

[10] Huang X., Zhi C., Jiang P., Golberg D., Bando Y., Tanaka T.: Polyhedral oligosilsesquioxane-modified boron nitride nanotube based epoxy nanocomposites: An ideal dielectric material with high thermal conductivity. Advanced Functional Materials, **23**, 1824–1831 (2013). DOI: 10.1002/adfm.201201824

[11] Ishida H., Rimdusit S.: Very high thermal conductivity obtained by boron nitride-filled polybenzoxazine. Thermochimica Acta, **320**, 177–186 (1998). DOI: 10.1016/S0040-6031(98)00463-8

[12] Kozako M., Okazaki Y., Hikita M., Tanaka T.: Preparation and evaluation of epoxy composite insulating materials toward high thermal conductivity. in '10th IEEE International Conference on Solid Dielectrics (ICSD), Potsdam, Germany' p.4 (2010). DOI: 10.1109/ICSD.2010.5568250

[13] Zhou S., Chen Y., Zou H., Liang M.: Thermally conductive composites obtained by flake graphite filling immiscible polyamide 6/polycarbonate blends. Thermochimica Acta, **566**, 84–91 (2013). DOI: 10.1016/j.tca.2013.05.027

[14] Balandin A. A., Ghosh S., Bao W., Calizo I., Teweldebrhan D., Miao F., Lau C. N.: Superior thermal conductivity of single-layer graphene. Nano Letters, **8**, 902–907 (2008). DOI: 10.1021/nl0731872

[15] Kim P., Shi L., Majumdar A., McEuen P.: Thermal transport measurements of individual multiwalled nanotubes. Physical Review Letters, **87**, 215502/1–215502/4 (2001). DOI: 10.1103/PhysRevLett.87.215502

[16] Kwon S. Y., Kwon I. M., Kim Y-G., Lee S., Seo Y-S.: A large increase in the thermal conductivity of carbon nanotube/polymer composites produced by percolation phenomena. Carbon, **55**, 285–290 (2013). DOI: 10.1016/j.carbon.2012.12.063

[17] Wang J., Jia H., Tang Y., Ji D., Sun Y., Gong X., Ding L.: Enhancements of the mechanical properties and thermal conductivity of carboxylated acrylonitrile butadiene rubber with the addition of graphene oxide. Journal of Materials Science, **48**, 1571–1577 (2013).
DOI: 10.1007/s10853-012-6913-1

[18] Dai W., Yu J., Liu Z., Wang Y., Song Y., Lyu J., Bai H., Nishimura K., Jiang N.: Enhanced thermal conductivity and retained electrical insulation for polyimide composites with SiC nanowires grown on graphene hybrid fillers. Composites Part A: Applied Science and Manufacturing, **76**, 73–81 (2015).
DOI: 10.1016/j.compositesa.2015.05.017

[19] Zhang W-B., Zhang Z-X., Yang J-H., Huang T., Zhang N., Zheng X-T., Wang Y., Zhou Z-W.: Largely enhanced thermal conductivity of poly(vinylidene fluoride)/carbon nanotube composites achieved by adding graphene oxide. Carbon, **90**, 242–254 (2015).
DOI: 10.1016/j.carbon.2015.04.040

[20] Novoselov K. S., Fal'ko V., Colombo L., Gellert P., Schwab M., Kim K.: A roadmap for graphene. Nature, **490**, 192–200 (2012).
DOI: 10.1038/nature11458

[21] Zhang X., Pan Y., Cheng J., Yi X.: The influence of low-melting-point alloy on the rheological properties of a polystyrene melt. Journal of Materials Science, **35**, 4573–4581 (2000).
DOI: 10.1023/A:1004845426786

[22] Suplicz A., Kovács J. G.: Development of thermally conductive polymer materials and their investigation. Materials Science Forum, **729**, 80–84 (2012).
DOI: 10.4028/www.scientific.net/MSF.729.80

[23] Wierzbicki Ł., Pusz A.: Thermal conductivity of the epoxy resin filled by low melting point alloy. Archives of Materials Science and Engineering, **61**, 22–29 (2013).

[24] Yuan Z. F., Mukai K., Takagi K., Ohtaka M., Huang W. L., Liu Q. S.: Surface tension and its temperature coefficient of molten tin determined with the sessile drop method at different oxygen partial pressures. Journal of Colloid and Interface Science, **254**, 338–345 (2002).
DOI: 10.1006/jcis.2002.8589

[25] Wilkinson A. N., Clemens M. L., Harding V. M.: The effects of SEBS-*g*-maleic anhydride reaction on the morphology and properties of polypropylene/PA6/SEBS ternary blends. Polymer, **45**, 5239–5249 (2004).
DOI: 10.1016/j.polymer.2004.05.033

[26] Li L-P., Yin B., Zhou Y., Gong L., Yang M-B., Xie B-H., Chen C.: Characterization of PA6/EPDM-g-MA/HDPE ternary blends: The role of core-shell structure. Polymer, **53**, 3043–3051 (2012).
DOI: 10.1016/j.polymer.2012.05.003

[27] He J., Liu T., Yi Y., Tan X., Luo J., Lu A.: Internal mixing behavior and electrical conductivity of low-melting-point metals/polyethylene composites (in Chinese). Polymer Materials Science and Engineering, **28**, 110–117 (2012).

[28] Ding F., Xie W. Z.: Thermally conductive composites (in Chinese). Acta Materiae Compositae Sinica, **10**, 19–24 (1993).

[29] Pietralla M.: High thermal conductivity of polymers: Possibility or dream? Journal of Computer-Aided Materials Design, **3**, 273–280 (1996).
DOI: 10.1007/BF01185664

[30] Ehrenstein G. W., Riedel G., Trawiel P.: Thermal analysis of plastics: Theory and practice. Hanser, Berlin (2012).

[31] Amesöder S., Heinle C., Ehrenstein G., Schmachtenberg E.: Injection moulding of thermally conducting polymers for mechatronic applications. in 'The Polymer Processing Society 23rd Annual Meeting, Salvador, Brasil' p.5 (2007).

[32] Ruh R., Donaldson K. Y., Hasselman D. P. H.: Thermal conductivity of boron carbide–boron nitride composites. Journal of the American Ceramic Society, **75**, 2887–2890 (1992).
DOI: 10.1111/j.1151-2916.1992.tb05525.x

[33] Pettersson S., Mahan G. D.: Theory of the thermal boundary resistance between dissimilar lattices. Physical Review B, **42**, 7386/1–7386/5 (1990).
DOI: 10.1103/PhysRevB.42.7386

[34] Kude Y., Sohda Y.: Thermal management of carbon-carbon composites by functionally graded fiber arrangement technique. in 'Functionally graded materials' (eds.: Shiota I., Miyamoto Y.) Elsevier, Oxford, 239–244 (1996).
DOI: 10.1016/B978-044482548-3/50040-8

[35] Bertram A., Beasley K., Torre W.: An overview of navy composite developments for thermal management. Naval Engineers Journal, **104**, 276–285 (1992).
DOI: 10.1111/j.1559-3584.1992.tb02246.x

[36] van Beek L. K. H., van Pul B. I. C. F.: Internal field emission in carbon black-loaded natural rubber vulcanizates. Journal of Applied Polymer Science, **6**, 651–655 (1962).
DOI: 10.1002/app.1962.070062408

[37] Ramesh C., Gowd E. B.: High-temperature X-ray diffraction studies on the crystalline transitions in the α-and γ-forms of nylon-6. Macromolecules, **34**, 3308–3313 (2001).
DOI: 10.1021/ma0006979

[38] Liu T., Phang I. Y., Shen L., Chow S. Y., Zhang W-D.: Morphology and mechanical properties of multiwalled carbon nanotubes reinforced nylon-6 composites. Macromolecules, **37**, 7214–7222 (2004).
DOI: 10.1021/ma049132t

[39] Zheng W., Lu X., Wong S-C.: Electrical and mechanical properties of expanded graphite-reinforced high-density polyethylene. Journal of Applied Polymer Science, **91**, 2781–2788 (2004).
DOI: 10.1002/app.13460

[40] Sorrentino L., Aurilia M., Cafiero L., Cioffi S., Iannace S.: Mechanical behavior of solid and foamed polyester/expanded graphite nanocomposites. Journal of Cellular Plastics, **48**, 355–368 (2012).
DOI: 10.1177/0021955X12449641

[41] Cerezo F. T., Preston C. M., Shanks R. A.: Morphology, thermal stability, and mechanical behavior of [poly (propylene)-grafted maleic anhydride]-layered expanded graphite oxide composites. Macromolecular Materials and Engineering, **292**, 155–168 (2007). DOI: 10.1002/mame.200600303

[42] Phang I. Y., Ma J., Shen L., Liu T., Zhang W-D.: Crystallization and melting behavior of multi-walled carbon nanotube-reinforced nylon-6 composites. Polymer International, **55**, 71–79 (2006). DOI: 10.1002/pi.1920

[43] Cheng H. K. F., Sahoo N. G., Pan Y., Li L., Chan S. H., Zhao J., Chen G.: Complementary effects of multiwalled carbon nanotubes and conductive carbon black on polyamide 6. Journal of Polymer Science Part B: Polymer Physics, **48**, 1203–1212 (2010). DOI: 10.1002/polb.22010

[44] Wu Q., Liu X., Berglund L. A.: An unusual crystallization behavior in polyamide 6/montmorillonite nanocomposites. Macromolecular Rapid Communications, **22**, 1438–1440 (2001). DOI: 10.1002/1521-3927(20011101)22:17<1438::AID-MARC1438>3.0.CO;2-U

[45] Anderson W. P., Burdett J. K., Czech P. T.: What is the metallic bond? Journal of the American Chemical Society, **116**, 8808–8809 (1994). DOI: 10.1021/ja00098a050

[46] Nittono O., Ogawa T., Gong S. K., Nagakura S.: *In situ* observation on melt growth process of tin crystal by means of synchrotron X-ray topography. Japanese Journal of Applied Physics, **23**, L581–L583 (1984). DOI: 10.1143/JJAP.23.L581

[47] Guerret-Piécourt C., Le Bouar Y., Lolseau A., Pascard H.: Relation between metal electronic structure and morphology of metal compounds inside carbon nanotubes. Nature, **372**, 761–765 (1994). DOI: 10.1038/372761a0

[48] Rao A. M., Eklund P., Bandow S., Thess A., Smalley R. E.: Evidence for charge transfer in doped carbon nanotube bundles from Raman scattering. Nature, **388**, 257–259 (1997). DOI: 10.1038/40827

[49] Kitaura R., Imazu N., Kobayashi K., Shinohara H.: Fabrication of metal nanowires in carbon nanotubes *via* versatile nano-template reaction. Nano Letters, **8**, 693–699 (2008). DOI: 10.1021/nl073070d

[50] Subrahmanyam K., Manna A. K., Pati S. K., Rao C.: A study of graphene decorated with metal nanoparticles. Chemical Physics Letters, **497**, 70–75 (2010). DOI: 10.1016/j.cplett.2010.07.091

[51] Kim I-H., Jeong Y. G.: Polylactide/exfoliated graphite nanocomposites with enhanced thermal stability, mechanical modulus, and electrical conductivity. Journal of Polymer Science Part B: Polymer Physics, **48**, 850–858 (2010). DOI: 10.1002/polb.21956

[52] Zhao Y. F., Xiao M., Wang S. J., Ge X. C., Meng Y. Z.: Preparation and properties of electrically conductive PPS/expanded graphite nanocomposites. Composites Science and Technology, **67**, 2528–2534 (2007). DOI: 10.1016/j.compscitech.2006.12.009

eXPRESS Polymer Letters Vol.10, No.8 (2016) 693–700
Available online at www.expresspolymlett.com
DOI: 10.3144/expresspolymlett.2016.62

Synthesis of polyisobutylene-polycaprolactone block copolymers using enzyme catalysis

M. Castano[1,2], *A. Alvarez*[1,2], *M. L. Becker*[2], *J. E. Puskas*[1,2*]

[1]Department of Chemical and Biomolecular Engineering, The University of Akron, 44325 Akron, USA
[2]Department of Polymer Science, The University of Akron, 44325 Akron, USA

Received 21 December 2015; accepted in revised form 12 March 2016

Abstract. The synthesis of poly(isobutylene-*b*-ε-caprolactone) diblock and poly(ε-caprolactone-*b*-isobutylene-*b*-ε-caprolactone) triblock copolymers was accomplished using a combination of living carbocationic polymerization of isobutylene (IB) with the ring-opening polymerization (ROP) of ε-caprolactone (ε-CL). OH-PIB-allyl was prepared by living carbocationic polymerization of IB initiated with 1,2-propylene oxide/$TiCl_4$ followed by termination with allyltrimethylsilane. Hydroxyl telechelic HO-PIB-OH was obtained by living IB polymerization initiated by 2,4,4,6-tetramethyl-heptane-2,6-diol/$TiCl_4$, termination with allyltrimethylsilane and subsequent thiol-ene click reaction with mercaptoethanol. The structure of the hydroxyl PIBs was confirmed by ^{1}H NMR (proton Nuclear Magnetic Resonance spectroscopy). OH-PIB-allyl and HO-PIB-OH were then successfully used as macroinitiators for the polymerization of ε-CL catalyzed by *Candida antarctica Lipase B* (CALB), yielding poly(ε-caprolactone-*b*-isobutylene) diblock and poly(ε-caprolactone-*b*-isobutylene-*b*-ε-caprolactone) triblock copolymers, respectively. Differential Scanning Calorimetry (DSC), Transition Electron Microscopy (TEM) and Atomic Force Microscopy (AFM) demonstrated that the amorphous PIB and the semicrystalline PCL block segments phase separated, creating nanostructured phase morphology.

Keywords: *polymer synthesis, enzyme catalysis, block copolymers, polyisobutylene, polycaprolactone*

1. Introduction

The design of novel macromolecular architectures is a continuous focus in polymer science. Many of these architectures, such as block copolymers, possess unique properties, which make them interesting candidates for special applications in nanotechnology and biomedical materials. Controlled ring-opening polymerization (ROP) of cyclic esters, such as lactide, glycolide, cyclic carbonate, and/or ε-caprolactone (ε-CL), have received significant attention due to the good mechanical properties, degradation behavior and biocompatibility of the resulting polymers [1–3]. Polyisobutylene (PIB) has been combined with materials widely used for biomedical applications (polyacrylates and -methacrylates, polysiloxanes, polylactones, polyurethanes, poly(ethylene oxide), and poly (vinyl alcohol)), and some devices that use PIB-based materials are approved by the Food and Drug Administration (FDA) [4–6]. One of the most relevant combinations is poly(styrene-*b*-isobutylene-*b*-styrene) (SIBS). SIBS is a very soft, transparent material resembling silicone rubber, with superior mechanical properties. It is used as a drug-eluting coating of coronary stents [6–8]. PIB is not degradable under biological conditions, however, its copolymers can be. Block copolymers of PIB with L-lactide [9] and pivalolactone [10] have been synthesized from primary hydroxyl functionalized PIBs and metal-containing activators. It was found that the blocks had phase-separated morphologies, and the crystallization behavior of the polylactide and polypivalolactone was influenced by the presence of the PIB blocks. However,

*Corresponding author, e-mail: jpuskas@uakron.edu

we found only two papers discussing the synthesis of PIB-PCL block copolymers [11, 12]. Both papers used telechelic HO-PIB-OH macroinitiators obtained by multistep processes, and triethyl aluminum or $HCl{\cdot}Et_2O$ catalyst. The first paper concentrated on structural analysis without investigating the phase morphology of the products [11]. The second paper reported microphase-separation based on Differential Scanning Calorimetry (DSC) that found two transitions: T_g = –60 °C for the PIB segment and T_m = 60 ºC for the PCL block [12].

This paper reports the facile synthesis of a poly(isobutylene-*b*-ε-caprolactone) diblock and poly(ε-caprolactone-*b*-isobutylene-*b*-ε-caprolactone) triblock copolymers using PIB-OH and HO-PIB-OH macroinitiators [13–15], and ROP of ε-CL catalyzed by *Candida antarctica lipase B* (CALB). Enzyme-catalyzed ROP [16–21] is one of the most promising tools and avoids the use of organo-metallic catalysts (Zn, Al, Sn or Ge), which are known to be cytotoxic to cellular systems and are often difficult to remove from polymeric products [2]. Gross and Hillmyer used anionically synthesized monohydroxyl-functional polybutadiene of various molecular mass (M_n ~ 2600–19 000 g/mol) to initiate the ROP of ε-CL and pentadecalactone catalyzed by CALB to make diblock copolymers. However, the products contained 10–30 wt% homoPCL after methanol precipitation, so they developed a fractionation method to purify the diblocks [19]. Tang and coworkers [20, 21] used hydroxyl- and ester-functionalized polyoctadiene to initiate ROP of ε-CL and ω-pentadecalactone using CALB, but did not investigate the phase morphology of the resulting block copolymers. PIB-containing block copolymers have never been synthesized using CALB-catalyzed ROP of lactones. We report conditions leading to pure di- and triblock copolymers.

2. Experimental section

2.1. Materials

HO-PIB-allyl (M_n = 4300 g/mol, $Đ_M$ = 1.21) [18] and HO-PIB-OH (M_n =4100 g/mol, $Đ_M$ =1.2) [14, 15] macroinitiators were synthesized by recently reported facile new methodologies. ε-caprolactone (ε-CL, Sigma Aldrich, 97%), methylene chloride (CH_2Cl_2, ≥99.8%, EMD Chemicals) and toluene (Sigma Aldrich, 99%) were dried over CaH_2 (95%, Aldrich)) and distilled under vacuum. Methanol (MeOH, 99.8%, Fisher Scientific) was used as received. Lipase B from *Candida antarctica* immobilized on microporous acrylic resin (20 wt% CALB, Novozyme 435, Sigma Aldrich), deuterated chloroform ($CDCl_3$, 99.8%, Chemical Isotope Laboratories) were used as received.

2.2. Procedures

2.2.1. Synthesis of poly(isobutylene-*b*-ε-caprolactone)

A solution of HO-PIB-allyl (0.18 g, $8.05{\cdot}10^{-3}$ mol/L) and dry toluene (5.0 mL) were transferred via syringe under dry N_2 atmosphere into a flask containing immobilized CALB (75 mg, 20% CALB, $4.33{\cdot}10^{-4}$ mol/L). The suspension, as well as a separate flask containing ε-CL, was equilibrated for 15 min at the reaction temperature (70 °C). Thereafter, ε-CL (0.2 g, 0.35 mol/L) was transferred to the reaction flask via syringe under dry N_2 atmosphere to start the polymerization. After 24 h reaction time the reaction mixture was cooled to room temperature and CALB was removed by filtration. The polymer was precipitated in methanol and dried under vacuum for 24 h at room temperature (yield 0.235 g, ε-CL conversion 28%).

2.2.2. Synthesis of poly(ε-caprolactone-*b*-isobutylene-*b*-ε-caprolactone)

A solution of HO-PIB-OH (0.090 g, $8.13{\cdot}10^{-3}$ mol/L) and dry toluene (2.5 mL) were transferred via syringe under dry N_2 atmosphere into a flask containing immobilized CALB – (40 mg, 20% CALB, $4.45{\cdot}10^{-4}$ mol/L). The suspension, as well as a separate flask containing ε-CL, was equilibrated for 15 min at the reaction temperature (70 °C). Thereafter, ε-CL (0.2 mL, 0.67 mol/L) was transferred to the reaction flask via syringe under dry N_2 atmosphere to start the polymerization. After 24 h reaction time the reaction mixture was cooled to room temperature and CALB was removed by filtration. The polymer was precipitated in methanol and dried under vacuum for 24 h at room temperature (yield 0.14 g, ε-CL conversion 25%).

2.3. Characterization

2.3.1. Size exclusion chromatography (SEC)

The molecular mass and molecular mass distribution ($Đ_M$) of the polymers were determined by SEC con-

sisting of a Waters 515 HPLC Pump, a Waters 2487 Dual Absorbance UV Detector (UV), a Wyatt OPTILAB DSP Interferometric Refractometer (RI), a Wyatt DAWN EOS multi-angle light scattering detector (LS), a Wyatt ViscoStar viscometer (VIS), a Wyatt QELS quasi-elastic light scattering instrument (QELS), a Waters 717 plus autosampler and 6 Styragel® columns (HR6, HR5, HR4, HR3, HR1 and H0.5). The columns were thermostated at 35 °C and THF, continuously distilled from CaH_2, was used as the mobile phase at a flow rate of 1 mL/min. The results were analyzed by using the ASTRA software (Wyatt Technology). Block copolymer dn/dc was calculated based on the weight fraction and dn/dc of the individual components; PCL = 0.053 [22] and PIB = 0.108 [23]. The results agreed with data obtained assuming 100% mass recovery.

2.3.2. Nuclear Magnetic Resonance (NMR) spectroscopy

^{1}H NMR spectra were recorded on a Varian Mercury-500 NMR spectrometer in $CDCl_3$. The resonance at δ = 7. 27 ppm (^{1}H NMR) was used as internal reference. Spectra were acquired with 128 transients and a relaxation time of 5 sec.

2.3.3. Differential scanning calorimetry (DSC)

DSC was carried out on a TA Q2000 instrument. 5 mg of the sample was subjected to heating/cooling cycles at 10 °C/min in the temperature range of –100 to 150 °C. Nitrogen atmosphere was used to minimize thermal degradation of the polymers. T_g and T_m were calculated as the mean value between the onset and end point temperatures of the second cycle.

2.3.4. Optical microscopy

Optical images were collected with an Olympus BX51 optical microscope using reflected light.

2.3.5. Transmission electron microscopy (TEM)

TEM was carried out on a Philips Tecnai 12 instrument at an accelerating voltage of 120 kV. Thin films were prepared on a carbon coated glass surface by spin coating one drop of a 1% polymer solution in THF. The carbon coated glass surface with the spin coated copolymer was immersed into a distilled water bath. The polymeric film along with the carbon layer floated onto the water surface, and then was picked up by clean TEM copper grids (400 mesh, SPI). Before TEM observation, the samples on the grids were annealed for 5 min at 70 °C and then 15 h at 40 °C. The samples were stained with 1% OsO_4.

2.3.6. Atomic Force Microscopy (AFM)

AFM images were taken using a Veeco Instruments Multimode AFM with a Nanoscope IV controller, operated in the tapping-mode with height and phase images collected simultaneously. Silicon cantilevers with a nominal resonance frequency of 170 kHz (Aspire CT170R) were used, with typical medium-light tapping forces as characterized by a 2.0 V free amplitude and a 1.6 V set point amplitude.

3. Results and discussion

3.1. Synthesis of poly(isobutylene-*b*-ε-caprolactone) diblock

The enzyme-catalyzed ROP of ε-CL was initiated using the HO-PIB-allyl macroinitiator (M_n = 4300 g/mol with $Đ_M$ = 1.21) as shown in Figure 1. In this case [monomer]/[OH] ~40 was used based on Storey's previous report [11]. Higher ratios were tried but did not yield clean diblocks.

Figure 2 shows the ^{1}H NMR spectrum of PIB-*b*-PCL. The resonances at δ = 5.04 ppm (f) and δ = 5.77 ppm (e) belong to the allylic protons of the HO-PIB-allyl macroinitiator. Signals for structural analysis included those at 3.68 and 4.33 (h, J 6.5 Hz, $–CH_2–OH$), due to the methylene protons of PCL chain-end units and resonances at 4.11 ppm (g) and 2.32 ppm (m), due to the methylene protons in the PCL repeat unit. The M_n of the poly(ε-caprolactone) block was calculated from the ratio of the integral of the methylene protons of the repeat unit of PCL (g) at δ = 4.23 ppm and the methylene proton of the allyl end group of

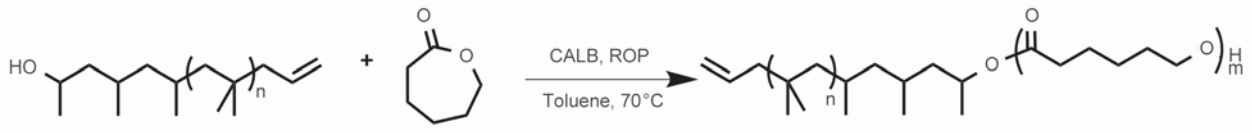

Figure 1. CALB catalyzed ROP of ε-CL using allyl-PIB-OH as macroinitiator. [HO-PIB-allyl] = $8.05 \cdot 10^{-3}$ mol/L, [ε-CL] = 0.35 mol/L; [CALB] = $4.33 \cdot 10^{-4}$ mol/L.

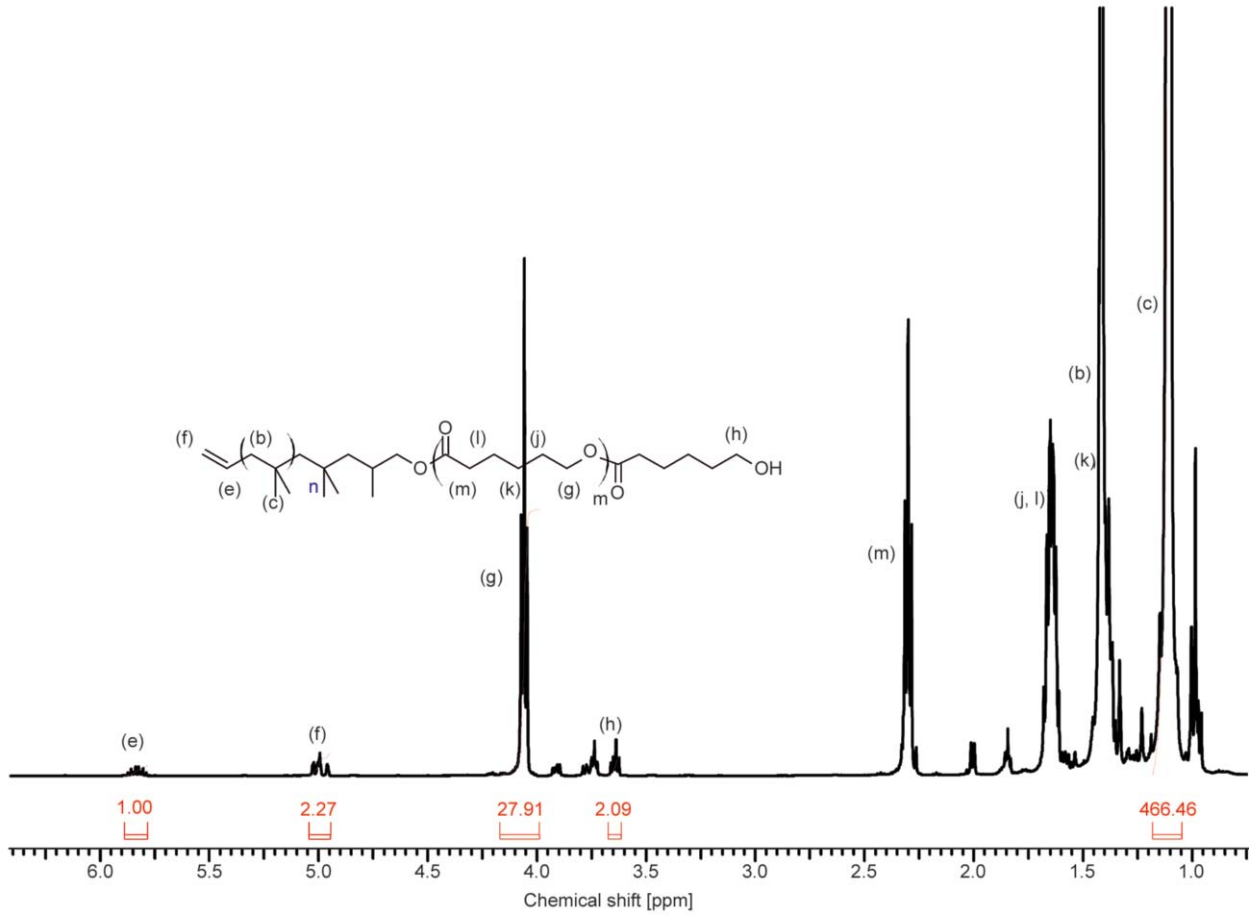

Figure 2. [1]H NMR spectrum of PIB-*b*-PCL

HO-PIB-allyl (e) at δ = 5.77 ppm as M_n = 1590 g/mol. Thus the total diblock molecular weight is M_n = 5890 g/mol, corresponding to 26.8 wt% PCL. Figure 3 shows the SEC traces of the macroinitiator and the diblock copolymer (PIB-*b*-PCL).

Relative to the starting HO-PIB-allyl (M_n = 4300 g/mol), the SEC RI traces of PIB-*b*-PCL diblock copolymer shifted to higher molecular mass and the molecular mass distribution remained narrow. The M_n = 6100 g/mol and $Đ_M$ = 1.26 were determined by SEC using d*n*/d*c* = 0.093. This corresponds to a PIB_{4300}-*b*-PCL_{1800} structure (29.5 wt% PCL), which is in good agreement with the NMR data.

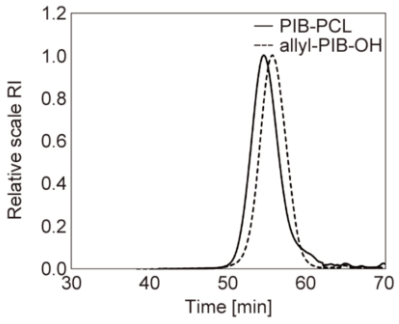

Figure 3. SEC traces of HO-PIB-allyl and PIB-*b*-PCL

3.2. Synthesis of poly(ε-caprolactone-*b*-isobutylene-*b*-ε-caprolactone) triblock

Figure 4 shows the triblock synthesis. HO-PIB-OH (M_n = 4100 g/mol, $Đ_M$ =1.2) was used as a macroinitiator.

Figure 5 shows the [1]H NMR spectrum of PCL-PIB-PCL. The signal of the methylene protons of the HO-PIB-OH macroinitiator (h) at 3.77 ppm disappeared. Signals for structural analysis included those at 3.68 and 4.33 (h, J 6.5 Hz, $–CH_2–OH$), due to the meth-

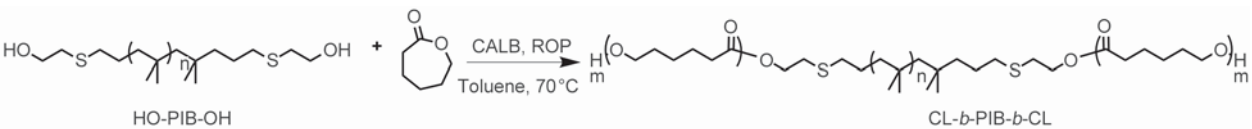

Figure 4. Synthesis of PCL-PIB-PCL. [HO-PIB-OH] = $8.13 \cdot 10^{-3}$ mol/L, [ε-CL] = 0.67 mol/L; [CALB] = $4.45 \cdot 10^{-4}$ mol/L.

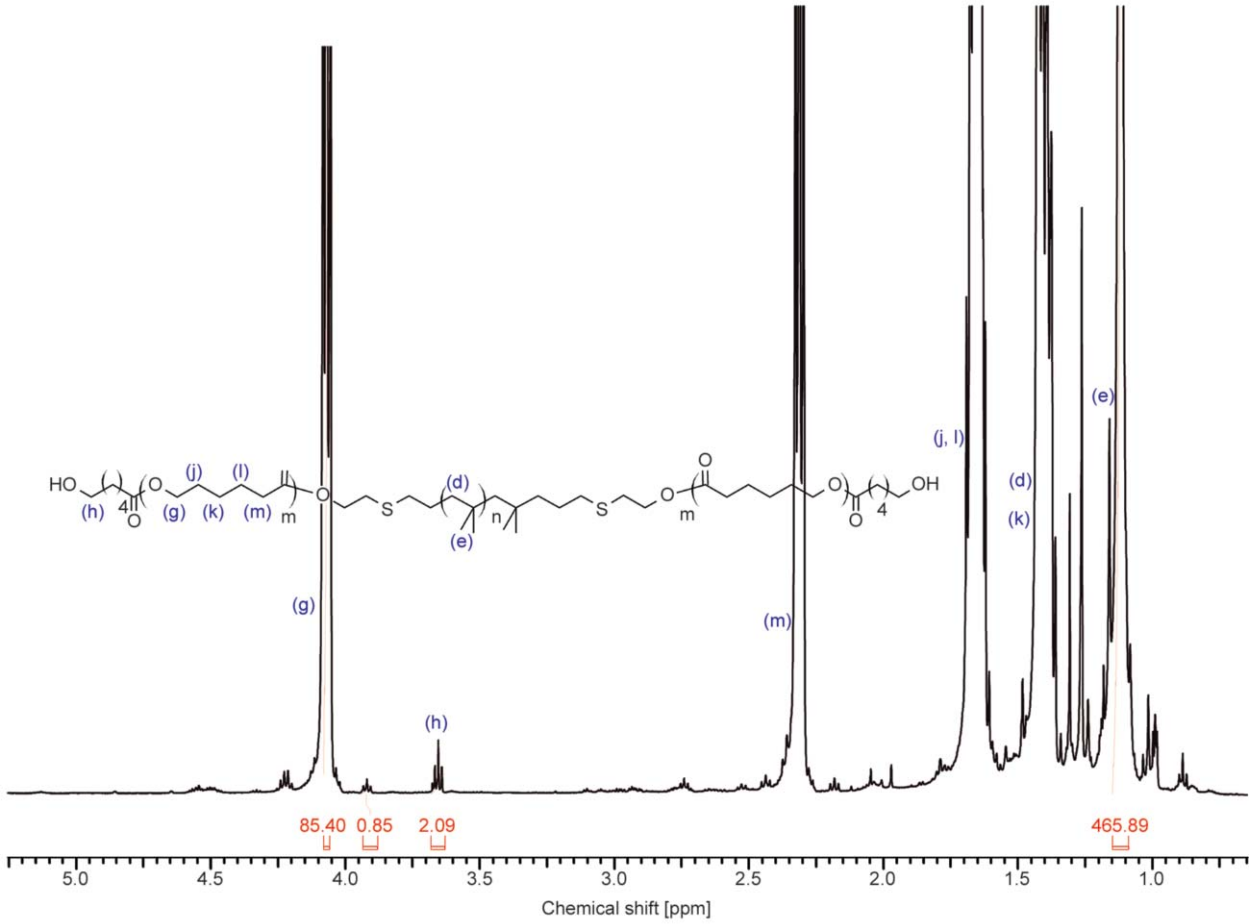

Figure 5. ^{1}H NMR spectrum PCL-PIB-PCL

ylene protons of PCL chain-end units and resonances at 4.11 ppm (g) and 2.32 ppm (m), due to the methylene protons in the PCL repeat unit. The proton resonances at δ = 1.13 ppm (e) and δ = 1.45 ppm (d) correspond to the methyl and methylene protons, respectively, of the repeat unit of PIB.

M_n = 2200 g/mol was calculated for the PCL blocks from the ratio of the integral of the methylene protons of the repeat unit of PCL (h) at δ = 3.99–4.11 ppm and the methyl protons of the repeat unit of PIB (e), and using M_n = 4090 g/mol for the starting HO-PIB-OH. Thus the PIB center block is flanked on either side by PCL outer blocks, giving a structure of PCL_{2200}-*b*-PIB_{4090}-*b*-PCL_{2200} and 52.8 wt% PCL content. The SEC traces are shown in Figure 6. SEC analysis yielded M_n = 8400 g/mol ($Đ_M$ = 1.48), in good agreement with the NMR data.

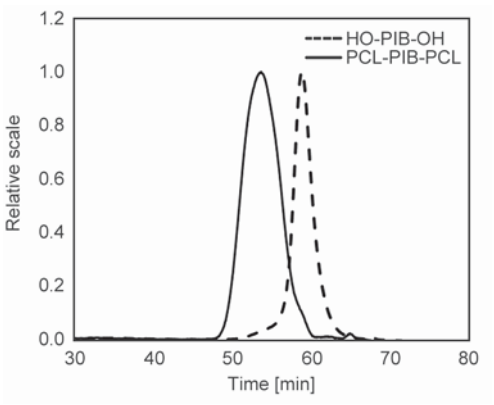

Figure 6. SEC traces of HO-PIB-OH and PCL-*b*-PIB-*b*-PCL

3.3. Phase morphology

DSC thermograms are presented in Figure 7.

The diblock copolymer exhibited the T_g of the amorphous rubbery PIB segment at T_g = –70.1 °C and another transition at 45.9 °C. The DSC of the triblock showed the PIB T_g at –67.2 °C and a very sharp transition at 51.3 °C with a shoulder at 55.1 °C. T_g = –60 °C and T_m ranging between 59–64 °C were reported in the literature for PCL [24]. In our case, the T_g transition for the PCL blocks was barely detectable at –60.2 °C These observations clearly indicate microphase-separation in the block copolymers between

the soft PIB phase and the PCL hard phases. The sharp and prominent high temperature transition in the DSC indicates that the PCL blocks in the triblock have very high crystalline fractions. This may be due to confinement by the PIB phases. We will investigate this phenomenon in more detail.

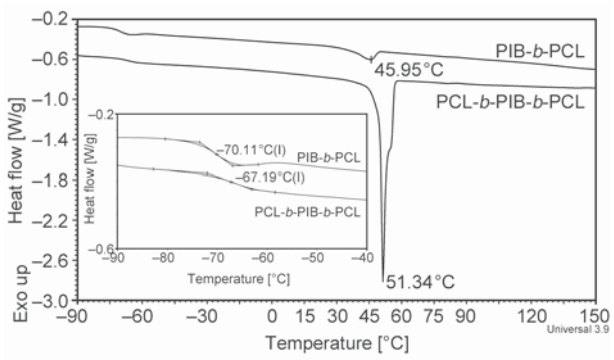

Figure 7. DSC thermograms of PIB-*b*-PCL and PCL-*b*-PIB-*b*-PCL

Figures 8a and b shows the optical images of the diblock and triblock copolymers. We have no explanation for these strange patterns: crystalline PCL normally displays the well-known 'Maltese cross' pattern [25].

The AFM images (Figures 9) are also unusual and need further investigation.

The TEM of the diblock in Figure 10a did not show clear features. The TEM of the triblock copolymer in Figure 10b indicates a lamellar structure, but the lamella thickness appears to be too large. This will require more detailed investigations. However, all images show phase-separation.

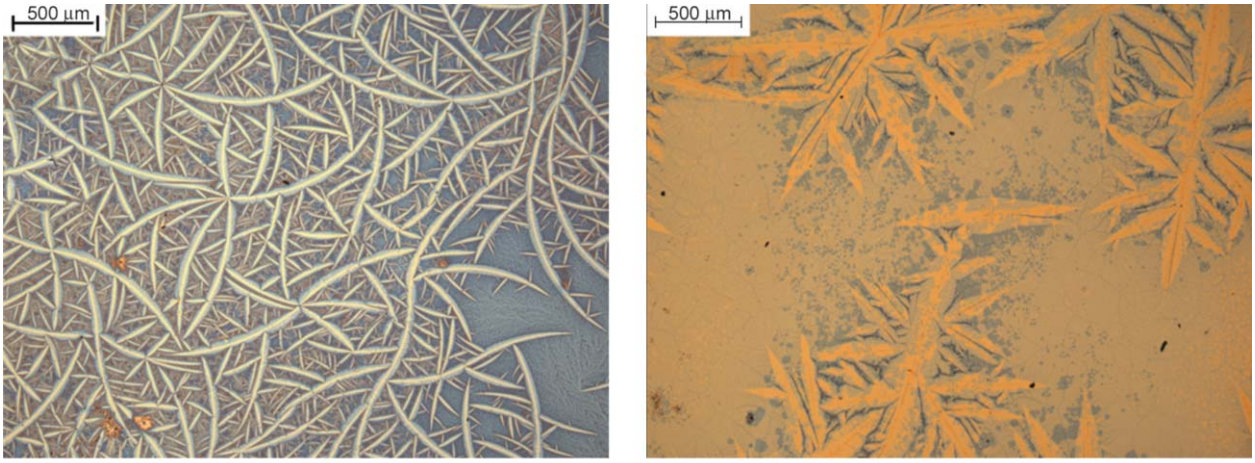

Figure 8. Optical images of (a) PIB-*b*-PCL and (b) PCL-*b*-PIB-*b*-PCL

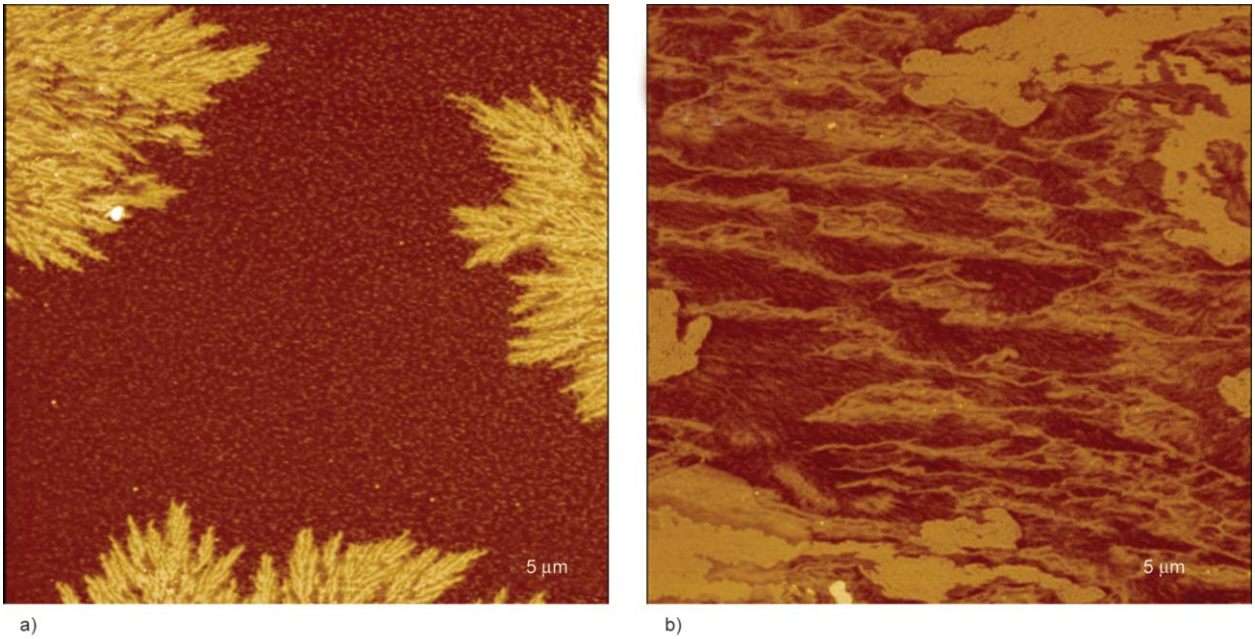

Figure 9. AFM images of (a) PIB-*b*-PCL and (b) PCL-*b*-PIB-*b*-PCL

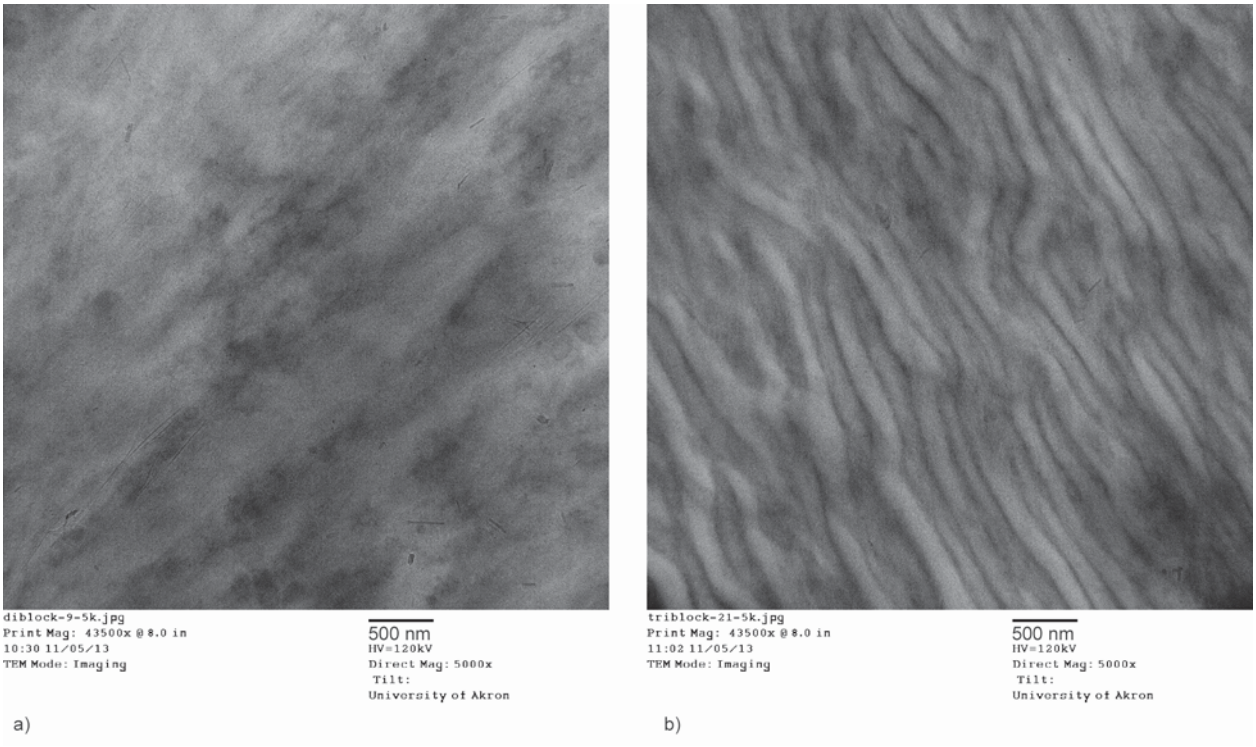

Figure 10. TEM images of (a) PIB-*b*-PCL and (b) PCL-*b*-PIB-*b*-PCL

4. Conclusions

The combination of carbocationic and enzymatic polymerization yielded PIB-*b*-PCL and PCL-*b*-PIB-*b*-PCL. The use of enzyme catalysis resulted in the metal-free synthesis of poly(caprolactone) blocks, which normally requires the use of tin or other transition metals, which are difficult to remove. This methodology can be expanded to the synthesis of other cyclic monomers to yield functional biomaterials containing degradable polyester blocks. The phase morphology of the blocks requires further investigation.

Acknowledgements

This material is based upon work supported by the National Science Foundation under DMR-0804878 and the Ohio Board of Regents. We wish to thank The Ohio Board of Regents and The National Science Foundation for funds used to purchase the NMR (CHE-0341701 and DMR-0414599) and MS (CHE-1012636 and DMR-0821313) instruments used in this work.

References

[1] Coates G. W., Hillmyer M. A.: A virtual issue of *macromolecules:* 'Polymers from renewable resources'. Macromolecules, **42**, 7987–7989 (2009).
DOI: 10.1021/ma902107w

[2] Albertsson A-C., Varma I. K.: Recent developments in ring opening polymerization of lactones for biomedical applications. Biomacromolecules, **4**, 1466–1486 (2003).
DOI: 10.1021/bm034247a

[3] Kamber N. E., Jeong W., Waymouth R. M., Pratt R. C., Lohmeijer B. G. G., Hedrick J. L.: Organocatalytic ring-opening polymerization. Chemical Reviews, **107**, 5813–5840 (2007).
DOI: 10.1021/cr068415b

[4] Puskas J. E., Chen Y., Dahman Y., Padavan D.: Polyisobutylene-based biomaterials. Journal of Polymer Science Part A: Polymer Chemistry, **42**, 3091–3109 (2004).
DOI: 10.1002/pola.20114

[5] Pinchuk L., Wilson G. J., Barry J. J., Schoephoerster R. T., Parel J-M., Kennedy J. P.: Medical applications of poly(styrene-block-isobutylene-block-styrene) ('SIBS'). Biomaterials, **29**, 448–460 (2008).
DOI: 10.1016/j.biomaterials.2007.09.041

[6] Puskas J. E., Muñoz-Robledo L. G., Hoerr R. A., Foley J., Schmidt S. P., Evancho-Chapman M., Dong J., Frethem C., Haugstad G.: Drug-eluting stent coatings. Wiley Interdisciplinary Reviews: Nanomedicine and Nanobiotechnology, **1**, 451–462 (2009).
DOI: 10.1002/wnan.38

[7] Puskas J. E., Hoerr R. A.: Drug release from novel rubbery coatings. Macromolecular Symposia, **291–292**, 326–329 (2010).
DOI: 10.1002/masy.201050538

[8] Ranade S. V., Miller K. M., Richard R. E., Chan A. K., Allen M. J., Helmus M. N.: Physical characterization of controlled release of paclitaxel from the TAXUS™ Express²™ drug-eluting stent. Journal of Biomedical Materials Research Part A, **71**, 625–634 (2004). DOI: 10.1002/jbm.a.30188

[9] Sipos L., Zsuga M., Deák Gy.: Synthesis of poly(L-lactide)-*block*-polyisobutylene-*block*-poly(L-lactide), a new biodegradable thermoplastic elastomer. Macromolecular Rapid Communications, **16**, 935–940 (1995). DOI: 10.1002/marc.1995.030161209

[10] Kwon Y., Faust R., Chen C. X., Thomas E. L.: Synthesis and characterization of poly(isobutylene-*b*-pivalolactone) diblock and poly(pivalolactone-*b*-isobutylene-*b*-pivalolactone) triblock copolymers. Macromolecules, **35**, 3348–3357 (2002). DOI: 10.1021/ma011739b

[11] Storey R. F., Brister L. B., Sherman J. W.: Structural characterization of poly(ε-caprolactone) and poly(ε-caprolactone-*b*-isobutylene-*b*-ε-caprolactone) block copolymers by MALDI-TOF mass spectrometry. Journal of Macromolecular Science Part A: Pure and Applied Chemistry, **38**, 107–122 (2001). DOI: 10.1081/MA-100103337

[12] Kim M. S., Faust R.: Synthesis of poly(ε-caprolactone-*b*-isobutylene) diblock copolymer and poly(ε-caprolactone-*b*-isobutylene-*b*-ε-caprolactone) triblock copolymer. Polymer Bulletin, **48**, 127–134 (2002). DOI: 10.1007/s00289-002-0019-x

[13] Iván B., Kennedy J. P.: Living carbocationic polymerization. XXX. One-pot synthesis of allyl-terminated linear and tri-arm star polyisobutylenes, and epoxy- and hydroxy-telechelics therefrom. Journal of Polymer Science Part A: Polymer Chemistry, **28**, 89–104 (1990). DOI: 10.1002/pola.1990.080280107

[14] Albarran A. A., Silantyeva E., Seo K. S., Puskas J. E.: Synthesis of functionalized polyisobutylenes using the propylene epoxide/$TiCl_4$ initiating system. Polymer Chemistry, **5**, 4710–4714 (2014). DOI: 10.1039/C4PY00363B

[15] Castano M., Becker M. L., Puskas J. E.: New method for the synthesis of fully aliphatic telechelic α,ω-dihydroxy-polyisobutylene. Polymer Chemistry, **5**, 5436–5442 (2014). DOI: 10.1039/C4PY00569D

[16] Kumar A., Gross R. A.: *Candida antartica* Lipase B catalyzed polycaprolactone synthesis: Effects of organic media and temperature. Biomacromolecules, **1**, 133–138 (2000). DOI: 10.1021/bm990510p

[17] Bankova M., Kumar A., Impallomeni G., Ballistreri A., Gross R. A.: Mass-selective lipase-catalyzed poly(ε-caprolactone) transesterification reactions. Macromol-ecules, **35**, 6858–6866 (2002). DOI: 10.1021/ma0202282

[18] Kobayashi S., Uyama H., Kimura S.: Enzymatic polymerization. Chemical Reviews, **101**, 3793–3818 (2001). DOI: 10.1021/cr9901211

[19] Kumar A., Gross R. A., Wang Y., Hillmyer M. A.: Recognition by lipases of ω-hydroxyl macroinitiators for diblock copolymer synthesis. Macromolecules, **35**, 7606–7611 (2002). DOI: 10.1021/ma020060k

[20] Xiang S., Zhang Q., Zhang G., Jiang W., Wang Y., Zhou H., Li Q., Tang J.: Facile synthesis of block copolymers by tandem ROMP and eROP from esters precursors. Biomacromolecules, **15**, 3112–3118 (2014). DOI: 10.1021/bm500723k

[21] Jiang W., An N., Zhang Q., Xiang S., Bai Z., Han H., Li X., Li Q., Tang J.: One-pot combination of eROP and ROMP for the synthesis of block copolymers. Macromolecular Chemistry and Physics, **216**, 2107–2114 (2015). DOI: 10.1002/macp.201500313

[22] Baśko M., Kubisa P.: Polyester oligodiols by cationic AM copolymerization of L,L-lactide and ε-caprolactone initiated by diols. Journal of Polymer Science Part A: Polymer Chemistry, **45**, 3090–3097 (2007). DOI: 10.1002/pola.22065

[23] Puskas J. E., Chen Y., Kulbaba K., Kaszas G.: Effect of the molecular weight and architecture on the size and glass transition of arborescent polyisobutylenes. Journal of Polymer Science Part A: Polymer Chemistry, **44**, 1770–1776 (2006). DOI: 10.1002/pola.21273

[24] Wunderlich B., Bodily D. M., Kaplan M. H.: Theory and measurements of the glass–transformation interval of polystyrene. Journal of Applied Physics, **35**, 95–102 (1964). DOI: 10.1063/1.1713105

[25] Chen H-L., Li L-J., Ou-Yang W-C., Hwang J. C., Wong W-Y.: Spherulitic crystallization behavior of poly(ε-caprolactone) with a wide range of molecular weight. Macromolecules, **30**, 1718–1722 (1997). DOI: 10.1021/ma960673v

eXPRESS Polymer Letters Vol.10, No.8 (2016) 701–709
Available online at www.expresspolymlett.com
DOI: 10.3144/expresspolymlett.2016.63

Molecular orientation behavior of isotactic polypropylene under uniaxial stretching by rheo-Raman spectroscopy

T. Kida, Y. Hiejima, K.-H. Nitta*

Department of Chemical and Materials Science, Kanazawa University, Kakuma Campus, 920-1192 Kanazawa, Japan

Received 8 January 2016; accepted in revised form 12 March 2016

Abstract. The molecular orientation behavior of isotactic polypropylene (iPP) is investigated by using *in situ* Raman spectroscopy under tensile tests. A versatile method of the tilt-angle correction for the orientation parameters is newly developed, where the molecular orientation in highly oriented specimens is assumed to be entropically favorable. The real-time changes of orientation parameters and orientation distribution functions are determined for the molecular chain axis of iPP during uniaxial stretching. The molecular orientation remains random in the elastic region, and increases after the first yield point. In the yielding region, a broad distribution of orientation toward an intermediate angle of 30–70° from the stretching direction is observed. This is interpreted as reorientation of the crystalline chains being hindered by rigid, bulky lamellar cluster units. After the yielding region, orientation toward the stretching direction proceeds rapidly, approaching highly oriented states.

Keywords: *mechanical properties, Raman spectroscopy, molecular orientation, isotactic-polypropylene*

1. Introduction

Isotactic polypropylene (iPP) is a semi-crystalline polymer which exhibits high strength, workability and transparency and has low cost. iPP is commonly used in films, plastic moldings and structural materials. The molecular orientation of the crystalline and amorphous chains greatly influences the mechanical properties of such semi-crystalline polymers [1, 2]. For example, a high degree of orientation along the stretching axis is required for fabricating very strong fibers.

The molecular orientation of semi-crystalline polymers has been investigated by various experimental methods. Birefringence is a simple and fundamental technique which gives a qualitative measure of the overall orientation in bulk specimens, including the crystalline and amorphous regions [3, 4]. Wide-angle X-ray diffraction (WAXD) basically provides the distribution of molecular orientation of the crystalline chain, while that of the amorphous chains are also determined by the synchrotron WAXD measurements [5, 6]. Infrared (IR) spectroscopy can separately evaluate the average molecular orientations of both crystalline and amorphous chains [7, 8], using its dichroic ratio. However, IR spectroscopy is unsuitable for thick samples such as plastic molds and structural materials, then, it has been applied for the sliced samples, because of high extinction coefficients in the IR region.

Recent improvements in laser light sources, optical devices and detectors have promoted the application of Raman spectroscopy across various research fields. Raman spectroscopy is a vibrational spectroscopy technique with several advantages over the above-mentioned techniques. First, its sufficiently short acquisition time enables measurements to be carried out *in situ* [9–11]. The stress relaxation upon unloading polymeric samples can result in appreciable structural changes, including molecular orientation. Rheo-Raman spectroscopy which is the simultane-

*Corresponding author, e-mail: hiejima@se.kanazawa-u.ac.jp

ous measurement of Raman spectra and mechanical tests enables real-time monitoring of the microscopic deformation mechanism. Second, polarized Raman spectroscopy detects the molecular orientations of both crystalline and amorphous chains. Raman spectroscopy has been used to evaluate the molecular orientations of crystalline and amorphous chains in iPP films [12, 13], and *in situ* micro-Raman spectroscopy has also been applied to investigate the microscopic mechanism of iPP during uniaxial deformation [9]. Third, the distribution of molecular orientations is determined by calculating the orientation distribution function (ODF) from the orientation parameters $\langle P_2 \rangle$ and $\langle P_4 \rangle$ [14, 15]. In contrast, IR spectroscopy can only provide the orientation function as a measure of the average orientation. Finally, since typical optical setups for the scattering measurements are more flexible than those for the transmission measurements, Raman spectroscopy can provide non-contact and non-destructive technique to probe the molecular orientation of plastic molds without any pretreatments.

The crystalline chain of iPP has a 3_1 helical structure [16], so the principal axis of the Raman tensor is not parallel to the molecular chain axis [13, 17]. A correction for the tilt angle between these two axes is required to evaluate the orientation of the molecular chains. Tanaka and Young reported tilt-angle corrections using WAXD measurements [13, 18], and obtained ODF values using the 1000 cm^{-1} band of highly drawn iPP. The ODF values of poly(lactic acid), which also forms helical chains in the crystalline phase, have been determined from highly drawn samples [13, 18, 19].

In the current study, rheo-Raman spectroscopy is used to elucidate the molecular orientation behavior of iPP during elongation. A new method for correcting the tilt angle between the molecular axis and the principal axis of the Raman tensor is applied. ODF values and orientation parameters for the crystalline chains of iPP are obtained. The microscopic mechanism of deformation of iPP under uniaxial tensile testing is discussed, by comparing the current results with previous results for high-density polyethylene (HDPE) [10, 11].

2. Methods

2.1. Sample and apparatus

Ziegler-Natta-catalyzed homo iPP pellets ($M_w = 4.9 \cdot 10^5$, $M_w/M_n = 4.4$) supplied by Union Polymer Material Co., Ltd (Dalian, China, Grade: YD101-A) were used in this study. The pellets were compression molded in a hot press at 230 °C and 20 MPa for 5 min, to prepare a sheet with thickness of about 1 mm. The sample sheet was removed from the hot press, quenched in boiled water at 100 °C. The density of the sample was determined to be 908 kg m^{-3} by the Archimedes method. Its volumetric crystallinity was determined to be 66%, where the densities of the amorphous and crystalline regions were assumed to be $\rho_a = 854$ and $\rho_c = 936$ kg m^{-3}, respectively [20]. Test specimens for tensile tests were cut out of the sample sheet with a notch-shaped die (2 mm gauge length, 4 mm width in Figure 1).

The rheo-Raman spectroscopy apparatus is shown schematically in Figure 2. A custom-made tensile tester with a double-drawing mechanism was installed in the Raman spectroscopic apparatus, the details of which are reported elsewhere [10, 11]. Laser light from a DPSS laser (LASOS, Jena, Germany, 637.9 nm, 200 mW) was monochromated with a laser line filter, and irradiated into the notched portion of the specimen, with a spot size of 1 mm in diameter. The elongation speed was set to 1 mm/min, and the stretching temperature was 20 °C. The scattered light was collected with a pair of convex lenses, where the excitation light was removed with a Raman long-pass filter. A charge-coupled device camera equipped with a monochromator (PIXIS100 and SpectraPro 2300i, Princeton Instruments, Trenton, USA, NJ) was used as the detector. For polarized Raman spectroscopy, a pair of wire-grid polarizers was inserted as the polarizer and

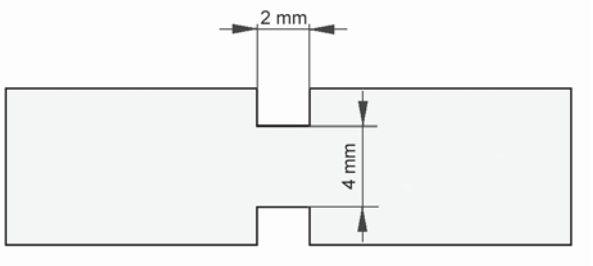

Figure 1. Schematic illustraion of sample specimen

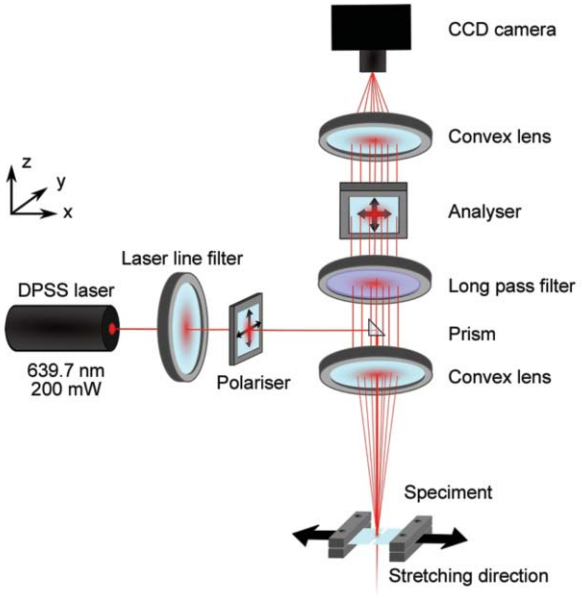

Figure 2. Schematic illustration of rheo-Raman spectroscopic apparatus

analyzer. The polarized spectra were collected in the *zz*, *yz*, and *yy* geometries and accumulated 10 times with an exposure time of 500 ms. It is noteworthy that the total exposure time of 5 s can be shortened up to ~1 s, with maintaining sufficient signal to noise ratio.

2.2. *In situ* Raman spectroscopy

Typical *in situ* polarized Raman spectra are shown in Figure 3. Assignments of the Raman bands of iPP are listed in Table 1 [13, 21]. The Raman spectra of undrawn specimens were independent of polarization, indicating that the molecular orientation was random. After elongation, the anti-symmetric (975 cm^{-1}) and symmetric (809 cm^{-1}) stretching modes were strongly dependent on the polarization conditions, suggesting that highly oriented states were attained. The Raman spectra were fitted with a sum of Voigt functions using a nonlinear Levenberg-Marquardt method, and the areas for the two peaks were determined. The errors of the peak areas in the curve fitting were less than ±2.0% for the 809 cm^{-1} band, and ±4.0% for the 975 cm^{-1} band.

Table 1. Vibrational and phase assignments for the Raman spectrum of iPP [13, 21]

Peak position [cm^{-1}]	Vibrational mode*	Phase	Raman tensor form
809	v_s(C–C) + r(CH_2)	Crystalline	A
830	v(C–C)	Amorphous	A
840	r(CH_2)	Crystalline + Amorphous	A
975	v_{as}(C–C) + r(CH_3)	Crystalline	A

*v: stretching vibration (*as*: anti-symmetric, *s*: symmetric), r: rocking vibration

2.3. Orientation parameters

The orientation parameters $\langle P_2 \rangle$ and $\langle P_4 \rangle$ which represented the molecular orientation were defined as given by Equations (1) and (2):

$$\langle P_2 \rangle = \frac{3\langle \cos^2\theta \rangle - 1}{2} \tag{1}$$

$$\langle P_4 \rangle = \frac{35\langle \cos^4\theta \rangle - 30\langle \cos^2\theta \rangle + 3}{8} \tag{2}$$

where θ denotes the angle between the principal axis of the Raman tensor and the stretching axis. The orientation parameters were obtained from the intensities of the polarized Raman spectra as defined by Equations (3)–(6) [15, 19, 22–24]:

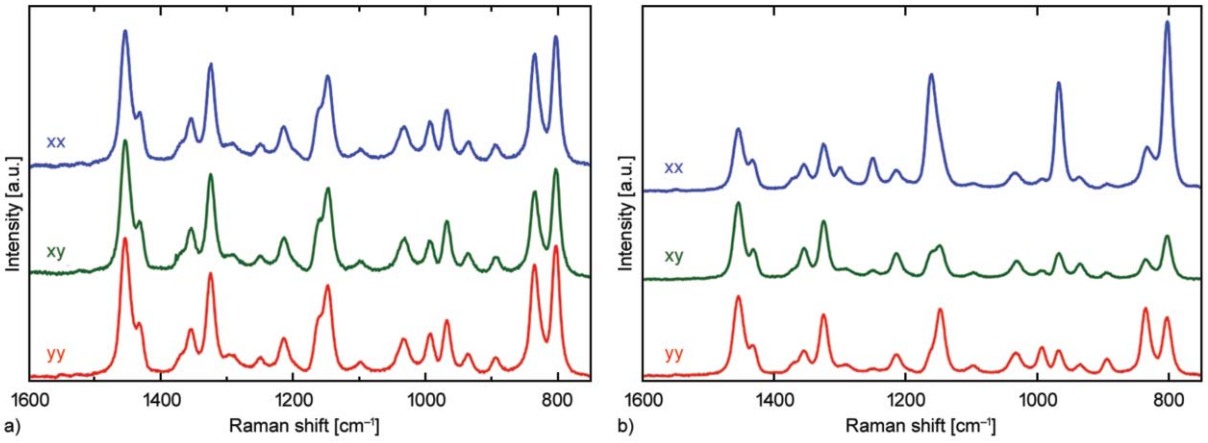

Figure 3. *In situ* polarized Raman spectra of iPP at (a) $\varepsilon = 0$ and (b) $\varepsilon = 8$. The polarization conditions are attached to each spectrum

$$I_{yy} = b\left(\frac{8a^2+4a+3}{15} + 2\langle P_2\rangle\frac{4a^2-a-3}{21} + 3\langle P_4\rangle\frac{a^2-2a+1}{21}\right) \quad (3)$$

$$I_{xx} = b\left(\frac{8a^2+4a+3}{15} - 4\langle P_2\rangle\frac{4a^2-a-3}{21} + 8\langle P_4\rangle\frac{a^2-2a+1}{35}\right) \quad (4)$$

$$I_{xy} = b\left(\frac{a^2-2a+1}{15} + \langle P_2\rangle\frac{a^2-2a+1}{21} - 4\langle P_4\rangle\frac{a^2-2a+1}{35}\right) \quad (5)$$

with

$$\frac{I_{xy}}{I_{xx}} = \frac{a^2-2a+1}{8a^2+4a+3} \quad (6)$$

where I_{ij} denotes the integrated intensity for the *i*-polarized excitation and *j*-polarized scattered light. The terms *a* and *b* were associated with the principal elements of the Raman tensor [15, 22].

The crystalline chain of iPP has C_3 symmetry, because of its 3_1 helical conformation. Thus, the forms of the Raman tensor were classified mainly as type A or E [15]. Raman bands classified as type A can be used to calculate the orientation parameters [13, 22–24], so the Raman bands at 809 and 975 cm^{-1} were used. Both of these are classified as type A, and were sufficiently strong to calculate the orientation parameters.

2.4. Tilt-angle correction

The orientation parameters obtained by solving Equations (3)–(6) provided information on the orientation of the principal axis of the Raman tensor, but not on the orientation of the molecular chain axis. Given that 3_1 helical chains were formed in the crystalline phase of iPP, a correction for the tilt angle between the principal and molecular axes was required [13, 17, 19]. The *l*-th orientation parameters $\langle P_l^{chain}\rangle$ corrected for the tilt angle β can be written as shown in Equation (7) [13, 17]:

$$\langle P_l^{chain}\rangle = \frac{\langle P_l\rangle}{P_l(\cos\beta)} \quad (7)$$

where $P_l(x)$ is the *l*-th Legendre polynomial.

The values of the tilt-angle β of several Raman bands of iPP had been determined by using the results of the WAXD experiments [13]. They had successfully estimated the value of $\langle P_2^{chain}\rangle$ for drawn specimens of iPP for the Raman band at 998 cm^{-1}, though they had failed to use the Raman band at 810 and 1221 cm^{-1} [13]. To determine the value of β solely from the Raman spectra in a self-consistent manner, we assumed that the molecular orientation at high extensional ratio was described by an ideal uniaxial orientation around the stretching direction; $\langle P_4^{chain}\rangle$ and $P_4(\cos\beta)$ were assumed to be replaced by their entropically favorable values $\langle P_4^{chain}\rangle_{mp}$ and $P_{4,mp}(\cos\beta)$, respectively [11, 24]. In fact, the values of $\langle P_4^{chain}\rangle$ at high extensional ratios are very close to that of $\langle P_4^{chain}\rangle_{mp}$ for HDPE [11, 24], iPP [13], and poly(ethylene terephthalate) [24]. Then, at high extensional rates, Equation (7) for $l = 2$ and 4 can be written as Equations (8) and (9):

$$\langle P_2^{chain}\rangle = \frac{\langle P_2\rangle}{P_2(\cos\beta)} \quad (8)$$

$$\langle P_4^{chain}\rangle = \frac{\langle P_4\rangle}{P_{4,mp}(\cos\beta)} \quad (9)$$

respectively. The most-probable values $\langle P_4\rangle_{mp}$ were determined to maximize the information entropy, and approximately written as the polynomials of $\langle P_2\rangle$ as Equations (10) and (11) [24, 25]:

$$\langle P_4\rangle_{mp} = -0.083\langle P_2\rangle + 1.366\langle P_2\rangle^2 - 1.899\langle P_2\rangle^3 + 1.616\langle P_2\rangle^4 \quad (10)$$

for positive $\langle P_2\rangle$ values, and

$$\langle P_4\rangle_{mp} = -0.052\langle P_2\rangle + 1.574\langle P_2\rangle^2 + 3.968\langle P_2\rangle^3 + 8.058\langle P_2\rangle^4 \quad (11)$$

for negative $\langle P_2\rangle$ values. By combining Equations (8)–(11), the tilt angle β was estimated from the experimental $\langle P_2\rangle$ and $\langle P_4\rangle$ at high extensional ratios. Thus, Equation (7) with the obtained value of β gives the tilt-angle correction for the orientation parameters. It is noteworthy that the present method provides the corrected orientation parameters from a set of polarized Raman spectra of specimens under stretching with no auxiliary experiments.

2.5. Orientation distribution function (ODF)

The ODF $N(\theta)$ which represented the angular distribution of the molecular orientation was defined asby Equation (12) [15, 25]:

$$N(\theta) = \sum_{l=0}^{\infty} \left(\frac{2l+1}{2} \right) \langle P_l^{\text{chain}} \rangle P_l(\cos\theta) \tag{12}$$

Although the polarized Raman spectrum gives only two orientation parameters ($\langle P_2^{\text{chain}} \rangle$ and $\langle P_4^{\text{chain}} \rangle$), the orientation parameters at higher ranks can also be determined by maximizing the information entropy [13, 25]. The most probable orientation distribution function was described asby Equation (13) [13, 25]:

$$N(\theta) = \frac{\exp[\lambda_2 P_2(\cos\theta) + \lambda_4 P_4(\cos\theta)]}{\int_0^{\pi} \sin\theta d\theta \, \exp[\lambda_2 P_2(\cos\theta) + \lambda_4 P_4(\cos\theta)]} \tag{13}$$

where the Lagrange multipliers λ_2 and λ_4 are determined to satisfy the following two constraints, described by Equations (14) and (15) for the experimental values of $\langle P_2^{\text{chain}} \rangle$ and $\langle P_4^{\text{chain}} \rangle$:

$$\langle P_2^{\text{chain}} \rangle = \int_0^{\pi} \sin\theta d\theta \, P_2(\cos\theta) N(\theta) \tag{14}$$

$$\langle P_4^{\text{chain}} \rangle = \int_0^{\pi} \sin\theta d\theta \, P_4(\cos\theta) N(\theta) \tag{15}$$

3. Results and discussion

Figure 4 shows the strain dependences of the orientation parameters for the principal axis of the Raman tensors of the symmetric and anti-symmetric C–C stretching modes. While the orientation parameters show similar strain dependence, the values for the 809 cm^{-1} band are substantially smaller than those for the 975 cm^{-1} band.

Table 2. Tilt angle β calculated from Raman spectroscopy and WAXD data [13]

Raman band [cm^{-1}]	β (Raman)	β (WAXD)
809	29.2	~28.0
975	16.0	16.6

In Table 2, the tilt angles β obtained by the tilt-angle correction with Equations (8) and (9) are compared with those previously determined by WAXD [13]. These values agree well with each other, suggesting that the present analysis can be safely applied for the tilt-angle correction of iPP.

In Figure 5, the orientation parameters for the molecular chain are obtained with the tilt-angle correction with Equation (7). The values of $\langle P_2^{\text{chain}} \rangle$ and $\langle P_4^{\text{chain}} \rangle$ for the Raman band at 809 cm^{-1} agree well with those for the 975 cm^{-1} band. This suggests that the apparent difference in the orientation parameters in Figure 4 is caused by the tilt angle. The slight difference in the orientation parameters between these two bands seems to result from uncertainty in the curve fitting. This is because fitting of the 809 cm^{-1} band is slightly affected by a nearby weak broad peak of the amorphous phase [9]. The consistency of the orientation parameters and the close agreement of tilt angles demonstrate that the present tilt angle correction gives $\langle P_2^{\text{chain}} \rangle$ and $\langle P_4^{\text{chain}} \rangle$ solely from a set of rheo-Raman spectra in a self-consistent method.

In the elastic region, $\langle P_2^{\text{chain}} \rangle$ remains almost zero, indicating that the orientation of the crystalline chain remains random. While the macroscopic stress loaded

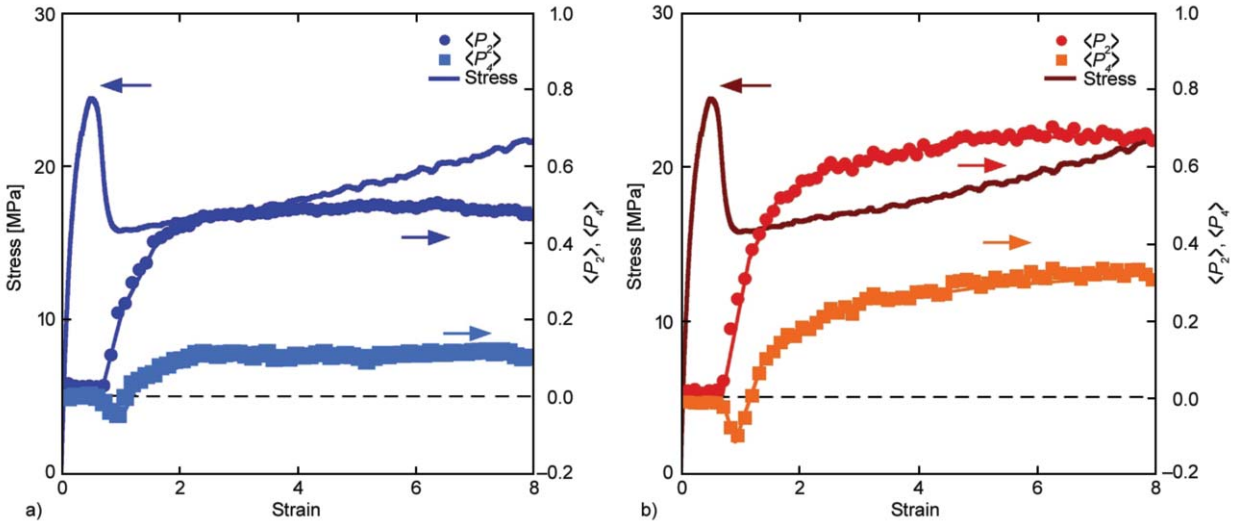

Figure 4. Stress–strain curves and strain dependences of the orientaion parameters for the principal axis of the Raman tensor of the Raman bands at (a) 809 and (b) 975 cm^{-1}

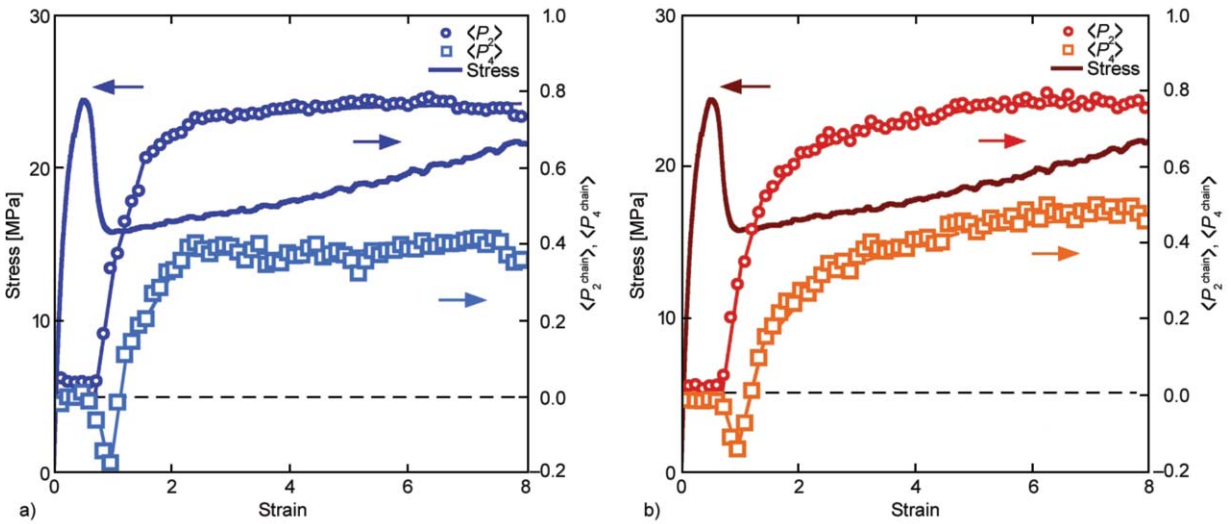

Figure 5. Stress–strain curves and strain dependences of the orientaion parameters for the molecular chain axis calculated from the Raman bands at (a) 809 and (b) 975 cm^{-1}

on the specimen sharply increases with increasing strain, no orientational change is observed for the crystalline chains. This suggests that microscopic deformation takes place only in the amorphous phase. The amorphous phase in spherulites is reportedly mainly deformed in the elastic region [26, 27]. Recent *in situ* micro-SAXS measurements indicate that the thickness of the amorphous layers in spherulites is drastically changed; thickening and thinning of the amorphous layers in the polar and equatorial zones, respectively [28]. The inhomogeneous changes in the amorphous phase in spherulites have been assigned as the dominant mechanism during elastic deformation.

$\langle P_2^{chain} \rangle$ begins to increase after the first yield point (the maximum point of stress at around a strain of 0.5), and then sharply increases after the yielding region. This behavior of $\langle P_2^{chain} \rangle$ indicates that the crystalline chains are oriented toward the stretching direction after yielding. In the strain-hardening region, $\langle P_2^{chain} \rangle$ reaches an asymptotic value of ~0.8. The strain dependence of $\langle P_2^{chain} \rangle$ under uniaxial stretching is in good agreement with previous results from *in situ* IR spectroscopy studies, [7, 29] and Raman spectroscopy results of drawn samples [9, 13].

While the values of $\langle P_4^{chain} \rangle$ remain constant in the elastic region, $\langle P_4^{chain} \rangle$ decreases with increasing strain and exhibits a minimum in the yielding region. This behavior of $\langle P_4^{chain} \rangle$ during yielding has also been observed for HDPE. [10, 11] After the yielding region, $\langle P_4^{chain} \rangle$ shows similar strain dependence with that of $\langle P_2^{chain} \rangle$. The values of $\langle P_4^{chain} \rangle$ at high extensional ratios are also consistent with those of highly drawn iPP films and fibers [13, 30].

Figure 6 shows the ODF values calculated from the orientation parameters for the 975 cm^{-1} band. In the elastic region, the ODF is constant irrespective of the polar angle, indicating that the crystalline chain has a random orientation. In the yielding region, where $\langle P_4^{chain} \rangle$ shows a minimum, the ODF shows a broad peak at an intermediate angle of $\theta = 30–70°$ from the stretching direction. This orientational behavior during yielding has also been observed for HDPE [10, 11, 5]. It has been interpreted as the orientation of crystalline chains being hindered by rigid and bulky stacked lamellae (lamellar cluster units) [10, 11, 5]. The interpretation of lamellar cluster units appears to also be valid for iPP, because these units have also been observed in iPP [31]. The peak of the ODF at

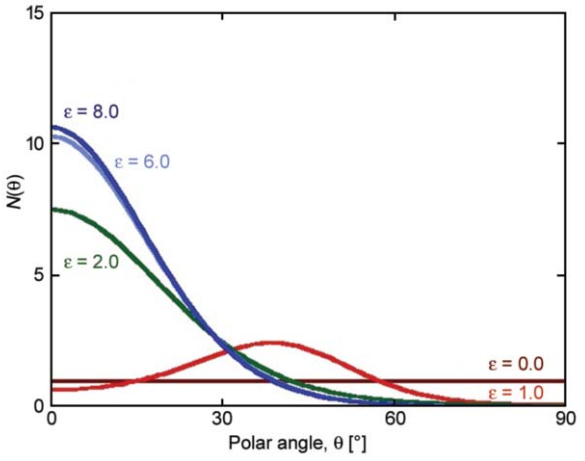

Figure 6. Orientation distribution functions of iPP at various strains

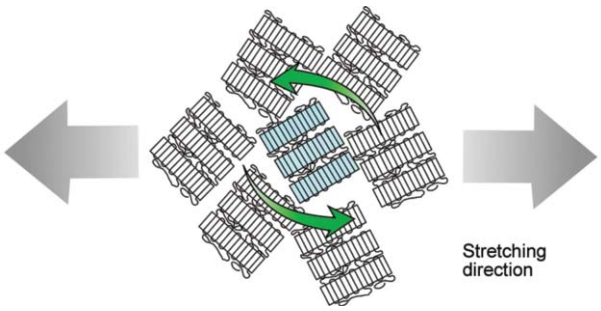

Figure 7. Schematic illustration of reorientation of the lamellar cluster units in the yielding region

30–70° for iPP in the yielding region is slightly shaper than that for HDPE, which may be explained by the size of their lamellar clusters (61 nm for iPP, 40 nm for HDPE) [11, 31, 32]. Reorientation of the lamellar cluster units is considered to be the dominant mechanism of molecular orientation in the yielding region, and the orientation of the crystalline chains toward the stretching direction is suppressed because one lamellar cluster units is surrounded by other cluster units as shown in Figure 7 [33]. Therefore, the reorientation of larger units for iPP is likely to be more hindered.

In the strain-hardening region, each ODF has a prominent peak at the stretching direction, and the ODF values above $\theta = 60°$ are practically zero. These observations indicate that the crystalline chains are oriented towards the stretching direction. The unimodal distribution around the stretching direction is consistent with those of drawn iPP films and rod samples determined from WAXD experiments [34, 35].

4. Conclusions

The molecular orientation of the crystalline chains of iPP under uniaxial deformation was investigated by rheo-Raman spectroscopy. A new method of tilt-angle correction between the molecular chain axis and principal axis of the Raman tensor was proposed, and the real-time monitoring of the molecular orientation of iPP under stretching was performed. By using this method, the orientation parameters of the crystalline chain were calculated from the symmetric C–C stretching mode at 809 cm^{-1}, as well as the anti-symmetric C–C stretching mode at 975 cm^{-1}. The molecular orientation of the crystalline chains started after the first yield point, and proceeded rapidly in the yielding region. The ODF exhibited a broad peak in the yielding region, suggesting that molecular orientation was suppressed. This was attributed to the reorientation of bulky rigid lamellar cluster units being hindered by their large exclude volume. The assumption of entropically-favorable orientations for highly-stretched specimens seems to be valid in many polymeric systems. Thus, rheo-Raman spectroscopy combined with the present tilt-angle correction can be widely utilized to elucidate orientational behavior at the molecular level. This methodology is currently being applied to other semi-crystalline polymers in our laboratory.

Acknowledgements

The authors thank Dr. Takashi Uneyama from Kanazawa University for providing the software to calculate ODF values. YH is thankful for financial support by JSPS KAKENHI (Grant Number 26410221).

References

[1] Ward I. M.: Structure and properties of oriented polymers. Chapman and Hall, London (1997).

[2] Ward I. M., Sweeney J.: Mechanical properties of solid polymers. Wiley, London (2013).

[3] Satija S. K., Wang C. H.: Polarized Raman scattering studies of chain orientation in hydrostatically extruded polypropylene. The Journal of Chemical Physics, **69**, 2739–2744 (1978).
DOI: 10.1063/1.436870

[4] Lefévre T., Pellerin C., Michel P.: Characterization of molecular orientation. in 'Comprehensive analytical chemistry' (eds.: Chalmers J. M., Meier R. J.) Elsevier, Oxford, Vol **53**, 295–335 (2008).

[5] Jiang Z., Tang Y., Rieger J., Enderle H-F., Lilge D., Roth S. V., Gehrke R., Wu Z., Li Z., Men Y.: Structural evolution of tensile deformed high-density polyethylene at elevated temperatures: Scanning synchrotron small- and wide-angle X-ray scattering studies. Polymer, **50**, 4101–4111 (2009).
DOI: 10.1016/j.polymer.2009.06.063

[6] Voyiatzis G., Petekidis G., Vlassopoulos D., Kamitsos E. I., Bruggeman A.: Molecular orientation in polyester films using polarized laser raman and fourier transform infrared spectroscopies and X-ray diffraction. Macromolecules, **29**, 2244–2252 (1996).
DOI: 10.1021/ma951199g

[7] Song Y., Nitta K-H., Nemoto N.: Deformation mechanisms of polymer thin films by simultaneous kinetic measurement of microscopic infrared dichroism and macroscopic stress. Part III: Influence of morphology on molecular orientation of isotactic polypropylene films subjected to uniaxial stretching. Nihon Reoroji Gakkaishi, **31**, 131–141 (2003).
DOI: 10.1678/rheology.31.131

[8] Li H., Zhou W., Ji Y., Hong Z., Miao B., Li X., Zhang J., Qi Z., Wang X., Li L., Li Z-M.: Spatial distribution of crystal orientation in neck propagation: An *in-situ* microscopic infrared imaging study on polyethylene. Polymer, **54**, 972–979 (2013).
DOI: 10.1016/j.polymer.2012.12.012

[9] Martin J., Ponçot M., Hiver J. M., Bourson P., Dahoun A.: Real-time Raman spectroscopy measurements to study the uniaxial tension of isotactic polypropylene: A global overview of microstructural deformation mechanisms. Journal of Raman Spectroscopy, **44**, 776–784 (2013).
DOI: 10.1002/jrs.4244

[10] Kida T., Hiejima Y. Nitta K-H.: Rheo-optical Raman study of microscopic deformation in high-density polyethylene under hot drawing. Polymer Testing, **44**, 30–36 (2015).
DOI: 10.1016/j.polymertesting.2015.03.018

[11] Kida T., Oku T., Hiejima Y., Nitta K-H.: Deformation mechanism of high-density polyethylene probed by *in situ* Raman spectroscopy. Polymer, **58**, 88–95 (2015).
DOI: 10.1016/j.polymer.2014.12.030

[12] Maxfield J., Stein R. S., Chen M. C.: Polarized Raman studies of crystalline and amorphous orientation in polyethylene. Journal of Polymer Science Polymer Physics Edition, **16**, 37–48 (1978).
DOI: 10.1002/pol.1978.180160104

[13] Tanaka M., Young R. J.: Molecular orientation distributions in the crystalline and amorphous regions of uniaxially oriented isotactic polypropylene films determined by polarized Raman spectroscopy. Journal of Macromolecular Science Part B: Physics, **44**, 967–991 (2005).
DOI: 10.1080/00222340500323599

[14] Lapersonne P., Bower D. I., Ward I. M.: Molecular orientation and conformational changes due to uniaxial-planar deformation of poly(ethylene terephthalate) films. Polymer, **33**, 1277–1283 (1992).
DOI: 10.1016/0032-3861(92)90774-Q

[15] Bower D. I.: Investigation of molecular orientation distributions by polarized Raman scattering and polarized fluorescence. Journal of Polymer Science Part B: Polymer Physics Edition, **10**, 2135–2153 (1972).
DOI: 10.1002/pol.1972.180101103

[16] Moore E. P. Jr.: Polypropylene handbook. Hanser, Cincinnati (1996).

[17] Lovell R., Mitchell G.: Molecular orientation distribution derived from an arbitrary reflection. Acta Crystallographica Section A, **37**, 135–137 (1981).
DOI: 10.1107/S0567739481000247

[18] Tanaka M., Young R. J.: Molecular orientation distributions in uniaxially oriented poly(L-lactic acid) films determined by polarized Raman spectroscopy. Macromolecules, **39**, 3312–3321 (2006).
DOI: 10.1021/ma0526286

[19] Tanaka M., Young R. J.: Review polarised Raman spectroscopy for the study of molecular orientation distributions in polymers. Journal of Materials Science, **41**, 963–991 (2006).
DOI: 10.1007/s10853-006-6595-7

[20] Brandrup J., Immergut E., Grulke E. A., Abe A., Bloch D. R.: Polymer handbook. Wiley, New York (1999).

[21] Tadokoro H., Kobayashi M., Ukita M., Yasufuku K., Murahashi S., Torii T.: Normal vibrations of the polymer molecules of helical conformation. V. Isotactic polypropylene and its deuteroderivatives. The Journal of Chemical Physics, **42**, 1432–1449 (1965).
DOI: 10.1063/1.1696134

[22] Pigeon M., Prud'homme R. E., Pezolet M.: Characterization of molecular orientation in polyethylene by Raman spectroscopy. Macromolecules, **24**, 5687–5694 (1991).
DOI: 10.1021/ma00020a032

[23] Richard-Lacroix M., Pellerin C.: Novel method for quantifying molecular orientation by polarized Raman spectroscopy: A comparative simulations study. Applied Spectroscopy, **67**, 409–419 (2013).
DOI: 10.1366/12-06879

[24] Richard-Lacroix M., Pellerin C.: Accurate new method for molecular orientation quantification using polarized Raman spectroscopy. Macromolecules, **46**, 5561–5569 (2013).
DOI: 10.1021/ma400955u

[25] Bower D. I.: Orientation distribution functions for uniaxially oriented polymers. Journal of Polymer Science Polymer Physics Edition, **19**, 93–107 (1981).
DOI: 10.1002/pol.1981.180190108

[26] Nitta K-H., Takayanagi M.: Direct observation of the deformation of isolated huge spherulites in isotactic polypropylene. Journal of Materials Science, **38**, 4889–4894 (2003).
DOI: 10.1023/B:JMSC.0000004410.56145.f1

[27] Nitta K-H.: A molecular theory of stress–strain relationship of spherulitic materials. Computational and Theoretical Polymer Science, **9**, 19–26 (1999).
DOI: 10.1016/S1089-3156(98)00047-6

[28] Xiong B., Lame O., Chenal J-M., Rochas C., Seguela R., Vigier G.: *In-situ* SAXS study of the mesoscale deformation of polyethylene in the pre-yield strain domain: Influence of microstructure and temperature. Polymer, **55**, 1223–1227 (2014).
DOI: 10.1016/j.polymer.2014.02.004

[29] Song Y., Nitta K-H., Nemoto N.: Deformation mechanisms of polymer thin films by simultaneous kinetic measurement of microscopic infrared dichroism and macroscopic stress. 2. Molecular orientation during necking process of isotactic polypropylene. Macromolecules, **36**, 1955–1961 (2003).
DOI: 10.1021/ma0214254

[30] Wang X., Michielsen S.: Isotactic polypropylene morphology–Raman spectra correlations. Journal of Applied Polymer Science, **82**, 1330–1338 (2001).
DOI: 10.1002/app.1968

[31] Takayanagi M., Nitta K-H., Kojima O.: Application of lamellar clustering theory to isotactic polypropylene and direct observation of lamellar cluster morphology by electron microscopy. Journal of Macromolecular Science Part B: Physics, **42**, 1049–1059 (2003).
DOI: 10.1081/MB-120023557

[32] Nitta K-H., Takanayagi M.: Novel proposal of lamellar clustering process for elucidation of tensile yield behavior of linear polyethylenes. Journal of Macromolecular Science Part B: Physics, **42**, 107–126 (2003).
DOI: 10.1081/MB-120015754

[33] Kuriyagawa M., Nitta K-H.: Structural explanation on natural draw ratio of metallocene-catalyzed high density polyethylene. Polymer, **52**, 3469–3477 (2011).
DOI: 10.1016/j.polymer.2011.05.028

[34] Lee W. B., Wu S. Z., Song M. S.: Characterization of the orientation structure and distribution in rolled polypropylene. Journal of Materials Engineering and Performance, **5**, 637–645 (1996).
DOI: 10.1007/BF02646094

[35] Lafrance C-P., Prud'homme R. E: Characterization of the molecular orientation in highly oriented rolled polypropylene sheets by X-ray diffraction. Polymer, **35**, 3927–3935 (1994).
DOI: 10.1016/0032-3861(94)90277-1

eXPRESS Polymer Letters Vol.10, No.8 (2016) 710–720
Available online at www.expresspolymlett.com
DOI: 10.3144/expresspolymlett.2016.64

Thermal sensitivity of carbon nanotube and graphene oxide containing responsive hydrogels

E. Manek[1], B. Berke[1,2], N. Miklósi[1], M. Sajbán[1], A. Domán[1], T. Fukuda[3], O. Czakkel[2], K. László[1]*

[1]Budapest University of Technology and Economics, Department of Physical Chemistry and Materials Science, 1521 Budapest, Hungary
[2]Institut Laue Langevin, CS 20156, F - 38042 Grenoble Cedex 9, France
[3]Toyo University, Bio-Nano Research Centre, 350-8585 Kujirai, 2100 Kawagoe, Japan

Received 27 November 2015; accepted in revised form 20 March 2016

Abstract. Comparative investigations are reported on poly(*N*-isopropylacrylamide) (PNIPA) gels of various carbon nanotube (CNT) and graphene oxide (GO) contents synthesized under identical conditions. The kind and concentration of the incorporated carbon nanoparticles (CNPs) influence the swelling and stress-strain behaviour of the composites. Practically independently of the filler content, incorporation of CNPs appreciably improves the fracture stress properties of the gels. The time constant and the swelling ratio of the shrinkage following an abrupt increase in temperature of the swelling medium from 20 to 50 °C can be adjusted by selecting both the type and the amount of nanoparticle loading. This offers a means of accurately controlling the deswelling kinetics of drug release with PNIPA systems, and could be employed in sensor applications where fast and excessive shrinkage are a significant drawback. Both CNTs and GO enhance the infrared sensitivity of the PNIPA gel, thus opening a route for the design of novel drug transport and actuator systems. It is proposed that the influence of the CNPs depends more on their surface reactivity during the gel synthesis rather than on their morphology. One of the important findings of this study is the existence of a thermally conducting network in the GO filled gels.

Keywords: *polymer composites, nanocomposites, polymer gels, nanocarbon hybrids, thermal relaxation*

1. Introduction

Smart hydrogels display a marked response under changes in certain external factors [1, 2] such as composition of the solvent mixture [3], pH [4], temperature [5], photons, electric or magnetic fields [6]. Their softness, biocompatibility, excellent swelling properties and ability to deform reversibly, make them desirable as vehicles for controlled drug delivery [7, 8], sensors [9] or actuators [10]. Poly(*N*-isopropylacrylamide) (PNIPA) based hydrogels are among the most studied temperature-responsive systems, as they exhibit a volume phase transition around 34 °C, close to the temperature of the (human) body. This property can be of use in biomedical applications [11, 12]. These systems nevertheless have drawbacks, such as weak mechanical strength, which restricts applications involving repetitive loading. Composite hydrogels that incorporate nanoparticles in the matrix may offer a solution. Nanoparticles can either be physically trapped within the hydrogel matrix or cross-linked into the network structure by surface functionalities, resulting in nanocomposite materials that possess not only improved mechanical strength but also well-defined optical, thermal, electronic, magnetic, etc. properties [13].

The outstanding mechanical and conductive properties of carbon nanoparticles (CNPs), together with their unique structure and low density, place them among the most common fillers. Carbon nanofiber and carbon nanotubes (CNT) [14–20] as well as graphene

*Corresponding author, e-mail: klaszlo@mail.bme.hu

and its derivatives [21–24], mainly graphene oxide (GO), have attracted marked interest in the last few years. In biomedical applications, however, the uncertainty surrounding the toxicity of CNTs [14] could affect choices of nanocarbon filler. GO, by contrast, is reported to be non-toxic and highly biocompatible [14].

In addition to mechanical reinforcement, the strong light absorption of nanocarbons can add new functional sensitivity to composite gels [25]. Fast reversible optical response has been observed under near infrared (NIR) laser excitation in CNT [26, 27] and GO [25] containing composite PNIPA hydrogels. NIR irradiation causes strong warming of the GO composite gels, while in hydrogels without GO no heating is observed [25].

CNP containing composite systems have been widely investigated in the recent years. In most cases, a synergetic effect is clearly observed upon incorporation of nanofillers into a polymer matrix, although in certain cases negative synergy has been reported. The preparation process and the type of carbon filler used determine the interactions between the filler particles as well as between the fillers and the polymer matrix [28]. Investigations regarding CNT [29–31] and GO [32–34] containing PNIPA based composite systems show improved mechanical properties (elastic modulus and compressive strength). As these gels were investigated with a variety of cross-link densities and/or with different co-monomers, as well as diverse conditions of synthesis, it is not possible to evaluate the effects of the different nanoparticles.

In this paper we describe results from CNT and GO containing PNIPA gels synthesized under identical conditions. This allows a direct comparison of the macroscopic (swelling and stress-strain behaviour) and microscopic (scanning electron microscopic) properties of these systems. The application related performance of these composites is characterized by their infrared sensitivity and the kinetic response of their volume after an external temperature jump.

2. Materials and methods

2.1. Carbon nanoparticles

Typical images of the CNPs investigated are shown in Figure 1. The dispersibility of the CNTs in aqueous medium was improved by oxidizing commercial multi-wall CNT (external diameter: 10–20 nm; length: 10–30 μm according to the supplier) produced by Chengdu Organic Chemicals Co. Ltd. (Sichuan, China) in concentrated HNO_3 (65%, Merck) (3 hours, 110 °C) in accordance with the procedure (including purification) of ref [35]. The oxidation process had practically no effect on the external diameter of the CNTs. The C/O ratio of the CNT (from X-ray photoelectron spectroscopy XPS) and the surface area S_{BET} (determined from low temperature nitrogen adsorption applying the Brunauer-Emmett-Teller model) were respectively 11.2 and 221 m^2/g.

Graphene oxide (GO) was obtained from natural graphite (from Madagascar) by the improved Hummer method [36]. The pristine GO suspension was purified by successive centrifugation (Jouan BR4i Multifunction Centrifuge, Thermo Scientific, USA;

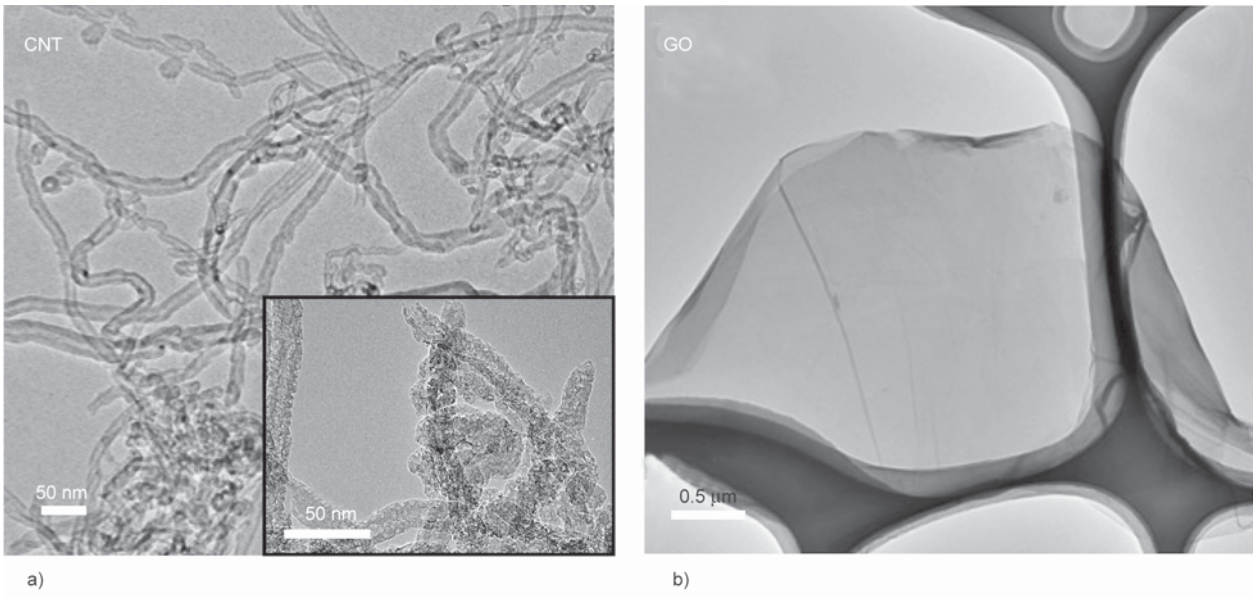

Figure 1. High resolution transmission electron microscopy (HRTEM) images of oxidized CNT (a) and GO (b)

5000 min^{-1}) and thorough washing with 1 M HCl and doubly distilled water. The stock suspension contained 0.2 w/w% GO. The C/O ratio and S_{BET} meast respectively.

2.2. Gel synthesis

The PNIPA polymer gel was synthesised from *N*-isopropylacrylamide (NIPA) monomer (Tokyo Chemical Industry Co., LTD., Tokyo, Japan) and *N,N′*-methylenebisacrylamide (BA) cross-linker (Sigma Aldrich) in aqueous medium with nominal molar ratio of [NIPA]/[BA] = 150 at 20 °C by free radical polymerization. The reaction was initiated by ammonium persulphate (APS, Sigma Aldrich) and *N,N,N′,N′* tetramethylethylenediamine (TEMED, Fluka). A detailed description is given elsewhere [37]. All chemicals were used as received except NIPA, which was recrystallized from toluene-hexane mixture prior to the synthesis. 2 mm thick films and 10×10 mm isometric cylinders were cast. Doubly distilled water was used in all experiments, including both synthesis and dialysis.

To obtain composite gels the aqueous CNP suspension of the required concentration was mixed with the precursor solution. For the CNT containing composites ultrasonication was used to ensure homogeneity of the dispersion. Gels with ≥20 mg GO/g NIPA content were prepared by adding in succession solid NIPA and BA to the GO suspension. The reaction medium was stirred in an ice-bath for 15 min after addition of each component. The precursor suspensions were polymerised and purified in the same way as the nanoparticle-free PNIPA gel. No external field was applied. The films were stored in the swollen state for later use, unless mentioned otherwise.

2.3. Scanning electron microscopy (SEM)

Dialysed gel films fully swollen at room temperature were frozen in liquid nitrogen and broken immediately (Figure 2) prior to lyophilization (Scanvac Coolsafe freeze dryer, Lynge, Denmark; T =25 °C, p = 10^{-2} mbar, 24 hours). After coating with metal alloy (atomic ratio Au:Pd = 1.5:1), SEM images were taken with a Hitachi SU6600 analytical variable pressure scanning electron microscope equipped with a ZrO/W Schottky field emission electron source and an environmental secondary electron detector (Hitachi Ltd., Tokyo, Japan). The size distribution of the pores was determined from 80–100 data for each sample.

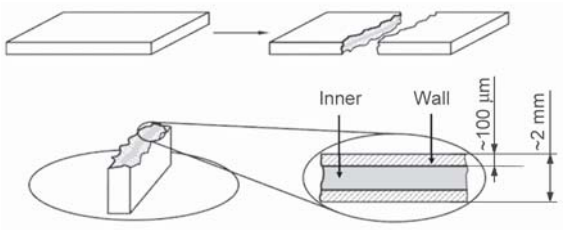

Figure 2. Preparation of gel films for SEM observation. The upper cartoon shows how the film was broken prior to freeze-drying. The lower cartoon shows how the sample was fixed on the SEM sample holder and gives the tentative thickness of the wall and bulk regions, respectively.

2.4. Macroscopic characterisation

To determine the equilibrium swelling degree m/m_0 (where m and m_0 are the mass of the swollen and the dry gel sample, respectively), 7 mm diameter discs cut from the dialysed swollen film were dried to constant mass in a desiccator over concentrated H_2SO_4, and then re-swollen to equilibrium in excess water at 20.0±0.2 °C.

Stress-strain studies were performed on fully swollen isometric (10×10 mm) gel cylinders with an INSTRON 5543 (INSTRON, Norwood, USA) mechanical testing equipment at ambient temperature. Samples were compressed until fracture, in steps of 0.1 mm in the small deformation region (<10% of their initial height) and in steps of 0.5 mm thereafter. The relaxation time and force threshold was 4×4 s and 300 N, respectively. The elastic modulus was determined by the method of Horkay and Zrínyi [38] in the small deformation region.

2.5. Kinetics of temperature induced phase transition

Prior to the measurements disks of 13 mm diameter were cut from the swollen film and kept at 20±0.2 °C for 2 days to allow them to reach equilibrium. The samples were then plunged into a water bath at 50±1 °C. The shrinkage induced by the thermal shock was recorded photographically by monitoring the diameter D of the disks. D values are given as the average of five different measurements read from the images by JMicroVision software and compared to the initial diameter D_0 of the fully swollen gels.

2.6. IR sensitivity

The surface of 10×10 mm swollen gel films, placed on a glass plate, was exposed to a CO_2 laser beam (wavelength: 10.6 μm, power: 0.500 W, spotsize: 15 mm). Thermal maps were recorded at ambient conditions as video files by a Testo 890 thermal imaging camera (Testo, Alton, UK) for 30 seconds prior to the irradiation, then during the 2 minute period of laser exposure. After irradiation the cooling of the gels was monitored for 2.5 minutes. During the irradiation the gel samples collapsed in a circular zone of 5 mm around the centre of the incident beam. The temperature of the irradiated gels was determined as the average temperature of 20 positions within this zone.

3. Results and discussion

3.1. Characterization

When CNPs were incorporated the transparent PNIPA gel became either brown (with GO), or black (with CNT). In CNT@PNIPA gels macroscopic heterogeneity due to aggregation can be observed (Figure 3). A 'wall region' and an 'inner region' are clearly distinguishable in the images (not shown here). Typical SEM images of both regions are displayed in Figure 4. In pure PNIPA films these two regions are very similar: wide amorphous pores separated by thin polymer walls. In the composite samples the morphology depends on the type of CNP. Both with CNT and GO the wall and inner regions, respectively, are significantly different, indicating that the orientation of the CNPs might be influenced by interaction with the wall. Nevertheless, the heat transfer during the freezing process may also lead to layer formation. In the composite gel cylinders further morphological differences developed along the axis, as a consequence of sedimentation during gelation, particularly with CNT. The pore size distributions of the CNT containing composites are not very different from pure PNIPA. By contrast, the influence on the pore structure of the GO content is unmistakably stronger (Figure 5). Interestingly, the effect at lower GO content is more marked.

On comparing the swelling degree and the elastic modulus of the hydrogels significant differences appear between the two sets of composites (Figure 6). CNT reduces the swelling degree slightly but monotonically, possibly in part due to the loss of volume occupied by the carbon. CNT has practically no effect on the elastic modulus of these gels.

A more pronounced, non-linear, effect is observed in the GO composites. Even 15 mg GO/g_{NIPA} content caused an abrupt drop by ca. 33% in the swelling degree. Further increase of the GO content has no observable effect on the swelling (Figure 6a). Such behaviour arises when the concentration of filler particles reaches the percolation threshold. The elastic modulus increases monotonically in the whole concentration range examined (Figure 6b). A similar observation has been reported by Fan *et al*. [39] for sodium alginate/polyacrylamide (PAM) hydrogels with comparable GO content (0.5–5 w/w%). PNIPA systems with significantly higher cross-link ratio and 1–10 w/w% GO content exhibit a contrary trend [34]. Figure 6c illustrates the influence of water content on the modulus. Incorporation of the CNPs substantially improves the compressive strength of the gels (Figure 6d). CNT@NIPA gels tolerate greater deformation before they break, while GO@PNIPA gels withstand higher stress at smaller deformation. The

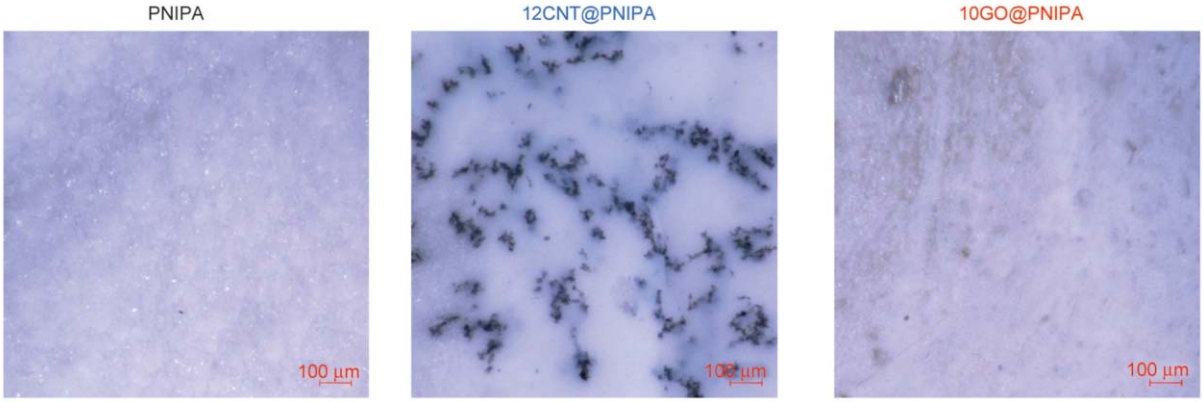

Figure 3. Digital optical microscopic images of the lyophilized cross section of the lyophilised gel films

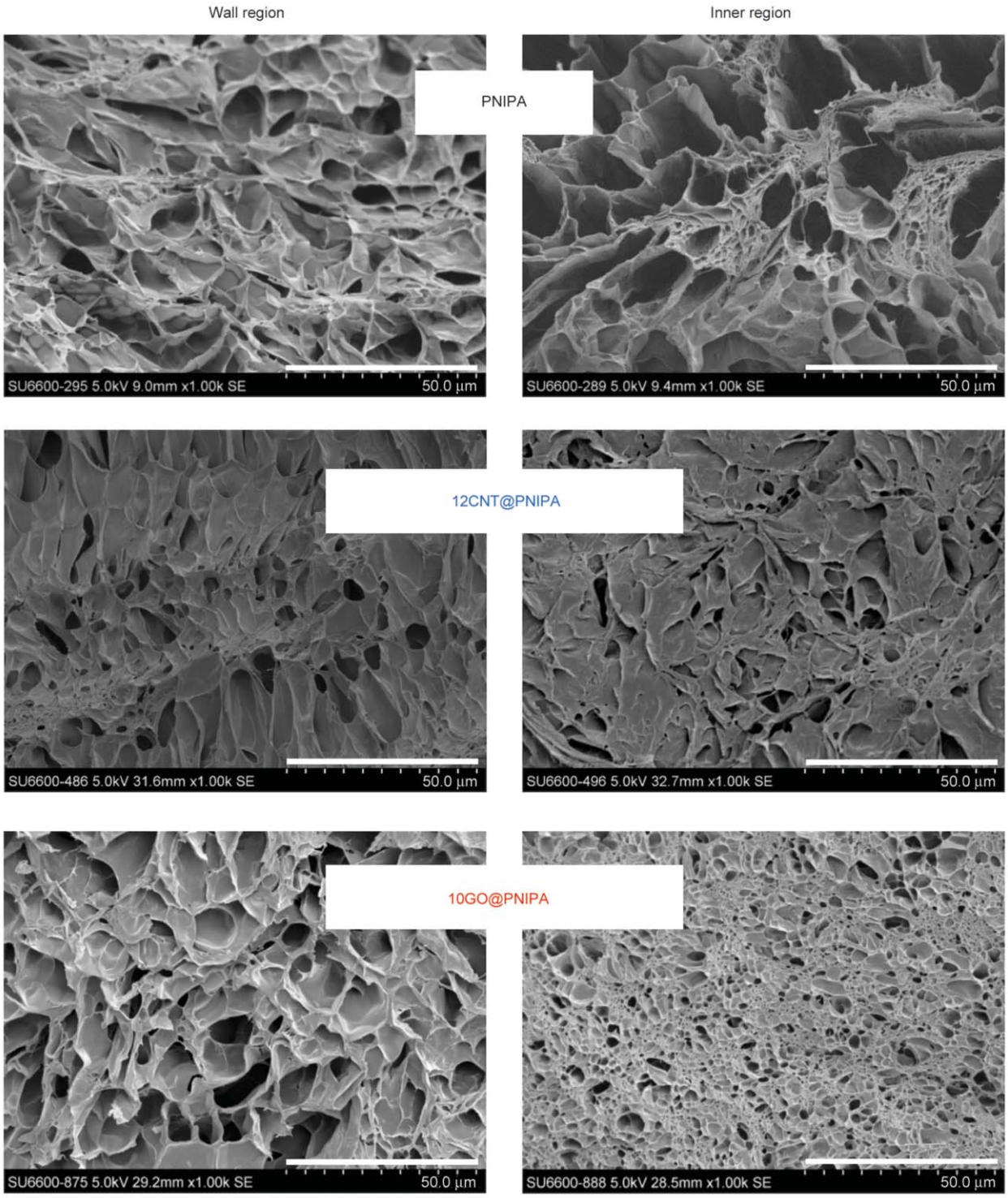

Figure 4. SEM images of CNP@PNIPA gel films dried in cryogenic conditions. Scale bar 50 µm.

effect of loading on the compressive strength with both fillers is plotted in Figure 6e. When GO is incorporated the compressive strength in PNIPA gels increases by almost an order of magnitude, and is independent of GO content; with CNT@NIPA gels the enhancement is slightly smaller.

3.2. Deswelling kinetics

On immersion in warm water disks of CNT@NIPA and GO@NIPA samples immediately turn white, similarly to pure PNIPA. Figure 7 shows that the presence of CNPs appreciably modifies the kinetic response of the PNIPA gel. During the temperature-

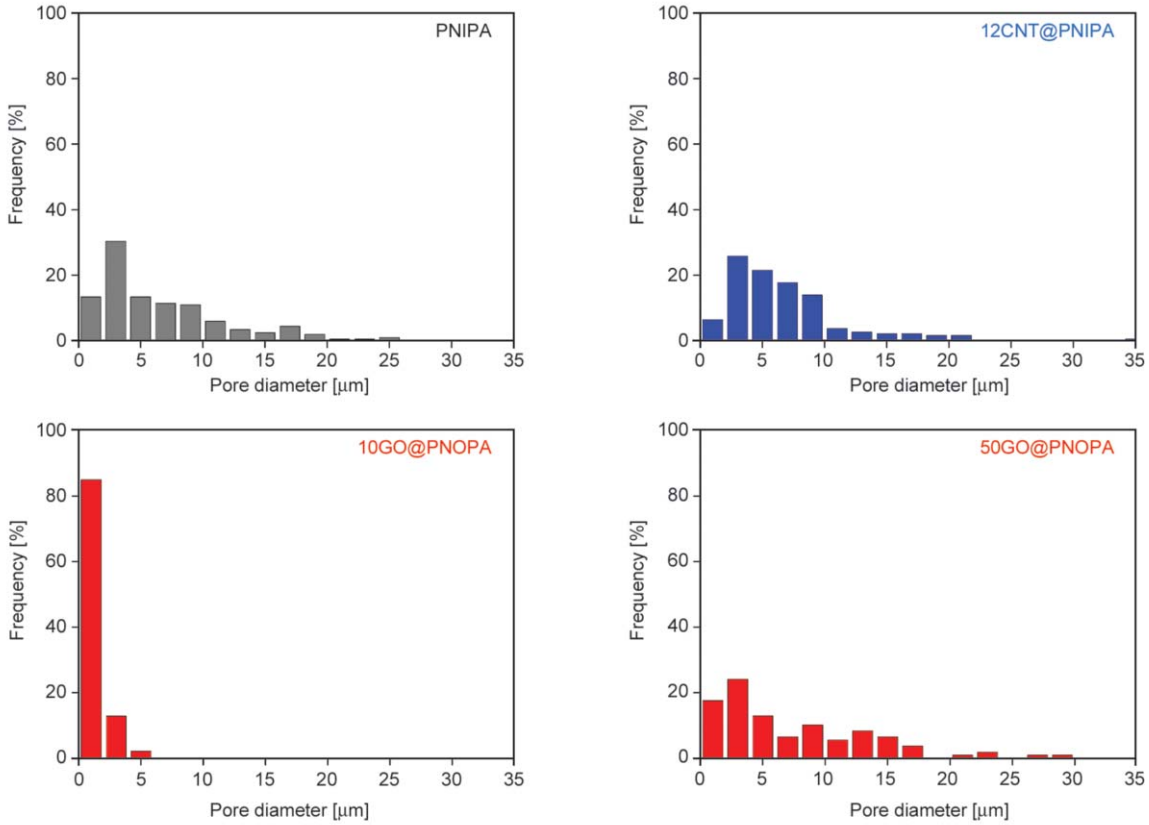

Figure 5. Pore size distribution of the bulk of CNP@PNIPA gel films dried in cryogenic condition

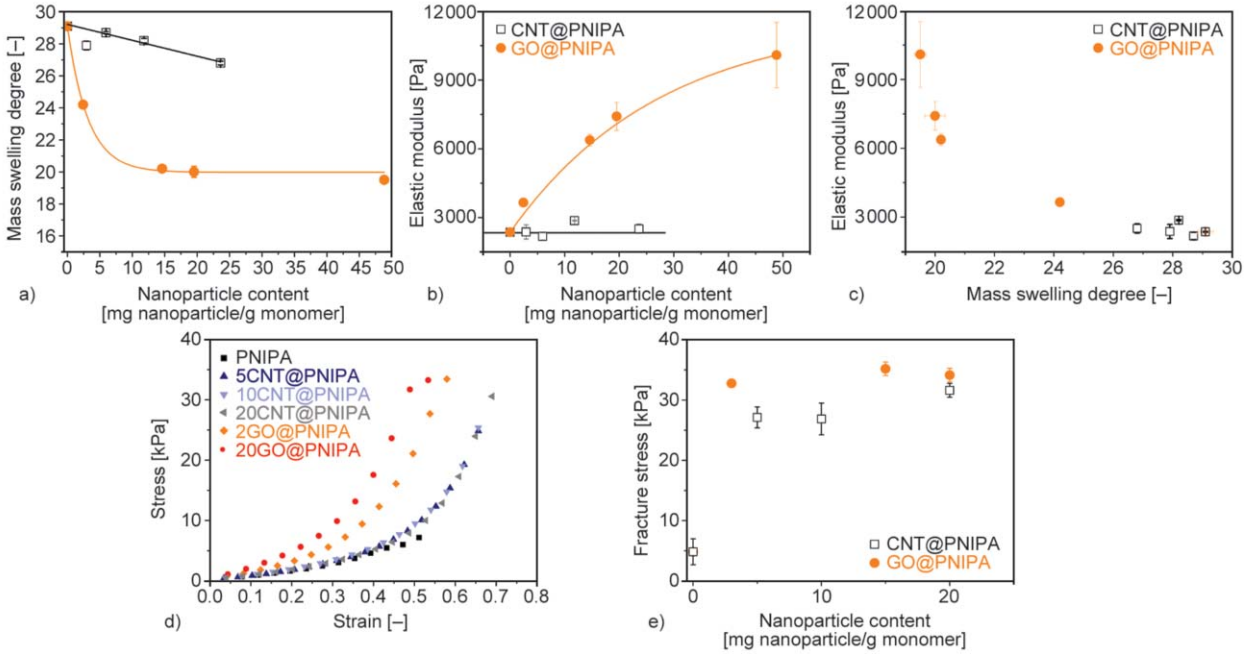

Figure 6. Mass swelling degree in pure water at 20 °C (a) and elastic modulus (b) of composite gels. Solid lines are guides for the eye. Correlation of modulus and swelling degree (c). Stress-strain curves (d). Compressive strength of composite gels (e).

jump the behaviour of the composite gels is strongly affected by both the quality and quantity of the CNPs. To quantify the effects the experimental shrinkage-curves were fit to a modified exponential decay function shown in Equation (1):

$$\frac{D}{D_0} = \left(\frac{D}{D_0}\right)_{\text{fin}} + A_1 \, \mathrm{e}^{-\left(\frac{t}{\tau}\right)^p} \tag{1}$$

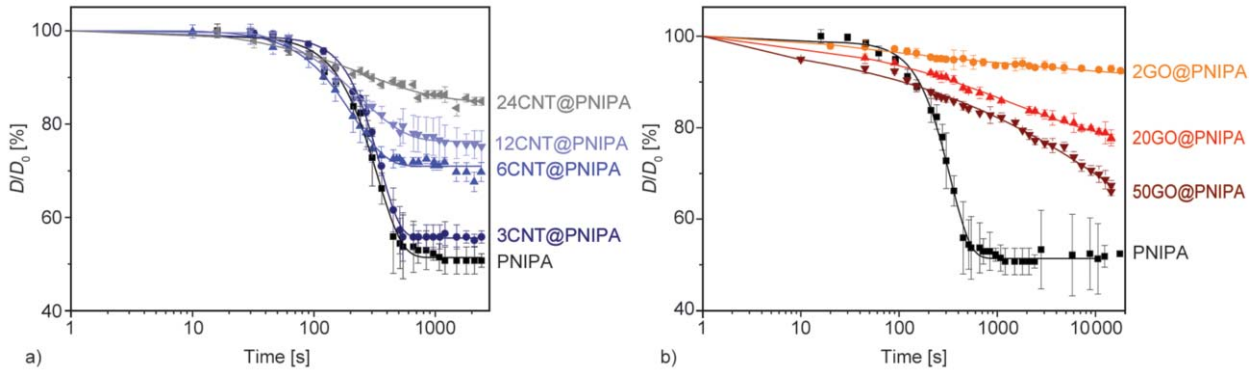

Figure 7. Deswelling kinetics of CNT@PNIPA (a) and GO@PNIPA (b) at 50 °C. Note the order of magnitude difference in range of the *x*-axis scales. Symbols are experimental data, continuous lines are fits to Equation (1).

where $(D/D_0)_{fin}$ is the final relative diameter, A is a pre-exponential constant and τ is the time constant of the overall volumetric thermal response. The results are listed in Table 1. The shrinkage curve of the pure PNIPA could be fit by a compressed exponential function ($p > 1$), indicating possible jamming behaviour, with a time constant in good agreement with previous observations [40]. The time constants of the CNT@PNIPA systems are shorter, i.e., CNT slightly accelerates the response of the pure PNIPA gel [40]. $(D/D_0)_{fin}$ correlates with the CNT content: higher loading results in more limited shrinkage. The value of exponent p decreases systematically and significantly with increasing CNT loading, a sign that deswelling becomes more complex at higher CNT concentrations (Table 1). In 24CNT@PNIPA (the highest CNT content tested) stretched exponential behaviour ($p > 1$) was found, characteristic of multiple relaxation processes with different timescales.

Whereas 2000 s was largely sufficient for the relaxation of CNT@PNIPA composites, a timeframe of even an order of magnitude longer was insufficient for the GO@PNIPA gels (Figure 7). For the GO@PNIPA samples the values of the fitting parameters (Table 1) can be used only for qualitative comparisons, as the absence of a measured asymptotic value of $(D/D_0)_{fin}$ makes the fitting parameters uncertain. It can nevertheless be concluded that, unlike CNT, the lowest GO content has the strongest effect on deswelling kinetics. Substantial slowing down of the thermal response is observed at all three concentrations (Figure 8), which resembles the effect of increased cross-linking density in pure PNIPA gels [40]. All curve fits yielded a stretching parameter $p < 1$, indicating multiple processes.

3.3. IR sensitivity

Recent experimental and theoretical studies found that the presence of network structure increases thermal diffusivity in PNIPA gels compared to pure water. It was also observed that latent heat influences thermal diffusivity [41].

Carbon materials including nanoparticles are known for their high IR absorption. As expected [25–27],

Table 1. Fitting parameters of the temperature induced phase transition from Equation (1)

Sample	$\left(\frac{D}{D_0}\right)_{fin}$ [%]	A [%]	τ [s]	p	R^2
PNIPA	51.4	47.5	334	2.14	0.995
3CNT@PNIPA	55.6	43.2	348	2.58	0.997
6CNT@PNIPA	71.0	29.1	211	1.60	0.990
12CNT@PNIPA	76.3	25.4	241	1.15	0.987
24CNT@PNIPA	84.9	16.0	259	0.721	0.971
2GO@PNIPA	90.5	9.5	1437	0.266	0.932
20GO@PNIPA	76.5	23.7	1470	0.412	0.994
50GO@PNIPA	34.2	60.1	53762	0.286	0.992

$(D/D_0)_{fin}$: relative diameter, A: pre-exponential factor; τ: time constant of deswelling response; p: exponent; R^2: coefficient of determination

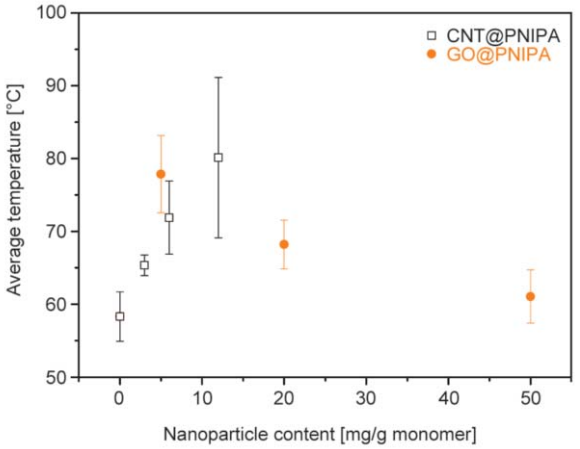

Figure 8. Average temperature values of PNIPA composites during IR laser exposure

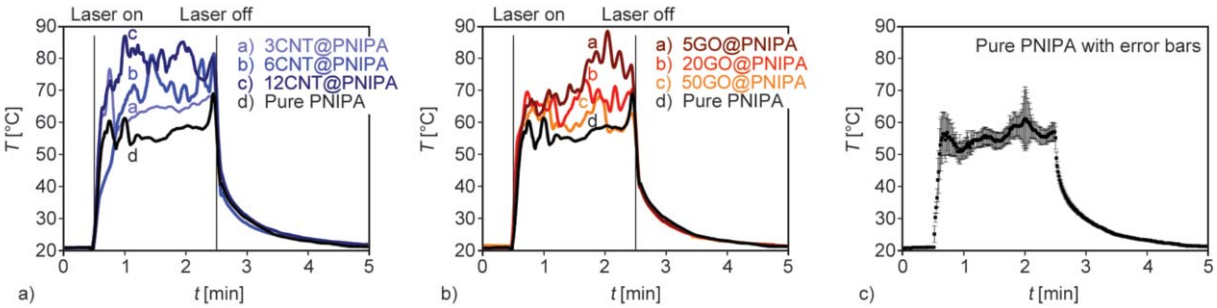

Figure 9. Temperature (T) profile of PNIPA composites upon IR laser exposure (t: observation time) at 20 °C (a, b), temperature profile of pure PNIPA with error bars (c)

addition of both CNT and GO results in enhanced IR sensitivity (Figures 8 and 9). The doped systems, however, display significant differences according to the type and concentration of nanoparticle incorporated.

Fast shrinkage on exposure to IR laser irradiation, and quick recovery of the gels after exposure is observed in all cases. During the exposure the gel samples collapse in a circular zone of diameter 5 mm centred around the incident beam. The measured temperature fluctuations may be attributed to the low thermal conductivity of the gel, even in the presence of CNPs (Figure 9a and Figure 9b). In both sets of systems a monotonic correlation was found between the nanoparticle content and the temperature of the sample, but with different trend. In the CNT@PNIPA systems the temperature rise in the gels with increasing CNT concentration was proportionally higher (Figure 8). Incorporating a small amount of GO into PNIPA resulted in the same enhanced response as CNT@NIPA with a similar CNT content, but further addition of GO systematically reduced the effect.

3.4. Discussion

The differences observed between the effects of the two different types of CNPs may stem more from their chemical behaviour than their geometrical shape. Multiwall carbon nanotubes contain Russian doll-like concentric tubes consisting of graphite like carbon arrays. The outermost cylinder is decorated with O-containing surface functional groups, but their concentration is relatively low. Therefore the functional groups do not significantly modify the aromatic graphitic structure. That is, during the PNIPA synthesis, the reactivity of the CNTs present in the radical polymerization is modest. However, as their surface is predominantly hydrophobic, they tend to aggregate, even after intense ultrasonication. GO, by contrast, is composed of a few strongly damaged graphene sheets richly decorated with O. The delocalised electron system is therefore severely disrupted and most of the electrons are localised as C=C double bonds, which are reactive in radical reactions. The hydrophilic surface also ensures good dispersibility. Owing to their surface chemistry, the GO platelets are well distributed in the polymerisation medium, which allows them to form a percolating GO network, consisting of hubs that are each covalently linked to several polymer chains; this outcome is less probable with the CNT aggregates. This difference in behaviour affects the response of the loaded gels during the swelling and stress-strain observations. While GO units build up to form an interpenetrating network that is strongly connected to the polymer chains, the CNTs act as 'free' aggregates. Increasing the CNT content increases the number of aggregates in the precursor solution. Hydrophilic GO forms bulky, randomly oriented GO clusters only at high concentrations.

The difference in electron structure also leads to the different heat conductivity and IR absorption performance of the gels when the two CNPs are present. At low concentration CNT has only a limited influence on the deswelling kinetics. Although increasing the CNT content may improve the heat conductivity, higher amounts of CNT filler delay the relaxation and increase the time constant. The chains must relax in the vicinity of more and more aggregates. Also, with CNTs, the higher their amount in the gel the greater is their IR absorption.

In the GO@PNIPA systems, the complexity of the deswelling process is reflected by the $p < 1$ relation that appears already at the lowest concentration. Several process may superimpose: i) increasing the GO units increases the number of potentially reactive

double bonds with no increase in the NIPA and BA concentration; ii) at a certain threshold concentration the GO platelets percolates and forms a connected interpenetrating network; iii) overall gel collapse is a slow process that requires ordering or stacking of the platelets. The strong IR absorption at low GO concentration and weaker absorption at high concentration than with CNT is further evidence of its connected network structure. In spite of the lower intrinsic thermal conductivity of GO, its percolating network inside the gel conducts heat more efficiently from the polymer matrix into the substrate than do the isolated CNT clusters [42].

4. Conclusions

Incorporation of CNT and GO into PNIPA hydrogels produces different effects on the behaviour of the hybrids. Apart from influencing the porous morphology of the composites, their effect on the swelling degree and the elastic modulus shows a different trend. The elastic modulus of PNIPA gel is enhanced by GO, while the swelling degree of the GO@PNIPA systems decreases significantly. By contrast, the swelling and mechanical properties of CNT@PNIPA composites are similar to those of pure PNIPA. Both types of particle substantially enhance the fracture stress tolerance of the PNIPA hydrogel.

Significant differences are observed in the thermal response of the two systems. The time constant and swelling ratio of the temperature-induced shrinkage can therefore be adjusted by selecting the type and amount of nanoparticle loading. This could provide a means for accurately controlling deswelling kinetics, e.g., in the drug release profile of PNIPA systems. This capacity could also be employed in sensor applications, where fast and excessive shrinkage can be a significant drawback. Both CNT and GO enhance the infrared sensitivity of the PNIPA gel, thus opening a route for constructing novel drug transport and actuator systems. The novelty of the present findings is to show that the influence on the gel behaviour of CNT and GO is different. This difference stems both from their different chemical reactivity during the gel synthesis and from their different geometry. In the one case the CNTs aggregate into separate clusters, while in the other the GO disperses in the gel to form a percolating, thermally conducting, network.

Acknowledgements

The authors thank Prof. K. Kaneko for providing the graphite sample and Prof. T. Maekawa for his valuable advice in the IR experiments. The financial support of Hungarian grant OTKA K101861 and EU project FP7-PEOPLE-2010-IRSES-269267 is acknowledged.

References

[1] Bradbury J. H., Fenn M. D., Gosney I.: The change of volume associated with the helix-coil transition in poly-γ-benzyl-L-glutamate. Journal of Molecular Biology, **11**, 137–140 (1965). DOI: 10.1016/S0022-2836(65)80179-6

[2] Heskins M., Guillet J. E.: Solution properties of poly (*N*-isopropylacrylamide). Journal of Macromolecular Science Part A: Chemistry, **2**, 1441–1455 (1968). DOI: 10.1080/10601326808051910

[3] Tanaka T.: Collapse of gels and the critical endpoint. Physical Review Letters, **40**, 820–823 (1978). DOI: 10.1103/PhysRevLett.40.820

[4] Ricka J., Tanaka T.: Swelling of ionic gels: Quantitative performance of the Donnan theory. Macromolecules, **17**, 2916–2921 (1984). DOI: 10.1021/ma00142a081

[5] Bae Y. H., Okano T., Kim S. W.: Temperature dependence of swelling of crosslinked poly(*N,N′*-alkyl substituted acrylamides) in water. Journal of Polymer Science Part B: Polymer Physics, **28**, 923–936 (1990). DOI: 10.1002/polb.1990.090280609

[6] Reinicke S., Döhler S., Tea S., Krekhova M., Messing R., Schmidt A. M., Schmalz H.: Magneto-responsive hydrogels based on maghemite/triblock terpolymer hybrid micelles. Soft Matter, **6**, 2760–2773 (2010). DOI: 10.1039/c000943a

[7] Schmaljohann D.: Thermo- and pH-responsive polymers in drug delivery. Advanced Drug Delivery Reviews, **58**, 1655–1670 (2006). DOI: 10.1016/j.addr.2006.09.020

[8] Manek E., Domján A., Madarász J., László K.: Interactions in aromatic probe molecule loaded poly(*N*-isopropylacrylamide) hydrogels and implications for drug delivery. European Polymer Journal, **68**, 657–664 (2015). DOI: 10.1016/j.eurpolymj.2015.03.043

[9] Kumar A., Srivastava A., Galaev I. Y., Mattiasson B.: Smart polymers: Physical forms and bioengineering applications. Progress in Polymer Science, **32**, 1205–1237 (2007). DOI: 10.1016/j.progpolymsci.2007.05.003

[10] Ionov L.: Hydrogel-based actuators: Possibilities and limitations. Materials Today, **17**, 494–503 (2014). DOI: 10.1016/j.mattod.2014.07.002

[11] Depa K., Strachota A., Šlouf M., Hromádková J.: Fast temperature-responsive nanocomposite PNIPAM hydrogels with controlled pore wall thickness: Force and rate of T-response. European Polymer Journal, **48**, 1997–2007 (2012).
DOI: 10.1016/j.eurpolymj.2012.09.007

[12] Coughlan D. C., Corrigan O. I.: Drug–polymer interactions and their effect on thermoresponsive poly(*N*-isopropylacrylamide) drug delivery systems. International Journal of Pharmaceutics, **313**, 163–174 (2006).
DOI: 10.1016/j.ijpharm.2006.02.005

[13] Schexnailder P., Schmidt G.: Nanocomposite polymer hydrogels. Colloid and Polymer Science, **287**, 1–11 (2009).
DOI: 10.1007/s00396-008-1949-0

[14] Cirillo G., Hampel S., Spizzirri U. G., Parisi O. I., Picci N., Iemma F.: Carbon nanotubes hybrid hydrogels in drug delivery: A perspective review. BioMed Research International, **2014**, 825017/1–825017/17 (2014).
DOI: 10.1155/2014/825017

[15] Sahoo N. G., Rana S., Cho J. W., Li L., Chan S. H.: Polymer nanocomposites based on functionalized carbon nanotubes. Progress in Polymer Science, **35**, 837–867 (2010).
DOI: 10.1016/j.progpolymsci.2010.03.002

[16] Pandey G., Wolters M., Thostenson E. T., Heider D.: Localized functionally modified glass fibers with carbon nanotube networks for crack sensing in composites using time domain reflectometry. Carbon, **50**, 3816–3825 (2012).
DOI: 10.1016/j.carbon.2012.04.008

[17] Tsonos C., Pandis C., Soin N., Sakellari D., Myrovali E., Kripotou S., Kanapitsas A., Siores E.: Multifunctional nanocomposites of poly(vinylidene fluoride) reinforced by carbon nanotubes and magnetite nanoparticles. Express Polymer Letters, **9**, 1104–1118 (2015).
DOI: 10.3144/expresspolymlett.2015.99

[18] Voitko K., Tóth A., Demianenko E., Dobos G., Berke B., Bakalinska O., Grebenyuk A., Tombácz E., Kuts V., Tarasenko Y., Kartel M., László K.: Catalytic performance of carbon nanotubes in H_2O_2 decomposition: Experimental and quantum chemical study. Journal of Colloid and Interface Science, **437**, 283–290 (2015).
DOI: 10.1016/j.jcis.2014.09.045

[19] Tóth A., Törőcsik A., Tombácz E., Oláh E., Heggen M., Li C., Klumpp E., Geissler E., László K.: Interaction of phenol and dopamine with commercial MWCNTs. Journal of Colloid and Interface Science, **364**, 469–475 (2011).
DOI: 10.1016/j.jcis.2011.08.044

[20] Yun J., Im J. S., Lee Y-S., Kim H-I.: Electro-responsive transdermal drug delivery behavior of PVA/PAA/MWCNT nanofibers. European Polymer Journal, **47**, 1893–1902 (2011).
DOI: 10.1016/j.eurpolymj.2011.07.024

[21] Kim H., Abdala A. A., Macosko C. W.: Graphene/polymer nanocomposites. Macromolecules, **43**, 6515–6530 (2010).
DOI: 10.1021/ma100572e

[22] Kuila T., Bose S., Mishra A. K., Khanra P., Kim N. H., Lee J. H.: Chemical functionalization of graphene and its applications. Progress in Materials Science, **57**, 1061–1105 (2012).
DOI: 10.1016/j.pmatsci.2012.03.002

[23] Wu X., Lin T. F., Tang Z. H., Guo B. C., Huang G. S.: Natural rubber/graphene oxide composites: Effect of sheet size on mechanical properties and straininduced crystallization behavior. Express Polymer Letters, **9**, 672–685 (2015).
DOI: 10.3144/expresspolymlett.2015.63

[24] Pedrazzoli D., Dorigato A., Conti T., Vanzetti L., Bersani M., Pegoretti A.: Liquid crystalline polymer nanocomposites reinforced with *in-situ* reduced graphene oxide. Express Polymer Letters, **9**, 709–720 (2015).
DOI: 10.3144/expresspolymlett.2015.66

[25] Zhu C-H., Lu Y., Peng J., Chen J-F., Yu S-H.: Photothermally sensitive poly(*N*-isopropylacrylamide)/graphene oxide nanocomposite hydrogels as remote light-controlled liquid microvalves. Advanced Functional Materials, **22**, 4017–4022 (2012).
DOI: 10.1002/adfm.201201020

[26] Miyako E., Nagata H., Hirano K., Hirotsu T.: Photodynamic thermoresponsive nanocarbon–polymer gel hybrids. Small, **4**, 1711–1715 (2008).
DOI: 10.1002/smll.200800601

[27] Zhang X., Pint C. L., Lee M. H., Schubert B. E., Jamshidi A., Takei K., Ko H., Gillies A., Bardhan R., Urban J. J., Wu M., Fearing R., Javey A.: Optically- and thermally-responsive programmable materials based on carbon nanotube-hydrogel polymer composites. Nano Letters, **11**, 3239–3244 (2011).
DOI: 10.1021/nl201503e

[28] Szeluga U., Kumanek B., Trzebicka B.: Synergy in hybrid polymer/nanocarbon composites. A review. Composites Part A: Applied Science and Manufacturing, **73**, 204–231 (2015).
DOI: 10.1016/j.compositesa.2015.02.021

[29] Chen Y-S., Tsou P-C., Lo J-M., Tsai H-C., Wang Y-Z., Hsiue G-H.: Poly(*N*-isopropylacrylamide) hydrogels with interpenetrating multiwalled carbon nanotubes for cell sheet engineering. Biomaterials, **34**, 7328–7334 (2013).
DOI: 10.1016/j.biomaterials.2013.06.017

[30] Islam M. F., Alsayed A. M., Dogic Z., Zhang J., Lubensky T. C., Yodh A. G.: Nematic nanotube gels. Physical Review Letters, **92**, 088303/1–088303/4 (2004).
DOI: 10.1103/PhysRevLett.92.088303

[31] Yang Z., Cao Z., Sun H., Li Y.: Composite films based on aligned carbon nanotube arrays and a poly(*N*-isopropyl acrylamide) hydrogel. Advanced Materials, **20**, 2201–2205 (2008).
DOI: 10.1002/adma.200701964

[32] Li Z., Shen J., Ma H., Lu X., Shi M., Li N., Ye M.: Preparation and characterization of pH- and temperature-responsive hydrogels with surface-functionalized graphene oxide as the crosslinker. Soft Matter, **8**, 3139–3145 (2012).
DOI: 10.1039/c2sm07012j

[33] Lo C-W., Zhu D., Jiang H.: An infrared-light responsive graphene-oxide incorporated poly(*N*-isopropylacrylamide) hydrogel nanocomposite. Soft Matter, **7**, 5604–5609 (2011).
DOI: 10.1039/c1sm00011j

[34] Ma X., Li Y., Wang W., Ji Q., Xia Y.: Temperature-sensitive poly(*N*-isopropylacrylamide)/graphene oxide nanocomposite hydrogels by *in situ* polymerization with improved swelling capability and mechanical behavior. European Polymer Journal, **49**, 389–396 (2013). DOI: 10.1016/j.eurpolymj.2012.10.034

[35] Wang Z., Shirley M. D., Meikle S. T., Whitby R. L. D., Mikhalovsky S. V.: The surface acidity of acid oxidised multi-walled carbon nanotubes and the influence of in-situ generated fulvic acids on their stability in aqueous dispersions. Carbon, **47**, 73–79 (2009).
DOI: 10.1016/j.carbon.2008.09.038

[36] Marcano D. C., Kosynkin D. V., Berlin J. M., Sinitskii A., Sun Z., Slesarev A., Alemany L. B., Lu W., Tour J. M.: Improved synthesis of graphene oxide. ACS Nano, **4**, 4806–4814 (2010).
DOI: 10.1021/nn1006368

[37] László K., Kosik K., Rochas C., Geissler E.: Phase transition in poly(*N*-isopropylacrylamide) hydrogels induced by phenols. Macromolecules, **36**, 7771–7776 (2003).
DOI: 10.1021/ma034531u

[38] Horkay F., Zrínyi M.: Studies on the mechanical and swelling behavior of polymer networks based on the scaling concept. 4. Extension of the scaling approach to gels swollen to equilibrium in a diluent of arbitrary activity. Macromolecules, **15**, 1306–1310 (1982).
DOI: 10.1021/ma00233a018

[39] Fan J., Shi Z., Lian M., Li H., Yin J.: Mechanically strong graphene oxide/sodium alginate/polyacrylamide nanocomposite hydrogel with improved dye adsorption capacity. Journal of Materials Chemistry A, **1**, 7433–7443 (2013).
DOI: 10.1039/c3ta10639j

[40] László K., Fluerasu A., Moussaïd A., Geissler E.: Deswelling kinetics of PNIPA gels. Soft Matter, **6**, 4335–4338 (2010).
DOI: 10.1039/C0SM00297F

[41] Tél A., Bauer R. A., Varga Z., Zrínyi M.: Heat conduction in poly(*N*-isopropylacrylamide) hydrogels. International Journal of Thermal Sciences, **85**, 47–53 (2014).
DOI: 10.1016/j.ijthermalsci.2014.06.005

[42] Karásek L., Meissner B., Asai S., Sumita M.: Percolation concept: Polymer-filler gel formation, electrical conductivity and dynamic electrical properties of carbon-black-filled rubbers. Polymer Journal, **28**, 121–126 (1996).
DOI: 10.1295/polymj.28.121